

<sup>1</sup> Observation of the Higgs boson in the  $WW^*$   
<sup>2</sup> channel and search for Higgs boson pair  
<sup>3</sup> production in the  $b\bar{b}b\bar{b}$  channel with the  
<sup>4</sup> ATLAS detector

<sup>5</sup> A DISSERTATION PRESENTED  
<sup>6</sup> BY  
<sup>7</sup> TOMO LAZOVICH  
<sup>8</sup> TO  
<sup>9</sup> THE DEPARTMENT OF PHYSICS

<sup>10</sup> IN PARTIAL FULFILLMENT OF THE REQUIREMENTS  
<sup>11</sup> FOR THE DEGREE OF  
<sup>12</sup> DOCTOR OF PHILOSOPHY  
<sup>13</sup> IN THE SUBJECT OF  
<sup>14</sup> PHYSICS

<sup>15</sup> HARVARD UNIVERSITY  
<sup>16</sup> CAMBRIDGE, MASSACHUSETTS  
<sup>17</sup> MAY 2016

<sup>18</sup> ©2016 – TOMO LAZOVICH

<sup>19</sup> ALL RIGHTS RESERVED.

20      **Observation of the Higgs boson in the  $WW^*$  channel and search  
 21      for Higgs boson pair production in the  $b\bar{b}b\bar{b}$  channel with the  
 22      ATLAS detector**

23      ABSTRACT

24      This dissertation presents two studies: the observation and measurement of the Higgs boson in the  
 25       $H \rightarrow WW^* \rightarrow \ell\nu\ell\nu$  channel at  $\sqrt{s} = 7$  TeV and  $\sqrt{s} = 8$  TeV and a search for Higgs pair pro-  
 26      duction in the  $HH \rightarrow b\bar{b}b\bar{b}$  channel at  $\sqrt{s} = 13$  TeV with the ATLAS detector in  $pp$  collisions at the  
 27      Large Hadron Collider.

28      First, the discovery of a particle consistent with the Higgs in  $4.8 \text{ fb}^{-1}$  at  $\sqrt{s} = 7$  TeV and  $5.8 \text{ fb}^{-1}$  at  
 29       $\sqrt{s} = 8$  TeV is discussed. Then, the measurement of the Higgs boson signal strength and cross section  
 30      in both the gluon fusion and vector boson fusion (VBF) production modes using  $20.3 \text{ fb}^{-1}$  of  $\sqrt{s} =$   
 31       $8$  TeV data combined with  $4.8 \text{ fb}^{-1}$  of  $7$  TeV data is shown. The combined signal strength is measured  
 32      to be  $\mu = 1.09^{+0.23}_{-0.21}$ . The total observed significance of the  $H \rightarrow WW^*$  process is observed to be  
 33       $6.1\sigma$  (with  $5.8\sigma$  expected). Advanced methods for background reduction and estimation, particularly in  
 34      same-flavor lepton final states, are shown. The VBF signal strength is measured to be  $\mu_{\text{VBF}} = 1.27^{+0.53}_{-0.45}$   
 35      with an observed significance of  $3.2\sigma$  (with  $2.7\sigma$  expected). In the VBF channel, a selection requirement  
 36      based method, the precursor to the final multivariate technique used for the result, is detailed.

37      Finally, a search for Higgs pair production in the  $b\bar{b}b\bar{b}$  final state with  $3.2 \text{ fb}^{-1}$  at  $\sqrt{s} = 13$  TeV  
 38      is presented. A particular focus is placed on a tailored signal region for resonant production of Higgs  
 39      pairs at high masses, utilizing novel techniques in object reconstruction to increase signal acceptance in  
 40      boosted final state topologies. No significant excesses are observed, and upper limits on cross sections are  
 41      placed for spin-2 Randall Sundrum gravitons (RSG) and narrow spin-0 resonances. The cross section of  
 42       $\sigma(pp \rightarrow G_{\text{KK}}^* \rightarrow hh \rightarrow b\bar{b}b\bar{b})$  with  $k/\bar{M}_{\text{Pl}} = 1$  is constrained to be less than  $70 \text{ fb}$  for masses in the  
 43      range  $600 < m_{G_{\text{KK}}^*} < 3000 \text{ GeV}$ . For the RSG model with  $k/\bar{M}_{\text{Pl}} = 2$ , cross sections limits between  
 44       $40 \text{ fb}$  and  $200 \text{ fb}$  are set for the mass range of  $500 < m_{G_{\text{KK}}^*} < 3000 \text{ GeV}$ . The cross section upper  
 45      limits for  $\sigma(pp \rightarrow H \rightarrow hh \rightarrow b\bar{b}b\bar{b})$  ranges from  $30$  to  $300 \text{ fb}$  in the mass range of  $500 < m_H <$   
 46       $3000 \text{ GeV}$ .

# Contents

47

48	o INTRODUCTION	I
49	I Theoretical and Experimental Background	5
50	I.1 THE PHYSICS OF THE HIGGS BOSON	6
51	I.1.1 The Standard Model of Particle Physics	6
52	I.1.2 Electroweak Symmetry Breaking and the Higgs	8
53	I.1.3 Higgs Boson Production and Decay	II
54	I.1.4 Higgs Pair Production in the Standard Model	15
55	I.1.5 Higgs Pair Production in Theories Beyond the Standard Model	16
56	I.1.6 Conclusion	21
57	2 THE ATLAS DETECTOR AND THE LARGE HADRON COLLIDER	22
58	2.1 The Large Hadron Collider	23
59	2.2 The ATLAS Detector	25
60	2.3 The ATLAS Muon New Small Wheel Upgrade	36
61	2.4 Object Reconstruction in ATLAS	40
62	II Observation and measurement of Higgs boson decays to $WW^*$ in LHC	
63	Run 1 at $\sqrt{s} = 7$ and 8 TeV	49
64	3 $H \rightarrow WW^* \rightarrow \ell\nu\ell\nu$ ANALYSIS STRATEGY	50
65	3.1 Introduction	50
66	3.2 The $H \rightarrow WW^* \rightarrow \ell\nu\ell\nu$ signal in ATLAS	51
67	3.3 Background processes	52
68	3.4 Shared signal region selection requirements	56
69	3.5 Background reduction in same-flavor final states	58
70	3.6 Parameters of interest and statistical treatment	64
71	4 THE DISCOVERY OF THE HIGGS BOSON AND THE ROLE OF THE $H \rightarrow WW^* \rightarrow \ell\nu\ell\nu$ CHANNEL	
72	4.1 Introduction	70

74	4.2	Data and simulation samples . . . . .	71
75	4.3	$H \rightarrow WW \rightarrow e\nu\mu\nu$ search . . . . .	71
76	4.4	$H \rightarrow \gamma\gamma$ search . . . . .	76
77	4.5	$H \rightarrow ZZ \rightarrow 4\ell$ search . . . . .	77
78	4.6	Combined results . . . . .	79
79	4.7	Conclusion . . . . .	81
80	5	OBSERVATION OF VECTOR BOSON FUSION PRODUCTION OF $H \rightarrow WW^* \rightarrow \ell\nu\ell\nu$ . . . . .	83
81	5.1	Introduction . . . . .	83
82	5.2	Data and simulation samples . . . . .	84
83	5.3	Object selection . . . . .	88
84	5.4	Analysis selection . . . . .	91
85	5.5	Background estimation . . . . .	99
86	5.6	Systematic uncertainties . . . . .	110
87	5.7	Results . . . . .	114
88	6	COMBINED RUN I $H \rightarrow WW^* \rightarrow \ell\nu\ell\nu$ RESULTS . . . . .	119
89	6.1	Introduction . . . . .	119
90	6.2	Results of dedicated gluon fusion $H \rightarrow WW^* \rightarrow \ell\nu\ell\nu$ search . . . . .	120
91	6.3	Signal strength measurements in ggF and VBF production . . . . .	122
92	6.4	Measurement of Higgs couplings to vector bosons and fermions . . . . .	125
93	6.5	Higgs production cross section measurement . . . . .	126
94	6.6	Conclusion . . . . .	127
95	III	Search for Higgs pair production in the $HH \rightarrow b\bar{b}b\bar{b}$ channel in LHC	
96		Run 2 at $\sqrt{s} = 13$ TeV . . . . .	129
97	7	SEARCH FOR HIGGS PAIR PRODUCTION IN BOOSTED $b\bar{b}b\bar{b}$ FINAL STATES . . . . .	130
98	7.1	Introduction . . . . .	130
99	7.2	Motivation . . . . .	131
100	7.3	Data and simulation samples . . . . .	133
101	7.4	Event reconstruction and object selection . . . . .	135
102	7.5	Event selection . . . . .	138
103	7.6	Data-driven background estimation . . . . .	141
104	7.7	Systematic uncertainties . . . . .	147
105	7.8	Results . . . . .	150

<sup>106</sup>	<b>8 COMBINED LIMITS FROM BOOSTED AND RESOLVED SEARCHES</b>	<sup>152</sup>
<sup>107</sup>	<b>8.1 Introduction</b> . . . . .	<sup>152</sup>
<sup>108</sup>	<b>8.2 Resolved results</b> . . . . .	<sup>153</sup>
<sup>109</sup>	<b>8.3 Search technique and results</b> . . . . .	<sup>153</sup>
<sup>110</sup>	<b>8.4 Limit setting</b> . . . . .	<sup>154</sup>
<sup>111</sup>	<b>IV Looking ahead</b>	<sup>158</sup>
<sup>112</sup>	<b>9 CONCLUSION</b>	<sup>159</sup>
<sup>113</sup>	<b>APPENDIX A OPTIMIZATION OF <math>b</math>-TAGGING WORKING POINT IN <math>X \rightarrow HH \rightarrow b\bar{b}b\bar{b}</math></b>	
<sup>114</sup>	<b>SEARCH</b>	<sup>161</sup>
<sup>115</sup>	<b>APPENDIX B <math>b</math>-TAGGING EFFICIENCY AT HIGH <math>p_T</math></b>	<sup>162</sup>
<sup>116</sup>	<b>REFERENCES</b>	<sup>171</sup>

# Listing of figures

118	1.1	The particles of the Standard Model and their properties[1]. . . . .	7
119	1.2	The four most common Higgs boson production modes at the LHC: (a) gluon-gluon fusion, (b) vector boson fusion, (c) $W/Z + H$ production, (d) $t\bar{t}H$ production . . . . .	II
120	1.3	Higgs production cross sections as a function of center of mass energy ( $\sqrt{s}$ ) at a $pp$ collider[2]. . . . .	12
121	1.4	Higgs boson branching ratios as a function of $m_H$ [2]. . . . .	14
122	1.5	The two leading diagrams for Standard Model di-Higgs production at the LHC: (a) box diagram, (b) Higgs self coupling . . . . .	16
123	1.6	Diagrams with new vertices for non-resonant Higgs pair production arising in composite Higgs models . . . . .	17
124	1.7	Generic Feynman diagram for resonant Higgs pair production in BSM theories . . . . .	18
125	1.8	Branching ratios for a spin-2 Randall-Sundrum graviton as a function of mass computed in MadGraph with the CP3-Origins implementation [3, 4] . . . . .	18
126	1.9	$\sigma \times BR(HH)$ for RSG as a function of mass computed in MadGraph with the CP3-Origins implementation [3, 4] . . . . .	19
127	1.10	RSG width as a function of mass computed in MadGraph with the CP3-Origins implementation [3, 4] . . . . .	20
128	1.11	Branching ratios for heavy Higgs $H$ in Type I (left) and Type II (right) 2HDM models with $\tan \beta = 1.5$ and $\cos(\beta - \alpha) = 0.1(0.01)$ for Type I (Type II). [5] . . . . .	21
129	2.1	A schematic view of the LHC ring [6] . . . . .	23
130	2.2	A full diagram of the ATLAS detector [7] . . . . .	26
131	2.3	The ATLAS coordinate system . . . . .	27
132	2.4	Layout of the ATLAS Inner Detector system [8] . . . . .	28
133	2.5	Layout of the ATLAS calorimeter system [7] . . . . .	30
134	2.6	Layout of the ATLAS muon system [7] . . . . .	32
135	2.7	Predicted field integral as a function of $ \eta $ for the ATLAS magnet system [7] . . . . .	34
136	2.8	ATLAS trigger rates for Level-1 triggers as a function of instantaneous luminosity in 2012 and 2015 operation. These are single object triggers for electromagnetic clusters (EM), muons (MU), jets (J), missing energy (XE), and $\tau$ leptons (TAU). The threshold of the trigger is given in the name in GeV. [9] . . . . .	35
137	2.9	Instantaneous luminosity as a function of time for data recorded by ATLAS at different center of mass energies [10, 11] . . . . .	36

149	2.10	MDT tube hit (solid) and segment (dashed) efficiency as a function of hit rate per tube [12]	38
150	2.11	Trigger rate as a function of $p_T$ threshold with and without the NSW upgrade [12] . . . . .	38
151	2.12	Illustrations of the geometry (left) and operating principle (right) of the micromegas detector [12] . . . . .	39
153	2.13	Geometry of the sTGC detector [12] . . . . .	40
154	2.14	Illustration of particle interactions in ATLAS [13] . . . . .	41
155	2.15	Electron performance: (a) reconstruction efficiency as a function of electron $E_T$ [14] (b) energy resolution in simulation as a function of $ \eta $ for different energy electrons [15] . . . . .	42
157	2.16	Muon performance: (a) reconstruction efficiency as a function of muon $p_T$ (b) dimuon mass resolution as a function of average $p_T$ [16] . . . . .	44
159	2.17	Jet energy response after calibration as a function of true $p_T$ in simulation [17] . . . . .	45
160	2.18	Light jet rejection (1/efficiency) vs. $b$ -jet efficiency for MV1 and its input algorithms (a) [18] and MV2 (b) [19] in simulated $t\bar{t}$ events. The numbers in the algorithm names in (b) refer to the fraction of charm events used in the MV2 training. . . . .	46
163	2.19	Resolution of $E_T^{\text{miss}}$ components as a function of $\sum E_T$ before pileup suppression with different pileup techniques [20] . . . . .	48
165	3.1	Branching ratios for a $WW$ system. $q$ refers to quarks. $\ell$ can be either an electron or muon, and the leptonic branching ratios of the $\tau$ are included. For example, the $\ell\nu qq$ final state includes one $W$ decaying to $e\nu$ , $\mu\nu$ , or $\tau\nu$ . $\tau_h$ refer to hadronic decays of the $\tau$ . . . . .	52
166	3.2	Feynman diagram for Standard Model $WW$ production . . . . .	53
169	3.3	Feynman diagrams for top pair production (left) and $Wt$ production (right) . . . . .	54
170	3.4	An example Feynman diagram of $W + \text{jets}$ production . . . . .	54
171	3.5	An example Feynman diagram of $Z + \text{jets}$ production . . . . .	55
172	3.6	An illustration of the unique analysis signal regions[21] . . . . .	56
173	3.7	A graphical illustration of the $E_{T,\text{rel}}^{\text{miss}}$ calculation . . . . .	58
174	3.8	Predicted backgrounds (compared with data) as a function of $n_j$ (a and b) and $n_b$ (c) . . . . .	59
175	3.9	An event display of a $Z/\gamma^* + \text{jets}$ event illustrating the effect of pileup interactions . . . . .	60
176	3.10	The RMS of different missing transverse momentum definitions as a function of the average number of interactions per bunch crossing . . . . .	61
177	3.11	The difference between the true and reconstructed values of the missing transverse momentum (a) and $m_T$ (b) in a gluon fusion signal sample . . . . .	62
180	3.12	Comparison of $f_{\text{recoil}}$ distributions for $Z/\gamma^* + \text{jets}$ , $H \rightarrow WW^*$ , and other backgrounds with real neutrinos. . . . .	63
182	3.13	Signal significance as a function of required value for $f_{\text{recoil}}$ and $p_{T,\text{rel}}^{\text{miss}(\text{trk})}$ in the ggF $H \rightarrow WW^*$ with $n_j = 0$ . . . . .	64

184	4.1	Jet multiplicity distribution in data and MC after applying lepton, jet, and $E_{\text{T},\text{rel}}^{\text{miss}}$ selections.	
185		The $WW$ and top backgrounds have been normalized using control samples, and the hashed	
186		band indicates the total uncertainty on the prediction. [22] . . . . .	72
187	4.2	Comparison of $m_{\text{T}}$ between data and simulation in the $n_j = 0$ $WW$ (a) and $n_j = 1$	
188		top (b) control samples [22] . . . . .	74
189	4.3	$m_{\text{T}}$ distribution in the $H \rightarrow WW \rightarrow e\nu\mu\nu n_j \leq 1$ channels for 8 TeV data[22]. . . . .	76
190	4.4	Diphoton mass spectrum in 7 and 8 TeV data. Panel a) shows the unweighted data distri-	
191		bution superimposed on the background fit, while panel c) shows the data where each event	
192		category is weighted by its signal to background ratio. Panels b) and d) show the respective	
193		distributions with background subtracted[22]. . . . .	77
194	4.5	Four lepton invariant mass spectrum ( $m_{4\ell}$ ) in 7 and 8 TeV data compared to background	
195		estimate. A 125 GeV SM Higgs signal is shown in blue[22]. . . . .	78
196	4.6	Local $p_0$ distribution as a function of hypothesized Higgs mass for the $H \rightarrow ZZ^* \rightarrow 4\ell$	
197		(a), $H \rightarrow \gamma\gamma$ (b), and $H \rightarrow WW^* \rightarrow \ell\nu\ell\nu$ (c) channels. Dashed curves show expected	
198		results, while solid curves show observed. Red curves are from 7 TeV data, blue curves from	
199		8 TeV, and black curved combined[22]. . . . .	80
200	4.7	Combined 95% CL limits (a), local $p_0$ values (b), and signal strength measurement (c) as a	
201		function of Higgs mass[22]. . . . .	81
202	4.8	Comparison of measured signal strength $\mu$ for a 126 GeV Higgs in the 7 and 8 TeV datasets[22].	82
203	4.9	Two dimensional likelihood as a function of signal strength $\mu$ and Higgs mass $m_H$ [22]. . . . .	82
204	5.1	A comparison of the subleading lepton $p_{\text{T}}$ spectrum between VBF $H \rightarrow WW^*$ production	
205		and $t\bar{t}$ background . . . . .	85
206	5.2	Leading jet $\eta$ in VBF $H \rightarrow WW^*$ (red) and $t\bar{t}$ (black) . . . . .	93
207	5.3	Distributions of (a) $m_{jj}$ , (b) $\Delta y_{jj}$ , (c) $C_{\ell 1}$ , and (d) $\sum m_{\ell j}$ , for the VBF analysis. The top	
208		panels compare simulation and data, while the bottom panels show normalized distributions	
209		for all background processes and signal[21]. . . . .	95
210	5.4	A cartoon of the $WW$ final state. Momenta are represented with thin arrows, spins with thick	
211		arrows. [21] . . . . .	96
212	5.5	Event display of a VBF candidate event[21]. . . . .	97
213	5.6	Distributions of $m_{\ell\ell}$ (top left), $\Delta\phi_{\ell\ell}$ (top right), and $m_{\text{T}}$ (bottom), Higgs topology vari-	
214		ables used in the selection requirements of the cut-based signal region and as inputs to the	
215		BDT result. These are plotted after all of the BDT pre-training selection cuts[21]. . . . .	100
216	5.7	Distributions of $m_{jj}$ (top left), $\Delta y_{jj}$ (top right), $\sum C_{\ell}$ (bottom), VBF topology variables	
217		used in the selection requirements of the cut-based signal region and as inputs to the BDT	
218		result. These are plotted after all of the BDT pre-training selection cuts[21]. . . . .	101
219	5.8	Distributions of $m_{jj}$ (a) and $O_{\text{BDT}}$ (b) in the VBF $n_b = 1$ top CR [21]. . . . .	103

220	5.9	Comparison of $m_{jj}$ shape in a same flavor $Z \rightarrow \ell\ell$ control region and the VBF cut-based signal region. . . . .	105
221	5.10	General illustration of the ABCD region definitions for $Z/\gamma^* \rightarrow \ell\ell$ background estimation. . . . .	106
222	5.11	Distribution of $m_{T2}$ in the $WW$ validation region of the VBF analysis[21]. . . . .	107
223	5.12	Extrapolation factors for the $W + \text{jets}$ estimate derived for muons (a) and electrons (b) as a function of lepton $p_T$ [21]. . . . .	109
224	5.13	Background composition in final VBF signal region[21]. . . . .	110
225	5.14	Variations in the top background extrapolation factor in the cut-based analysis due to PDF uncertainties, binned in $m_T$ . . . . .	112
226	5.15	Variations in the top background extrapolation factor in the cut-based analysis due to QCD scale uncertainties, binned in $m_T$ . . . . .	113
227	5.16	Postfit distributions in the cut-based VBF analysis. Panel (a) shows the one-dimensional $m_T$ distribution, while (b) shows the data candidates split into the bins of $m_T$ and $m_{jj}$ used in the final fit[21]. . . . .	116
228	5.17	Postfit distributions in the BDT VBF analysis[21]. . . . .	117
229	5.18	Overlap between cut-based and BDT VBF signal region candidates in the $m_{jj}$ - $m_T$ plane. .	117
230	6.1	Post-fit $m_T$ distribution in the $n_j \leq 1$ regions[21]. . . . .	121
231	6.2	Best fit signal strength $\hat{\mu}$ as a function of hypothesized $m_H$ [21]. . . . .	123
232	6.3	Local $p_0$ as a function of $m_H$ [21]. . . . .	123
233	6.4	Likelihood as a function of $\mu_{\text{VBF}}/\mu_{\text{ggF}}$ [21]. . . . .	124
234	6.5	Likelihood scan as a function of $\mu_{\text{VBF}}$ and $\mu_{\text{ggF}}$ [21]. . . . .	125
235	6.6	Likelihood scan as a function of $\kappa_F$ and $\kappa_V$ [21]. . . . .	126
236	6.7	Comparison of signal strength measurements in different Higgs decay channels on ATLAS[23].	128
237	7.1	Parton luminosity ratios as a function of resonance mass $M_X$ for 13/8 TeV and 7/8 TeV [24].	131
238	7.2	Summary of $HH$ branching ratios [25]. . . . .	132
239	7.3	Minimum $\Delta R$ between $B$ decay vertices for different RSG masses in a $G_{\text{KK}}^* \rightarrow HH \rightarrow 4b$ sample with $c = 1$ . . . . .	133
240	7.4	Trigger efficiency for events passing all signal region selections as a function of mass in $G_{\text{KK}}^* \rightarrow HH \rightarrow 4b$ samples with $c = 1$ [26]. In the trigger names, “j” refers to a jet or jets. “ht” refers to $H_T$ , the scalar sum of transverse momenta in the event. “bloose” refers to a loose $b$ -tagging requirement applied to the jet. “aior” refers to anti- $k_T$ jets with $R = 1.0$ . The numbers at the end are the thresholds on the given quantity in GeV. . . . .	135
241	7.5	Comparison of untrimmed and trimmed jet masses for large radius jets in a RSG sample with $m_{G_{\text{KK}}^*} = 1$ TeV. JES (JMS) refers to the standard jet energy (mass) scale calibration for ATLAS [17].	136

255	7.6 Efficiency of finding two $b$ -jets from each Higgs in an RSG event using calorimeter jets with $R = 0.3$ or different track jet radii [27] . . . . .	137
256		
257	7.7 Illustration of the boosted selection requirements on Higgs candidates. Each large-radius calorime- ter jet (Higgs candidate) must contain two track jets . . . . .	139
258		
259	7.8 Acceptance $\times$ efficiency as a function of mass for (a) RSG and (b) narrow heavy scalar sig- nal models [28]. . . . .	140
260		
261	7.9 Efficiency of requiring 3 or 4 $b$ -tagged track jets vs. RSG mass. The efficiency quoted is rel- ative to the previous selection requirements (rather than an absolute efficiency). . . . .	141
262		
263	7.10 $M_J^{\text{sublead}}$ vs. $M_J^{\text{lead}}$ in a 2 $b$ -tag data sample. The signal region is defined by the inner black contour ( $X_{hh} < 1.6$ ) and the sideband region is defined by the outer contour ( $R_{hh} >$ 35.8 GeV). The region between the black contours is the control region. The mass region which is enriched in $t\bar{t}$ background is also shown for illustration. [28] . . . . .	143
264		
265	7.11 An illustration of the data-driven background estimation technique for the boosted anal- ysis . . . . .	144
266		
267	7.12 Leading large-R jet mass in the 3 $b$ (a) and 4 $b$ (b) sideband regions. The multijet and $t\bar{t}$ back- grounds are estimated using the data-driven methods described above. Because their normal- izations are derived in the sideband region, the total background normalization is constrained by default to match the normalization of the data [28]. . . . .	145
268		
269	7.13 Di-jet invariant mass ( $M_{2,J}$ ) in the 3 $b$ (a) and 4 $b$ (b) control regions. The multijet and $t\bar{t}$ back- grounds are estimated using the data-driven methods described above [28]. . . . .	146
270		
271	7.14 Di-jet invariant mass ( $M_{2,J}$ ) in the 3 $b$ (a) and 4 $b$ (b) signal regions. The multijet and $t\bar{t}$ back- grounds are estimated using the data-driven methods described above. In the 3 $b$ region, a graviton signal with $m_{G_{\text{KK}}^*} = 1.8$ TeV and $c = 1$ is overlaid, with the cross section mul- tiplied by a factor of 50 so that the signal is visible. In the 4 $b$ region, signals with $m_{G_{\text{KK}}^*} =$ 1.0 TeV and $m_{G_{\text{KK}}^*} = 1.5$ TeV are overlaid, both with $c = 1$ and the yields multiplied by factors of 2 and 5 respectively [28]. . . . .	151
272		
273		
274		
275		
276		
277		
278		
279		
280		
281	8.1 Di-jet invariant mass ( $M_{2,J}$ ) in the resolved signal region. Agraviton signal with $m_{G_{\text{KK}}^*} =$ 800 GeV and $c = 1$ is overlaid. [28]. . . . .	154
282		
283	8.2 Expected and observed upper limit as a function of mass for $G_{\text{KK}}^*$ in the RSG model with (a) $c = 1$ and (b) $c = 2$ , as well as (c) $H$ with fixed $\Gamma_H = 1$ GeV, at the 95% confidence level in the $CL_s$ method. [28] . . . . .	157
284		
285		

# Listing of tables

286

287	1.1	Production cross sections for a 125 GeV Higgs boson at $\sqrt{s} = 8$ TeV with scale and PDF uncertainties [2]. . . . .	13
288	1.2	Branching ratios for a 125 GeV Higgs boson[2]. . . . .	15
289	1.3	Possible channels for Higgs searches. Checkmarks denote the most sensitive production modes [29]. . . . .	15
290			
291			
292	1.4	Production cross sections for pair production of a 125 GeV Higgs boson at $\sqrt{s} = 14$ TeV with total uncertainty [30]. The uncertainties include QCD scale and PDF variations as well as uncertainties on $\alpha_S$ . . . . .	16
293			
294			
295	2.1	Evolution of LHC machine conditions [31, 32] . . . . .	25
296	2.2	Performance requirements for the ATLAS detector [7]. . . . .	37
297	2.3	Signal efficiencies for $WH$ production with $H \rightarrow b\bar{b}$ and $H \rightarrow WW^* \rightarrow \mu\nu qq$ under different trigger configurations [12]. . . . .	40
298			
299	3.1	A summary of backgrounds to the $H \rightarrow WW^* \rightarrow \ell\nu\ell\nu$ signal . . . . .	55
300			
301	4.1	Monte carlo generators used to model signal and background for the Higgs search[22]. . . . .	71
302	4.2	Normalization factors (ratio of data and MC yields in a control sample) for the Standard Model $WW$ and top backgrounds in the $H \rightarrow WW^* \rightarrow \ell\nu\ell\nu$ analysis [22]. Only statistical uncertainties are shown. . . . .	74
303			
304	4.3	Data and expected yields for signal and background in the final $H \rightarrow WW^* \rightarrow \ell\nu\ell\nu$ signal region. Uncertainties shown are both statistical and systematic. [22] . . . . .	75
305			
306	4.4	Summary of the expected and observed significance and measured signal strengths in the combined 7 and 8 TeV datasets for the Higgs discovery analysis[22]. . . . .	79
307			
308	5.1	Single lepton triggers used for electrons and muons. A logical “or” of the triggers listed for each lepton type is taken. Units are in GeV, and the $i$ denotes an isolation requirement in the trigger. . . . .	85
309			
310			
311	5.2	Di-lepton triggers used for different flavor combinations. The two thresholds listed refer to leading and sub-leading leptons, respectively. The di-muon trigger only requires a single lepton at level-i. . . . .	85
312			
313			

314	5.3	Trigger efficiency for signal events and relative gain of adding a dilepton trigger on top of the single lepton trigger selection. The first lepton is the leading, while the second is the sub-leading. Efficiencies shown here are for the ggF signal in the $n_j = 0$ category but are comparable for the VBF signal. . . . .	86
315			
316	5.4	Monte Carlo samples used to model the signal and background processes[21]. . . . .	87
317			
318	5.5	$p_T$ dependent isolation requirements for muons. Muons are required to have the amount of calorimeter or track based cone sums be less than this fraction of their $p_T$ . . . . .	89
319			
320	5.6	$p_T$ dependent requirements for electrons. Electrons are required to have the amount of calorimeter or track based cone sums be less than this fraction of their $E_T$ . . . . .	90
321			
322	5.7	Event selection for the $n_j \geq 2$ VBF analysis in the 8 TeV cut-based analysis[21]. . . . .	98
323			
324	5.8	Top normalization factors computed at each stage of the cut-based selection. Uncertainties are statistical only. . . . .	102
325			
326	5.9	Top normalization factors computed for each bin of $O_{\text{BDT}}$ . Uncertainties are statistical only. . . . .	102
327			
328	5.10	$Z/\gamma^* \rightarrow \tau\tau$ correction factors for the VBF cut-based analysis. Uncertainties are statistical only. . . . .	105
329			
330	5.11	$Z/\gamma^* \rightarrow \ell\ell$ normalization factors for cut-based and BDT analyses. Uncertainties are statistical only. . . . .	107
331			
332	5.12	Systematic uncertainties for various processes in the cut-based VBF analysis, given in units of % change in yield. Values are given for the low $m_{jj}$ signal region. . . . .	III
333			
334	5.13	Composition of the post-fit uncertainties (in %) on the total signal ( $N_{\text{sig}}$ ), total background ( $N_{\text{bkg}}$ ), and individual background yields in the VBF analysis[21]. . . . .	114
335			
336	5.14	Event selection for the VBF BDT analysis. The event yields in (a) are shown after the pre-selection and the additional requirements applied before the BDT classification (see text). The event yields in (b) are given in bins in $O_{\text{BDT}}$ after the classification[21]. . . . .	115
337			
338	6.1	All signal regions definitions input into final statistical fit[21]. . . . .	120
339	6.2	Post-fit yields in the different ggF and VBF dedicated signal regions[21]. . . . .	121
340			
341	7.1	Summary of requirements on objects used in the $X \rightarrow HH \rightarrow b\bar{b}b\bar{b}$ search . . . . .	138
342	7.2	Effect of boosted selection on data, RSG signal models, $t\bar{t}$ , and $Z+\text{jets}$ . The numbers from simulation are normalized with the MC generator cross section and do not take into account the data driven estimates described in section 7.6 [33]. . . . .	142
343			
344	7.3	Mass region definitions used for background estimation . . . . .	143
345	7.4	Parameters derived for exponential fit to background $M_{2J}$ shape in the 3 $b$ and 4 $b$ signal regions [33] . . . . .	146
346			
347	7.5	The number of events in data and predicted background events in the boosted 3-tag and 4-tag sideband and control regions. The uncertainties shown are statistical only. [28] . . . . .	147
348			

349	7.6	Summary of systematic uncertainties in the total background and signal event yields (expressed in %) in the boosted 3-tag and 4-tag signal regions. Systematic uncertainties on the signal normalization are shown for models with $m_{G_{\text{KK}}^*} = 1.5 \text{ TeV}$ and both $c = 1$ and $c = 2$ as well as a narrow width heavy scalar. . . . .	149
350	7.7	Alternate fit functions used to model the $M_{JJ}$ distribution in the QCD multijet background. In the equations, $x = M_{JJ}/\sqrt{s}$ . . . . .	150
351	7.8	Observed yields in the 3-tag and 4-tag signal regions for the boosted analysis compared to the predicted number of background events Errors correspond to the total uncertainties in the predicted event yields. The yields for a graviton with $m_{G_{\text{KK}}^*} = 1 \text{ TeV}$ and $c = 1$ are also shown. [28] . . . . .	151
352			
353	8.1	Observed yields in the resolve selection 4-tag signal region compared to the predicted num- ber of background events Errors correspond to the total uncertainties in the predicted event yields. The yields for a graviton with $m_{G_{\text{KK}}^*} = 800 \text{ GeV}$ and $c = 1$ are also shown. [28] . .	153
354			
355			
356			
357			
358			
359			
360			
361			



# Acknowledgments

364 I have been a member of the Harvard ATLAS group for many years now, first as an undergraduate  
 365 and then as a graduate student. As a result, I have had the privilege of interacting with many amazing  
 366 people there over the years and have accumulated a large list of folks to thank.

367 First and foremost, I must thank the two people who have effectively been my academic parents since  
 368 I started in the Harvard group: Joao Guimaraes da Costa and Melissa Franklin. Melissa Franklin and  
 369 Joao Guimaraes da Costa. They have both been so important to both my academic and personal devel-  
 370 opment that I can't even put one before the other. Joao has been an excellent PhD advisor, showing me  
 371 how to look at the big picture and helping me navigate the sometimes complicated politics of ATLAS.  
 372 He got me started on my first projects with ATLAS as a young college sophomore before there was even  
 373 beam in the LHC (go cosmic ray muons!). He has also been a constant source of advice and support,  
 374 even when we have been on different continents. Melissa gave me my start in HEP as a summer student  
 375 on CDF and has been an unbelievable mentor throughout my time at Harvard. I still remember our  
 376 weekly chalkboard particle physics lessons after that first summer. She also graciously took me on as a  
 377 co-advisee after Joao moved on to his new position at IHEP. I am incredibly lucky to have had both of  
 378 them as advisors.

379 Another mentor who was essential to my development as a graduate student is Paolo Giromini. His  
 380 uncanny knowledge and intuition about detectors is unmatched and I am very grateful to have had  
 381 the chance to work with him on the micromegas for the ATLAS New Small Wheel upgrade project. I  
 382 owe essentially all my practical knowledge about detectors (and building things in general) to him. I also  
 383 appreciated his unique sense of humor which made sometimes difficult tasks much easier to get through.

384 I am grateful to John Huth and Masahiro Morii for their helpful advice as the other professors in the  
 385 Harvard ATLAS group as well. I especially thank John for helping me get started on the micromegas  
 386 trigger project and being a great professor to TF particle physics for.

387 I also owe enormous thanks to Hugh Skottowe, the postdoc that I worked most closely with in my  
 388 early years as a graduate student. He was always able to help me through complicated tasks in everything  
 389 from writing code to understanding difficult physics concepts. I particularly enjoyed walking down to  
 390 his office in Palfrey at random times and talking through whatever problem I was tackling on that day.

391 Alex Tuna, the second postdoc that I worked closely with at Harvard, deserves great thanks as well.  
 392 He helped me push through to the end of my graduate career and offered great advice along the way.

393 Being at Harvard, I have seen an incredible array of graduate students graduate before me: Ben Smith,  
 394 Verena Martinez Outschoorn, Srivas Prasad, Michael Kagan, Giovanni Zevi Della Porta, Laura Jeanty,  
 395 Kevin Mercurio, William Spearman, and Andy Yen. I want to thank them all for showing me what a

396 good physicist looks like and for patiently answering my questions and offering insightful advice about  
397 physics and life.

398 Getting through graduate school would not have been possible without the support and friendship  
399 of the other students in our group. Thanks to Emma Tolley for geeking out with me about cool com-  
400 puting stuff, going to taste delicious beers with me, and helping start the Palfrey tradition of Taco Tues-  
401 days. Thanks to Brian Clark for being a great friend and housing companion both in Kirkland House  
402 and in our tiny summer apartment in Geneva (and thanks to his partner Allison Goff for the same rea-  
403 sons!). Thanks to Siyuan Sun for giving me my first aikido lesson and always being there for great con-  
404 versations, big and small. Tony (Baojia) Tong deserves special recognition for working with me on the  
405  $4b$  analysis and putting up with my sometimes strange requests (and giving me rides to the Val Thoiry  
406 Migros so I wouldn't have to pay exorbitant Geneva grocery prices!). Stephen Chan is probably the only  
407 student in the group who both understands my references to the Sopranos and makes some of his own.  
408 To the younger graduate students - Karri Di Petrillo, Jennifer Roloff, Julia Gonski, and Ann Wang - I  
409 want to say thank you for making the group a fun and lively place to be and giving all of us energy that  
410 the older graduate students like myself can sometimes lack.

411 I'd like to thank Annie Wei and Gray Putnam, the two undergraduates I have worked with as a gradu-  
412 ate student. Their unbelievable intuition and quickness in picking up difficult particle physics concepts  
413 is inspiring.

414 I would also like to thank all of the postdocs that I have interacted with in my time in the Harvard  
415 group: Kevin Black, Alberto Belloni (who would always ask me "Do you have it?"...I can now say that  
416 I do!), Shulamit Moed, Corrinne Mills, Geraldine Conti, David Lopez Mateos, Chris Rogan, Valerio  
417 Ippolito, and Stefano Zambito.

418 There are many people on ATLAS who have helped me get to this point as well. In the  $WW$  group,  
419 I have to thank Jonathan Long, Joana Machado Miguens, Ben Cerio, Philip Chang, Bonnie Chow,  
420 Richard Polifka, Heberth Torres, Tae Min Hong, and Jennifer Hsu for being wonderful colleagues and  
421 making the entire analysis run smoothly. In the  $4b$  group, I have to thank Qi Zeng, Tony Tong, Alex  
422 Tuna, Michael Kagan, Max Bellomo, John Alison, and Patrick Bryant.

423 Kirkland House was my home for the last three years of graduate school and was an wonderful envi-  
424 ronment and support system. I want to thank my fellow tutors, especially Brian Clark and Allison Goff  
425 (again), Zach Abel, Kelly Bodwin, Alex Lupsasca, John and Pam Park, Luke and Erin Walczewski, and  
426 Philip Gant for their friendship and support. I also want to thank Kate Drizos Cavell, Bob Butler, and  
427 the Faculty Deans Tom and Verena Conley.

428 There are still a few friends that haven't been covered yet and deserve great thanks. Jake Connors and  
429 Meredith MacGregor have been absolutely wonderful friends and I thank them in particular for the  
430 many home-cooked meals and great conversations we've had in their apartment. Nihar Shah has been  
431 my friend and confidant since we were both wee freshmen in Harvard Yard. Gareth Kafka, though he  
432 sits on the "neutrino" side of Palfrey House, has made days there more fun and has also been an enthusi-

433 astic participant in the Palfrey Taco Tuesdays.

434 Being at Harvard necessarily means having to navigate through bureaucracy at some point or another.  
435 I thank Lisa Cacciabaudo, Carol Davis, and Jacob Barandes for always having open doors and being the  
436 most kind, helpful people in the Physics department.

437 I thank Venky Narayananamurti for putting on a great SPU course that I was proud to be a part of and  
438 TF for. I'd also like to thank Jim Waldo for offering me much advice about working in Computer Science  
439 and giving me a fun data project to be a part of in my free time.

440 I grew up in a very tight knit Serbian community on the south side of Chicago which helped make  
441 me the person I am today. I would like to thank all of the people at St. Simeon Mirotochivi Serbian  
442 Orthodox Church who have always been sources of enthusiasm and support in my life.

443 I would not be here without the unconditional love and constant support and encouragaement of my  
444 family. To my pokojni Dedas Branko and Miloje, my pokojni Baba Milka, and my Baba Desa, I want to  
445 say thank you for instilling in me at an early age the love of curiosity and storytelling that I have carried  
446 throughout my life. To my sister Angelina, I want to say thank you for always loving me and being my  
447 partner in crime throughout our childhoods. To my parents, Miroljub and Nada, Tata and Mama, I  
448 really cannot express how grateful I am to you and how much I owe you. As I look back now I see how  
449 I am a combination of both of your best qualities and every day I am in situations where I understand  
450 more and more the lessons you made sure to teach me and the sacrifices you made to make sure I got the  
451 best possible education. I love you all.

452 Finally, I have to thank my soul mate, the one person in my life who understands me more than any-  
453 one else, my fiancee Kelly Brock. You are my sounding board, my support system, my cheerleader (fig-  
454 uratively and literally!), my best friend, my role model, and my everything. I would not have gotten  
455 through graduate school without you and my life would not be the same without you. I cannot wait to  
456 start our new lives together as the married doctors, tackling whatever comes our way with the same zeal  
457 with which we tackled graduate school. I love you with all my heart and soul.

# 0

458

459

## Introduction

460 The Higgs boson is often described as one of the cornerstones of the Standard Model. Since the con-  
461 ception of the Higgs mechanism as the source of electroweak symmetry breaking in the early 1960s,  
462 countless collider experiments have searched for this elusive particle. This dissertation presents multi-  
463 ple studies of the Higgs boson with the ATLAS detector at the Large Hadron Collider (LHC).

464 One of the first priorities of the early LHC was the search for the Higgs boson. This search was first  
465 tackled in three main channels:  $H \rightarrow \gamma\gamma$ ,  $H \rightarrow ZZ^*$ , and  $H \rightarrow WW^*$ . Each channel has its own  
466 merits, but the  $WW^*$  is particularly suited to searching over a wide range of masses. The  $H \rightarrow WW$   
467 branching ratio is large and it is the primary decay channel above the  $2m_W$  mass threshold.

468 While the rate of events produced in  $H \rightarrow WW^*$  is large, the channel poses some challenges. First,  
469 the most common mode of study for this channel is  $H \rightarrow WW^* \rightarrow \ell\nu\ell\nu$ . With neutrinos in the  
470 final state, it is not possible to fully reconstruct the invariant mass of the parent Higgs like the  $\gamma\gamma$  and  
471  $ZZ \rightarrow 4\ell$  channels. Second, the final state topology is mimicked by a wide variety of backgrounds that

472 need to be properly estimated. This means tailored selection requirements for background reduction  
473 and robust background estimation techniques must both be developed.

474 In 2012, the ATLAS and CMS experiments announced the discovery of a new particle consistent with  
475 the Higgs boson [22, 34]. In ATLAS, this discovery was made with  $4.8 \text{ fb}^{-1}$  collected at  $\sqrt{s} = 7 \text{ TeV}$   
476 and  $5.8 \text{ fb}^{-1}$  at  $\sqrt{s} = 8 \text{ TeV}$ . The  $H \rightarrow WW^* \rightarrow \ell\nu\ell\nu$  analysis played an important role in this  
477 discovery. After the discovery, measurement of the properties of the newly discovered particle and con-  
478 firmation of its consistency with the Standard Model Higgs were the main priorities. The  $WW^*$  chan-  
479 nel is also uniquely suited to these types of measurements. Because of its good rate, it offers some of the  
480 best cross section measurements available among the various Higgs decay modes. It is also suited for  
481 measurement of multiple Higgs production modes, like the vector boson fusion (VBF) mode, where in-  
482 coming quarks radiate  $W/Z$  bosons which fuse to make a Higgs. In VBF production with the  $WW^*$   
483 decay channel, the coupling of the Higgs to the  $W$  boson is present in both the production and decay  
484 which allows for more precise measurements of this coupling than other channels which rely on gluon  
485 fusion production (where gluons couple to the Higgs through a top loop in the production). The mea-  
486 surement of VBF carries the additional challenge that its cross section is an order of magnitude smaller  
487 than that of gluon fusion, meaning that the large branching ratio to  $WW^*$  offers an additional advan-  
488 tage in isolating this production mode. In the final ATLAS Run 1 results, combining  $20.3 \text{ fb}^{-1}$  taken at  
489  $\sqrt{s} = 8 \text{ TeV}$  with the  $4.8 \text{ fb}^{-1}$  collected at  $\sqrt{s} = 7 \text{ TeV}$ , the  $WW^*$  channel achieved its first observa-  
490 tion of VBF production of the Higgs.

491 After Run 1 of the LHC, with the existence of the Higgs now firmly established, the focus shifted to  
492 searches for physics beyond the Standard Model. In particular, searches for high mass resonances benefit  
493 from the LHC's increase to  $\sqrt{s} = 13 \text{ TeV}$  in Run 2. The newly discovered Higgs can be used as a tool  
494 in these searches. Higgs pair production in the Standard Model has a low cross section that requires large  
495 datasets (on the order of the LHC's lifetime) for full measurement. However, new physics can modify  
496 this cross section, especially new resonances which decay to two Higgs bosons. A search for Higgs pair  
497 production in the  $HH \rightarrow b\bar{b}b\bar{b}$  final state was performed with  $3.2 \text{ fb}^{-1}$  collected with ATLAS at  $\sqrt{s} =$   
498  $13 \text{ TeV}$  in 2015.

499 This dissertation begins by discussing the discovery of the Higgs and the role of the  $H \rightarrow WW^* \rightarrow$   
500  $\ell\nu\ell\nu$  channel. It then discusses the first observation of the VBF production mode in  $H \rightarrow WW^* \rightarrow$   
501  $\ell\nu\ell\nu$  with the full ATLAS Run 1 dataset, as well as the final combined Run 1 measurements from this  
502 channel. Finally, it presents a search for Higgs pair production in the  $HH \rightarrow b\bar{b}b\bar{b}$  channel. It is orga-  
503 nized into four parts.

504 Part 1 presents the theoretical and experimental background required for the subsequent parts. Chap-  
505 ter 1 gives an overview of Higgs physics, particularly single and double Higgs production in the Standard  
506 Model and beyond. Chapter 2 presents details regarding the Large Hadron Collider and the ATLAS  
507 experiment. The evolution of machine conditions, descriptions of the ATLAS sub-detectors, and an  
508 overview of object reconstruction in ATLAS are all shown. A brief interlude on the ATLAS Muon New  
509 Small Wheel upgrade is also given, as this upgrade has been a focus of my graduate work and will have  
510 important impact on ATLAS' ability to study the Higgs at the High Luminosity LHC.

511 Part 2 discusses the observation and measurement of the Higgs in the  $H \rightarrow WW^* \rightarrow \ell\nu\ell\nu$   
512 channel in the ATLAS Run 1 dataset at  $\sqrt{s} = 7$  and 8 TeV. Because I worked in this channel from  
513 before the discovery through to the final analysis of the Run 1 dataset, Part 2 is organized in such a way  
514 to allow easy presentation of multiple analyses on different subsets of the full Run 1 dataset. Chapter 3  
515 presents a general overview of the  $H \rightarrow WW^*$  analysis strategy and defines many of the variables and  
516 common elements used in the rest of Part 2. Chapter 4 presents the discovery of the Higgs boson, fo-  
517 cusing on the role of the  $WW^*$  channel in this discovery. Chapter 5 presents the first observation of the  
518 VBF production mode of the Higgs in the  $WW^*$  channel, a study which was done on the full Run 1  
519 ATLAS dataset. In this chapter, the focus is mainly on the selection cut-based VBF analysis. The cut-  
520 based analysis was an important first step to the final VBF result which used a Boosted Decision Tree  
521 (BDT). Where appropriate, connections between the cut-based and BDT analyses are shown and their  
522 compatibility is discussed. Finally, the VBF analysis was an important input into the combined Run 1  
523  $H \rightarrow WW^* \rightarrow \ell\nu\ell\nu$  result, which used both the gluon fusion and VBF channels in a combined  
524 fit to infer properties of the Higgs, including its couplings to the gauge bosons and its production cross  
525 section. This is the topic of Chapter 6.

526        Part 3 presents a search for Higgs pair production in the  $HH \rightarrow b\bar{b}b\bar{b}$  channel. Chapter 7 presents  
527        an overview of this search in the boosted regime, where the Higgs pairs are the result of the decay of a  
528        heavy resonance. Chapter 8 shows the combined results between the boosted regime and the resolved  
529        regime, which is sensitive to lower mass resonances and non-resonant Higgs pair production. Finally,  
530        Part 4 presents a conclusion and brief outlook of future Higgs physics with ATLAS.

<sup>531</sup>

## Part I

<sup>532</sup>

## Theoretical and Experimental Background

# 1

533

534

## The Physics of the Higgs Boson

535 This chapter presents an overview of the Standard Model of Particle Physics and in particular the physics  
536 of the Higgs boson. First, a brief overview of the Standard Model and its history are presented. Then, a  
537 description of the Higgs mechanism of electroweak symmetry breaking is given. Next, the physics of sin-  
538 gle Higgs boson production and decay is described. The Standard Model also allows for production of  
539 two Higgs bosons and this is detailed as well. Finally, di-Higgs production in two beyond the Standard  
540 Model (BSM) theories - Randall-Sundrum gravitons (RSG) and Two Higgs Doublet Models (2HDM) -  
541 is shown.

### 542 1.1 THE STANDARD MODEL OF PARTICLE PHYSICS

543 The Standard Model (SM) of Particle Physics is a quantum field theory describing the fundamental  
544 particles of nature and the forces that govern their interactions. Several comprehensive treatments of  
545 the SM already exist in the literature[1, 29, 35–38] and this section will not rehash those. Rather, this

546 section presents a brief overview of the SM particles and forces in order to define them for subsequent  
 547 discussions.

548 The Standard Model consists of two primary categories of fundamental particles: fermions (spin 1/2  
 549 particles) and bosons (integer spin particles). The SM also describes three forces: electromagnetism, the  
 550 weak nuclear force, and the strong nuclear force. Gravity is not included in the theory and is largely irrele-  
 551 vant at the scales currently probed by collider experiments. Within the fermions, there are both quarks  
 552 (which interact via all three forces) and the leptons. The charged leptons interact via electromagnetic and  
 553 weak interactions, while neutrinos (neutral leptons) interact only via the weak force. Within the bosons,  
 554 there are the  $W^\pm$  and  $Z$  bosons (the mediators of the weak force), the gluon ( $g$ , the mediator of the  
 555 strong force), and the photon ( $\gamma$ ), the mediator of the electromagnetic force. Finally, there is the Higgs  
 556 boson, a fundamental spin-0 particle resulting from the Higgs mechanism of electroweak symmetry  
 557 breaking. Figure 1.1 summarizes the fermions and bosons of the SM.

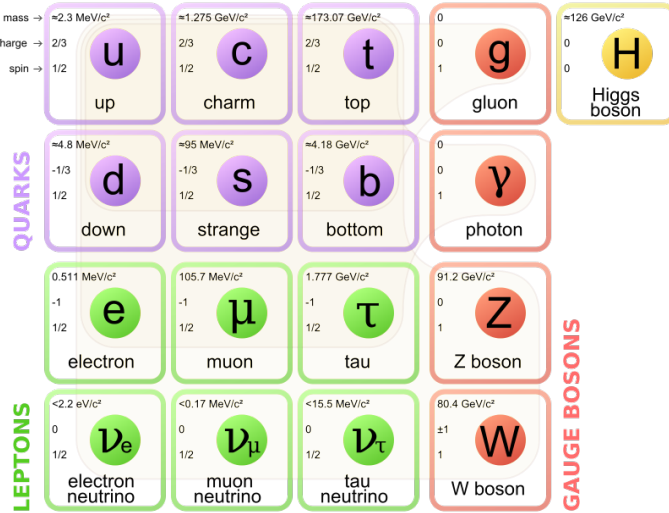


Figure 1.1: The particles of the Standard Model and their properties[1].

558 The Standard Model coalesced into a unified theoretical framework in the 1960s through the work of  
 559 Glashow, Weinberg, Salam, and others on the theory of electroweak interactions[39–42]. This theory  
 560 characterized both the electromagnetic and weak interactions as unified under a single gauge symme-  
 561 try group, namely  $SU(2) \times U(1)$ . At low enough energy scales (on the order of the  $W$  and  $Z$  masses,  
 562 the electroweak symmetry is broken, as evidenced by the fact that the weak bosons have mass while the

563 photon does not. The discovery of the Higgs boson in 2012 confirmed the Higgs mechanism as the most  
 564 likely candidate for this electroweak symmetry breaking[22, 34]. The electroweak theory is then com-  
 565 bined with the theory of quantum chromodynamics (which models the strong sector as a non-Abelian  
 566  $SU(3)$  gauge group) to form the complete SM[43].

## 567 1.2 ELECTROWEAK SYMMETRY BREAKING AND THE HIGGS

568 In the Standard Model Lagrangian, it is difficult to include mass terms for the  $W$  and  $Z$  bosons without  
 569 breaking the fundamental gauge symmetry of the Lagrangian. A traditional mass term does not preserve  
 570 the  $SU(2) \times U(1)$  symmetry. Additionally, scattering of massive  $W$  and  $Z$  bosons violate unitarity  
 571 and these diagrams diverge at high energy scales. In the 1960s, Higgs, Brout, Englert, Guralnik, Kibble,  
 572 and Hagen developed a mechanism for spontaneous symmetry breaking via the addition of a complex  
 573 scalar doublet to the SM. Three of the four real degrees of freedom of this complex field would go to the  
 574 longitudinal modes of the  $W^\pm$  and  $Z$ , thus allowing them to have mass[44–47]. The remaining degree  
 575 of freedom would manifest as an additional scalar, known now as the Higgs boson.

576 The mechanism works by introducing a Lagrangian for the newly introduced field that still respects  
 577 the symmetry of the Standard Model inherently, but with a minimum at a non-zero vacuum expecta-  
 578 tion value for the field. In this minimum of the potential, the electroweak symmetry is broken. Specifi-  
 579 cally, consider a complex scalar doublet  $\Phi$  with four degrees of freedom, as shown in equation 1.1.

$$\Phi = \begin{pmatrix} \phi^+ \\ \phi^0 \end{pmatrix} = \frac{1}{\sqrt{2}} \begin{pmatrix} \phi_1^+ + i\phi_2^+ \\ \phi_1^0 + i\phi_2^0 \end{pmatrix} \quad (1.1)$$

580 The minimal potential of a self-interacting Higgs that still respects the SM symmetry is given in equa-  
 581 tion 1.2.

$$V(\Phi) = \mu^2 \Phi^\dagger \Phi + \lambda (\Phi^\dagger \Phi)^2 \quad (1.2)$$

582 If the  $\mu^2$  term of this potential is positive, then the potential has a minimum at  $\Phi = 0$  and the SM

<sup>583</sup> symmetry is preserved. However, if instead  $\mu^2 < 0$ , then the minimum is at a finite value of  $\Phi$ , namely

$$\Phi_{\min} = \frac{1}{\sqrt{2}} \begin{pmatrix} 0 \\ v \end{pmatrix} \quad (1.3)$$

<sup>584</sup> where  $v = \sqrt{\mu^2/\lambda}$ . Because this is the location of the minimum, it corresponds to the vacuum expecta-  
<sup>585</sup> tion value for the field ( $\langle \Phi \rangle = \Phi_{\min}$ ). The excitations of the Higgs can then be parameterized as

$$\Phi = \frac{1}{\sqrt{2}} \begin{pmatrix} 0 \\ v + H \end{pmatrix} \quad (1.4)$$

<sup>586</sup> The full scalar Lagrangian, including the kinetic term, is then given as

$$\mathcal{L}_s = (D^\mu \Phi)^\dagger (D_\mu \Phi) - V(\Phi) \quad (1.5)$$

<sup>587</sup> where the covariant derivative is defined as

$$D_\mu = \partial_\mu + \frac{ig}{2} \tau^a W_\mu^a + ig' Y B_\mu \quad (1.6)$$

<sup>588</sup> and  $W^1, W^2, W^3$  and  $B$  are the  $SU(2)$  and  $U(1)$  gauge fields of the electroweak theory, respectively.  $g$   
<sup>589</sup> and  $g'$  are the corresponding coupling constants. With the scalar Lagrangian in place, the physical gauge  
<sup>590</sup> fields can then be written as

$$W_\mu^\pm = \frac{1}{\sqrt{2}} (W_\mu^1 \mp i W_\mu^2) \quad (1.7)$$

<sup>591</sup>

$$Z_\mu = \frac{-g'B_\mu + gW_\mu^3}{\sqrt{g^2 + g'^2}} \quad (1.8)$$

<sup>592</sup>

$$A_\mu = \frac{gB_\mu + g'W_\mu^3}{\sqrt{g^2 + g'^2}} \quad (1.9)$$

<sup>593</sup> Equation 1.7 corresponds to the charged  $W^+$  and  $W^-$  bosons, equation 1.8 corresponds to the neutral

594  $Z$  boson, and equation 1.9 corresponds to the neutral photon. The masses of the particles also arise from  
595 the Lagrangian. The photon has zero mass, while the masses of the  $W$  and  $Z$  bosons are given in equa-  
596 tion 1.10.

$$\begin{aligned} M_W^2 &= \frac{1}{4}g^2v^2 \\ M_Z^2 &= \frac{1}{4}(g^2 + g'^2)v^2 \end{aligned} \tag{1.10}$$

597 The fermion masses also arise through a coupling with the Higgs via the Yukawa interaction (for a de-  
598 tailed description, see [38]). In this case the coupling between the Higgs and the fermions goes as

$$g_{Hf\bar{f}} = \frac{m_f}{v} \tag{1.11}$$

599 The full Lagrangian of Higgs interactions can be written as

$$\mathcal{L}_{\text{Higgs}} = -g_{Hf\bar{f}}\bar{f}fH + \frac{g_{HHH}}{6}H^3 + \frac{g_{HHHH}}{24}H^4 + \delta_V V_\mu V^\mu \left( g_{HVV}H + \frac{g_{HHVV}}{2}H^2 \right) \tag{1.12}$$

600 with

$$\begin{aligned} g_{HVV} &= \frac{2m_V^2}{v} & g_{HHVV} &= \frac{2m_V^2}{v^2} \\ g_{HHH} &= \frac{3m_H^2}{v} & g_{HHHH} &= \frac{3m_H^2}{v^2} \end{aligned} \tag{1.13}$$

601 Here,  $V$  refers to the  $W^\pm$  and  $Z$ , and  $\delta_W = 1$  while  $\delta_Z = 1/2$ . Phenomenologically, there are a few  
602 features of this Lagrangian that are useful to note. First, note that the Higgs mass is a free parameter  
603 of the theory that must be determined experimentally. Second, note that the coupling of the Higgs to  
604 the vector bosons and fermions scales with the masses of these particles, a fact that is important when  
605 considering both the production and decays of the particle. Also note that the branching ratio of the  
606 Higgs to  $W$  bosons will be twice that of the branching ratio to  $Z$  if the Higgs mass is large enough to  
607 produce the particles on shell because of the extra symmetry factor associated with the  $W$  coupling.  
608 Finally, note the presence of the cubic and quartic Higgs self interaction terms, which can lead to final  
609 states with multiple Higgs bosons produced.

610 1.3 HIGGS BOSON PRODUCTION AND DECAY

611 This section discusses the properties of Higgs production and decay mechanisms. The details presented  
612 here will focus on the properties of a 125 GeV Higgs boson, as this is the mass closest to that of the  
613 newly discovered Higgs.

614 1.3.1 HIGGS PRODUCTION

615 The Higgs is produced by four main production modes at the Large Hadron Collider - gluon-gluon  
616 fusion (ggF), vector boson fusion (VBF), associated production with a  $W$  or  $Z$  boson, or associated  
617 production with top quarks ( $t\bar{t}H$ ). Figure 1.2 shows the Feynman diagrams for these four modes.

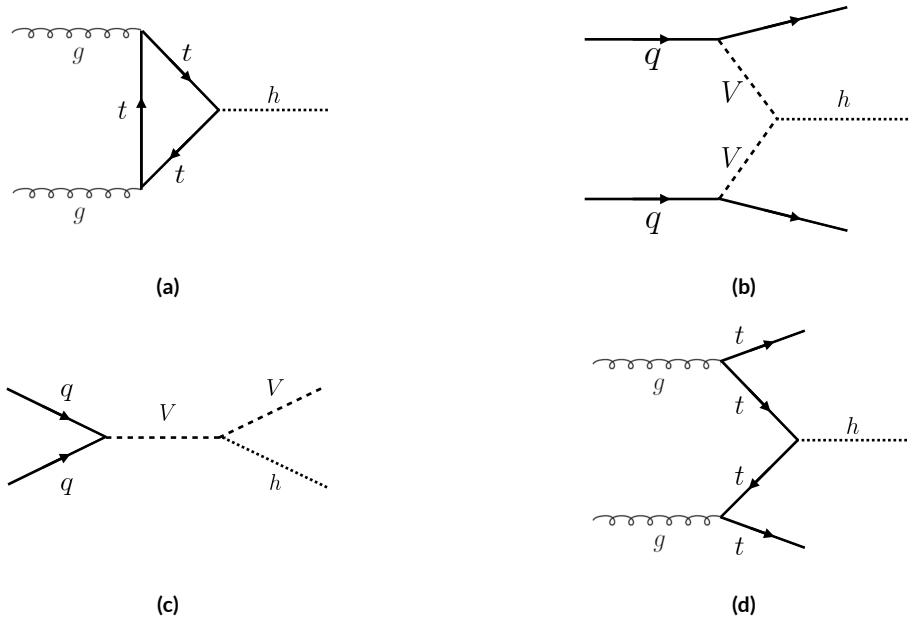
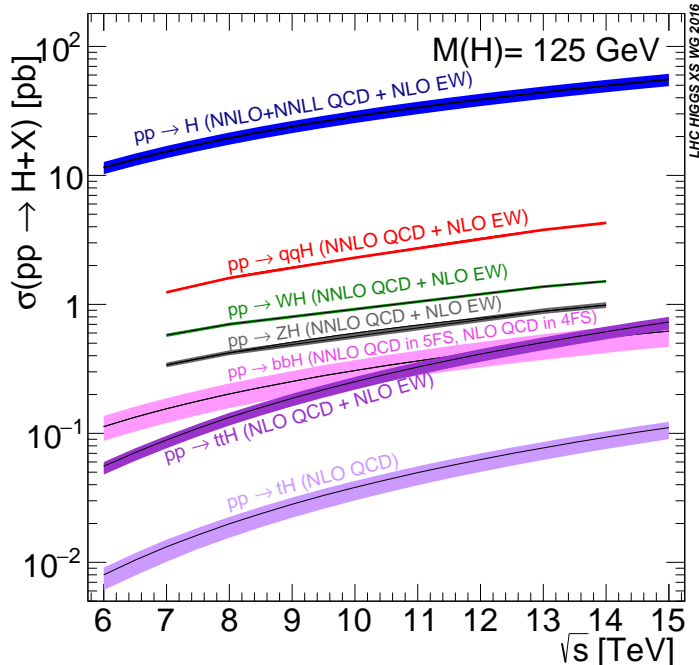


Figure 1.2: The four most common Higgs boson production modes at the LHC: (a) gluon-gluon fusion, (b) vector boson fusion, (c)  $W/Z + H$  production, (d)  $t\bar{t}H$  production

618 In gluon-gluon fusion, gluons from the incoming protons fuse via a top-quark loop to produce a  
619 Higgs. The top quark is the dominant contribution in the loop due to its heavy mass and the fact that  
620 the Higgs-fermion coupling constant scales with fermion mass. In vector boson fusion, the incoming  
621 quarks each radiate a  $W$  or  $Z$  boson which fuse to produce the Higgs. This production mode results in  
622 a final state with a Higgs boson and two additional jets which tend to be forward because they carry the

623 longitudinal momentum of the incoming partons. The Higgs can also be produced in association with a  
 624  $W$  or  $Z$  boson. The  $W/Z$  is produced normally and then radiates a Higgs (this mode is also sometimes  
 625 known as “Higgs-strahlung”). Finally, the Higgs can be produced in association with two top quarks.  
 626 Each incoming gluon splits into a  $t\bar{t}$  pair, and one of the top pairs combines to create a Higgs.

627 Figure 1.3 shows the production cross section for a 125 GeV Higgs boson in each of these modes at a  
 628  $pp$  collider as a function of center of mass energy.



**Figure 1.3:** Higgs production cross sections as a function of center of mass energy ( $\sqrt{s}$ ) at a  $pp$  collider[2].

629 In figure 1.3, note that gluon fusion has the largest cross section, while VBF is the second largest at  
 630 approximately a factor of 10 smaller. The figure also includes the less commonly studied  $b\bar{b}H$  and  $tH$   
 631 modes. The  $b\bar{b}H$  and  $tH$  modes are not studied as commonly as  $t\bar{t}H$  due to the larger background con-  
 632 tributions and lower cross sections, respectively. At  $\sqrt{s} = 8$  TeV, ggF production of a 125 GeV Higgs  
 633 has a cross section of 19.47 pb, while VBF has a cross section of 1.601 pb[2]. The cross sections of all  
 634 of the main Higgs production modes at this center of mass energy, as well as their uncertainties from  
 635 varying the renormalization and factorization scales and PDFs, are summarized in table 1.1 for a 125 GeV  
 636 Higgs.

Production mode	$\sigma$ ( pb)	QCD scale uncert. (%)	PDF + $\alpha_s$ uncert. (%)
Gluon fusion	19.47	+7.3 / - 8.0	3.1
Vector boson fusion	1.601	+0.3 / - 0.2	2.2
$WH$	0.7026	+0.6 / - 0.9	2.0
$ZH$	0.4208	+2.9 / - 2.4	1.7
$t\bar{t}H$	0.1330	+4.1 / - 9.2	4.3
$b\bar{b}H$	0.2021	+20.7 / - 22.3	
$tH$ ( $t$ -channel)	0.01869	+7.3 / - 16.5	4.6
$tH$ ( $s$ -channel)	$1.214 \times 10^{-3}$	+2.8 / - 2.4	2.8

**Table 1.1:** Production cross sections for a 125 GeV Higgs boson at  $\sqrt{s} = 8$  TeV with scale and PDF uncertainties [2].

### 637 1.3.2 HIGGS BRANCHING RATIOS

638 The fact that the Higgs couples more strongly to more massive particles is crucial for understanding its  
 639 branching ratios. The width for Higgs decays to fermions is given in equation 1.14 [29].

$$\Gamma(H \rightarrow f\bar{f}) = \frac{N_c \sqrt{2} G_F m_f^2 m_H}{8\pi} \quad (1.14)$$

640 In this case,  $N_c$  is the number of colors,  $G_F$  is the Fermi constant,  $m_f$  is the mass of the fermion, and  
 641  $m_H$  is the mass of the Higgs. Note that the width scales with the square of the fermion mass. (This also  
 642 assumes that the Higgs mass is large enough to decay with both the fermions on shell.)

643 The decay width to  $WW$  is given in equation 1.15 [29].

$$\Gamma(H \rightarrow W^+W^-) = \frac{\sqrt{2} G_F M_W^2 m_H}{16\pi} \frac{\sqrt{1-x_W}}{x_W} (3x_W^2 - 4x_W + 4) \quad (1.15)$$

644 where  $m_W$  is the mass of the  $W$  and  $x_W = 4M_W^2/m_H^2$ . To get the branching ratio to  $ZZ$ , the  
 645 equation is divided by 2 to account for identical particles in the final state, and  $x_W$  is replaced with  
 646  $x_Z = 4M_Z^2/m_H^2$ . This is shown in equation 1.16 [29].

$$\Gamma(H \rightarrow ZZ) = \frac{\sqrt{2} G_F M_Z^2 m_H}{32\pi} \frac{\sqrt{1-x_Z}}{x_Z} (3x_Z^2 - 4x_Z + 4) \quad (1.16)$$

647 These formulas can also be visualized as a function of Higgs mass. Figure 1.4 shows the branching

648 ratios as a function of the Higgs mass.

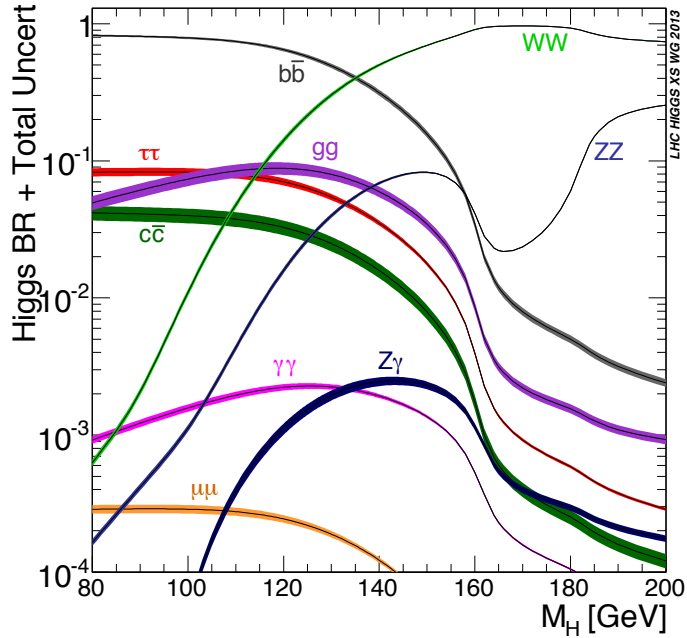


Figure 1.4: Higgs boson branching ratios as a function of  $m_H$  [2].

649 There are a few interesting features to note in this figure. First, note that at high Higgs masses, once  
 650 on-shell production of both  $W$  and  $Z$  bosons is possible, these two decays are the dominant ones due to  
 651 the large masses of the  $W/Z$ . Also note that the branching ratio to  $W$ s is twice that of  $Z$ s at these large  
 652 masses due to the  $\delta_V$  symmetry factor noted previously. At 125 GeV, the Higgs is accessible through  
 653 many different decay modes. The largest branching ratio is the decay  $H \rightarrow b\bar{b}$  at 58.24% [2]. This  
 654 branching is larger than the  $WW/ZZ$  decays because one of the two bosons must be produced off-  
 655 shell for  $m_H = 125$  GeV. The second largest branching ratio is to  $WW^*$  at 21.37 % (before taking  
 656 into account the branching ratios of the  $W$ ). Table 1.2 summarizes the branching ratios for a 125 GeV  
 657 Higgs. Note that there is in fact a Higgs branching ratio to  $\gamma\gamma$  even though photons are massless. This  
 658 decay happens through a loop (the largest contributions to the loop are top and  $W$ ) which suppresses  
 659 the branching ratio.

660 Note that the branching ratios alone do not tell the full story of which Higgs channels are the most  
 661 sensitive. For example, a  $H \rightarrow b\bar{b}$  search in gluon fusion production is incredibly difficult due to the

Decay	Branching ratio (%)
$b\bar{b}$	58.24
$WW^*$	21.37
$gg$	8.187
$\tau\tau$	6.272
$c\bar{c}$	2.891
$ZZ^*$	2.619
$\gamma\gamma$	0.2270
$Z\gamma$	0.1533
$\mu\mu$	0.02176

**Table 1.2:** Branching ratios for a 125 GeV Higgs boson[2].

large QCD dijet background at the LHC. However, in associated production of the Higgs, where a  $W$  or  $Z$  gives additional final state particles that can be used to reduce background, a search for  $H \rightarrow b\bar{b}$  can be sensitive. The combinations of production and decay modes that are most commonly studied are summarized in table 1.3 [29].

Decay	Inclusive (incl. ggF)	VBF	$WH/ZH$	$t\bar{t}H$
$H \rightarrow \gamma\gamma$	✓	✓	✓	✓
$H \rightarrow b\bar{b}$			✓	✓
$H \rightarrow \tau^+\tau^-$		✓		
$H \rightarrow WW^* \rightarrow \ell\nu\ell\nu$	✓	✓	✓	
$H \rightarrow ZZ \rightarrow 4\ell$	✓			
$H \rightarrow Z\gamma \rightarrow \ell\ell\gamma$	very low			

**Table 1.3:** Possible channels for Higgs searches. Checkmarks denote the most sensitive production modes [29].

#### 1.4 HIGGS PAIR PRODUCTION IN THE STANDARD MODEL

The Standard Model also allows for processes that produce two Higgs bosons in the final state, known as Higgs pair production or di-Higgs production. The two main production mechanisms are shown in figure 1.5.

The two diagrams in figure 1.5 interfere destructively with one another, resulting in a low overall cross section for di-Higgs production at the LHC. Nevertheless, Higgs pair production is quite interesting to study because it gives direct access to the  $\lambda$  parameter of the Higgs potential, also known as the Higgs self

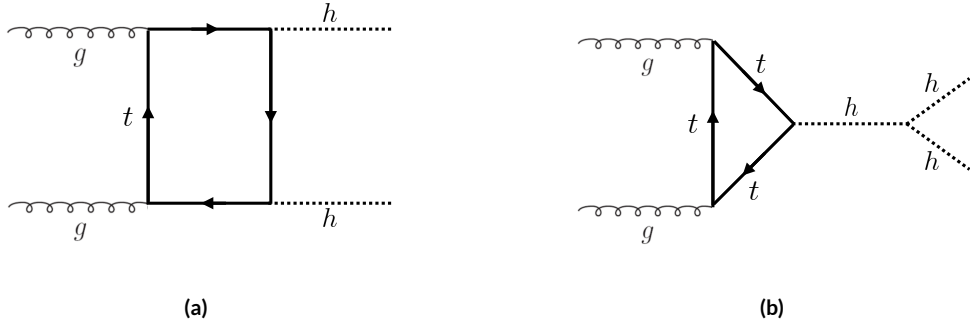


**Figure 1.5:** The two leading diagrams for Standard Model di-Higgs production at the LHC: (a) box diagram, (b) Higgs self coupling

coupling. The diagram in figure 1.5(b) is sensitive to this coupling through the triple Higgs vertex.

One can substitute the gluon fusion production of diagram 1.5(b) with any of the other production modes previously discussed. These other modes do not suffer from interference with the box diagram in figure 1.5(a) due to the presence of additional particles in the final state. They still have a lower cross section than the gluon fusion mode, however. The cross sections for di-Higgs production in the different modes, as well as their uncertainties, are shown in table 1.4 [30]. These are shown for  $\sqrt{s} = 14$  TeV as the higher center of mass energy is more sensitive to this process. Note that the scale of cross section quoted is now in fb rather than pb.

Production mode	$\sigma$ (fb)	Total uncert. (%)
Gluon fusion	33.89	+37.2 / - 27.8
Vector boson fusion	2.01	+7.6 / - 5.1
$W H H$	0.57	+3.7 / - 3.3
$Z H H$	0.42	+7.0 / - 5.5
$t\bar{t}H$	1.02	-

**Table 1.4:** Production cross sections for pair production of a 125 GeV Higgs boson at  $\sqrt{s} = 14$  TeV with total uncertainty [30]. The uncertainties include QCD scale and PDF variations as well as uncertainties on  $\alpha_S$ .

680

## 1.5 HIGGS PAIR PRODUCTION IN THEORIES BEYOND THE STANDARD MODEL

The Standard Model Higgs pair production cross section is rather small, and datasets on the scale of the full lifetime of the LHC will be required to obtain sensitive measurements of the Higgs self-coupling.

684 However, the discovery of the Higgs also gives particle physicists a new tool that can be exploited in the  
 685 search for new physics beyond the Standard Model. In particular, Higgs pair production is a promising  
 686 channel in the search for new physics. The cross section for di-Higgs production can be altered through  
 687 both resonant and non-resonant production of Higgs pairs. In non-resonant production, di-Higgs pro-  
 688 duction vertices can arise from the presence of a new strong sector and additional colored particles[48–  
 689 50]. Figure 1.6 shows examples of the types of vertices that can arise. In the resonant case, new heavy  
 690 particle can decay to Higgs pairs. Such new particles can include heavy Higgs bosons arising in two  
 691 Higgs doublet models (2HDM) or Higgs portal models as well as heavy gravitons in Randall-Sundrum  
 692 theories[3, 5, 48, 51–55]. Figure 1.7 shows a generic diagram for a heavy resonance decaying to two Higgs  
 693 bosons. In the 2HDM,  $X$  corresponds to the heavy CP-even scalar  $H$ . In the Randall-Sundrum model,  
 694  $X$  corresponds to a heavy spin-2 graviton  $G$ .

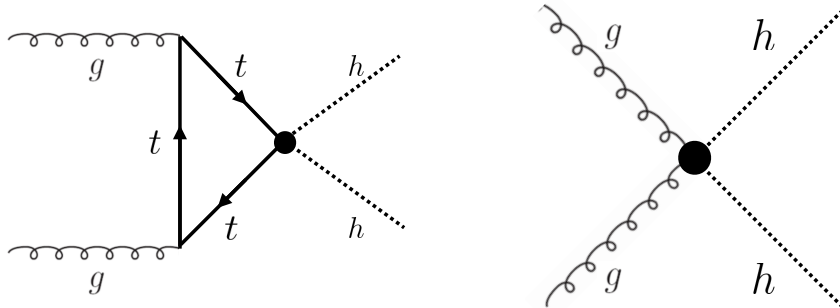


**Figure 1.6:** Diagrams with new vertices for non-resonant Higgs pair production arising in composite Higgs models

695 The next sections provide more detail on the phenomenology of resonant Higgs production in  
 696 Randall-Sundrum and 2HDM models, as these models will later be tested in a dedicated search for reso-  
 697 nant production of boosted Higgs pairs.

### 698 1.5.1 RANDALL-SUNDRUM GRAVITONS

699 The Randall-Sundrum model is a proposed solution to the hierarchy problem that posits a five-dimensional  
 700 warped spacetime that contains two branes: one where the force of gravity is very strong and a second  
 701 brane at the TeV scale corresponding to the known Standard Model sector [51]. In the theory, the  
 702 branes are weakly coupled and the graviton probability function drops exponentially going from the

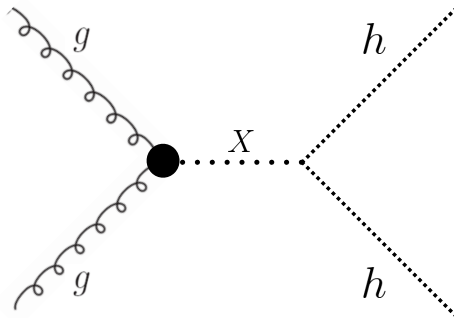


**Figure 1.7:** Generic Feynman diagram for resonant Higgs pair production in BSM theories

703 gravity brane to the SM brane, rendering gravity weak on the SM brane. The experimental consequence  
 704 of this theory is a tower of widely spaced (in mass) Kaluza-Klein graviton resonances. In theories where  
 705 the fermions are localized to the SM brane, production of gravitons from fermion pairs is suppressed  
 706 and the primary mode of production is gluon fusion[3]. These gravitons have a substantial branching  
 707 fraction to Higgs pairs, ranging from 6.43% for gravitons with a mass of 500 GeV to 7.66% at 3 TeV.  
 708 Figure 1.8 shows the branching ratios of the spin-2 Randall Sundrum graviton (RSG) as a function of its  
 709 mass. The predominant decays are to  $t\bar{t}$  above the mass threshold for that channel.

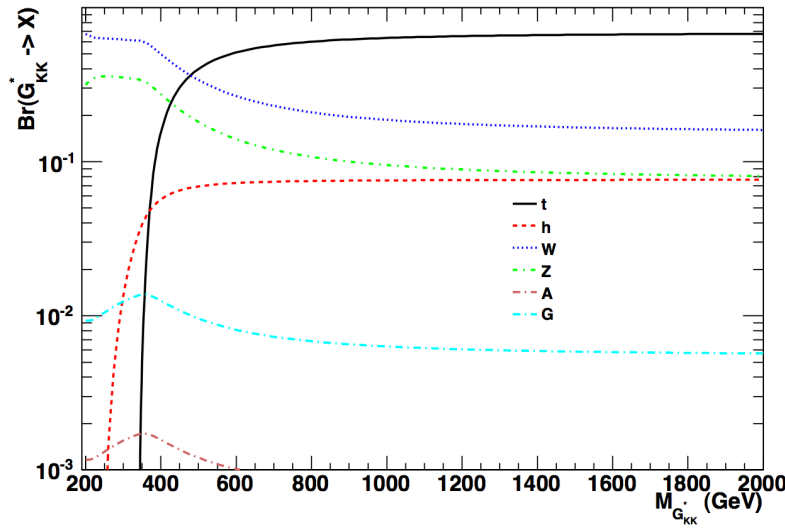


**Figure 1.8:** Branching ratios for a spin-2 Randall-Sundrum graviton as a function of mass computed in MadGraph with the CP3-Origins implementation [3, 4]

710 These models have two free parameters - the mass of the graviton and a curvature parameter  $k$ . Typ-

711 ically, rather than  $k$ , the theory is parameterized using  $c \equiv k/\bar{M}_{\text{pl}}$ , where  $\bar{M}_{\text{pl}}$  is the reduced Planck  
 712 mass. The cross section for production of the RSG decreases as a function of mass and is strongly depen-  
 713 dent on the gluon PDF. The increase in center of mass energy from 8 to 13 TeV in LHC Run 2 greatly  
 714 increases the cross section at higher mass. Figure 1.9 shows the cross section as a function of graviton  
 715 mass at  $\sqrt{s} = 13$  TeV for RSG models with  $c = 1.0$  and  $c = 2.0$ .

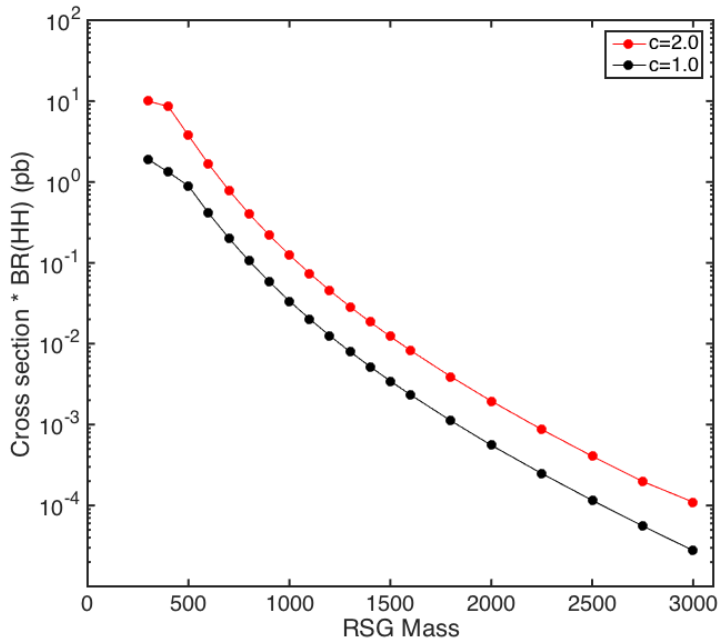


**Figure 1.9:**  $\sigma \times \text{BR}(HH)$  for RSG as a function of mass computed in MadGraph with the CP3-Origins implementation [3, 4]

716 Another interesting feature of the theory is that the width of the graviton increases with both  $c$  and  
 717  $m_G$ . Figure 1.10 shows the graviton width for both  $c = 1.0$  and  $c = 2.0$  as a function of mass. In  
 718  $c = 1.0$ , the width starts at 8.365 GeV for a mass of 300 GeV and increases to 187.2 GeV at a mass of  
 719 3 TeV. Similarly, with  $c = 2.0$ , the width starts at 33.46 GeV for  $m_G = 300$  GeV and increases to  
 720 748.8 GeV at a mass of 3 TeV.

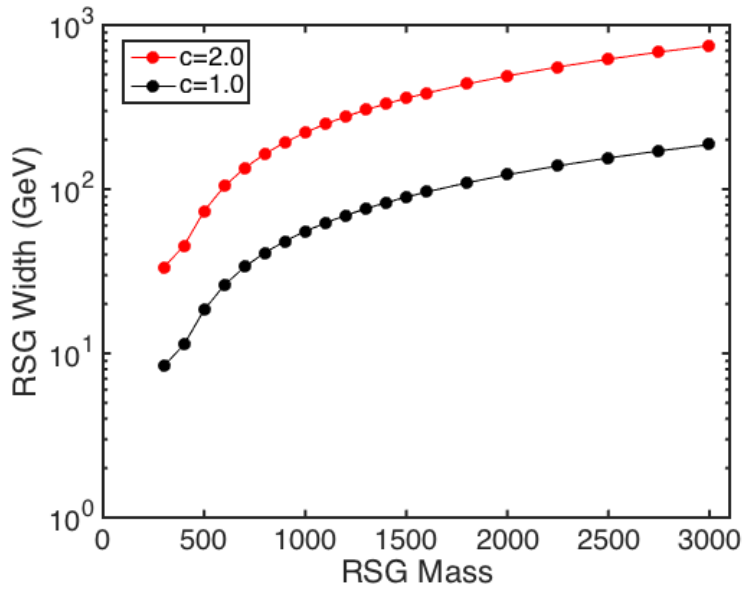


**Figure 1.10:** RSG width as a function of mass computed in MadGraph with the CP3-Origins implementation [3, 4]

### 721 1.5.2 TWO HIGGS DOUBLET MODELS

722 In Two Higgs Doublet Models (2HDM), a second complex scalar doublet is added to SM[5, 53, 54]. In  
 723 this case, all four degrees of freedom in the second doublet correspond to new particles, meaning that  
 724 there are five total scalars from the two Higgs doublets -  $h$  (light CP-even Higgs),  $H$  (heavy CP-even  
 725 Higgs),  $A$  (heavy CP-odd Higgs), and  $H^\pm$  (charged Higgs). The model is parameterized by two main  
 726 parameters. The first,  $\tan \beta \equiv \frac{v_2}{v_1}$ , is the ratio of the vacuum expectation values of the two Higgs dou-  
 727 blets (where  $v_1$  corresponds to the  $v$  in the SM Higgs model described above). The second parameter  
 728 is  $\alpha$ , a mixing angle between the heavy and light Higgs fields. Models are also often parameterized with  
 729  $\cos(\beta - \alpha)$  rather than  $\alpha$  directly. The limit where  $\cos(\beta - \alpha) = 0$  is called the alignment limit, and  
 730 it is in this limit that the light Higgs  $h$  has the same couplings as a Standard Model Higgs.

731 2HDM models are usually separated into two main types - Type I and Type II. In Type I models, the  
 732 charged fermions only couple to the second Higgs doublet, leading to a fermiophobic light Higgs. In  
 733 Type II models, up-type quarks couple to the first doublet while down-type quarks couple to the second  
 734 doublet. One specific realization of a Type II 2HDM is the Minimal Supersymmetric Standard Model  
 735 (MSSM).

736 Resonant di-Higgs production in this model can proceed through decays of the heavy CP-even Higgs  
 737  $H \rightarrow hh$ . The branching ratio for  $H \rightarrow hh$  depends on the model type as well as the values of  $\tan \beta$   
 738 and  $\cos(\beta - \alpha)$ . Figure 1.11 shows the branching ratios as a function of the mass of the heavy scalar  $H$  for  
 739 both Type I and Type II models. Depending on the type of model  $hh$  can be a substantial fraction of the  
 740 decays of  $H$ .

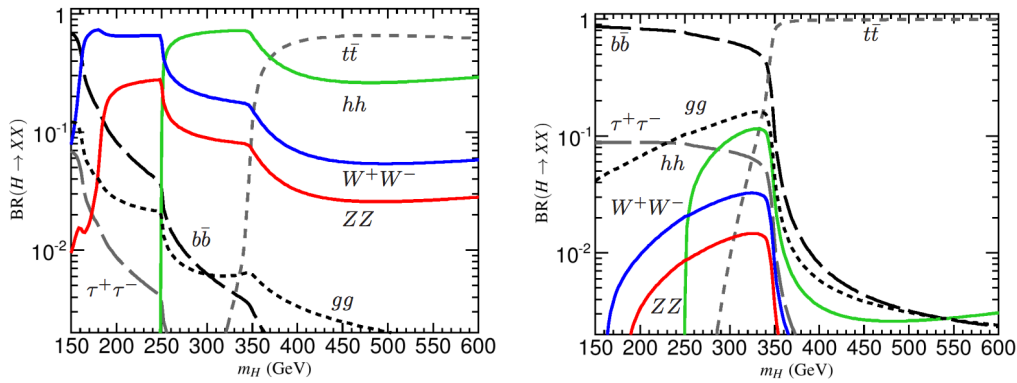


**Figure 1.11:** Branching ratios for heavy Higgs  $H$  in Type I (left) and Type II (right) 2HDM models with  $\tan \beta = 1.5$  and  $\cos(\beta - \alpha) = 0.1$  (Type I) ( $0.01$  for Type II). [5]

## 741 1.6 CONCLUSION

742 Studying the Higgs sector is essential for understanding the details of how mass arises in the Standard  
 743 Model and how the electroweak symmetry is broken. The discovery of the Higgs boson also opens the  
 744 door for its use as a tool to search for new physics, and Higgs pair production is an ideal candidate for  
 745 this study. Even if no BSM physics is found in Higgs pair production, searches for Higgs pairs will put  
 746 constraints on the Higgs self coupling and thus further knowledge of the Standard Model and the details  
 747 of the Higgs potential.

*This is some random quote to start off the chapter.*

Firstname lastname

# 2

748

749

750

## The ATLAS detector and the Large Hadron Collider

751 This chapter presents an overview of the experimental systems used to conduct the measurements pre-  
752 sented in this thesis. First, a brief overview of the accelerator, the Large Hadron Collider, will be given.  
753 In this section, the accelerator conditions relevant to data-taking are presented as well. Next, an overview  
754 of the ATLAS experiment is given. The basics of each sub-detector's role are summarized, as well as the  
755 details of the datasets accumulated. Then, a brief interlude on the ATLAS Muon New Small Wheel up-  
756 grade is presented. While this new detector does not have a direct impact on any of the datasets taken  
757 so far, it will have an impact on future analyses and the work done on it is briefly summarized here. Fi-  
758 nally, an overview of object reconstruction in ATLAS is given. While the details of all of the algorithms  
759 will not be presented in detail, aspects of the reconstruction performance such as object resolutions are  
760 shown as these are relevant to the two studies presented later in this thesis.

761 2.1 THE LARGE HADRON COLLIDER

762 The Large Hadron Collider (LHC) is a proton-proton collider at the CERN laboratory in Geneva,  
763 Switzerland[56]. It is designed for a maximum collision center of mass energy of  $\sqrt{s} = 14 \text{ TeV}$  and  
764 has a circumference of 26.7 kilometers. Four main experiments are located at the interaction points (IP)  
765 of the accelerator: ATLAS (A Toroidal LHC ApparatuS), CMS (the Compact Muon Solenoid), ALICE  
766 (A Large Ion Collider Experiment), and LHCb [7, 57–59]. The studies performed in this thesis were all  
767 completed with the ATLAS detector.

768 Figure 2.1 shows a schematic of the LHC ring and the various experiments.

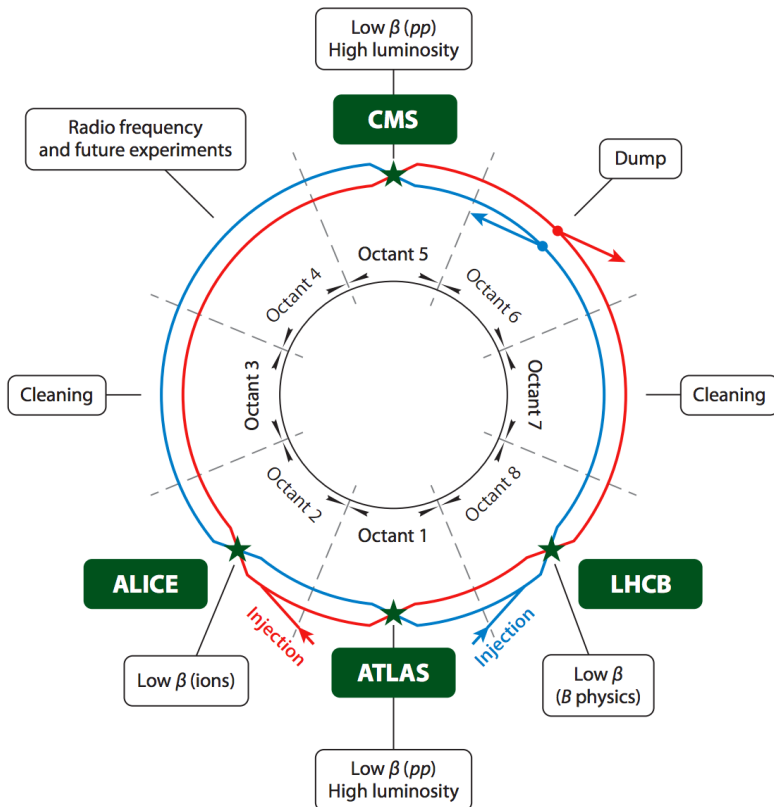


Figure 2.1: A schematic view of the LHC ring [6]

769 One of the most interesting features of the LHC is in its magnet design. Because the tunnel does not  
770 have room for separate superconducting magnets for each of the beam pipes, the LHC employs a twin-  
771 bore magnet design. Each magnet must hold an 8.3 Tesla magnetic field in order to bend the proton

<sup>772</sup> beams at  $\sqrt{s} = 14$  TeV. The superconducting magnets are cooled to a temperature of 1.9 Kelvin with  
<sup>773</sup> superfluid helium.

### <sup>774</sup> 2.1.1 INSTANTANEOUS LUMINOSITY

<sup>775</sup> The rate of physics events expected from the accelerator is dependent on the instantaneous luminosity  
<sup>776</sup> of the machine and the cross section of the physics process,  $R_{\text{events}} = L\sigma$ . Here,  $R_{\text{events}}$  is the number  
<sup>777</sup> of events per second,  $L$  is the instantaneous luminosity of the machine, and  $\sigma$  is the cross section for the  
<sup>778</sup> physics process being measured. The instantaneous luminosity of the LHC is determined by numerous  
<sup>779</sup> factors related to machine conditions. Equation 2.1 gives the equation for instantaneous luminosity of  
<sup>780</sup> Gaussian beam profile [6].

$$L = \frac{N_b^2 n_b f_{\text{rev}} \gamma_r}{4\pi \epsilon_n \beta^*} F \quad (2.1)$$

<sup>781</sup> The LHC collides protons in bunches, and in the above equation  $N_b$  is the number of protons per  
<sup>782</sup> bunch while  $n_b$  is the number of bunches per beam. Nominally, the LHC can hold up to 2808 pro-  
<sup>783</sup> ton bunches.  $f_{\text{rev}}$  is the revolution frequency.  $\epsilon_n$  is the normalized transverse beam emittance, a mea-  
<sup>784</sup> surement of the average spread of the particles position-momentum space which has the dimension of  
<sup>785</sup> length.  $\beta^*$  is the value of the *beta* function for the beam at the interaction point. It relates the emmi-  
<sup>786</sup> tance to the Gaussian width of the beam with  $\sigma_{\text{beam}} = \sqrt{\epsilon \cdot \beta}$ .  $F$  is a reduction factor that corrects for  
<sup>787</sup> the fact that the beams are colliding at an angle at the IP.

<sup>788</sup> Another way of writing the instantaneous luminosity is shown in equation 2.2. In this case, the in-  
<sup>789</sup> stantaneous luminosity is written as the ratio of the rate of inelastic collisions with the inelastic cross  
<sup>790</sup> section[60].

$$L = \frac{R_{\text{inel}}}{\sigma_{\text{inel}}} = \frac{\mu n_b f_{\text{rev}}}{\sigma_{\text{inel}}} \quad (2.2)$$

<sup>791</sup> In this case,  $\mu$  is the average number of interactions per bunch crossing in the accelerator.  $\mu$  is a useful  
<sup>792</sup> parameter for characterizing the amount of activity recorded in an experiment. As the instantaneous

793 luminosity and thus  $\mu$  increase, there are more interactions per bunch crossing and more activity in the  
 794 detector. This is often characterized with  $\langle \mu \rangle$ , the measured per bunch crossing  $\mu$  value averaged over  
 795 all bunch crossings. The interactions inside each bunch crossing that are not the main physics process of  
 796 interest are often referred to as “pileup” interactions, and  $\langle \mu \rangle$  is a measurement of the level of pileup in  
 797 the detector.

### 798 2.1.2 EVOLUTION OF MACHINE CONDITIONS

799 This thesis uses datasets taken at three different center of mass energies:  $\sqrt{s} = 7$  TeV data taken in the  
 800 year 2011,  $\sqrt{s} = 8$  TeV data taken in the year 2012, and  $\sqrt{s} = 13$  TeV dataa taken in the year 2015. In  
 801 addition to increasing center of mass energy, the instananeous luminosity and parameters that determine  
 802 it were evolving. Table 2.1 summarizes that machine conditions in each of these datasets.

	2011	2012	2015	Design
$\sqrt{s}$ [ TeV]	7	8	13	14
Number of bunches	1380	1380	1825	2808
Max. protons per bunch	$1.45 \times 10^{11}$	$1.7 \times 10^{11}$		$1.15 \times 10^{11}$
Bunch spacing [ns]	50	50	25	25
Max. instantaneous luminosity [ $\text{cm}^{-2}\text{s}^{-1}$ ]	$3.7 \times 10^{33}$	$7.7 \times 10^{33}$	$5 \times 10^{33}$	$10^{34}$
$\beta^*$ [m]	1.0	0.6	0.8	0.55
$\langle \mu \rangle$	11.6	20.7	13.7	-

Table 2.1: Evolution of LHC machine conditions [31, 32]

## 803 2.2 THE ATLAS DETECTOR

804 The ATLAS detector is a multi-purpose particle detector experiment at the LHC’s Point 1 [7]. It has  
 805 nearly  $4\pi$  coverage in solid angle around the interaction point. It consists of an inner detector for mea-  
 806 suring charged particles, electromagnetic and hadronic calorimeters, and a muon spectrometer. Fig-  
 807 ure 2.2 gives an overview of the detector.

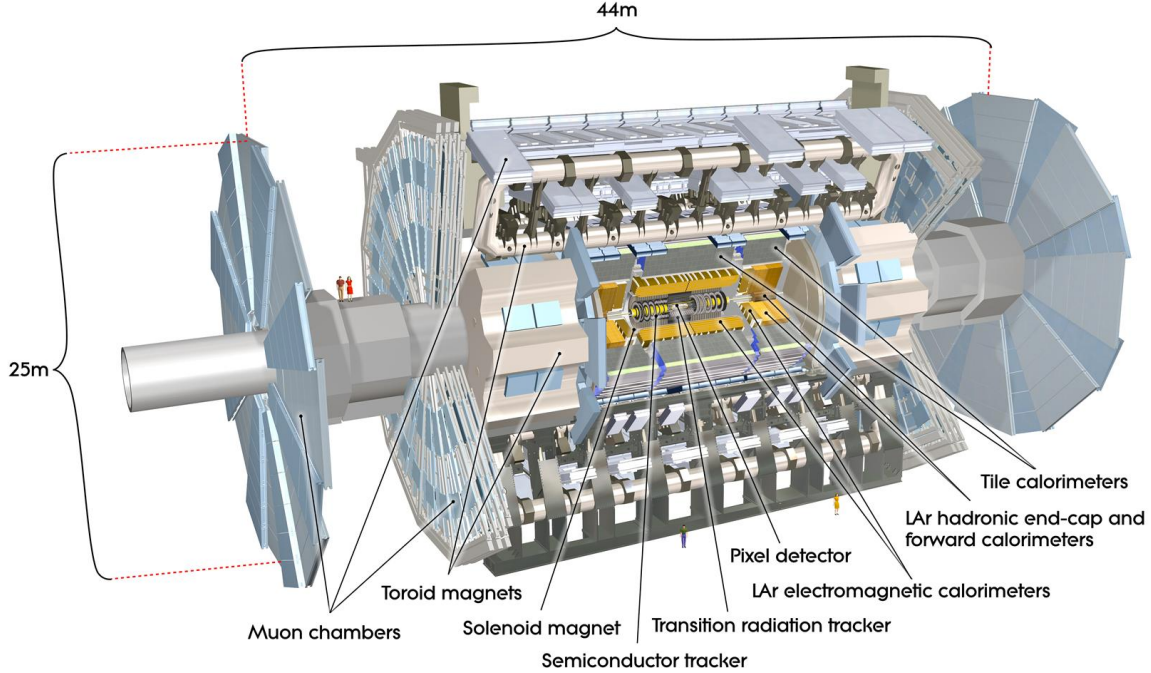


Figure 2.2: A full diagram of the ATLAS detector [7]

### 808 2.2.1 COORDINATE SYSTEM

809 Before defining the properties of the individual detectors, it is important to establish the coordinate  
 810 system used. Figure 2.3 shows a schematic of the coordinate system. The azimuthal plane (perpendicular  
 811 to the beam line) is defined as the  $x$ - $y$  plane. The angle in this plane is referred to as  $\phi$ . The angle relative  
 812 to the beam axis is referred to as  $\theta$ . Rather than using  $\theta$  directly as a coordinate, the experiment often  
 813 uses the pseudorapidity  $\eta$ .  $\eta$  is defined in equation 2.3.

$$\eta = \ln \left( \tan \left( \frac{\theta}{2} \right) \right) \quad (2.3)$$

814 Pseudorapidity is the massless approximation of rapidity, the angle used to parameterize boosts in  
 815 special relativity. This is important for two reasons. First, it means that differences in  $\eta$  are Lorentz in-  
 816 variant. Second, particle production is roughly constant in pseudorapidity. Particles with  $\eta$  close to zero  
 817 are referred to as “central”, while those at high  $|\eta|$  are called “forward”. In general, two main detector

818 topologies can be seen in figure 2.2. There are “barrel” elements, which surround the beam line cylind-  
 819 drically and are in the central region of the detector. In the forward region, there are “endcap” regions  
 820 which are arranged as disks perpendicular to the beam line.

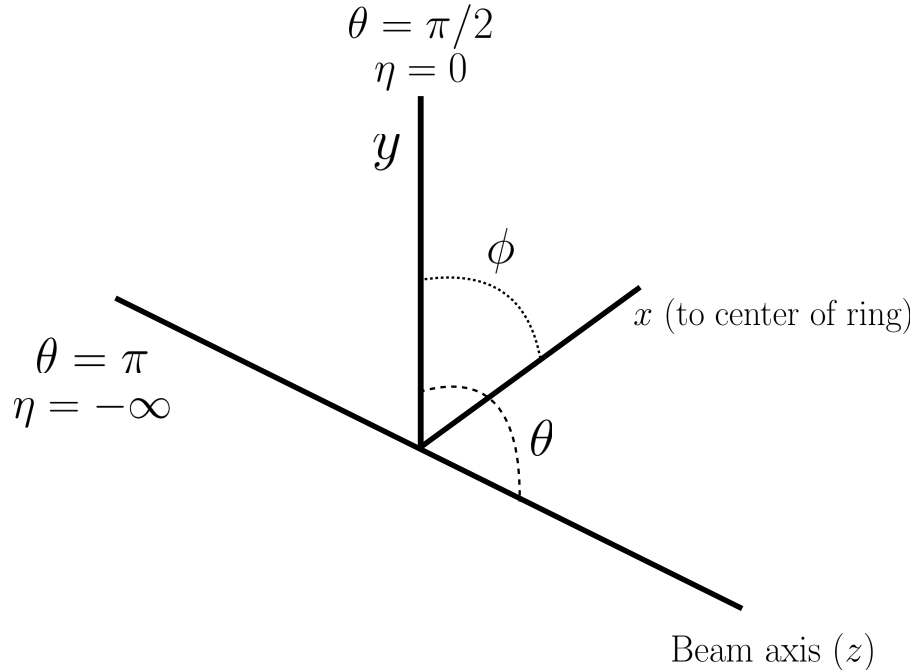


**Figure 2.3:** The ATLAS coordinate system

### 821 2.2.2 INNER DETECTOR

822 The ATLAS Inner Detector (ID) system is built for precision tracking of charged particles. It covers the  
 823 range  $|\eta| < 2.5$ . In this range, approximately 1000 particles are generated every bunch crossing in the  
 824 detector. This requires having fine granularity to achieve the resolutions required for good momentum  
 825 measurement and vertex reconstruction.

826 The ID consists of three sub-components: the pixel detector, semiconductor tracker (SCT), and trans-  
 827 sition radiation tracker (TRT). It is surrounded by a solenoid providing a 2 T axial magnetic field which  
 828 bends particles in the transverse plane to allow for momentum measurement. Figure 2.4 shows the layout  
 829 of each of these components.

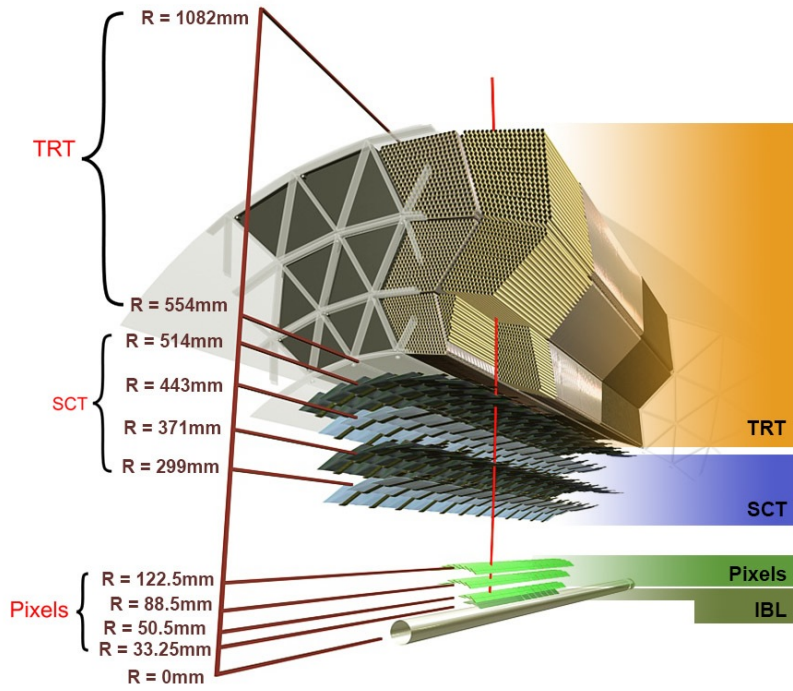


Figure 2.4: Layout of the ATLAS Inner Detector system [8]

### 830 PIXEL DETECTOR

831 The pixel detector is the first detector particles traverse after being generated in proton collisions and is  
 832 the most granular detector. Its operation is crucial for precision tracking and vertex reconstruction as  
 833 well as higher level object reconstruction like tagging of jets from  $b$ -quarks. The basic sensing element in  
 834 this subdetector is a silicon pixel detector. The operating principle for the silicon pixels is that of a  $p$ - $n$   
 835 junction. When a charged particle passes through, it creates electron-hole pairs that are then separated  
 836 by the electric field. The sensors are  $250 \mu\text{m}$  thick and use oxygenated  $n$ -type wafers with readout pixels  
 837 on the  $n^+$  side of the detector [7]. Overall, the pixel detector has 1744 sensors and 80.4 million readout  
 838 channels.

839 In the barrel region, the pixel detector has three concentric layers of sensors surrounding the beam-  
 840 line. In the endcap region, it consists of disks perpendicular to the beam axis. The detector is segmented  
 841 in the  $R$ - $\phi$  plane and in  $z$ . Usually, three pixel layers are crossed by a charged particle track. The intrinsic  
 842 accuracies of the sensors are  $10 \mu\text{m}$  in  $R$ - $\phi$  and  $115 \mu\text{m}$  in  $z$  (or  $R$  for the endcap).

843    **INSERTABLE B-LAYER**

844    In Run 2, a new innermost pixel layer, known as the insertable B-layer (IBL), was added to the Inner  
845    Detector [61]. This layer was added to cope with the higher luminosities planned in LHC Run 2 and  
846    at the high luminosity HL-LHC. Additionally it improves tracking position resolution which in turn  
847    improves the vertexing and  $b$ -tagging capabilities in ATLAS. The detector sits directly on a new beam  
848    pipe, only 33.25 mm away from the collision points in the azimuthal plane.

849    **SEMICONDUCTOR TRACKER (SCT)**

850    The semiconductor tracker (SCT) consists of silicon microstrips and comprises the next four layers of  
851    the ID. This sub-detector has 6.4cm long sensors that are daisy-chained into strips with a strip pitch of  
852     $80 \mu\text{m}$  [7]. Some of the strips have a small stereo angle to allow for measurement of both angular coor-  
853    dinates. In total there are 6.3 million readout channels. The intrinsic accuracies are  $17 \mu\text{m}$  in  $R\text{-}\phi$  and  
854     $580 \mu\text{m}$  in  $z$  (or  $R$  in the endcap).

855    **TRANSITION RADIATION TRACKER (TRT)**

856    The transition radiation tracker (TRT) serves two purposes. First, it consists of 4mm diameter straw  
857    tubes filled with a 70/27/3% gas mixture of xenon, carbon dioxide, and oxygen to provide tracking of  
858    charged particles. Particles typically have 36 TRT straw tube hits per track. The material in between  
859    the straws is designed to induce transition radiation which can be useful for particle identification. As  
860    particles pass between media with different dielectric constants, they emit transition radiation that can  
861    cause additional showers in the TRT. In particular it is useful for discrimination between electrons and  
862    pions or other charged hadrons, as the amount of transition radiation is proportional to the Lorentz  
863    factor of the particle.

864    **2.2.3 CALORIMETERS**

865    The calorimeter system consists of two main sub-components: a fine granularity electromagnetic calorime-  
866    ter tailored for the measurement of photons and electrons and multiple coarser hadronic calorimeters

867 dedicated to the measurement of hadronic showers [7]. The calorimeter system has broader coverage  
868 than the inner detector, covering the region out to  $|\eta| < 4.9$ . It is also designed to deliver good contain-  
869 ment of showers so as to limit leakage into the muon system. Figure 2.5 shows the layout of the calorime-  
870 ter system.

871 Both the electromagnetic and hadronic calorimeters are sampling calorimeters. They alternate active  
872 material for energy measurement with passive material for energy absorption. The materials used for  
873 each purpose vary based on the type of calorimeter and its location in the detector.

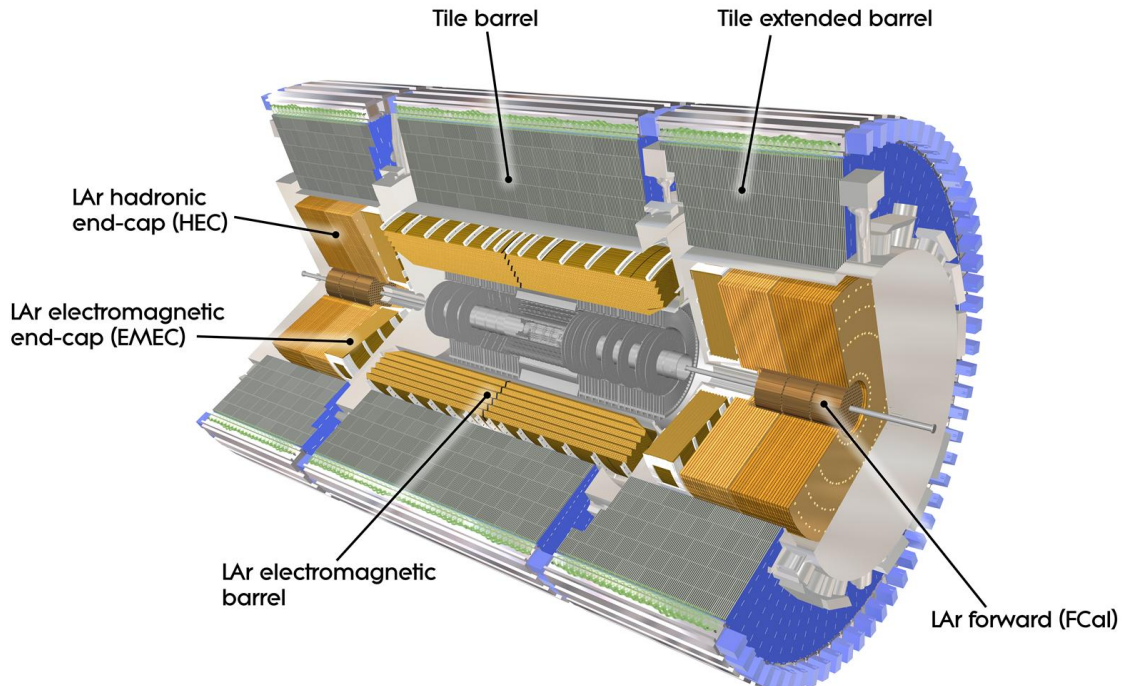


Figure 2.5: Layout of the ATLAS calorimeter system [7]

874 ELECTROMAGNETIC CALORIMETER

875 The electromagnetic calorimeter (EM calorimeter) use liquid Argon (LAr) as its active material and lead  
876 as its passive material. It is arrange in an accordion geometry to increase the absorption area while still  
877 allowing it to have no azimuthal cracks (complete symmetry in  $\phi$ ). The EM calorimeter is divided into a

878 barrel portion that extends to  $|\eta| < 1.475$  and an endcap portion going from  $1.375 < |\eta| < 3.2$ . The  
879 region where these two units overlap is called the “transition region”.

880 In order to provide good containment the calorimeter depth must be optimized. Typically, for elec-  
881 tromagnetic calorimeters the depth is measured in radiation lengths. In general, the intensity of a par-  
882 ticle beam attenuates exponentially in distance with a constant equal to the radiation length. That is,  
883  $I(x) = I_0 e^{-x/X_0}$ , where  $I$  is the intensity,  $x$  is the distance traveled, and  $X_0$  is the radiation length.  
884 The ATLAS EM calorimeter is designed to have  $> 22$  radiation lengths in the barrel and  $> 24$  in the  
885 endcap [7].

886 **HADRONIC CALORIMETERS**

887 There are three types of hadronic calorimeters present in ATLAS: the tile calorimeter (TileCal), hadronic  
888 endcap (HEC), and forward calorimeter (FCal). Each one is optimized for stopping of hadronic showers  
889 and the materials chosen are specific to their placement in the detector.

890 The TileCal is a scintillating tile calorimeter placed directly outside the EM calorimeter. It uses steel as  
891 the absorber and plastic scintillator tiles as the active material. It has coverage in the barrel at  $|\eta| < 1.0$   
892 and in the “extended barrel” region of  $0.8 < |\eta| < 1.7$ .

893 The HEC had two wheels perpendicular to the beam line per endcap and is located directly behind  
894 the EM calorimeter endcap modules. The HEC covers the region from  $1.5 < |\eta| < 3.2$ , overlapping  
895 slightly with both the tile calorimeter and the forward calorimeter. Like the EM calorimeter, it uses liq-  
896 uid Argon as the active material, but it uses copper as the absorber.

897 The FCal covers the most forward regions of the calorimeter system, extending to the region of  $3.1 <$   
898  $|\eta| < 4.9$ . It again uses liquid argon as its active material. For absorber, it consists of an innermost  
899 module made of copper followed by a module made of tungsten.

900 The hadronic equivalent of radiation length is called the interaction length and is denoted as  $\lambda$ . In the  
901 barrel, the hadronic calorimeter depth is approximately  $9.7\lambda$ , while in the endcap is is  $10\lambda$ . The outer  
902 supports contribute an additional  $1.3\lambda$ . This is been shown to be sufficient to limit punch-through of  
903 showers to the muon system [7].

904    2.2.4    MUON SPECTROMETER

905    The muon spectrometer is dedicated to measuring the momentum and position of muons. It consists  
906    of tracking and trigger chambers which are unique in the barrel and endcap regions. The magnetic field  
907    for bending of muons is provided by a system of three large air-core toroid magnets (from which ATLAS  
908    derives its name.) These magnets provide 1.5 to 5.5 Tm of bending power at  $0 < |\eta| < 1.4$  and approx-  
909    imately 1 to 7.5 Tm in the endcap region of  $1.6 < |\eta| < 2.7$ . The entire muon system covers the range  
910     $0 < |\eta| < 2.7$ . Monitored drift tubes (MDTs) are used for tracking in the barrel and the two outer  
911    layers of the endcap, while cathode strip chambers (CSCs) are used to provide tracking in the innermost  
912    endcap wheel. In the barrel, resistive plate chambers (RPCs) are used as trigger chambers while thin gap  
913    chambers (TGCs) are used in the endcap. Figure 2.6 shows the layout of the ATLAS muon system. The  
914    entire muon system is designed with the specification of providing a 10% momentum resolution for a  
915    1 TeV muon.

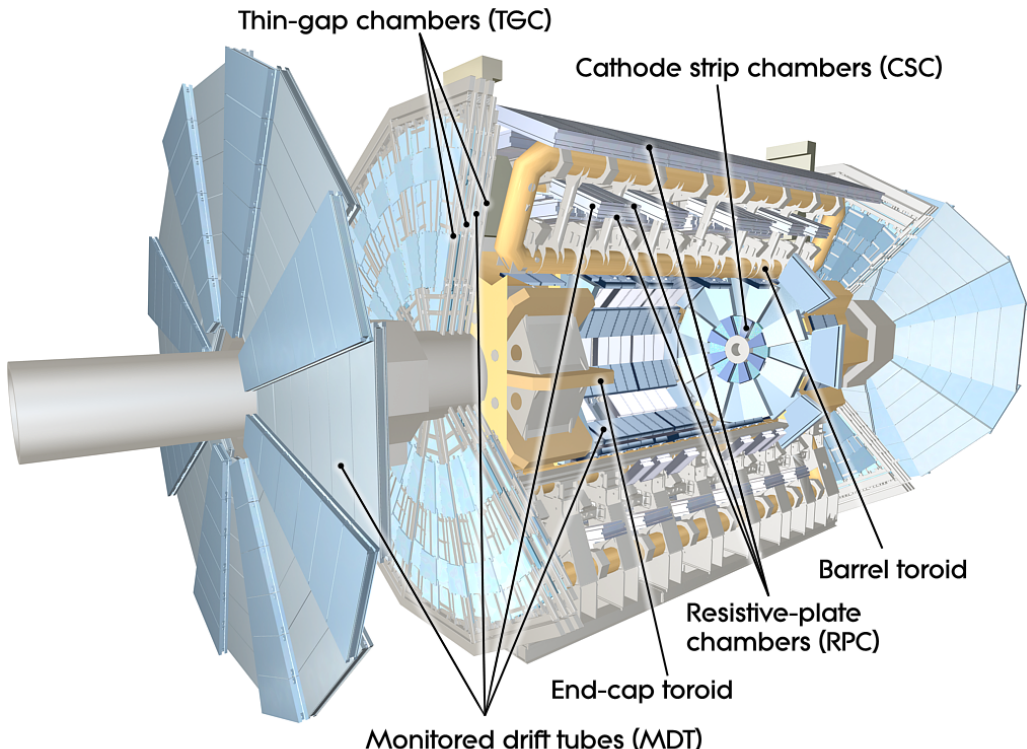


Figure 2.6: Layout of the ATLAS muon system [7]

916 MONITORED DRIFT TUBES (MDTs)

917 The monitored drift tubes (MDTs) are aluminum 3cm diameter tubes filled with a 93/7 % mixture of  
918 Argon and CO<sub>2</sub>, with trace amounts of water. As a charged particle traverses the tube, it ionizes the gas  
919 and the ions drift to a wire at the center of the tube. The radial distance of traversal of the particle in the  
920 tube is determined by the drift time of the electrons, allowing for fine position resolution. The tubes  
921 have an average resolution of 80  $\mu\text{m}$  per tube and a maximum drift time of approximately 700ns. The  
922 tubes are oriented so that they give precision measurement in  $\eta$  and run along  $\phi$ . They cover  $|\eta| < 2.7$ ,  
923 except in the innermost layer of the endcap where they only go to  $|\eta| < 2.0$  [7].

924 CATHODE STRIP CHAMBERS (CSCs)

925 The cathode strip chambers cover a narrow window of the innermost endcap region at  $2.0 < |\eta| <$   
926 2.7. In this region the background rates in the cavern are particularly high and the CSCs are designed  
927 to handle these higher rates. The CSCs are multiwire proportional chambers with wires pointing in  
928 the radial direction (away from the beam pipe). The wire serves as an anode and there are two types of  
929 segmented cathode strip, one perpendicular to the wires which gives the precision measurement and one  
930 parallel which provides the transverse coordinate. It has an 80/20 gas mixture of Argon and CO<sub>2</sub> [7].

931 RESISTIVE PLATE CHAMBERS (RPCs)

932 The resistive plate chambers (RPCs) are gaseous electrode-plate detectors covering the region  $|\eta| <$   
933 1.05. They consist of two resistive plates separated by a distance of 2 mm. The gas mixture used is a  
934 94.7/5/0.3% mixture of C<sub>2</sub>H<sub>2</sub>F<sub>4</sub>, Iso-C<sub>4</sub>H<sub>10</sub>, and SF<sub>6</sub>. It has readout strips with a pitch of 23-35 mm  
935 for both  $\eta$  and  $\phi$  measurement and thus provides measurement of the azimuthal coordinate in the barrel  
936 that the MDTs do not. The thin gas gap allows for a quick response time which makes it ideal for use in  
937 the trigger. There are three layers of RPCs which are referred to as the three trigger stations. They allwo  
938 for both a low  $p_T$  and high  $p_T$  trigger. The coincidence of hits in the innermost chambers allows for  
939 triggering of muons between 6 and 9 GeV, while the outermost layer allows the trigger to select high  
940 momentum tracks in the range of 9 to 35 GeV [7].

941 THIN GAP CHAMBERS (TGCs)

942 The thin gap chambers (TGCs) are multiwire proportional chambers where the wire to cathode dis-  
943 tance (1.4mm) is smaller than the wire-to-wire distance (1.8 mm). They contain a gas mixture of CO<sub>2</sub>  
944 and *n*-pentane and use a hih electric field to gain good time resolution. They serve two functions in the  
945 end-cap system. First, they serve as the trigger chambers. Second, they also provide azimuthal coordi-  
946 nate measurement which the MDTs do not. They sit on the inner and middle layers of the endcap. The  
947 outermost layer's azimuthal coordinate is determined by extrapolation [7].

948 2.2.5 MAGNET SYSTEM

949 As mentioned previously, there are two independent magnet systems in ATLAS. The first is a 2 T solenoid  
950 field in the inner detector which provides bending in the azimuthal plane. The second is an approxi-  
951 mately 0.5 T toroidal field in the muon system which provides bending in  $|\eta|$ . Figure 2.7 shows the pre-  
952 dicted field integral as a function of  $|\eta|$  [7].

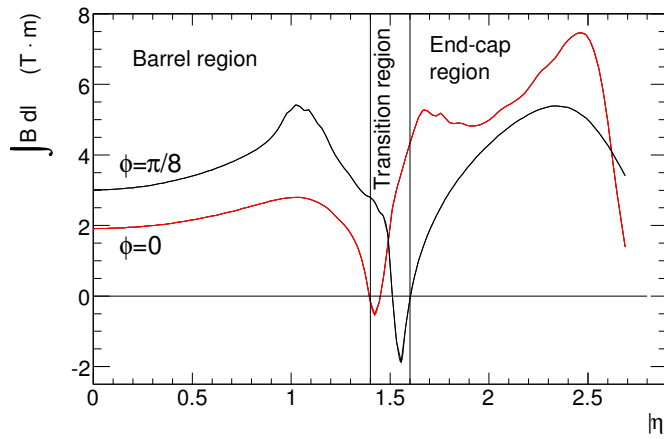


Figure 2.7: Predicted field integral as a function of  $|\eta|$  for the ATLAS magnet system [7]

953 2.2.6 TRIGGER SYSTEM

954 The ATLAS trigger system searches for signatures of muons, electrons, photons, hadronically decay-  
955 ing  $\tau$  leptons, and jets in order to save these events for further analysis. The trigger system in ATLAS

956 is designed to reduce the maximum LHC event rate of 40 MHz to a more reasonable rate that can be  
 957 recorded. The trigger first consists of a fast, hardware based system called the Level-1 (L1) trigger. The  
 958 L1 trigger consists of independent dedicated detector sub-components that can seed regions of in-  
 959 terest (RoIs) for further analysis downstream. For muons, the RPCs and TGCs are used, while in the  
 960 calorimeter coarsely grained sections of calorimeter cells called towers are used. Once regions of interest  
 961 are seeded, a software based system called the High Level Trigger (HLT) is used to reconstruct objects  
 962 and integrate information from different parts of the detector. In Run 1 of ATLAS, the HLT consisted  
 963 of two separate stages: the level 2 (L2) trigger and the event filter (EF).

964 The maximum trigger rate that the L1 trigger can handle is 75 kHz. In the HLT, the rate of events  
 965 written to disk is approximately 200 Hz. Figure 2.8 shows the trigger rates for different L1 triggers in  
 966 2012 and 2015 for ATLAS [9].

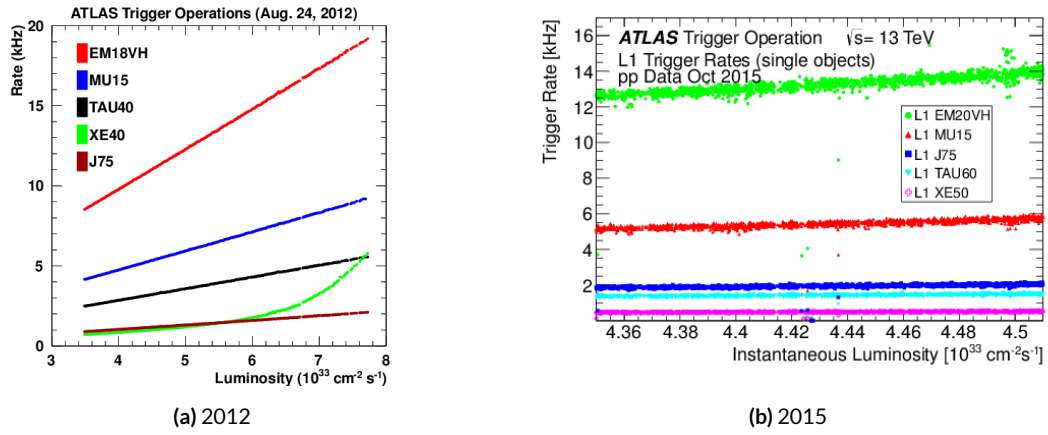


**Figure 2.8:** ATLAS trigger rates for Level-1 triggers as a function of instantaneous luminosity in 2012 and 2015 operation. These are single object triggers for electromagnetic clusters (EM), muons (MU), jets (J), missing energy (XE), and  $\tau$  leptons (TAU). The threshold of the trigger is given in the name in GeV. [9]

### 967 2.2.7 ATLAS DATASETS

968 ATLAS has collected data at center of mass energies of 7, 8, and 13 TeV. Figure 2.9 shows the integrated  
 969 luminosity as a function of time for each of the three collected datasets. At  $\sqrt{s} = 7$  TeV, ATLAS  
 970 recorded  $5.08 \text{ fb}^{-1}$ . Increased instantaneous luminosity in 2012 led to a larger dataset of  $21.3 \text{ fb}^{-1}$   
 971 recorded at  $\sqrt{s} = 8$  TeV. After Long Shutdown 1 (LS1) of the LHC and a restart in 2015, ATLAS

recorded  $3.9 \text{ fb}^{-1}$  of data at  $\sqrt{s} = 13 \text{ TeV}$ . [10, 11]

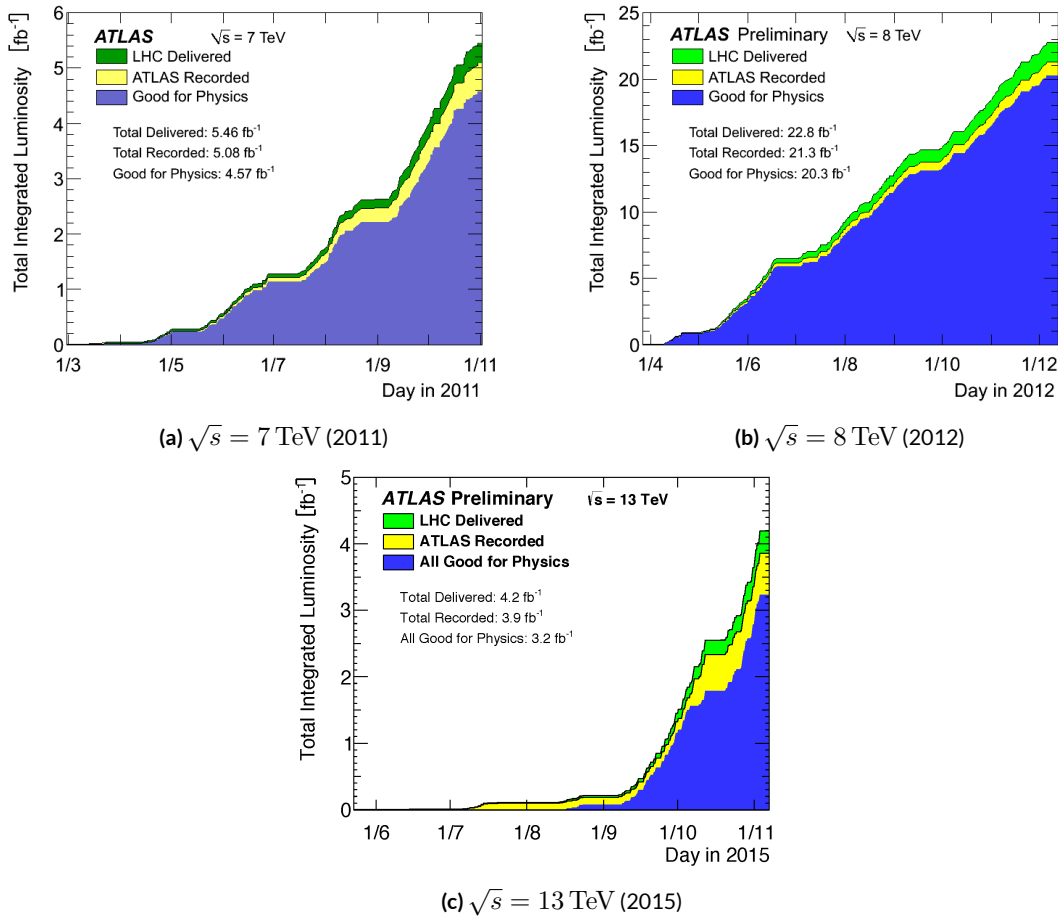


**Figure 2.9:** Instantaneous luminosity as a function of time for data recorded by ATLAS at different center of mass energies [10, 11]

### 2.2.8 DETECTOR PERFORMANCE

Table 2.2 summarizes the design requirements for each of the different sub-detectors. This table shows the energy and momentum resolution of each tracking, calorimetry, and muon measurements.

### 2.3 THE ATLAS MUON NEW SMALL WHEEL UPGRADE

As the LHC continues operation, it is scheduled to be upgraded in several phases to allow it to reach higher instantaneous luminosities and thus collect larger datasets. These conditions will open new doors

	Required resolution
Tracking	$\sigma_{p_T}/p_T = 0.05\% p_T \oplus 1\%$
EM calorimetry	$\sigma_E/E = 10\%/\sqrt{E} \oplus 0.7\%$
Hadronic calorimetry	
Barrel and end-cap	$\sigma_E/E = 50\%/\sqrt{E} \oplus 3\%$
Forward	$\sigma_E/E = 100\%/\sqrt{E} \oplus 10\%$
Muon spectrometer	$\sigma_{p_T}/p_T$ at $p_T = 1$ TeV

Table 2.2: Performance requirements for the ATLAS detector [7].

for study of rare physics processes but will also present interesting challenges that must be faced. ATLAS will require new detector technologies to cope with the increased background rates in the cavern in these high luminosity conditions. One such upgrade, scheduled to be installed during Long Shutdown 2 (LS2) of the LHC in 2018, is the ATLAS Muon New Small Wheel (NSW) upgrade [12]. The NSW will replace the innermost end-cap wheel of the muon system with new technologies, as this is the part of the muon detector closest to the beam and thus suffers from the highest rates.

### 2.3.1 MOTIVATION

The motivation of the NSW is two-fold. First, the objective is to alleviate the decreased tracking efficiency that comes in a high rate environment. As figure 2.10, at the LHC design luminosity both the efficiency of recording hits and reconstructing track segments in the MDTs decreases at the LHC design luminosity.

Second, the NSW will work to alleviate the rate of fake triggers arising in the endcap. Figure 2.11 shows the extrapolated trigger rates as a function of the  $p_T$  threshold with and without the NSW upgrade. As the figure shows, the NSW upgrade will reduce the trigger rate by an order of magnitude compared to the current endcap trigger system.

### 2.3.2 NSW DETECTOR TECHNOLOGIES

The NSW will use two new detector technologies - micromesh gaseous structure detectors (micromegas) and small-strip thin gap chambers (sTGCs) [12, 62]. Unlike the previous detectors, both of these detector technologies can be used for tracking or trigger. However, the micromegas is more suited to tracking

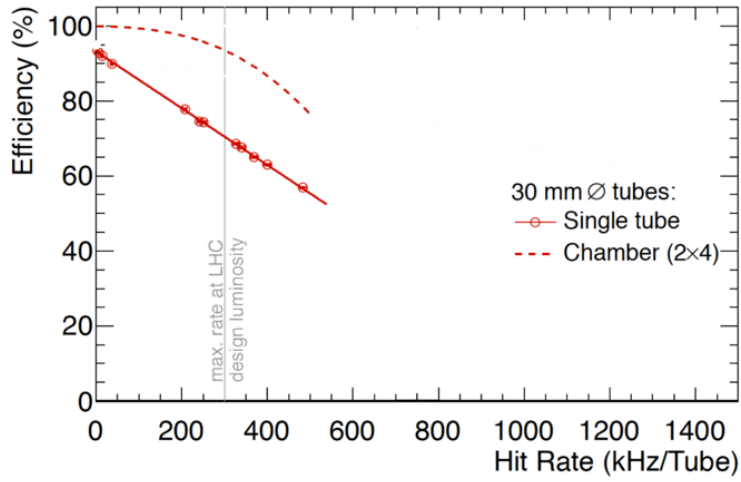


Figure 2.10: MDT tube hit (solid) and segment (dashed) efficiency as a function of hit rate per tube [12]

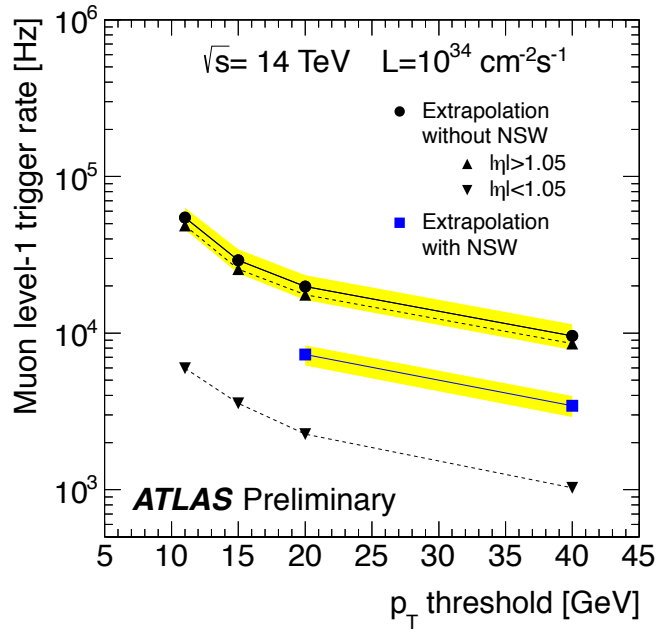


Figure 2.11: Trigger rate as a function of  $p_T$  threshold with and without the NSW upgrade [12]

<sup>998</sup> because of its good spatial resolution, while the sTGCs have better time resolution and are more suited  
<sup>999</sup> for the trigger. To maintain a fully redundant system, both technologies are used for both purposes.

1000 **MICROMEGAS**

1001 Micromegas detectors operate using a thin metallic mesh that sits approximately  $100 \mu\text{m}$  away from  
1002 the readout electrodes to create the amplification region. Above this mesh, there is a drift region on the  
1003 order of a few mm in length capped by a drift electrode. As a charged particle traverses the detector, it  
1004 ionizes gas and the electrons drift down towards readout strips. The timing of the drift can be used to  
1005 reconstruct the angle of traversal of the particle. This is illustrated in figure 2.12. The micromegas used in  
1006 ATLAS will be resistive micromegas, where the readout electrodes are topped with resistive strips [63].  
1007 This alleviates the risk of sparking in the large area detectors that ATLAS will use.

1008 In ATLAS, the micromegas drift gap will be 5 mm and the amplification gap will be  $128 \mu\text{m}$ . They  
1009 are filled with the same gas mixture as the MDTs. They will be stacked in an octuplet in an XXUV-  
1010 UVXX geometry, where X refers to straight strips and U and V refer to stero strips at an angle of  $\pm 1.5^\circ$ .  
1011 This arrangement allows for measurement of the azimuthal coordinate and gives a large lever arm be-  
1012 tween the straight strips for triggering purposes. Figure 2.12 shows the geometry of a single micromegas  
1013 detector as well as its operating principle [12].

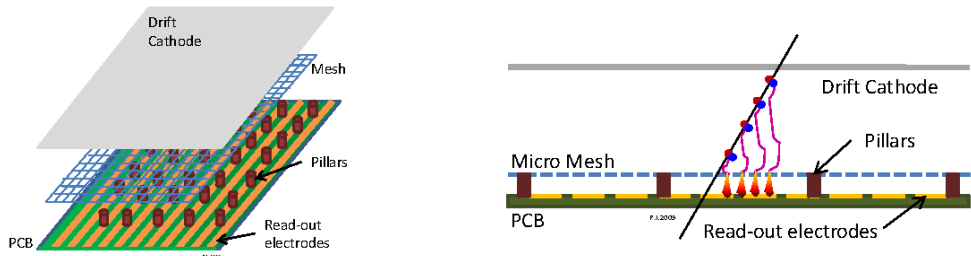
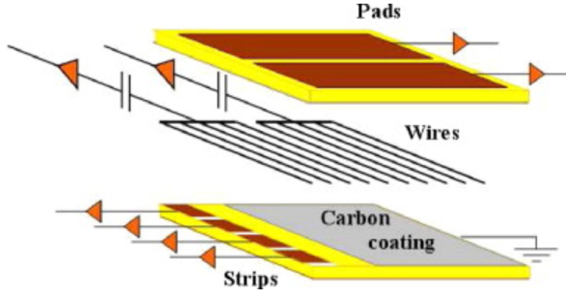


Figure 2.12: Illustrations of the geometry (left) and operating principle (right) of the micromegas detector [12]

1014 **sTGCs**

1015 The sTGCs are similar to the TGCs already described. They consist of gold-plated tungsten wires with  
1016 a 1.8 mm pitch between two cathode planes 1.4 mm away from the wire plane. One cathode plane  
1017 consists of strips with a 3.2 mm pitch (much smaller pitch than the TGCs), while the other consists  
1018 of coarser pads that are used for defining regions of interest in the sTGC trigger algorithm. Figure 2.13  
1019 shows the basic detector geometry.



**Figure 2.13:** Geometry of the sTGC detector [12]

1020 2.3.3 PHYSICS IMPACT

1021 Maintaining low  $p_T$  thresholds for muons while still staying within the trigger rate budget at Level 1  
 1022 (20 kHz) for the muon system is crucial for physics analyses to be successful in high luminosity condi-  
 1023 tions. One realm where the lepton trigger threshold is especially important is in Higgs physics. In the  
 1024  $H \rightarrow WW^*$  analysis, one of the  $W$  bosons is off shell and tends to decay to soft leptons. In associated  
 1025 production of a Higgs with a  $W$ , the lepton is also important because the lepton provides the main han-  
 1026 dle which allows the event to be triggered. Table 2.3 shows the impact of increasing the trigger thresholds  
 1027 on these analyses. It shows that either raising the threshold or using only the barrel both have signifi-  
 1028 cant impacts on the signal efficiency. With the NSW, the signal efficiency is largely maintained and the  
 1029 triggers can be unprescaled.

Threshold	$H \rightarrow b\bar{b}$ (%)	$H \rightarrow WW^*$ (%)
$p_T > 20$ GeV	93	94
$p_T > 40$ GeV	61	75
$p_T > 20$ GeV (barrel only)	43	72
$p_T > 20$ GeV (with NSW)	90	92

**Table 2.3:** Signal efficiencies for  $WH$  production with  $H \rightarrow b\bar{b}$  and  $H \rightarrow WW^* \rightarrow \mu\nu qq$  under different trigger configurations [12].

1030 2.4 OBJECT RECONSTRUCTION IN ATLAS

1031 ATLAS analyses first start by requiring the presence of certain reconstructed physics objects in the event.  
 1032 This section will present a brief overview of the algorithms used to reconstruct electrons, muons, jets

1033 (including  $b$ -jets), and missing energy<sup>\*</sup>. The performance of object reconstruction and measurement will  
1034 also be discussed as these are relevant to the analyses presented later. Figure 2.14 gives an overview of the  
1035 different sub-detectors that each type of particle will interact with in ATLAS.

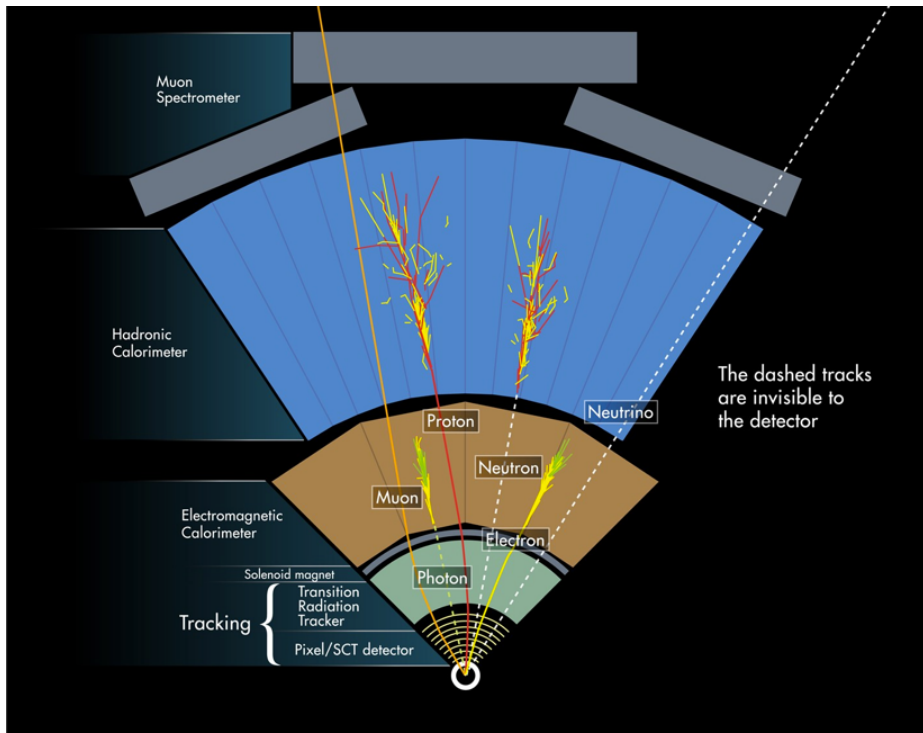


Figure 2.14: Illustration of particle interactions in ATLAS [13]

#### 1036 2.4.I ELECTRONS

1037 Electrons in ATLAS will leave tracks in the inner detector and energy deposits in the electromagnetic  
1038 calorimeter. The algorithm for recognizing the signature of electrons proceeds in two steps: reconstruc-  
1039 tion and identification.

1040 In reconstruction, an electron candidate is formed by matching EM calorimeter deposits with ID  
1041 tracks. The algorithm first chooses seed clusters in the EM calorimeter by using a sliding window algo-  
1042 rithm that searches for towers with transverse energy larger than 2.5 GeV. In addition to seed clusters,  
1043 track candidates must be identified in the ID. The algorithm selects seed tracks with  $p_T > 1$  GeV that

---

\*Reconstruction algorithms for other objects, such as photons and  $\tau$  leptons, are not detailed here as these objects are not used in the presented studies.

1044 do not fit well with a pion hypothesis. Once candidate tracks are selected, they are re-fit with a Gaussian Sum Filter (GSF) algorithm to estimate electron parameters [64]. Finally, an electron candidate is  
 1045 formed if at least one track matches to a seed cluster in the calorimeter. The full details of the reconstruction  
 1046 algorithm can be found in reference [14].  
 1047

1048 Once an electron candidate is present, identification criteria must be applied in order to reject fake  
 1049 electrons from background. Many different variables are used for this identification, most of them re-  
 1050 lated to the shower shape in the EM calorimeter and the amount of leakage into the hadronic calorime-  
 1051 ter, as well as information from the ID and in particular the TRT. There are both cut-based and likelihood-  
 1052 based criteria that range from “loose” to “very tight”. For details, see reference [14].

1053 Figure 2.15 shows the algorithm’s reconstruction efficiency of true electrons for different identification  
 1054 criteria as well as the electron energy resolution in simulation [14, 15]. The reconstruction efficiency is  
 1055 measured using both  $Z$  and  $J/\psi$  tag and probe techniques.

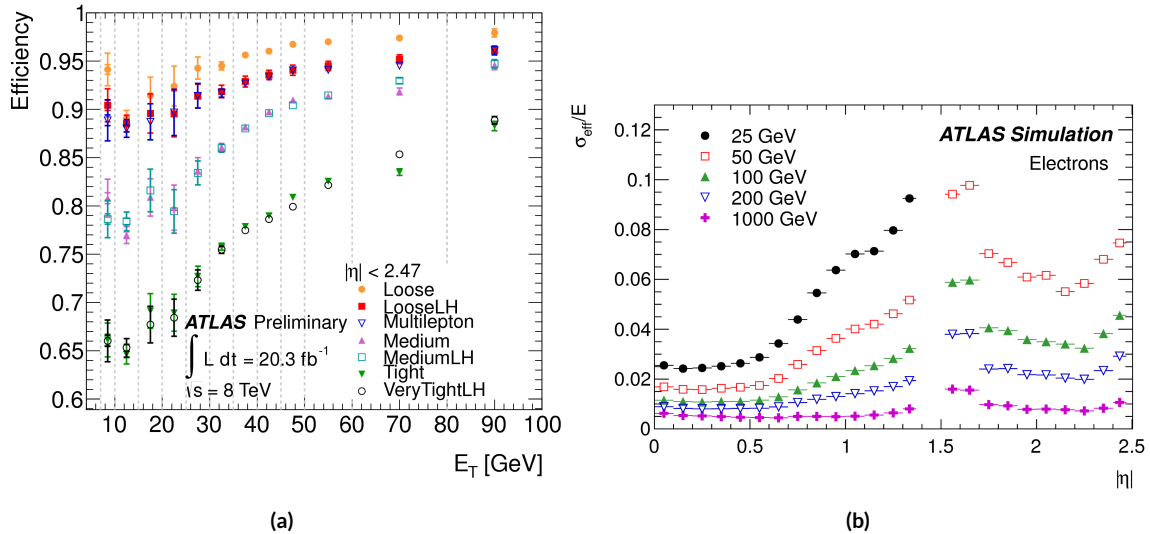


Figure 2.15: Electron performance: (a) reconstruction efficiency as a function of electron  $E_T$  [14] (b) energy resolution in simulation as a function of  $|\eta|$  for different energy electrons [15]

#### 1056 2.4.2 MUONS

1057 The ATLAS detector is designed to stop most particles before they reach the muon spectrometer. Muons,  
 1058 however, are minimum ionizing particles, meaning that they will not lose a significant amount of energy

1059 through interactions with the detector and will thus pass through. Therefore, the muon reconstruction  
1060 works to match tracks in the muon spectrometer with tracks in the inner detector.

1061 The first step of reconstruction is to reconstruct local straight line tracks, called segments, in each  
1062 muon chamber. Segments are then fit to larger tracks that traverse the entire muon spectrometer. Such  
1063 muon tracks are referred to as “standalone” tracks (SA) as they only use information from the muon  
1064 spectrometer. The standalone tracks are then matched to tracks in the inner detector to form “com-  
1065 bined” (CB) muons, where the combined ID and MS fit are used to determine the momentum and di-  
1066 rection of the muon. To improve acceptance, segment-tagged and calorimeter-tagged muons are also  
1067 reconstructed. In these cases, ID tracks are matched to segments in the MS and calorimeter deposits con-  
1068 sistent with a minimum ionizing particle, respectively. The details of the reconstruction can be found in  
1069 reference [16].

1070 As with electrons, once muon candidates are reconstructed they have identification criteria applied to  
1071 reduce background. These criteria include the  $\chi^2$  match between the ID and MS tracks, the number of  
1072 hits in the ID, overall ID and MS track fit quality, and additional variables [16]. The criteria range from  
1073 “loose” to “tight” as with electrons.

1074 Figure 2.16 shows the muon reconstruction efficiency (measured with  $Z$  and  $J/\psi$  tag and probe) and  
1075 invariant mass resolution [16].

#### 1076 2.4.3 JETS

1077 When a quark or gluon is produced in collisions, it is not measured directly in ATLAS. Rather, due to  
1078 QCD effects, it produces a collimated spray of hadrons in the direction of the original parton, which is  
1079 known as a jet. Jets are reconstructed in ATLAS using energy deposits in the hadronic calorimeter. The  
1080 first step is build “topological clusters” out of energy deposits in calorimeter cells [65, 66]. This is done  
1081 using strategy where seed cells are chosen by picking cells whose energy measurements are four times the  
1082 amount of noise expected for that cell. Adjacent cells with at least  $2\sigma$  energy measurements are added  
1083 to the cluster, then a final layer of clusters with energy above  $0\sigma$  are added. Once calorimeter clusters  
1084 are formed, they are clustered further into jet candidates using the anti- $k_T$  jet clustering algorithm [67].

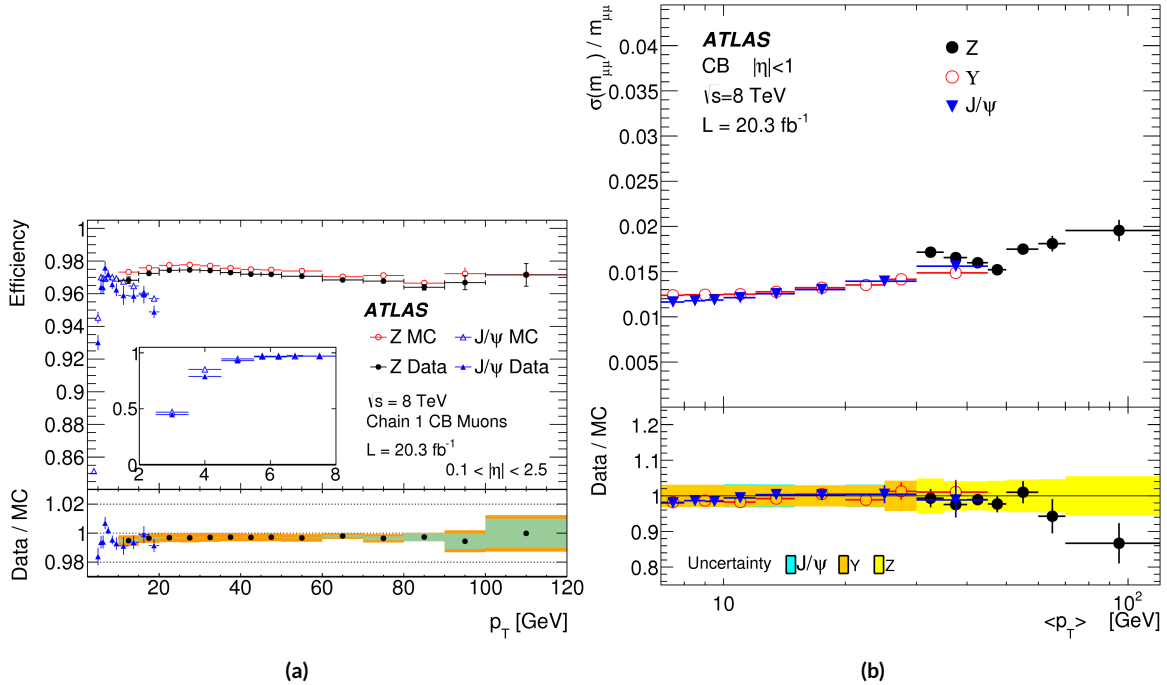


**Figure 2.16:** Muon performance: (a) reconstruction efficiency as a function of muon  $p_T$  (b) dimuon mass resolution as a function of average  $p_T$  [16]

This algorithm uses a parameter  $R$  that appears in the denominator of the clustering distance metric and defines the radial size of the jet in  $\eta$ - $\phi$  space.

The energy response of the calorimeter must be properly characterized in order to reconstruct jet energy. Calorimeter clusters can be calibrated either with the EM calibration, where each cluster is assumed to have come from the energy deposit of an electron or photon, or the LCW calibration, where local cluster weights are computed to allow for local calibration of clusters as hadronic or electromagnetic.

The details of the jet energy calibration are not detailed here and are discussed in reference [17].

Figure 2.17 shows the jet energy response after calibration in Monte Carlo as a function of the true  $p_T$  of the jet [17].

#### 2.4.4 $b$ -TAGGING

One important aspect of jet physics is the task of identifying the flavor of parton that produced the measured jet. While in general this is very difficult, jets from  $b$ -quarks offer an interesting case where such identification is possible.  $B$  mesons have a lifetime on the order of  $10^{-12}$  seconds, which makes a  $c\tau$

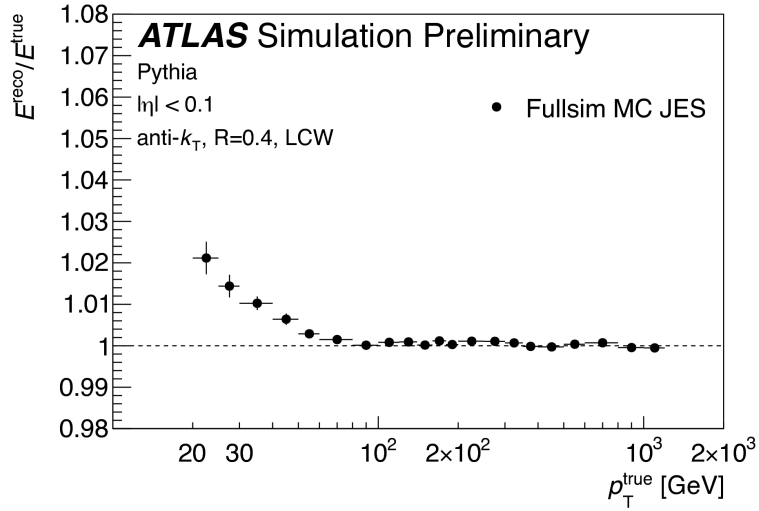


**Figure 2.17:** Jet energy response after calibration as a function of true  $p_T$  in simulation [17]

on the order of millimeters [1]. This type of displaced decay vertex can be identified in detectors like ATLAS and allows  $b$ -jets to be distinguished from other flavors of jets<sup>†</sup>.

ATLAS uses a multivariate machine learning algorithm to identify jets from  $b$ -quarks. The inputs to this algorithm are determined from lower level reconstruction algorithms. There are three distinct algorithms that reconstruct variables which are used as input to the multivariate technique.

The first family is referred to as IPxD (where the x can either be 2 or 3). These algorithms use the transverse and longitudinal impact parameters  $d_0$  and  $z_0$  of the tracks inside a jet to determine their consistency with the primary vertex. They two or three dimensional (hence the x) templates for light flavor, charm, and bottom jets and then evaluate the likelihood of the jet coming from each of these types. The likelihood ratios are used as inputs to the multivariate algorithm.

The next two algorithms used as input are referred to as the secondary vertex (SV) and JetFitter (JF) algorithms. The SV algorithm uses tracks inside the jet to fit for vertices that are displaced from the primary vertex. The JF algorithm attempts to reconstruct the full flight path of the  $b$  by looking for multiple displaced vertices along the same line (as  $B$  decays often result in subsequent  $c$  decays).

In Run 1, the multivariate  $b$ -tagging algorithm used a neural network and was referred to as MV1.

---

<sup>†</sup>Jets from charm quarks can also be detected in this way but they do not live quite as long so the displacement of the vertex is harder to distinguish

1113 The details of this algorithm and its inputs are given in reference [18]. In Run 2, the number of inputs  
 1114 was simplified and a boosted decision tree with 24 input variables was used, referred to as MV2. The  
 1115 details of this algorithm are in reference [19]. Figure 2.18 shows the performance of each of these algo-  
 1116 rithms.

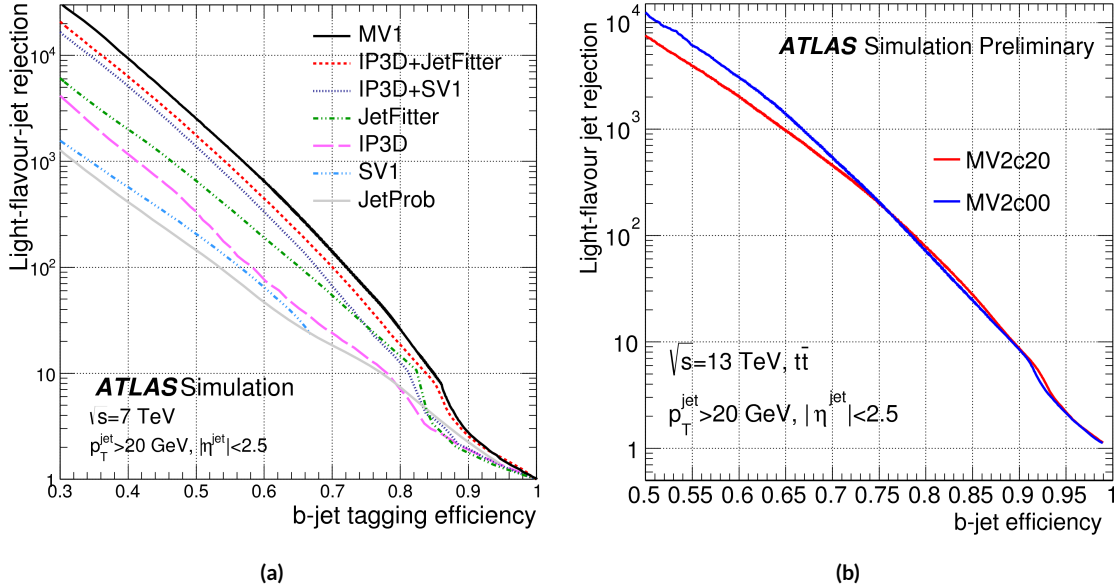


**Figure 2.18:** Light jet rejection ( $1/\text{efficiency}$ ) vs.  $b$ -jet efficiency for MV1 and its input algorithms (a) [18] and MV2 (b) [19] in simulated  $t\bar{t}$  events. The numbers in the algorithm names in (b) refer to the fraction of charm events used in the MV2 training.

#### 1117 2.4.5 MISSING TRANSVERSE ENERGY

1118 As noted in figure 2.14, neutrinos produced in ATLAS will pass through the detector without inter-  
 1119 acting. The only way of detecting the presence of particles like neutrinos (or BSM particles that are  
 1120 long-lived) is to use missing transverse momentum. The basic principle of missing transverse energy is  
 1121 to use the momentum balance of the incoming protons to infer the presence of missing particles. The  
 1122 net longitudinal momentum of the incoming partons that collide is not known (since each carries an un-  
 1123 known fraction of the proton's momentum). However, the protons (and thus incoming partons) have  
 1124 no net momentum in the plane transverse to the beam line (the  $x$ - $y$  plane). Therefore, if there are no  
 1125 un-measured particles in the final state, the transverse momenta of all of the final state particles should

balance. The magnitude of this imbalance is known as missing transverse momentum ( $E_T^{\text{miss}}$ ).

The basic calculation of missing transverse momentum from calorimeter cells is given in equation 2.4 [68].

$$\begin{aligned} E_x^{\text{miss}} &= -\sum_{i=1}^{N_{\text{cell}}} E_i \sin \theta_i \cos \phi_i \\ E_y^{\text{miss}} &= -\sum_{i=1}^{N_{\text{cell}}} E_i \sin \theta_i \sin \phi_i \end{aligned} \quad (2.4)$$

The  $E_T^{\text{miss}}$  calculation is separated into different terms based on the objects that the calorimeter clusters are associated with. This way, each cell's contribution is calibrated appropriately according to the object. This separation of terms is shown in equation 2.5 [68].

$$\begin{aligned} E_{x(y)}^{\text{miss,calo}} &= E_{x(y)}^{\text{miss},e} + E_{x(y)}^{\text{miss},\gamma} + E_{x(y)}^{\text{miss},\tau} + E_{x(y)}^{\text{miss,jets}} \\ &\quad + E_{x(y)}^{\text{miss,softjets}} + E_{x(y)}^{\text{miss},\mu} + E_{x(y)}^{\text{miss,CellOut}} \end{aligned} \quad (2.5)$$

The CellOut term of the above equation corresponds to calorimeter cells with energy deposits that are not associated with other objects. The soft jets term comes from cells associated to jets with  $p_T$  between 7 and 20 GeV, while the jets term comes from jets with  $p_T > 20$  GeV. Because muons do not deposit significant energy in the calorimeter, the muon momentum is used for the muon term [68]. The final  $E_T^{\text{miss}}$  is calculated using equation 2.6.

$$E_T^{\text{miss}} = \sqrt{(E_x^{\text{miss}})^2 + (E_y^{\text{miss}})^2} \quad (2.6)$$

Figure 2.19 shows the resolution of the components of the  $E_T^{\text{miss}}$  under different pileup suppression techniques [20].

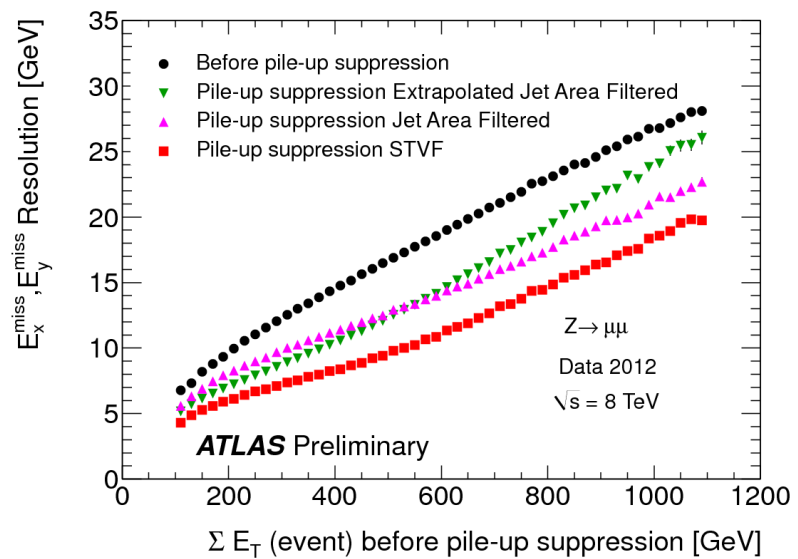


**Figure 2.19:** Resolution of  $E_T^{\text{miss}}$  components as a function of  $\sum E_T$  before pileup suppression with different pileup techniques [20]

1138

## Part II

1139

Observation and measurement of Higgs

1140

boson decays to  $WW^*$  in LHC Run I at

1141

$$\sqrt{s} = 7 \text{ and } 8 \text{ TeV}$$

*Basic research is what I am doing when I don't know  
what I am doing.*

Wernher von Braun

# 3

1142

1143

## $H \rightarrow WW^* \rightarrow \ell\nu\ell\nu$ Analysis Strategy

1144 3.1 INTRODUCTION

1145 This chapter presents an overview of the strategy for searching for a Higgs boson in the  $H \rightarrow WW^* \rightarrow$   
1146  $\ell\nu\ell\nu$  decay topology. Its purpose is to define in broad terms how the search and measurement are un-  
1147 dertaken, before going into details on the specific sub-categories within the larger analysis. First, the  
1148 properties of the Higgs signal are discussed and the associated backgrounds are presented. Next, the ob-  
1149 servables used to enhance the signal to background ratio are defined. Finally, the parameters of interest  
1150 in the search and measurement will be shown, along with a brief overview of the statistical treatment of  
1151 the final Higgs candidates.

1152 Following this chapter, the results of three different studies within the  $H \rightarrow WW^* \rightarrow \ell\nu\ell\nu$  channel  
1153 are shown. Chapter 4 presents a search for Higgs boson production in gluon fusion mode and the role  
1154 of the  $H \rightarrow WW^*$  channel in its discovery. Chapter 5 shows the search and first observation in ATLAS  
1155 of the Vector Boson Fusion (VBF) production mode of the Higgs in the  $H \rightarrow WW^*$  decay channel.

1156 Finally, chapter 6 shows the combined Run 1  $H \rightarrow WW^*$  results for the measurement of the Higgs  
1157 cross section and relative coupling strengths to other SM particles.

1158 3.2 THE  $H \rightarrow WW^* \rightarrow \ell\nu\ell\nu$  SIGNAL IN ATLAS

1159 The signal studied in this and subsequent chapters is the Higgs boson in the  $WW^*$  final state, where  
1160 each  $W$  boson subsequently decays into a charged lepton and a neutrino. In its simplest decay path, the  
1161 final state consists of two neutrinos and two charged leptons, each of which can be either an electron or  
1162 a muon. If one or both of the  $W$ s decay to  $\tau$  leptons, only leptonic decays of the  $\tau$  are considered. This  
1163 decay path produces additional neutrinos in the final state but still gives two charged leptons as before.  
1164 Neutrinos are not detected in ATLAS, so the final state ultimately consists of two reconstructed leptons  
1165 and missing transverse momentum (denoted as  $E_T^{\text{miss}}$ ). Final states where both of the charged leptons  
1166 are electrons or muons are referred to as the “same flavor” ( $ee/\mu\mu$ ) final states, while those with one  
1167 electron and one muon are referred to as “different flavor” ( $e\mu$  or  $\mu e$ ).

1168 While the basic final state consists of two leptons and  $E_T^{\text{miss}}$ , there can be additional objects depend-  
1169 ing on the production mode of the Higgs. As described in detail in Chapter 1, if the Higgs is produced  
1170 via vector boson fusion production, there will be two additional forward jets in the event. Even in gluon  
1171 fusion, one or more jets can be produced through initial state radiation from the incoming gluons. Be-  
1172 cause of the varying background composition as a function of jet multiplicity, each bin in this variable  
1173 has its own dedicated requirements applied in the search and measurement. The  $n_j = 0$  and  $n_j = 1$   
1174 bins are dedicated to gluon fusion production, while the  $n_j \geq 2$  bin has separate dedicated searches for  
1175 ggF and VBF production.

1176 Figure 3.1 shows the relative branching fractions for the  $H \rightarrow WW^*$  process, calculated from the  
1177 Particle Data Group values for the  $W$  and  $\tau$  branching ratios[?]. The largest branching ratio is both  
1178  $W$  bosons decaying to quark pairs at 45.44%. The next largest is one  $W$  decaying leptonically and the  
1179 other decaying to quarks, a branching ratio of 34.18%. In all cases,  $\ell$  denotes either an electron or muon,  
1180 and the leptonic branching ratios of the  $\tau$  are included. For example, the  $\ell\nu qq$  final state includes one  $W$   
1181 decaying to  $e\nu$ ,  $\mu\nu$ , or  $\tau\nu$ . In the case of the  $W \rightarrow \tau\nu$  decay, the  $\tau$  lepton then decays to an electron or

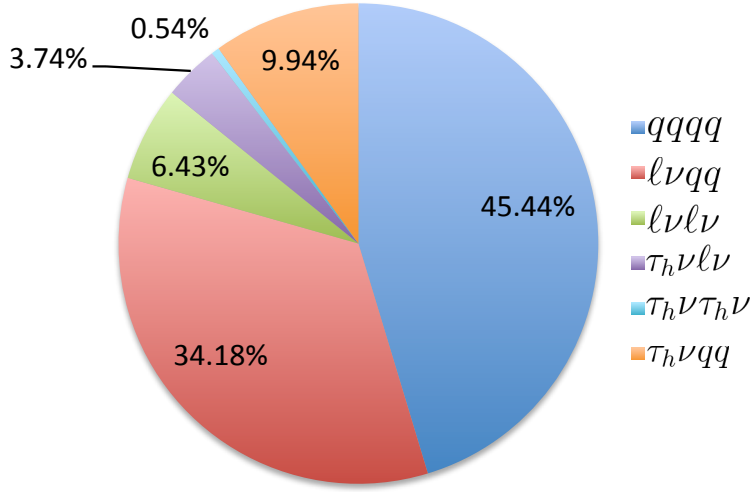


**Figure 3.1:** Branching ratios for a  $WW$  system.  $q$  refers to quarks.  $\ell$  can be either an electron or muon, and the leptonic branching ratios of the  $\tau$  are included. For example, the  $\ell\nu qq$  final state includes one  $W$  decaying to  $e\nu$ ,  $\mu\nu$ , or  $\tau\nu$ .  $\tau_h$  refer to hadronic decays of the  $\tau$ .

1182 muon via  $\tau \rightarrow \nu_\tau \ell \nu_\ell$ . Final states with a  $\tau_h$  refer to hadronic decays of the  $\tau$ . The branching ratio to the  
 1183  $\ell\nu\ell\nu$  final state is 6.43%.

1184 While the  $\ell\nu\ell\nu$  final state is not a large fraction of the branching ratio, there are significant advantages  
 1185 in this channel. First, both the  $qqqq$  and  $\ell\nu qq$  channels suffer from a large QCD multijet background,  
 1186 which is often difficult to model. Second, events in the the  $\ell\nu\ell\nu$  channel in data can be triggered more  
 1187 efficiently due to the presence of two leptons.

### 1188 3.3 BACKGROUND PROCESSES

1189 Many processes from the Standard Model can also produce a final state with two leptons and missing  
 1190 transverse momentum . This section lists the dominant backgrounds to Higgs production. It gives gen-  
 1191 eral descriptions of how the backgrounds mimic Higgs production and how they can be reduced. Ta-  
 1192 ble3.1 summarizes the different processes.

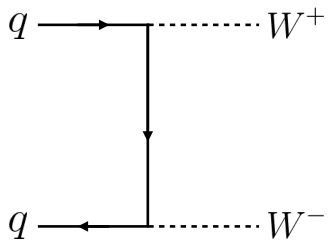


**Figure 3.2:** Feynman diagram for Standard Model WW production

### 1193 3.3.1 STANDARD MODEL WW PRODUCTION

1194 Non-resonant Standard Model diboson production, as shown in figure 3.2, is an irreducible background  
 1195 to Higgs boson production in the WW final state. It produces the same exact final state objects, namely  
 1196 leptonically decaying W bosons. There are no additional objects in the final state that allow for back-  
 1197 ground reduction. Therefore the analysis solely relies on the correlations between the leptons to reduce  
 1198 this background.

### 1199 3.3.2 TOP QUARK PRODUCTION

1200 Production of top quarks, either in pairs ( $t\bar{t}$  production) or singly (e.g.  $Wt$  production), can also mimic  
 1201 Higgs production. Because top quarks decay via  $t \rightarrow Wb$ , top pair production can produce a final state  
 1202 with two W bosons that then decay leptonically. In this case, however, there are two additional jets from  
 1203 the bottom quarks in the final state. This allows the analysis to veto on the presence of jets identified as  
 1204 originating from a  $b$  in order to reduce the size of the background.

1205 Single top production can occur via  $s$ -channel,  $t$ -channel, or associated production ( $Wt$ ). The mode  
 1206 which most closely resembles the Higgs final state is  $Wt$ . In this case, there are two real W bosons pro-  
 1207 duced, as with  $t\bar{t}$ . However, the decay of the single top quark will still also produce one  $b$ -jet, meaning a  
 1208  $b$  veto will reduce this background as well.

1209 Figure 3.3 shows the Feynman diagrams for  $t\bar{t}$  and  $Wt$  production.

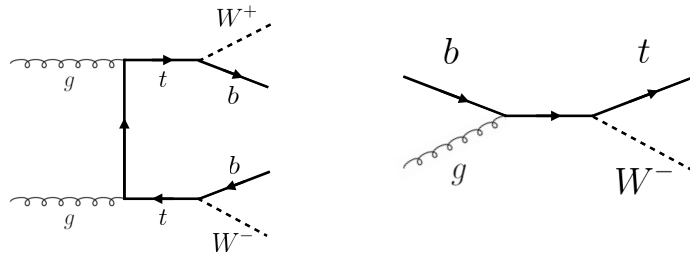


**Figure 3.3:** Feynman diagrams for top pair production (left) and  $Wt$  production (right)

### 1210 3.3.3 $W$ +JETS BACKGROUND

1211 Single  $W$  boson production, in association with jets, is a unique background. The other background  
 1212 considered so far have all included real leptons in the final state. In this case, however, only one real lep-  
 1213 ton from the decay of a  $W$  exists in the final state. The second reconstructed lepton can arise from two  
 1214 different cases. First, the lepton may truly be an algorithm “fake”, or a jet misidentified as a lepton by  
 1215 either the electron or muon reconstruction algorithms. Second, the lepton may be a real lepton but  
 1216 coming from semi-leptonic decays of particles inside the shower of the jet. This background can be re-  
 1217 duced by requiring that the reconstructed lepton have little activity surrounding it in the calorimeter  
 1218 (also known as an “isolated” lepton). Figure 3.4 shows the Feynman diagram for  $W$ +jets production.

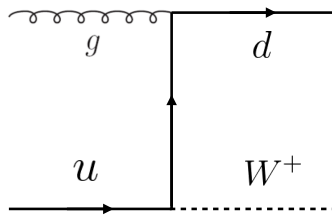


**Figure 3.4:** An example Feynman diagram of  $W$ +jets production

### 1219 3.3.4 $Z/\gamma^*$ +JETS BACKGROUND

1220 Production of a  $Z/\gamma^*$  in association with jets (also known as Drell-Yan) is also a background to Higgs  
 1221 production. In particular, the same flavor final states have a large  $Z$ +jets background, as the  $Z$  decays  
 1222 into two leptons of the same flavor. (This background also enters the different flavor final state through

1223 the leptonic decays of  $Z \rightarrow \tau\tau$ ). Figure 3.5 shows the production of a  $Z$  in association with one jet. Be-  
1224 cause there are no neutrinos in this final state, variables like  $E_T^{\text{miss}}$  can be used to reduce the background.

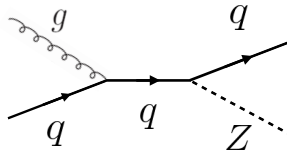


Figure 3.5: An example Feynman diagram of  $Z + \text{jets}$  production

### 1225 3.3.5 OTHER (SUBDOMINANT) BACKGROUNDS

1226 There are additional processes which contribute to the background composition but are not produced  
1227 as frequently as those listed already. The first of these are referred to as  $VV$  or “Other diboson” pro-  
1228 cesses and include multiple Standard Model diboson processes, including  $WZ$ ,  $ZZ$ ,  $W\gamma$ ,  $W\gamma^*$ , and  
1229  $Z\gamma$  production. Additionally, there is background from QCD multijet production, where two jets are  
1230 misidentified as leptons.

Category	Process	Description
SM $WW$	$WW \rightarrow \ell\nu\ell\nu$	Real leptons and neutrinos
Top quark production	$t\bar{t} \rightarrow WbWb \rightarrow \ell\nu b\ell\nu b$ $tW \rightarrow WbW \rightarrow \ell\nu\ell\nu b$ $t\bar{b}, t\bar{q}\bar{b}$	Real leptons, untagged $b$ s Real leptons, untagged $b$ Untagged $b$ , jet misidentified as lepton
Drell-Yan	$Z/\gamma^* \rightarrow ee, \mu\mu$ $Z/\gamma^* \rightarrow \tau\tau \rightarrow \ell\nu\ell\nu$	“Fake” $E_T^{\text{miss}}$ Real leptons and neutrinos
Other dibosons	$ZZ \rightarrow \ell\ell\nu\nu$ $W\gamma^*, WZ \rightarrow \ell\nu\ell\ell, ZZ \rightarrow \ell\ell\ell\ell$ $W\gamma, Z\gamma$	Real leptons and neutrinos Unreconstructed leptons $\gamma$ reconstructed as $e$ , unreconstructed lepton
$W + \text{jets}$	$Wj \rightarrow \ell\nu j$	Jet reconstructed as lepton
QCD multijet	$jj$	Jets reconstructed as leptons

Table 3.1: A summary of backgrounds to the  $H \rightarrow WW^* \rightarrow \ell\nu\ell\nu$  signal

1231 3.4 SHARED SIGNAL REGION SELECTION REQUIREMENTS

1232 As presented in section 3.2, there are many different combinations of objects that can define a  $H \rightarrow$   
 1233  $WW^* \rightarrow \ell\nu\ell\nu$  final state. The multiplicity of jets and the flavor combinations of the leptons both lead  
 1234 to many potential signal regions. Additionally, signal regions can be optimized separately to be sensi-  
 1235 tive to the distinct production modes of the Higgs. Gluon fusion, vector boson fusion, and associated  
 1236 production of a Higgs all lead to unique final state topologies. Figure 3.6 delineates the different signal  
 1237 regions used in the gluon fusion and vector boson fusion  $H \rightarrow WW^*$  analyses. While there are different  
 1238 optimizations possible in each signal region, there are also some commonly shared selections that will be  
 1239 described here.

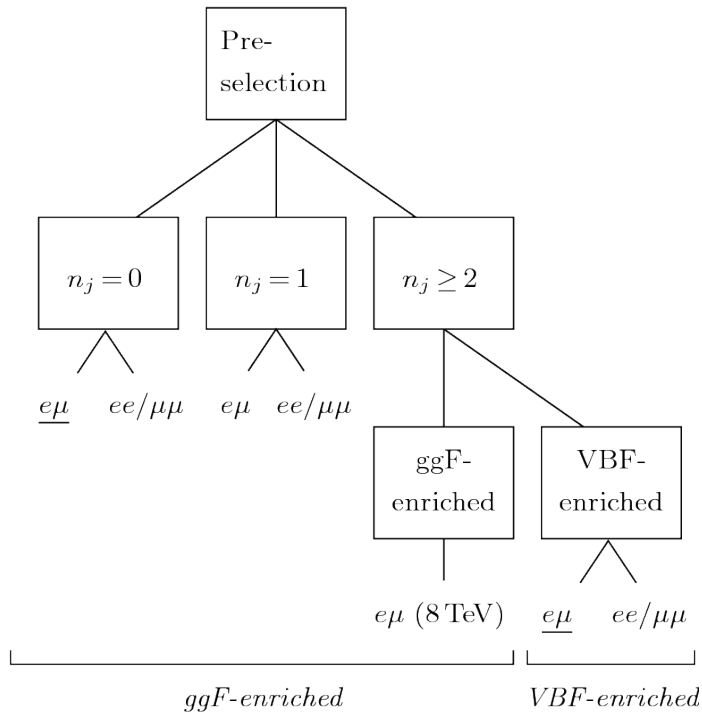


Figure 3.6: An illustration of the unique analysis signal regions[21]

1240 3.4.1 EVENT PRE-SELECTION

1241 Before being sorted into the distinct signal regions, basic requirements are applied on the reconstructed  
 1242 objects in the event to select Higgs-like event candidates. First, two oppositely charged leptons are re-

1243 quired.

1244 Once the leptons are selected, the last requirement for event pre-selection is the presence of neutrinos.  
1245 As neutrinos cannot be detected directly in ATLAS,  $E_T^{\text{miss}}$  can be used as a proxy for the combined neu-  
1246 trino momentum in the transverse plane. In general, it is expected that the signal should have a harder  
1247  $E_T^{\text{miss}}$  spectrum than backgrounds, especially if those backgrounds did not contain neutrinos. One ad-  
1248 ditional consideration when using  $E_T^{\text{miss}}$  is the fact that mis-measurements of objects in the detector  
1249 can lead to imbalances in the transverse plane that are not due to real particles escaping the detector.  
1250 One indicator that this is the case is that the  $E_T^{\text{miss}}$  vector in the transverse plane will be pointing in the  
1251 same direction as the mis-measured object. Therefore, a new variable,  $E_{T,\text{rel}}^{\text{miss}}$ , is used in the pre-selection.  
1252  $E_{T,\text{rel}}^{\text{miss}}$  is defined in equation 3.1.

$$E_{T,\text{rel}}^{\text{miss}} = \begin{cases} E_T^{\text{miss}} \sin \Delta\phi_{\text{near}} & \text{if } \Delta\phi_{\text{near}} < \pi/2 \\ E_T^{\text{miss}} & \text{otherwise,} \end{cases} \quad (3.1)$$

1253 If the closest object to the  $E_T^{\text{miss}}$  vector is within  $\pi/2$  radians in the transverse plane, the  $E_T^{\text{miss}}$  is pro-  
1254 jected away from this object. Otherwise, the normal  $E_T^{\text{miss}}$  vector is used. Figure 3.7 shows a graphical  
1255 illustration of this concept.

1256 Once both the lepton and  $E_T^{\text{miss}}$  pre-selections are made, the analysis can be divided into different  
1257 regions according to jet multiplicity.

### 1258 3.4.2 JET MULTIPLICITY

1259 Jet multiplicity, denoted as  $n_j$ , is used to sub-divide the analysis into its distinct signal regions. The rea-  
1260 son for this is twofold. First, different jet multiplicity bins will be more or less sensitive to different Higgs  
1261 production modes. For example, the  $n_j \geq 2$  region is more sensitive to VBF production because of  
1262 the two high momentum jets produced at matrix element level. For gluon fusion production to enter  
1263 this bin, two initial state radiation jets must be emitted. Second, background composition varies greatly  
1264 in different bins of  $n_j$ . Figure 3.8 shows the jet multiplicity in both the different flavor and same flavor  
1265 regions. It also shows the background composition in the bins of  $n_b$ . There are a few clear trends from

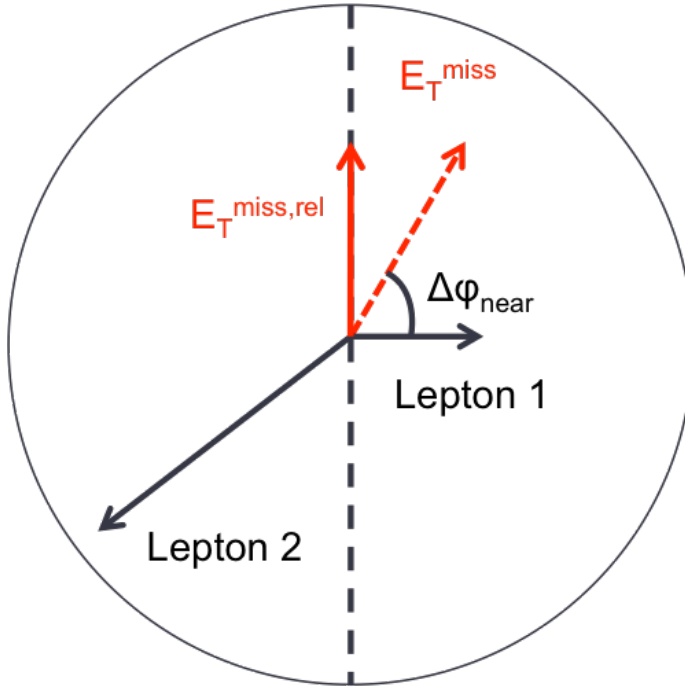


Figure 3.7: A graphical illustration of the  $E_{T,\text{rel}}^{\text{miss}}$  calculation

1266 this distribution. The first is that the Drell-Yan background dominates in the same flavor channels for  
 1267  $n_j \leq 1$ . Second, the top background becomes a clear contributor to the total background for  $n_j \geq 1$ .  
 1268 Lastly, the SM WW production dominates in the  $n_j = 0$  bin, as it is an irreducible background to  
 1269  $H \rightarrow WW^*$  production. Because of these distinct features, each jet multiplicity bin is treated separately.

### 1270 3.5 BACKGROUND REDUCTION IN SAME-FLAVOR FINAL STATES

1271 As described in section 3.4.2, the background composition of the same flavor final states is unique to that  
 1272 of the different flavor states. In particular, Drell Yan processes play a much larger role because the  $Z/\gamma^*$   
 1273 decays to same flavor leptons. Because real neutrinos are absent in the  $Z/\gamma^*$  decays to  $ee$  and  $\mu\mu$ , a re-  
 1274 quirement on  $E_T^{\text{miss}}$  should largely reduce the background. However, as this section will demonstrate,  
 1275 with increasing pileup conditions the resolution of the calorimeter-based  $E_T^{\text{miss}}$  degrades greatly. There-  
 1276 fore, two new variables for  $Z/\gamma^*$  background reduction are constructed and described in this section.

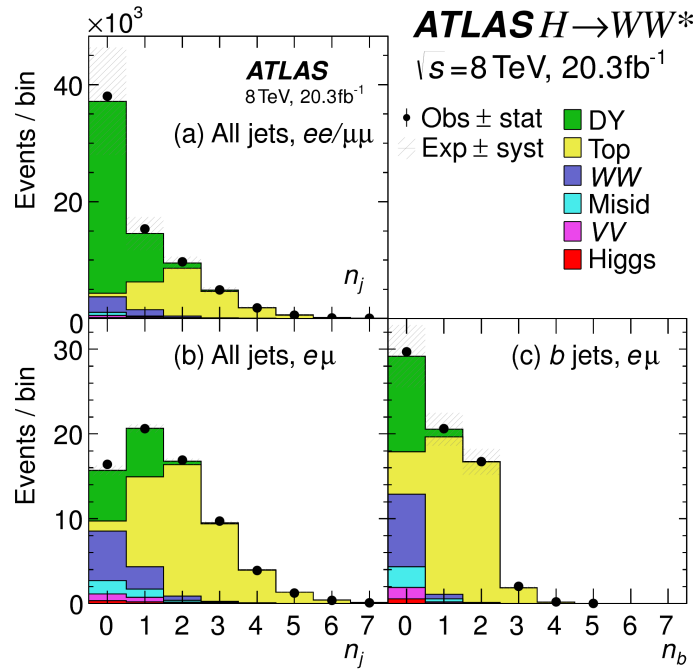


Figure 3.8: Predicted backgrounds (compared with data) as a function of  $n_j$  (a and b) and  $n_b$  (c)

### 1277 3.5.1 PILEUP AND $E_T^{\text{miss}}$ RESOLUTION

1278 Secondary interactions of protons in the colliding bunches of the LHC (known as pileup interactions,  
 1279 described in detail in Chapter 2) deposit energy into the ATLAS calorimeter on top of the energy that  
 1280 comes from the hard scatter process that is being searched for or analyzed. The calculation of  $E_T^{\text{miss}}$  is  
 1281 fundamentally Poissonian, as summing up all of the energy deposits in individual calorimeter cells or  
 1282 clusters is similar to a counting experiment. Thus, the energy resolution scales as  $\sqrt{E}$ , just as the error on  
 1283 a mean of  $N$  in a Poisson distribution is  $\sqrt{N}$ . As more energy is deposited in the calorimeter, the  $E_T^{\text{miss}}$   
 1284 resolution degrades, meaning that the  $E_T^{\text{miss}}$  resolution is particularly sensitive to LHC instantaneous  
 1285 luminosity conditions.

1286 Figure 3.9 shows an event display of a  $Z/\gamma^* + \text{jets}$  event candidate with the twenty-five reconstructed  
 1287 primary vertices. This display illustrates that while the interaction of interest only has tracks coming  
 1288 from the hardest primary vertex, all of the secondary interactions will deposit energy in the calorimeter as  
 1289 well.

1290 Figure 3.10 shows the RMS of the  $E_T^{\text{miss}}$  distribution in  $Z \rightarrow \mu\mu$  events (where there are no real neu-

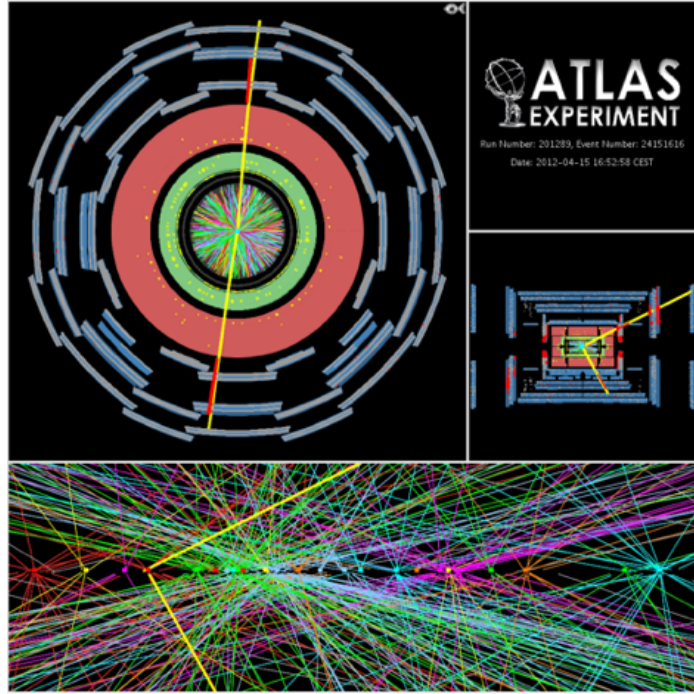


**Figure 3.9:** An event display of a  $Z/\gamma^*$  + jets event illustrating the effect of pileup interactions

trinos) as a function of the number of the average number of interactions. Under 2011 LHC conditions, this RMS was approximately 9 GeV, while under 2012 running conditions the resolution worsened to 12 GeV. This worsening dilutes the  $E_T^{\text{miss}}$  variable's ability to reduce the  $Z/\gamma^*$  background.

### 3.5.2 TRACK-BASED DEFINITIONS OF MISSING TRANSVERSE MOMENTUM

Because the increasing number of secondary proton-proton interactions degrades calorimeter-based  $E_T^{\text{miss}}$  resolution, a new variable using only contributions from the primary interaction vertex is necessary to further reduce the  $Z/\gamma^*$  background. While it is not possible to associate calorimeter energy deposits with a particular vertex, individual charged particle tracks in the Inner Detector are associated to unique vertices. Thus, two track-based definitions of missing transverse momentum , using only tracks coming from the primary vertex in the event, are used in the analysis. The simplest variable,  $p_T^{\text{miss}(\text{trk})}$ , is the vectorial sum of the  $p_T$  of all of the tracks from the primary vertex and the selected leptons (excluding the tracks associated with the selected leptons to avoid double counting). This is defined in equa-

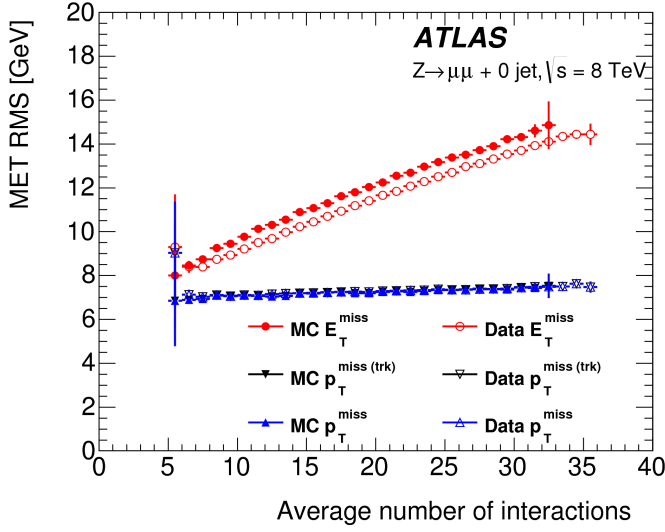


**Figure 3.10:** The RMS of different missing transverse momentum definitions as a function of the average number of interactions per bunch crossing

1303     tion 3.2.

$$p_T^{\text{miss}(\text{trk})} = - \left( \sum_{\text{selected leptons}} p_T + \sum_{\text{other tracks}} p_T \right), \quad (3.2)$$

1304     In events with hard jets, a better resolution on the missing transverse momentum is obtained by in-  
 1305     cluding the calorimeter based measurement of the hard jets rather than the track based measurements.  
 1306     Thus, another variable,  $p_T^{\text{miss}}$ , is defined, using the nominal measurements of  $p_T$  for the selected leptons  
 1307     and jets and using tracks rather than calorimeter clusters for the soft component of the missing transverse  
 1308     momentum . This is defined in equation 3.3.

$$p_T^{\text{miss}} = - \left( \sum_{\text{selected leptons}} p_T + \sum_{\text{selected jets}} p_T + \sum_{\text{other tracks}} p_T \right), \quad (3.3)$$

1309     Figure 3.10 illustrates that these two new variables accomplish their intended purpose. The resolution  
 1310     as a function of mean number of interactions for both  $p_T^{\text{miss}(\text{trk})}$  and  $p_T^{\text{miss}}$  is much flatter compared to  
 1311     the dependence for  $E_T^{\text{miss}}$ .

1312     Figure 3.11a shows the difference between the true and reconstructed values of missing transverse mo-

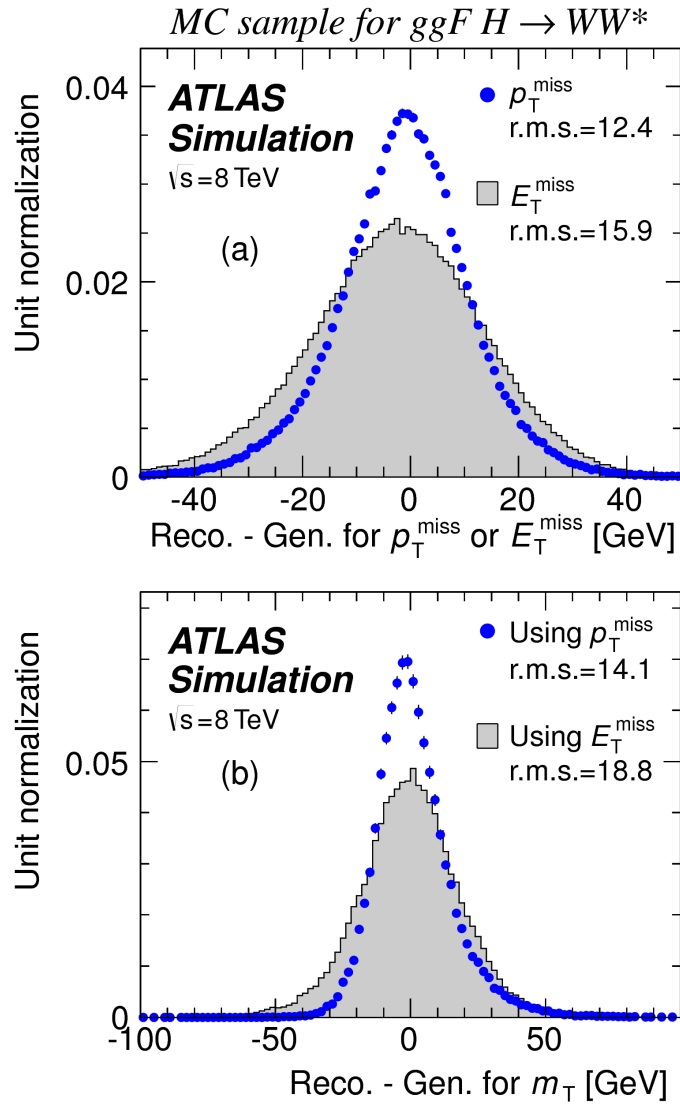


**Figure 3.11:** The difference between the true and reconstructed values of the missing transverse momentum (a) and  $m_T$  (b) in a gluon fusion signal sample

<sup>1313</sup> momentum using both the track-based  $p_T^{\text{miss}}$  and calorimeter based  $E_T^{\text{miss}}$ . The RMS of the distribution

<sup>1314</sup> improves by 3.5 GeV when using  $p_T^{\text{miss}}$ .

### <sup>1315</sup> 3.5.3 DISTINGUISHING $Z/\gamma^*$ +JETS AND $H \rightarrow WW^*$ TOPOLOGIES

<sup>1316</sup> The track-based definitions of missing transverse momentum were constructed to mitigate degrading

<sup>1317</sup> performance as a function of pileup. However, an additional variable can be constructed to exploit kine-

matic and topological differences between the  $Z/\gamma^*$  background and  $H \rightarrow WW^*$  signal. Because there  
 1318 are no real neutrinos in the final state (in the case of  $Z/\gamma^* \rightarrow ee, \mu\mu$  decays), the dilepton system of a  
 1319  $Z/\gamma^*$  will be balanced with the jets produced in the hard scatter. A new variable,  $f_{\text{recoil}}$ , is constructed  
 1320 to estimate the balance between the dilepton system and the jets in the quadrant opposite the dilepton  
 1321 vector in the transverse plane. It is defined in equation 3.4. The numerator of  $f_{\text{recoil}}$  is the magnitude of  
 1322 the vectorial sum of the  $p_T$  of jets in the quadrant opposite the dilepton system, weighted by each jet's Jet  
 1323 Vertex Fraction (JVF, described in chapter 2). The denominator is the magnitude of the dilepton  $p_T$ .  
 1324

$$f_{\text{recoil}} = \left| \sum_{\text{jets } j \text{ in } \wedge} \text{JVF}_j \cdot \mathbf{p}_T^j \right| / p_T^{\ell\ell}. \quad (3.4)$$

1325 Figure 3.12 shows a shape comparison of the distribution of  $f_{\text{recoil}}$  in a simulated  $Z/\gamma^* + \text{jets}$  sample,  
 1326 a  $H \rightarrow WW^*$  signal sample, and other backgrounds that contain real neutrinos. The  $Z/\gamma^* + \text{jets}$  events  
 1327 tend to be more balanced between the dilepton system and recoiling jets, while the processes containing  
 1328 real neutrinos are less balanced in the transverse plane. Thus, a requirement on  $f_{\text{recoil}}$  will also reduce  
 1329 the  $Z/\gamma^* + \text{jets}$  background while maintaining a good signal efficiency.

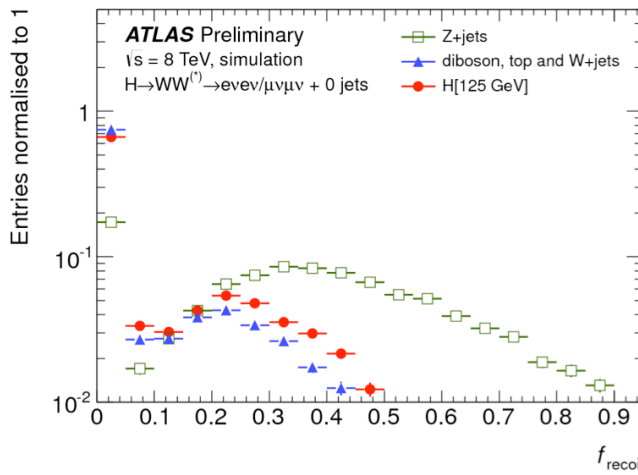


**Figure 3.12:** Comparison of  $f_{\text{recoil}}$  distributions for  $Z/\gamma^* + \text{jets}$ ,  $H \rightarrow WW^*$ , and other backgrounds with real neutrinos.

1330    3.5.4    OPTIMIZING BACKGROUND REDUCTION SELECTION REQUIREMENTS

1331    The requirements on  $p_T^{\text{miss(trk)}}$  and  $f_{\text{recoil}}$  used to reduce the Z+jets background must be optimized  
 1332    to maximize their efficacy. Figure 3.13 shows an early attempt to optimize the combination of the two  
 1333    requirements in the gluon fusion zero jet bin. Each bin shows the expected signal significance if the  
 1334     $p_{T,\text{rel}}^{\text{miss(trk)}}$  is required to be greater than the left edge of the bin and the  $f_{\text{recoil}}$  is required to be less than  
 1335    the top edge of the bin. The figure shows that the best signal significance comes from requiring low val-  
 1336    ues of  $f_{\text{recoil}} (< 0.05)$  and  $p_{T,\text{rel}}^{\text{miss(trk)}}$  values greater than 45 GeV.

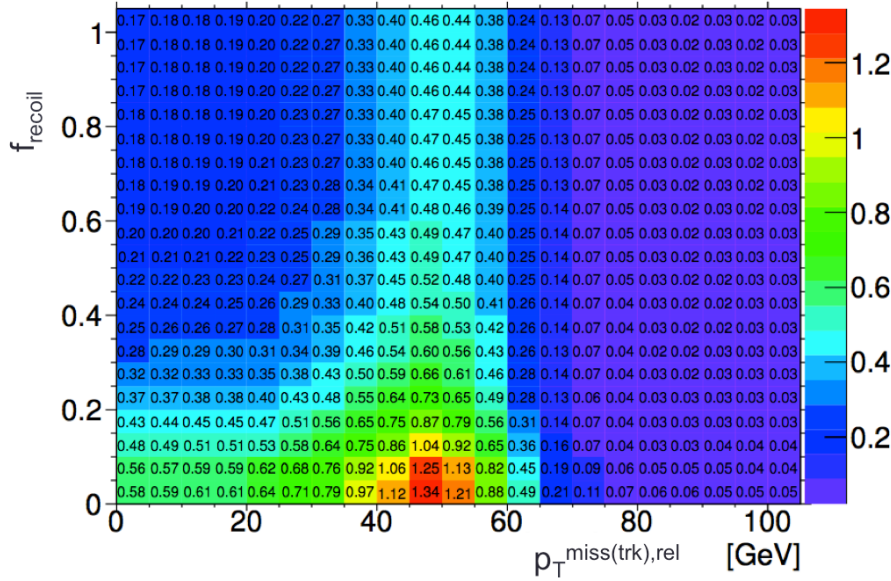


Figure 3.13: Signal significance as a function of required value for  $f_{\text{recoil}}$  and  $p_{T,\text{rel}}^{\text{miss(trk)}}$  in the ggF  $H \rightarrow WW^*$  with  $n_j = 0$

1337    3.6    PARAMETERS OF INTEREST AND STATISTICAL TREATMENT

1338    As with any search or measurement, there are particular parameters of the Higgs that the  $H \rightarrow WW^*$   
 1339    analysis is interested in measuring. In this case, the parameters of interest are the mass of the Higgs bo-  
 1340    son and its production cross section. Because the  $H \rightarrow WW^* \rightarrow \ell\nu\ell\nu$  process does not have a closed  
 1341    final state, it is not possible to measure the full invariant mass of the particle that may have produced  
 1342    the final state. However, a proxy for the invariant mass using transverse plane information can be de-

1343 fined. This is described in more detail in section 3.6.1. The second parameter of interest is the ratio of the  
1344 measured cross section to that expected from the Standard Model Higgs, which is denoted a  $\mu$ . This is  
1345 defined in equation 3.5.

$$\mu = \frac{\sigma}{\sigma_{\text{SM}}} \quad (3.5)$$

1346 All of the likelihoods used in the statistical analysis of the final signal region events are paramaterized  
1347 as a function of  $\mu$ .  $\mu$  is a natural variable for hypothesis testing, as  $\mu = 0$  corresponds to a background  
1348 only hypothesis and  $\mu = 1$  corresponds exactly to a Standard Model Higgs.

### 1349 3.6.1 TRANSVERSE MASS

1350 Because the longitudinal information about the neutrinos is not attainable, the  $H \rightarrow WW^* \rightarrow \ell\nu\ell\nu$   
1351 analysis uses a mass variable, the transverse mass, that exploits information in the transverse plane as a  
1352 proxy for the full invariant mass. The transverse mass is defined in equation 3.6.

$$m_T = \sqrt{(E_T^{\ell\ell} + p_T^{\text{miss}})^2 - |\mathbf{p}_T^{\ell\ell} + \mathbf{p}_T^{\text{miss}}|^2}, \quad (3.6)$$

1353 Here the  $E_T^{\ell\ell}$  and  $p_T^{\ell\ell}$  are the transverse energy and momentum of the dilepton system, while  $p_T^{\text{miss}}$  is  
1354 a proxy for the transverse momentum of the di-neutrino system. The track-based  $p_T^{\text{miss}}$  is used in the  $m_T$   
1355 rather than the calorimeter based  $E_T^{\text{miss}}$  because it has a better resolution on the true transverse mass.  
1356 Figure 3.11b shows the improvement in the RMS of the difference between the true and reconstructed  
1357 transverse mass in a ggF signal sample. The RMS improves by 4.7 GeV using  $p_T^{\text{miss}}$  in the  $m_T$  calcula-  
1358 tion.

1359    3.6.2 STATISTICAL TREATMENT<sup>\*</sup>

1360    LIKELIHOOD FUNCTION

1361    The statistical analysis of final event candidates is framed as a hypothesis test, where the null hypothe-  
1362    sis is background-only (no Standard Model Higgs). The first step in the analysis is to form a likelihood  
1363    function for the data. In its simplest form, this likelihood is the probability of observing the number  
1364    of events seen in the final signal region given knowledge of the signal strength. Because observation of  
1365    events is fundamentally a Poisson counting experiment, this simple likelihood can be expressed as a Pois-  
1366    son probability of observing  $N$  events given a total number of predicted signal and background events.  
1367    This basic likelihood is shown in equation 3.7.

$$\mathcal{L}(\mu) = P(N|\mu S + B) \quad (3.7)$$

1368    Here,  $P$  is the Poisson probability density function,  $N$  is the total number of observed events,  $\mu$  is  
1369    the signal strength,  $S$  is the predicted number of signal events, and  $B$  is the predicted number of back-  
1370    ground events.

1371    In particle physics, certain background estimates are commonly normalized in so-called “control” re-  
1372    gions and those predictions are scaled by the same normalization factor in the signal region. This leads  
1373    to a slightly more complicated likelihood, which is a function of both the signal strength and the back-  
1374    ground normalization. This is shown in equation 3.8.

$$\mathcal{L}(\mu, \theta) = P(N|\mu S + \theta B) P(N_{\text{CR}}|\theta B_{\text{CR}}) \quad (3.8)$$

1375    Here,  $\theta$  is a so-called “nuisance parameter”, a parameter that is not a primary parameter of interest but  
1376    still enters the likelihood. The second Poisson term adds an extra term to the likelihood, enforcing the  
1377    fact that the background normalization must be consistent with the number of observed events in data  
1378    in the control region,  $N_{\text{CR}}$ .

1379    So far, these two formulations of likelihoods have assumed a single signal region and do not take into

---

\*Many thanks to Aaron Armbruster, whose thesis[69] inspired parts of this section.

1380 account any shape information of potential discriminating variables. The  $H \rightarrow WW^*$  analysis is di-  
 1381 vided into many different categories, and we can perform the same counting experiment described above  
 1382 in each individual category. As mentioned in section 3.6.1, the transverse mass is used as the primary dis-  
 1383 criminating variable in many of the  $H \rightarrow WW^*$  sub-analyses, so additionally we can perform the same  
 1384 counting experiment in each bin of the  $m_T$  distribution to incorporate some shape information. Thus,  
 1385 the total likelihood becomes a product over signal regions and bins of the  $m_T$  distribution. Finally, there  
 1386 are usually many backgrounds that are normalized in control regions, so the new formulation of the like-  
 1387 lihood takes this into account as well by including a product over control regions in the second Poisson  
 1388 term. All of these modifications are shown in equation 3.9.

$$\mathcal{L}(\mu, \theta) = \prod_{\substack{\text{SRs } i \\ \text{bins } b}} P\left(N_{ib} \middle| \mu S_{ib} + \sum_{\text{bkg } k} \theta_k B_{kib}\right) \prod_{\text{CRs } l} P\left(N_l \middle| \sum_{\text{bkg } k} \theta_k B_{kl}\right) \quad (3.9)$$

1389 The final step to get the full likelihood used in the analysis is to add nuisance parameters for the sys-  
 1390 tematic uncertainties. In cases where the uncertainty does not affect the shape of  $m_T$  bin-by-bin, each  
 1391 systematic uncertainty  $\epsilon$  is allowed to affect the expected event yields through a linear response function  
 1392 of the nuisance parameter, namely  $\nu(\theta) = (1 + \epsilon)^\theta$ . If instead the uncertainty does affect the shape,  
 1393 the effect is instead parameterized by  $\nu_b(\theta) = 1 + \epsilon_b \theta$ . The value of the nuisance parameters for the  
 1394 systematic uncertainty are constrained with a Gaussian term that is added to the likelihood as well. This  
 1395 is of the form  $g(\delta|\theta) = e^{-(\delta-\theta)^2/2}/\sqrt{2\pi}$ , where  $\delta$  is the central value and  $\theta$  is a nuisance parameter.  
 1396 Finally, a last term is added to account for the statistical uncertainty in the Monte Carlo samples used,  
 1397 which adds an additional poisson term. The full likelihood used in the final statistical analysis is defined

<sup>1398</sup> in equation 3.10.

$$\begin{aligned} \mathcal{L}(\mu, \boldsymbol{\theta}) = & \prod_{\substack{\text{SRs i} \\ \text{bins b}}} P\left(N_{ib} \middle| \mu S_{ib} \cdot \prod_{\substack{\text{sig.} \\ r}} \nu_{br}(\theta_r) + \sum_{\text{bkg k}} \theta_k B_{kib} \cdot \prod_{\substack{\text{bkg.} \\ \text{syst.} \\ s}} \nu_{bs}(\theta_s)\right) \\ & \cdot \prod_{\text{CRs l}} P\left(N_l \middle| \sum_{\text{bkg k}} \theta_k B_{kl}\right) \\ & \cdot \prod_{\substack{\text{syst.} \\ t}} g(\delta_t | \theta_t) \cdot \prod_{\text{bkg k}} P(\xi_k | \zeta_k \theta_k) \end{aligned} \quad (3.10)$$

<sup>1399</sup> In the fourth term of the equation, quantifying uncertainty due to finite Monte Carlo sample size,  $\xi$   
<sup>1400</sup> represents the central value of the background prediction,  $\theta$  is the associated nuisance parameter,  $\zeta =$   
<sup>1401</sup>  $(B/\delta B)^2$ , where  $\delta B$  is the statistical uncertainty of  $B$ .

<sup>1402</sup> The best fit value of the signal strength  $\mu$  is determined by finding the values of  $\mu$  and  $\boldsymbol{\theta}$  that maxi-  
<sup>1403</sup> mize the likelihood, while setting  $\delta = 0$  and  $\xi = \zeta$ .

<sup>1404</sup> Once the likelihood is defined, a test statistic must be built for use in hypothesis testing.

#### <sup>1405</sup> TEST STATISTIC

<sup>1406</sup> To distinguish whether the data match a background only or background and signal hypothesis, a test  
<sup>1407</sup> statistic must be used. The  $H \rightarrow WW^*$  analysis used the profile likelihood technique[70]. The first step  
<sup>1408</sup> in formulating this test statistic is to define the profile likelihood ratio, shown in equation 3.11.

$$\lambda(\mu) = \frac{\mathcal{L}(\mu, \hat{\theta}_\mu)}{\mathcal{L}(\hat{\mu}, \hat{\theta})} \quad (3.11)$$

<sup>1409</sup> Here  $\hat{\theta}_\mu$  is the value of  $\theta$  that maximizes the likelihood for the choice of  $\mu$  being tested. Additionally,  
<sup>1410</sup>  $\hat{\theta}$  and  $\hat{\mu}$  represent the values of  $\theta$  and  $\mu$  that gives the overall maximum value of the likelihood.

<sup>1411</sup> Once this is defined, a test statistic  $q_\mu$  is constructed. This is shown in equation 3.12.

$$q_\mu = -2 \ln \lambda(\mu) \quad (3.12)$$

<sub>1412</sub> A higher value of  $q_\mu$  means that the data are more incompatible with the hypothesized value of  $\mu$ , and  
<sub>1413</sub>  $q_0$  then corresponds to the value of the test statistic for the background only hypothesis. A  $p_0$  value is  
<sub>1414</sub> then defined to quantify the compatibility between the data and the null hypothesis. The  $p_0$  value is the  
<sub>1415</sub> probability of obtaining a value of  $q_0$  larger than the observed value, and this is shown in equation 3.13.

$$p_0 = \int_{q_0^{\text{obs}}}^{\infty} f(q_\mu | \mu = 0) dq_\mu \quad (3.13)$$

<sub>1416</sub> Here  $f(q_\mu)$  is the probability distribution function of the test statistic. Finally, the  $p_0$  value can be  
<sub>1417</sub> converted into a signal significance, using the formula in equation 3.14, or the one-sided tail of the Gaussian distribution.

$$Z_0 = \sqrt{2} \operatorname{erf}^{-1}(1 - 2p_0) \quad (3.14)$$

<sub>1419</sub> The threshold for discovery used in particle physics is  $Z_0 \geq 5$ , more commonly known as a value of  
<sub>1420</sub>  $5\sigma$ .

*The real voyage of discovery consists not in seeking new landscapes, but in having new eyes.*

Marcel Proust

# 4

1421

1422

## The discovery of the Higgs boson and the 1423 role of the $H \rightarrow WW^* \rightarrow \ell\nu\ell\nu$ channel

1424 4.1 INTRODUCTION

1425 This chapter presents the results of the search for the Higgs boson in  $4.8 \text{ fb}^{-1}$  collected at  $\sqrt{s} = 7 \text{ TeV}$   
1426 and  $5.8 \text{ fb}^{-1}$  at  $\sqrt{s} = 8 \text{ TeV}$ . The results of three searches at  $\sqrt{s} = 8 \text{ TeV}$  in the  $H \rightarrow WW^* \rightarrow \ell\nu\ell\nu$   
1427,  $H \rightarrow \gamma\gamma$ , and  $H \rightarrow ZZ \rightarrow 4\ell$  channels are combined with results of searches at  $\sqrt{s} = 7 \text{ TeV}$   
1428 in the same search channels (as well as the  $H \rightarrow \tau\tau$  production and associated production searches for  
1429  $H \rightarrow b\bar{b}$ ). The results of this combination are a  $5.9\sigma$  detection of a new particle consistent with a Higgs  
1430 boson. Rather than going into detail for all of the different Higgs decay searches, this chapter will discuss  
1431 the three most sensitive channels and in particular focus on  $H \rightarrow WW^* \rightarrow \ell\nu\ell\nu$ . While the focus is  
1432 on  $WW^*$ , some of the  $ZZ^*$  and  $\gamma\gamma$  results are shown for completeness. The results not discussed here

1433 can be found in the ATLAS Higgs discovery publication[[22](#)].

1434 **4.2 DATA AND SIMULATION SAMPLES**

1435 The data sample used for the following results was taken in 2011 and 2012 at center of mass energies of 7  
1436 and 8 TeV, respectively, with  $4.8 \text{ fb}^{-1}$  collected at 7 TeV and  $5.8 \text{ fb}^{-1}$  collected at 8 TeV. Higgs pro-  
1437 duction in the gluon fusion and vector boson fusion modes is modeled with **POWHEG** for the hard scat-  
1438 tering event and **PYTHIA** for the showing and hadronization. Associated production of a Higgs with a  
1439 vector boson or top quarks is modeled via **PYTHIA**.

1440 Table 4.1 shows the Monte Carlo generators used for modeling the signal and background processes  
1441 relevant for the three analyses to be discussed.

Process	Generator
$\text{ggF}, \text{VBF } H$	<b>POWHEG + PYTHIA</b>
$WH, ZH, t\bar{t}H$	<b>PYTHIA</b>
$W + \text{jets}, Z/\gamma^* + \text{jets}$	<b>ALPGEN + HERWIG</b>
$t\bar{t}, tW, tb$	<b>MC@NLO + HERWIG</b>
$tqb$	<b>ACERMC + PYTHIA</b>
$q\bar{q} \rightarrow WW$	<b>MC@NLO + HERWIG</b>
$gg \rightarrow WW$	<b>GG2WW+ HERWIG</b>
$q\bar{q} \rightarrow ZZ$	<b>POWHEG + PYTHIA</b>
$gg \rightarrow ZZ$	<b>GG2ZZ+ HERWIG</b>
$WZ$	<b>MADGRAPH+ PYTHIA , HERWIG</b>
$W\gamma + \text{jets}$	<b>ALPGEN + HERWIG</b>
$W\gamma^*$	<b>MADGRAPH+ PYTHIA</b>
$q\bar{q}/gg \rightarrow \gamma\gamma$	<b>SHERPA</b>

**Table 4.1:** Monte carlo generators used to model signal and background for the Higgs search[[22](#)].

1442 **4.3  $H \rightarrow WW \rightarrow e\nu\mu\nu$  SEARCH**

1443 The  $H \rightarrow WW \rightarrow e\nu\mu\nu$  search is unique compared to the  $ZZ$  and  $\gamma\gamma$  channels. The Higgs mass can-  
1444 not be fully reconstructed due to the presence of neutrinos in the final state, so the transverse mass  $m_T$   
1445 is used as the final discriminating variable. Compared to the other channels, there are more backgrounds

1446 here as well, as discussed in chapter 3. The same flavor final states are excluded from this search due to  
1447 high pileup in the 8 TeV dataset.

1448 **4.3.1 EVENT SELECTION**

1449 The analysis requires two opposite charge isolated leptons, with the leading (sub-leading) lepton required  
1450 to have  $p_T > 25(15)$  GeV. The events are separated into different signal regions depending on which  
1451 flavor of lepton is leading ( $e\mu$  for leading electron,  $\mu e$  for leading muon). Strict lepton quality cuts are  
1452 applied to the sample to reduce backgrounds from fake leptons.

1453 Jets are reconstructed with the anti- $k_T$  algorithm with a radius parameter  $R = 0.4$ . The jets are  
1454 required to have  $p_T > 25$  GeV and  $|eta| < 4.5$ , with jets in the tracking volume required to have a  
1455 jet vertex fraction of 0.5 and jets in the forward region required to have  $p_T > 30$  GeV. The analysis is  
1456 separated into three different signal regions based on jet multiplicity:  $n_j = 0, 1, \geq 2$ .

1457 To indicate the presence of neutrinos in the event, a requirement of  $E_{T,\text{rel}}^{\text{miss}} > 25$  GeV is made\*. This  
1458 requirement significantly reduces the QCD multijet and  $Z/\gamma^*$  + jets backgrounds. Figure 4.1 shows the  
1459 distribution of  $n_j$  in data and simulation after applying these “pre-selection” requirements.

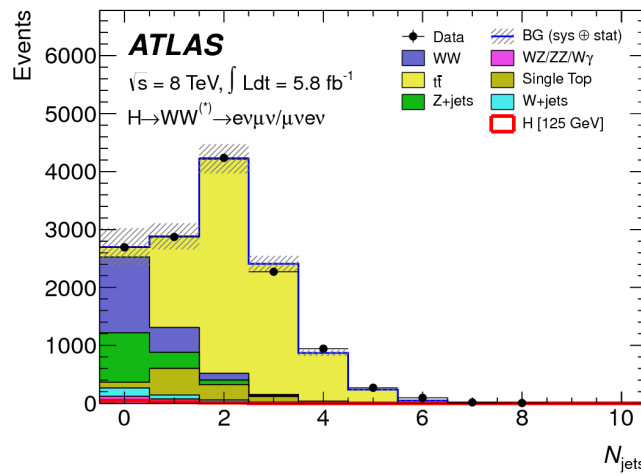


**Figure 4.1:** Jet multiplicity distribution in data and MC after applying lepton, jet, and  $E_{T,\text{rel}}^{\text{miss}}$  selections. The  $WW$  and top backgrounds have been normalized using control samples, and the hashed band indicates the total uncertainty on the prediction. [22]

\*For the definition of  $E_{T,\text{rel}}^{\text{miss}}$ , see chapter 3

1460     Additional selections are applied to require the dilepton topology to correspond to that of a SM  
1461     Higgs. The requirements are presented here - more detailed discussion on the motivation for each re-  
1462     quirement is saved for Chapter 5. In all of the jet multiplicity channels, the dilepton system is required to  
1463     have a small gap in azimuthal angle,  $\Delta\phi_{\ell\ell} < 1.8$ . Similarly, the  $m_{\ell\ell}$  is required to be less than 50 GeV  
1464     in the lower jet multiplicity channels and less than 80 GeV in the  $n_j \geq 2$  channel. In the  $n_j = 0$   
1465     channel, the magnitude of the dilepton  $p_T$ ,  $p_T^{\ell\ell}$ , is required to be greater than 30 GeV.

1466     In the higher jet multiplicity channels ( $n_j \geq 1$ ), the top background is a more important component  
1467     and must be reduced. The total transverse momentum  $p_T^{\text{sum}}$  is thus required to be less than 30 GeV.  
1468     Additionally, the di- $\tau$  invariant mass  $m_{\tau\tau}$  (dilepton mass computed under the assumption that the neu-  
1469     trinos from the  $\tau$  decay are emitted collinear to the charged leptons) is used to reject  $Z \rightarrow \tau\tau$  events by  
1470     requiring  $|m_{\tau\tau} - m_Z| > 25$  GeV. These variables are also discussed in more detail in Chapter 5.

1471     In the  $n_j \geq 2$  channel, requirements are made to isolate the VBF contribution to Higgs production.  
1472     The kinematics of the two leading jets are used to make these requirements. In particular, the event must  
1473     have  $\Delta y_{jj} > 3.8$  and  $m_{jj} > 500$  GeV, along with a veto on having any additional jets with rapidity  
1474     between the two leading jets.

#### 1475     4.3.2 BACKGROUND ESTIMATION

1476     The details of the background estimation techniques used in the  $H \rightarrow WW^* \rightarrow \ell\nu\ell\nu$  analysis are dis-  
1477     cussed in section 5.5. As that section refers to a later iteration of the analysis, a general discussion is given  
1478     here for completeness. The dominant backgrounds are SM  $WW$  production and top (both pair and  
1479     single) production, and these backgrounds have their normalizations estimated from dedicated control  
1480     regions while their shapes are taken from simulation.

1481     The control sample for the Standard Model  $WW$  background is defined by making the same require-  
1482     ments as the signal region with the  $m_{\ell\ell}$  requirement inverted (now requiring  $m_{\ell\ell} > 80$  GeV) and  
1483     removing the  $\Delta\phi_{\ell\ell}$  requirement. This creates a control sample that is 70% (40%) pure in the 0(1)-jet  
1484     region. The correction to the pure MC-based background estimate is quantified by defining a normal-  
1485     ization factor  $\beta$  which is the ratio of the data yield to the MC yield ( $N_{\text{data}}/N_{\text{MC}}$ ) in this control sample.

1486 Table 4.2 shows the  $WW$  normalization factors in the  $n_j = 0$  and  $n_j = 1$  bins (the  $n_j \geq 2$  estimate is  
 1487 taken directly from MC).

$n_j$	$\beta_{WW}$	$\beta_t$
= 0	$1.06 \pm 0.06$	$1.11 \pm 0.06$
= 1	$0.99 \pm 0.15$	$1.11 \pm 0.05$
$\geq 2$	-	$1.01 \pm 0.26$

**Table 4.2:** Normalization factors (ratio of data and MC yields in a control sample) for the Standard Model  $WW$  and top backgrounds in the  $H \rightarrow WW^* \rightarrow \ell\nu\ell\nu$  analysis [22]. Only statistical uncertainties are shown.

1488 The top background estimate is also computed separately in each jet multiplicity bin. In the  $n_j = 0$   
 1489 channel, the background is first normalized using data after pre-selection requirements with no selection  
 1490 on  $n_j$ . Then, a dedicated  $b$ -tagged control sample is used to evaluate the ratio of one-jet to two-jet events  
 1491 in data. The details of this technique are shown in reference [71]. In the  $n_j = 1$  and the  $n_j \geq 2$  regions,  
 1492 the top background is normalized in a control sample where the signal region selections are applied,  
 1493 but the  $b$ -jet veto is reversed and the Higgs topology requirements on  $m_{\ell\ell}$  and  $\Delta\phi_{\ell\ell}$  are removed. The  
 1494 resulting normalization factors for these techniques are shown in table 4.2.

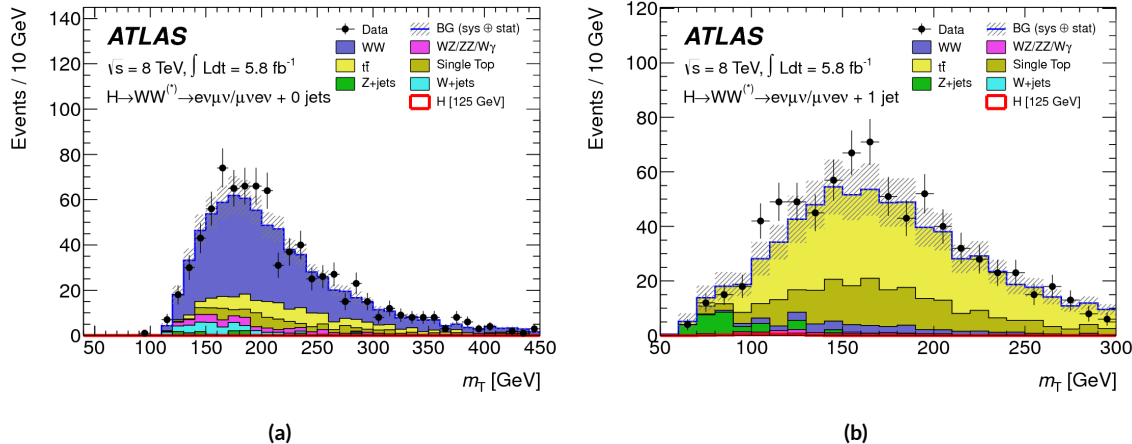


**Figure 4.2:** Comparison of  $m_T$  between data and simulation in the  $n_j = 0$   $WW$  (a) and  $n_j = 1$  top (b) control samples [22]

1495 The control samples which are used for background normalization can also be used to validate the  
 1496 modeling of the  $m_T$  distribution for each background. Figure 4.2 shows the comparison between data

1497 and MC for the  $m_T$  distribution after correcting the normalization of the backgrounds in the  $WW$  and  
 1498 top control regions. Good agreement between data and simulation is seen in both cases.

1499 The  $W + \text{jets}$  background estimate is taken entirely from data using a control sample with one well  
 1500 reconstructed lepton and one anti-identified lepton. All other backgrounds are taken purely from simu-  
 1501 lation.

#### 1502 4.3.3 SYSTEMATIC UNCERTAINTIES

1503 The systematic uncertainties that have the largest impact on the analysis are the theoretical uncertainties  
 1504 associated with the signal cross section, and these are shared with the  $ZZ^*$  and  $\gamma\gamma$  channels. The un-  
 1505 certainties resulting from variations of the QCD scale are  $+7\% / -8\%$  on the final singal yield. Those  
 1506 coming from variations of the parton distribution function (PDF) used in the simulation add a  $\pm 8\%$   
 1507 uncertainty on the yield. The uncertainties on the branching ratios of the Higgs are  $\pm 5\%$ .

1508 The main experimental uncertainties come from variations of the jet energy scale (JES), jet energy  
 1509 resolution, pile-up,  $E_T^{\text{miss}}$ ,  $b$ -tagging efficiency,  $W + \text{jets}$  background estimate, and integrated luminosity.  
 1510 For more details, see reference [22].

#### 1511 4.3.4 RESULTS

1512 Table 4.3 shows the signal and background yields in the final signal region after normalizing the back-  
 1513 grounds according to the methods described above.

	$n_j = 0$	$n_j = 1$	$n_j \geq 2$
Signal	$20 \pm 4$	$5 \pm 2$	$0.34 \pm 0.07$
$WW$	$101 \pm 13$	$12 \pm 5$	$0.10 \pm 0.14$
Other dibosons	$12 \pm 3$	$1.9 \pm 1.1$	$0.10 \pm 0.10$
$t\bar{t}$	$8 \pm 2$	$6 \pm 2$	$0.15 \pm 0.10$
Single top	$3.4 \pm 1.5$	$3.7 \pm 1.6$	-
$Z/\gamma^* + \text{jets}$	$1.9 \pm 1.3$	$0.10 \pm 0.10$	-
$W + \text{jets}$	$15 \pm 7$	$2 \pm 1$	-
Total background	$142 \pm 16$	$26 \pm 6$	$0.35 \pm 0.18$
Observed in data	185	38	0

Table 4.3: Data and expected yields for signal and background in the final  $H \rightarrow WW^* \rightarrow \ell\nu\ell\nu$  signal region.  
 Uncertainties shown are both statistical and systematic. [22]

1514     Figure 4.3 shows the  $m_T$  distribution in the  $n_j \leq 1$  channels for 8 TeV data. (No events are observed  
 1515     in data in the  $n_j \geq 2$  channels in this dataset). The excess shown here relatively flat as a function of  
 1516     hypothesized Higgs mass. The combined 7 and 8 TeV data gives an excess with local significance of  $2.8\sigma$   
 1517     with an expected significance of  $2.3\sigma$ , corresponding to a  $\mu$  measurement of  $1.3 \pm 0.5$ .

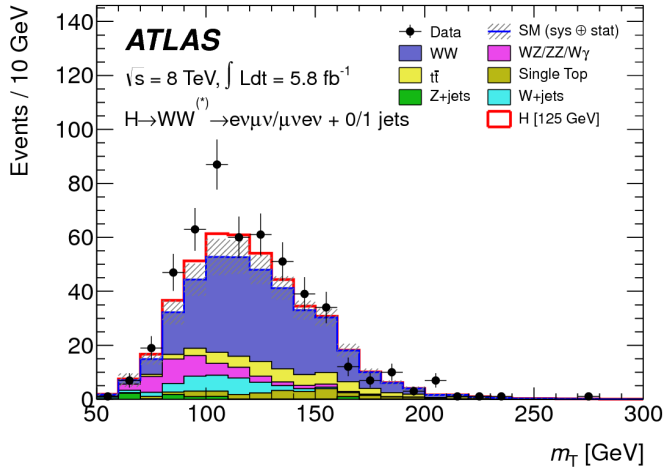


Figure 4.3:  $m_T$  distribution in the  $H \rightarrow WW \rightarrow e\nu\mu\nu$   $n_j \leq 1$  channels for 8 TeV data[22].

#### 1518    4.4    $H \rightarrow \gamma\gamma$ SEARCH

1519     The  $H \rightarrow \gamma\gamma$  search is in essence a search for a peaked excess above the falling SM diphoton mass spec-  
 1520     trum, with  $m_{\gamma\gamma}$  as the ultimate discriminating variable. Events are selected by requiring two isolated  
 1521     photons, with the leading (sub-leading) photon required to have  $E_T > 40(30)$  GeV. In the 8 TeV  
 1522     data, the photons are required to pass cut-based identification criteria consistent with a photon in the  
 1523     electromagnetic calorimeter and little leakage in the hadronic calorimeter.

1524     The main challenges for this analysis are accurate mass reconstruction and background estimation.  
 1525     In order to accurately reconstruct the invariant mass of the di-photon system, both the energy and di-  
 1526     rection of the photons must be measured well. Therefore, the identification of the primary vertex of the  
 1527     hard interaction is particularly important, and is done using a multivariate likelihood which combines  
 1528     information about the photon direction and vertex position. The background is modeled with a falling  
 1529     spectrum in  $m_{\gamma\gamma}$  that is parameterized by different functions depending on the category of the event.

1530 4.4.1 RESULTS

1531 The resulting diphoton mass spectrum is shown in figure 4.4. The best fit mass value in the  $\gamma\gamma$  channel  
 1532 alone in the combined 7 and 8 TeV data is 126.5 GeV. The local significance at this point is  $4.5\sigma$ , with  
 1533 an expected significance of  $2.5\sigma$ . Therefore, the measured signal strength  $\mu$  is  $1.8 \pm 0.5$  in this channel.

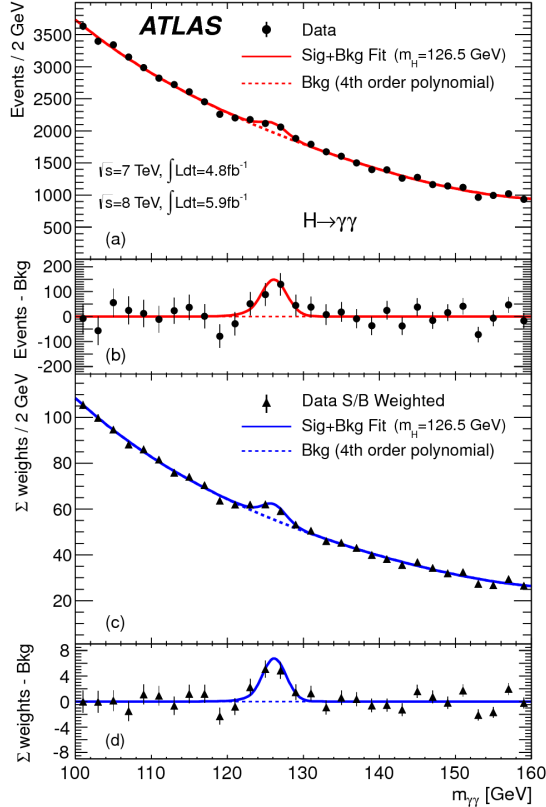


**Figure 4.4:** Diphoton mass spectrum in 7 and 8 TeV data. Panel a) shows the unweighted data distribution superimposed on the background fit, while panel c) shows the data where each event category is weighted by its signal to background ratio. Panels b) and d) show the respective distributions with background subtracted[22].

1534 4.5  $H \rightarrow ZZ \rightarrow 4\ell$  SEARCH

1535 The  $H \rightarrow ZZ \rightarrow 4\ell$  analysis searches for a Standard Model Higgs boson decaying to two  $Z$  bosons,  
 1536 each of which decays to a pair of same flavor, opposite charge isolated leptons. The ultimate discriminat-  
 1537 ing variable is  $m_{4\ell}$ , or the invariant mass of the four selected leptons. The  $\ell$  denotes an  $e$  or  $\mu$  as with the  
 1538  $H \rightarrow WW^* \rightarrow \ell\nu\ell\nu$  analysis.

1539     Four distinct signal regions are constructed depending on the flavors of the final state, additionally  
 1540     separated by the flavor of the leading lepton pair. These are referred to as  $4e$ ,  $2e2\mu$ ,  $2\mu2e$ ,  $4\mu$ .

1541     The main backgrounds in the  $H \rightarrow ZZ \rightarrow 4\ell$  search are continuum  $ZZ^*$  production,  $Z + \text{jets}$  pro-  
 1542     duction, and  $t\bar{t}$ . The  $m_{4\ell}$  distribution for background is estimated from simulation. The normalization  
 1543     of the SM  $ZZ^*$  background is also taken from MC simulation, while the  $Z + \text{jets}$  and  $t\bar{t}$  normalizations  
 1544     are taken from data-driven methods.

1545     **4.5.1 RESULTS**

1546     Figure 4.5 shows the  $m_{4\ell}$  spectrum measured in the 7 and 8 TeV datasets. The total number of events  
 1547     observed in the window between 120 and 130 GeV is 13, with 6 events in the  $4\mu$  channel, 2 events in  
 1548     the  $4e$  channel, and 5 events in the  $2e2\mu/2\mu2e$ . The best fit  $\mu$  value in the combined 7 and 8 TeV data  
 1549     occurs at 125 GeV and is measured to be  $1.2 \pm 0.6$ . The observed significance at this mass is  $3.6\sigma$ , with  
 1550     an expected significance of  $2.7\sigma$ .

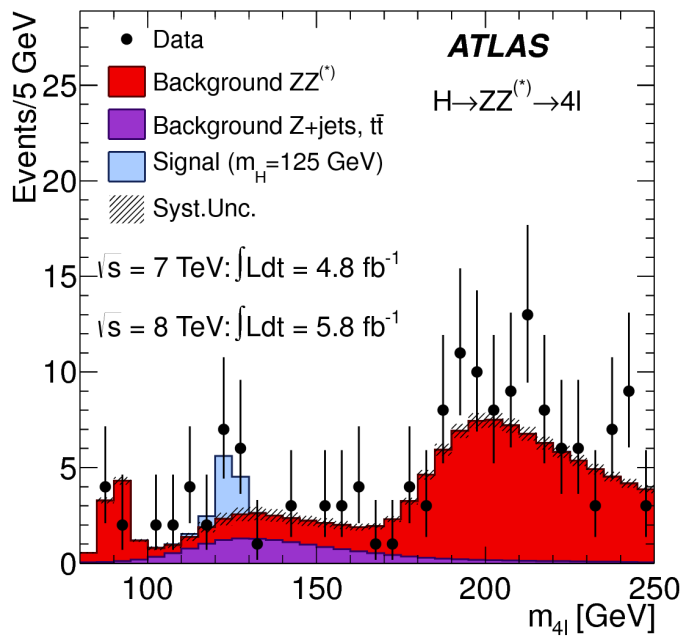


**Figure 4.5:** Four lepton invariant mass spectrum ( $m_{4\ell}$ ) in 7 and 8 TeV data compared to background estimate. A 125 GeV SM Higgs signal is shown in blue[22].

1551 4.6 COMBINED RESULTS

1552 The statistical interpretation of the combined results is undertaken as described in section 3.6.2, with a  
 1553 hypothesis test based on a likelihood ratio parameterized by the Higgs signal strength  $\mu$ . The null hy-  
 1554 pothesis corresponds to  $\mu = 0$ , while the SM Higgs corresponds to  $\mu = 1$ .

1555 Table 4.4 summarizes the properties of the individual channels as well as the significances of the ex-  
 1556 cesses seen. The most significant observed local excess comes from the  $\gamma\gamma$  channel. Figure 4.6 shows a  
 1557 comparison of the observed local  $p_0$  values as a function of hypothesized mass for the three different  
 1558 search channels. Both the  $ZZ^*$  and  $\gamma\gamma$  channels have very peaked excesses, while the  $WW^*$  excess can  
 1559 be seen as very broad because the  $m_T$  distribution does not provide detailed information about the true  
 1560 Higgs mass.

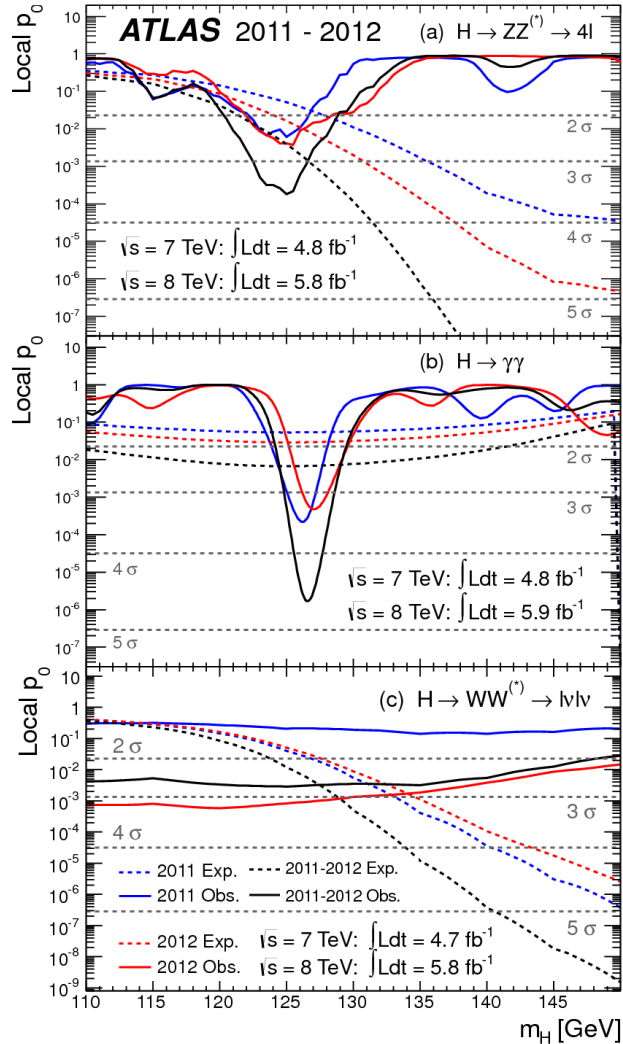
Channel	Fit var.	Observed $Z_l$	Expected $Z_l$	$\hat{\mu}$
$H \rightarrow ZZ^* \rightarrow 4\ell$	$m_{4\ell}$	3.6	2.7	$1.2 \pm 0.6$
$H \rightarrow \gamma\gamma$	$m_{\gamma\gamma}$	4.5	2.5	$1.8 \pm 0.5$
$H \rightarrow WW^* \rightarrow e\nu\mu\nu$	$m_T$	2.8	2.3	$1.3 \pm 0.5$
Combined	-	6.0	4.9	$1.4 \pm 0.3$

Table 4.4: Summary of the expected and observed significance and measured signal strengths in the combined 7 and 8 TeV datasets for the Higgs discovery analysis[22].

1561 Figure 4.7 shows the combined exclusion limit,  $p_0$ , and signal strength. The highest local excess comes  
 1562 at a value of 126.5 GeV and corresponds to a  $6.0\sigma$  observed excess.

1563 Figure 4.8 shows a comparison of the measured signal strengths between the different Higgs search  
 1564 channels. All measured  $\mu$  are consistent with unity within their uncertainty, and the combined  $\mu$  mea-  
 1565 surement is  $1.4 \pm 0.3$ .

1566 The likelihood can also be computed in a two-dimensional plane of  $m_H$  and  $\mu$ , and this is shown in  
 1567 figure 4.9. The figure shows that while the  $\gamma\gamma$  and  $ZZ^*$  channels have very good mass resolution, the  
 1568 excess in  $WW^*$  covers a broad mass range. The banana shape of the  $WW^*$  result is due to the fact that  
 1569 the excess in this channel can either be explained by increasing the signal strength or by changing the  
 1570 mass (and thus the cross section). The two parameters are correlated due to the lack of mass sensitivity in  
 1571 this channel.



**Figure 4.6:** Local  $p_0$  distribution as a function of hypothesized Higgs mass for the  $H \rightarrow ZZ^* \rightarrow 4\ell$  (a),  $H \rightarrow \gamma\gamma$  (b), and  $H \rightarrow WW^* \rightarrow \ell\nu\ell\nu$  (c) channels. Dashed curves show expected results, while solid curves show observed. Red curves are from 7 TeV data, blue curves from 8 TeV, and black curved combined[22].

Because multiple Higgs mass points are searched for, the local significance must be corrected for a look-elsewhere effect to compute a true global significance. The global significance for finding a Higgs anywhere in the mass range of 110 GeV to 600 GeV is  $5.1\sigma$ . This increases slightly to  $5.3\sigma$  if only mass range from 110 to 150 GeV.

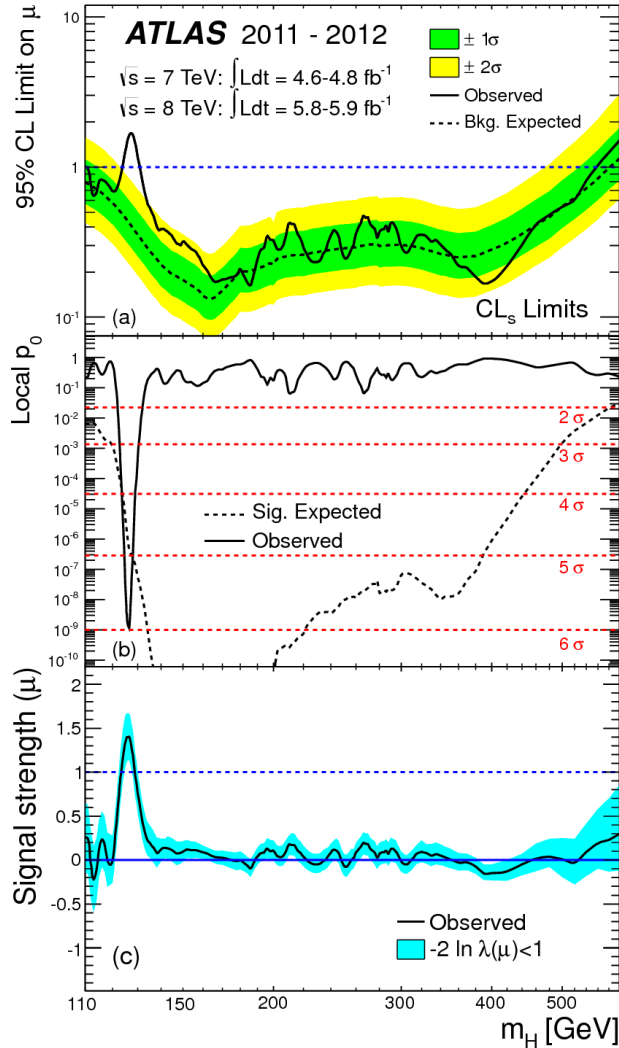


**Figure 4.7:** Combined 95% CL limits (a), local  $p_0$  values (b), and signal strength measurement (c) as a function of Higgs mass[22].

## 1576 4.7 CONCLUSION

1577 A search for the production of a Standard Model Higgs boson was conducted in  $4.8 \text{ fb}^{-1}$  collected at  
 1578  $\sqrt{s} = 7 \text{ TeV}$  and  $5.8 \text{ fb}^{-1}$  at  $\sqrt{s} = 8 \text{ TeV}$ . A new particle consistent with the Higgs boson was  
 1579 observed, with a mass of  $126.5 \text{ GeV}$  and a global (local) significance of  $5.1(6.0)\sigma$ . This is the first dis-  
 1580 covery level observation of a particle consistent with the Higgs.

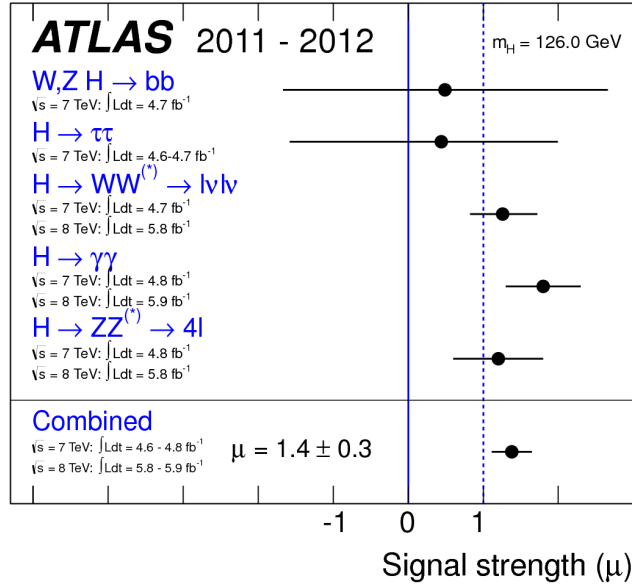


**Figure 4.8:** Comparison of measured signal strength  $\mu$  for a 126 GeV Higgs in the 7 and 8 TeV datasets[22].

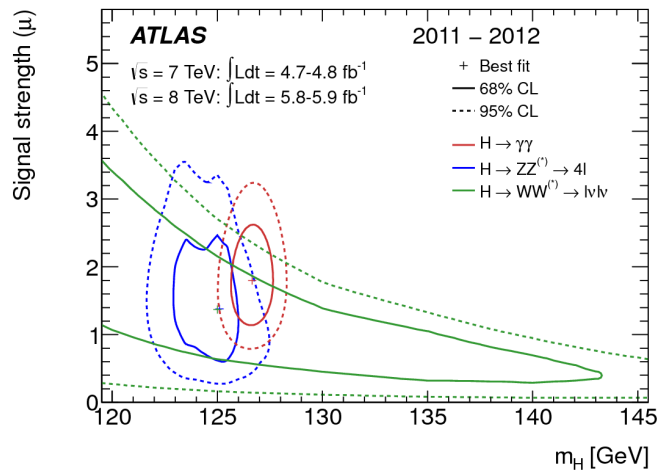


**Figure 4.9:** Two dimensional likelihood as a function of signal strength  $\mu$  and Higgs mass  $m_H$ [22].

*The imagination of nature is far, far greater than the  
imagination of man.*

Richard Feynman

# 5

1581

1582

## Observation of Vector Boson Fusion

1583

production of  $H \rightarrow WW^* \rightarrow \ell\nu\ell\nu$

1584 **5.1 INTRODUCTION**

1585 After the discovery of a particle consistent with the Higgs boson, the  $H \rightarrow WW^*$  analysis had two main  
1586 goals. The first goal was to increase the sensitivity of the analysis to fully confirm that the  $H \rightarrow WW^*$   
1587 process did indeed exist. The second goal was to characterize the particle as much as possible, including  
1588 searching for the lower cross-section production modes, in order to confirm that it was indeed a Higgs  
1589 boson. This chapter presents a dedicated search for Vector Boson Fusion (VBF) production of a Higgs  
1590 boson decaying via the  $H \rightarrow WW^* \rightarrow \ell\nu\ell\nu$  mode. First, basics of the topology of VBF production  
1591 are presented. Then, the details of the analysis are shown, including signal region definition, background  
1592 estimation techniques, and systematic uncertainties. Finally, the results of the analysis are presented. As

1593 will be shown, this analysis is the first and most sensitive observation of the VBF production mode of the  
1594 Higgs on ATLAS.

1595 In the VBF channel, there are both a selection requirement based signal region analysis (known as the  
1596 “cut-based”) and a multivariate analysis which uses a boosted decision tree (known as the BDT analysis).  
1597 The focus of this chapter will be on the cut-based signal region, as this is an important component of the  
1598 VBF analysis and in particular acts as strong validation for the final BDT result. Connections between  
1599 the cut-based and BDT analyses will be discussed where appropriate.

## 1600 5.2 DATA AND SIMULATION SAMPLES

1601 The results presented here are with  $20.3 \text{ fb}^{-1}$  taken at  $\sqrt{s} = 8 \text{ TeV}$  and  $4.5 \text{ fb}^{-1}$  taken at  $\sqrt{s} = 7 \text{ TeV}$ .  
1602 The details of the LHC and detector conditions during this period are given in Chapter 2. The trigger  
1603 selection defining the dataset is discussed in section 5.2.1. The simulation samples used for signal and  
1604 background modeling are given in section 5.2.2.

### 1605 5.2.1 TRIGGERS

1606 The analysis uses a combination of single lepton and dilepton triggers to allow lowering of the  $p_T$  thresh-  
1607 olds and increased signal acceptance. The  $p_T$  threshold on the leptons is a particularly important consid-  
1608 eration for this signal. Because the second  $W$  produced in the decay can be off-shell, it tends to pro-  
1609 duce lower momentum leptons. Thus, being able to lower the  $p_T$  threshold while still maintaining  
1610 a low background rate is critical. Figure 5.1 shows an example of the subleading lepton  $p_T$  for a VBF  
1611  $H \rightarrow WW^*$  signal compared to the corresponding  $t\bar{t}$  background. Note that the lepton  $p_T$  spectrum is  
1612 considerably softer in the signal sample.

1613 As discussed in Chapter 2, there are multiple levels in the ATLAS trigger system, and there are differ-  
1614 ent  $p_T$  thresholds imposed for the leptons at each level. Additionally, some triggers have a loose selection  
1615 on the isolation of the lepton (looser than that applied offline in the analysis object selection). Table 5.1  
1616 shows the thresholds used for single lepton triggers, while table 5.2 shows the thresholds coming from  
1617 di-lepton triggers. The single lepton trigger efficiency for muons that pass the analysis object selection is

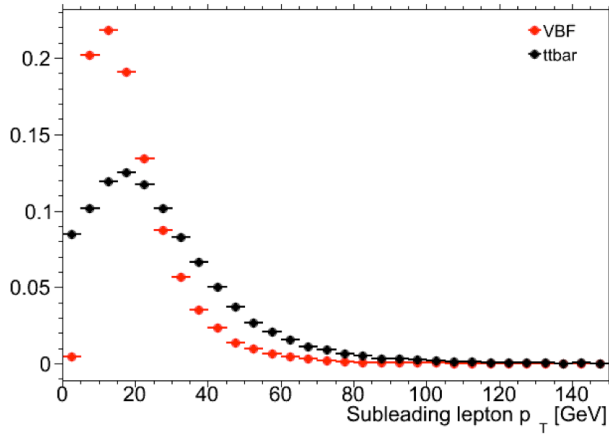


**Figure 5.1:** A comparison of the subleading lepton  $p_T$  spectrum between VBF  $H \rightarrow WW^*$  production and  $t\bar{t}$  background

1618 70% for muons in the barrel region ( $|\eta| < 1.05$ ) and 90% in the endcap region. The electron trigger ef-  
1619 ficiency increases with electron  $p_T$  but the average is approximately 90%. These efficiencies are measured  
1620 by combined performance and trigger signature groups[72, 73].

	Level-1 threshold	High-level threshold
Electron	18	$24i$
	30	60
Muon	15	$24i$
		36

**Table 5.1:** Single lepton triggers used for electrons and muons. A logical “or” of the triggers listed for each lepton type is taken. Units are in GeV, and the  $i$  denotes an isolation requirement in the trigger.

	Level-1 threshold	High-level threshold
$ee$	10 and 10	12 and 12
$\mu\mu$	15	18 and 8
$e\mu$	10 and 6	12 and 8

**Table 5.2:** Di-lepton triggers used for different flavor combinations. The two thresholds listed refer to leading and sub-leading leptons, respectively. The di-muon trigger only requires a single lepton at level-1.

1621 The combination of all triggers shown gives good efficiency for signal events. This efficiency is sum-  
1622 marized in table 5.3. The relative improvement in efficiency by adding the dilepton triggers is also shown  
1623 in the same table. The largest gain comes in the  $\mu\mu$  channel. Overall the trigger selection shows a good  
1624 efficiency for  $H \rightarrow WW^*$  signal events.

Channel	Trigger efficiency	Gain from $2\ell$ trigger
$ee$	97%	9.1%
$\mu\mu$	89%	18.5%
$e\mu$	95%	8.3%
$\mu e$	81%	8.2%

**Table 5.3:** Trigger efficiency for signal events and relative gain of adding a dilepton trigger on top of the single lepton trigger selection. The first lepton is the leading, while the second is the sub-leading. Efficiencies shown here are for the ggF signal in the  $n_j = 0$  category but are comparable for the VBF signal.

### 1625 5.2.2 MONTE CARLO SAMPLES

1626 Modeling of signal and background processes in the signal region, in particular for the  $m_T$  distribution,  
 1627 is an important consideration for the final interpretation of the analysis. Therefore, careful consideration  
 1628 must be paid to which Monte Carlo (MC) generators are used for specific processes. With the exception  
 1629 of the  $W + \text{jet}$  and multijet backgrounds, the  $m_T$  shape used as the final discriminant is taken from simu-  
 1630 lation. (Many backgrounds are normalized from data, as described in section 5.5).

1631 Table 5.4 shows the MC generators used for the signal and background processes, as well as their cross  
 1632 sections. In order to include corrections up to next-to-leading order (NLO) in the QCD coupling con-  
 1633 stant  $\alpha_s$ , the `POWHEG` [74] generator is often used. In some cases, only leading order generators like  
 1634 `ACERMC` [75] and `GG2VV` [76] are available for the process in question. If the process requires good  
 1635 modeling for very high parton multiplicities, the `SHERPA` [77] and `ALPGEN` [78] generators are used  
 1636 to provide merged calculations for five or fewer additional partons. These matrix element level calcula-  
 1637 tions must then be additionally matched to models of the underlying event, hadronization, and parton  
 1638 shower. There are four possible generators for this: `SHERPA`, `PYTHIA 6`[79], `PYTHIA 8`[80], or `HERWIG`  
 1639 [81] + `JIMMY` [82]. The simulation additionally requires an input parton distribution function (PDF).  
 1640 The `CT10`[83] PDFs are used for `SHERPA` and `POWHEG` simulated samples, while `CTEQ6Li`[84] is used  
 1641 for `ALPGEN + HERWIG` and `ACERMC` simulations. The Drell-Yan samples are reweighted to the `MRST`  
 1642 [85] PDFs, as these are found to give the best agreement between data and simulation.

1643 Once the basic hard scattering process is simulated, it must be passed through a detector simulation  
 1644 and additional pile-up events must be overlaid. The pile-up events are modeled with `PYTHIA 8`, and the

Process	MC generator	$\sigma \cdot \mathcal{B}$ (pb)
<b>Signal</b>		
ggF	$H \rightarrow WW^*$ POWHEG +PYTHIA 8	0.435
VBF	$H \rightarrow WW^*$ POWHEG +PYTHIA 8	0.0356
VH	$H \rightarrow WW^*$ PYTHIA 8	0.0253
<b><math>WW</math></b>		
$q\bar{q} \rightarrow WW$ and $qg \rightarrow WW$	POWHEG +PYTHIA 6	5.68
$gg \rightarrow WW$	GG2VV +HERWIG	0.196
$(q\bar{q} \rightarrow W) + (q\bar{q} \rightarrow W)$	PYTHIA 8	0.480
$q\bar{q} \rightarrow WW$	SHERPA	5.68
VBS $WW + 2$ jets	SHERPA	0.0397
<b>Top quarks</b>		
$t\bar{t}$	POWHEG +PYTHIA 6	26.6
$Wt$	POWHEG +PYTHIA 6	2.35
$tq\bar{b}$	ACERMC +PYTHIA 6	28.4
$t\bar{b}$	POWHEG +PYTHIA 6	1.82
<b>Other dibosons (<math>VV</math>)</b>		
$W\gamma$ ( $p_T^\gamma > 8$ GeV)	ALPGEN +HERWIG	369
$W\gamma^*$ ( $m_{\ell\ell} \leq 7$ GeV)	SHERPA	12.2
$WZ$ ( $m_{\ell\ell} > 7$ GeV)	POWHEG +PYTHIA 8	12.7
VBS $WZ + 2$ jets	SHERPA	0.0126
( $m_{\ell\ell} > 7$ GeV)		
$Z\gamma$ ( $p_T^\gamma > 8$ GeV)	SHERPA	163
$Z\gamma^*$ (min. $m_{\ell\ell} \leq 4$ GeV)	SHERPA	7.31
$ZZ$ ( $m_{\ell\ell} > 4$ GeV)	POWHEG +PYTHIA 8	0.733
$ZZ \rightarrow \ell\ell\nu\nu$ ( $m_{\ell\ell} > 4$ GeV)	POWHEG +PYTHIA 8	0.504
<b>Drell-Yan</b>		
$Z$ ( $m_{\ell\ell} > 10$ GeV)	ALPGEN +HERWIG	16500
VBF $Z + 2$ jets	SHERPA	5.36
( $m_{\ell\ell} > 7$ GeV)		

**Table 5.4:** Monte Carlo samples used to model the signal and background processes[21].

ATLAS detector is simulated with GEANT4[86]. Because of the unique phase space of the  $H \rightarrow WW^*$  analysis, events are sometimes filtered at generator level to allow for more efficient generation of relevant events. The efficiency of the trigger in MC simulation does not always match the measured efficiency in

1648 data, so trigger scale factors are applied to correct the MC efficiency to the data. These are derived by the  
1649 combined performance groups[[72](#), [73](#)].

### 1650 5.3 OBJECT SELECTION

1651 In order to define the signal region, the analysis must first select the objects to be considered. The de-  
1652 tails of the object reconstruction algorithms are discussed in Chapter 2, while this section gives specific  
1653 selection cuts used in the  $H \rightarrow WW^*$  analysis.

1654 The first step in this process is to select a primary vertex candidates. The event’s primary vertex is the  
1655 vertex with the largest sum of  $p_T^2$  for associated tracks and is required to have at least three tracks with  
1656  $p_T > 450$  MeV. Many of the object selection cuts are then made relative to this chosen primary vertex.

#### 1657 5.3.1 MUONS

1658 The analysis uses combined muon candidates, where a track in the Inner Detector has been matched  
1659 to a standalone track in the Muon Spectrometer. The track parameters are combined statistically in the  
1660 muon reconstruction algorithm[[16](#)]. The muons are required to be within  $|\eta| < 2.5$  and have a  $p_T >$   
1661 10 GeV. To reduce backgrounds coming from mis-reconstructed leptons, there are requirements on  
1662 the impact parameter of the muon relative to the primary vertex. The transverse impact parameter  $d_0$   
1663 is required to be small relative to its estimated uncertainty, the exact cut value being  $d_0/\sigma_{d_0} < 3$ . The  
1664 longitudinal impact parameter  $z_0$  must satisfy  $|z_0 \sin \theta| < 1$  mm.

1665 As discussed previously, the muons must also be isolated. There are two types of lepton isolations  
1666 that are calculated: track-based and calorimeter-based. For muons, the track-based isolation is defined  
1667 using the scalar sum  $\sum p_T$  for tracks with  $p_T > 1$  GeV (excluding the muon’s track) within a cone of  
1668  $\Delta R = 0.3$  ( $0.4$ ) for muon with  $p_T > 15$  GeV ( $10 < p_T < 15$  GeV). The final isolation requirement  
1669 is made my requiring that this scalar sum be no more than a certain fraction of the muon’s  $p_T$ . This re-  
1670 quirement varies with muon  $p_T$  and the exact cuts are defined in table 5.5.

1671 The calorimeter-based muon isolation is defined using as a  $\sum E_T$  calculated from calorimeter cells  
1672 using the same cone size as the track-based isolation but excluding cells with  $\Delta R < 0.05$  around the

1673 muon. This requirement is also defined as a cut on the ratio of the sum to the muon  $p_T$  and varies with  
1674 muon  $p_T$ . The cut values are also given in table 5.5.

1675 The isolation requirements loosen as a function of  $p_T$  to allow for larger signal acceptance. At low  $p_T$ ,  
1676 the isolation is tightened to reduce the  $W + \text{jets}$  background which arises from a misidentified lepton.

$p_T$ range (GeV)	Calorimeter isolation	Track isolation
10 – 15	0.06	0.06
15 – 20	0.12	0.08
20 – 25	0.18	0.12
> 25	0.30	0.12

Table 5.5:  $p_T$  dependent isolation requirements for muons. Muons are required to have the amount of calorimeter or track based cone sums be less than this fraction of their  $p_T$ .

### 1677 5.3.2 ELECTRONS

1678 Electrons are identified by matching reconstructed clusters in the electromagnetic calorimeter with tracks  
1679 in the inner detector. The electrons are identified using a likelihood based method[14, 64] which takes  
1680 into account the shower shapes in the calorimeter, the matching of tracks to clusters, and the amount of  
1681 transition radiation in the TRT. The electrons are required to have  $|\eta| < 2.47$ , and candidates in the  
1682 transition region between the barrel and endcap ( $1.37 < |\eta| < 1.52$ ) are excluded. As the muons, the  
1683 electrons are required to have transverse impact parameter significance  $< 3$ , while in the longitudinal  
1684 direction they must have  $|z_0 \sin \theta| < 0.4$  mm. Some electron requirements also vary with electron  $E_T$ ,  
1685 and these requirements are summarized in table 5.6.

1686 The isolation for electrons are defined similarly to the muons but with unique cuts on the objects in-  
1687 cluded. The track-based isolation is defined using tracks with  $p_T > 400$  MeV with cone sizes as defined  
1688 previously. The calorimeter-based isolation also uses the same cone size as the muon, but here the cells  
1689 within a  $0.125 \times 0.175$  area in  $\eta \times \phi$  around the electron cluster's barycenter are excluded. The other  
1690 difference with respect to muons is that the denominator of the isolation ratio is the electron's  $E_T$  rather  
1691 than  $p_T$ . The isolation cuts very with electron  $E_T$  and are defined in table 5.6.

1692 The electron is also required to not be consistent with a vertex coming from a photon conversion.

$p_T$ range (GeV)	Quality cut	Calorimeter isolation	Track isolation
10 – 15	Very tight LH	0.20	0.06
15 – 20	Very tight LH	0.24	0.08
20 – 25	Very tight LH	0.28	0.10
> 25	Medium	0.28	0.10

**Table 5.6:**  $p_T$  dependent requirements for electrons. Electrons are required to have the amount of calorimeter or track based cone sums be less than this fraction of their  $E_T$ .

### 1693 5.3.3 JETS

1694 Jets are clustered with the anti- $k_T$  reconstruction algorithm using a radius parameter of  $R = 0.4$ . They  
 1695 are required to have a jet vertex fraction (JVF) of at least 50%, meaning that half of the tracks associated  
 1696 with the jet originated from the primary vertex. Jets with no tracks associated (i.e. those outside the ac-  
 1697 ceptance of the ID) do not have this requirement applied. Jets are required to have  $p_T > 25$  GeV if  
 1698 they are within the tracking acceptance ( $|\eta| < 2.4$ ). Jets with  $2.4 < |\eta| < 4.5$  are required to have  
 1699  $p_T > 30$  GeV. This tighter requirement reduces jets from pileup in the region where JVF requirements  
 1700 cannot be applied. The two highest  $p_T$  jets in the event are referred to as the “VBF” jets and used to com-  
 1701 pute various analysis selections later.

1702 Identification of  $b$ -jets is done using the MV1 algorithm and is limited to the acceptance of the ID  
 1703 ( $|\eta| < 2.5$ ). The operating point of MV1 that is used is the one that is 85% efficient for identifying true  
 1704  $b$ -jets. This operating point has a 10.3% of mis-tagging a light quark jet as a  $b$ -jet. In order to improve  
 1705 the rejection of  $b$ -jets, a lower threshold than the nominal  $p_T$  threshold described above is used. For the  
 1706 purposes of counting the number of  $b$ -jets, jets with  $p_T$  down to 20 GeV are used.

### 1707 5.3.4 OVERLAP REMOVAL

1708 There are some cases where certain reconstructed objects will overlap and one will have to be chosen  
 1709 (for example, an electron and a jet in the calorimeter). First, the case of lepton overlap is dealt with. If  
 1710 an electron candidate extends into the muon spectrometer, it is removed. If a muon or electron have a  
 1711  $\Delta R < 0.1$ , the electron is removed and the muon is kept. If two electron candidates overlap within  
 1712 the same radius, then the higher  $E_T$  electron is kept. Next, the overlap between leptons and jets is con-

1713 sidered. If an electron and jet are within  $\Delta R < 0.3$  of one another, the electron is kept and the jet is  
1714 removed. However, if a muon and jet overlap within  $\Delta R < 0.3$ , the jet is kept (as it is likely that the  
1715 muon is the result of a semileptonic decay inside the jet).

1716 Once the overlap removal is complete, the final set of objects used in the analysis is defined.

#### 1717 5.4 ANALYSIS SELECTION

1718 The VBF analysis uses two distinct selections. The first is a more standard selection, referred to as “cut-  
1719 based”, that applies requirements on the VBF variables and uses  $m_T$  as the final discriminating variable.  
1720 The second is a looser selection that uses a Boosted Decision Tree (BDT) score as the final discriminator  
1721 in order to take advantage of the detailed correlations between the VBF variables. While the BDT analy-  
1722 sis is ultimately more sensitive, the cut-based serves as an important component of the analysis. First, the  
1723 cut-based allows for confirming the modeling and validity of many variables used as input to the BDT.  
1724 Second, because this is the first use of such an MVA technique in the  $H \rightarrow WW^*$  analysis, the cut-based  
1725 selection allows confirmation of the final BDT result with a more traditional analysis. The cut-based  
1726 techniques are the focus of this chapter, but connections to the BDT result will be illustrated when ap-  
1727 propriate.

1728 One important note is that because this analysis is dedicated to the measurement of the VBF pro-  
1729 duction mode of the Higgs, events coming from gluon fusion production with the Higgs decaying via  
1730  $H \rightarrow WW^* \rightarrow \ell\nu\ell\nu$  are treated as background events. This will be seen throughout the various  
1731 predictions shown.

##### 1732 5.4.1 COMMON PRE-SELECTION

1733 Both the cut-based and BDT analyses have a common pre-selection that is applied before the main signal  
1734 region requirements. The requirements on leptons are common to all  $n_j$  bins. The analysis requires two  
1735 oppositely charged leptons, with the leading lepton required to have  $p_T > 22$  GeV while the subleading  
1736 lepton must have  $p_T > 10$  GeV. Next, to remove low mass  $Z/\gamma^*$  events, a cut on the dilepton mass  
1737  $m_{\ell\ell} > 10$  (12) GeV is applied in the different (same) flavor channel. In the same flavor channels, there is

1738 an additional veto placed on the region around the Z peak, requiring that  $|m_{\ell\ell} - m_Z| > 15$  GeV.

1739 There are also requirements on the amount of missing transverse momentum in the event. These  
1740 are only applied in the same flavor channels, as in the different flavor channels  $t\bar{t}$  is the dominant back-  
1741 ground in  $n_j \geq 2$ . The BDT analysis requires  $p_T^{\text{miss}} > 40$  GeV and  $E_T^{\text{miss}} > 45$  GeV. The cut-  
1742 based analysis must select more tightly on these variables to have maximal sensitivity and thus requires  
1743  $p_T^{\text{miss}} > 50$  GeV and  $E_T^{\text{miss}} > 55$  GeV.

1744 Finally, because this analysis is focused on VBF, a requirement on the jet multiplicity is placed, with  
1745  $n_j \geq 2$ . Additionally, the analysis requires that there are no jets identified as b-quarks in the event, or  
1746  $n_b = 0$ .

#### 1747 5.4.2 CUT-BASED SELECTION

1748 The cut-based selection places sequential requirements on variables reconstructed from the VBF jets in  
1749 order to increase the signal to background ratio.

#### 1750 GENERAL BACKGROUND REDUCTION

1751 Top pair production is the primary background in the  $n_j \geq 2$  bin. Even though  $n_b = 0$  is required,  
1752 an additional variable is constructed to further suppress the top background. There is often additional  
1753 QCD radiation that accompanies the  $t\bar{t}$  system when it is produced. Therefore, a variable which tests for  
1754 the presence of this additional radiation,  $p_T^{\text{sum}}$ , is constructed. It is defined in equation 5.1.

$$p_T^{\text{sum}} = p_T^{\ell\ell} + p_T^{\text{miss}} + \sum p_T^j \quad (5.1)$$

1755 The first cut after pre-selection in the cut-based analysis requires  $p_T^{\text{sum}} < 15$  GeV to further suppress  
1756  $t\bar{t}$  production.

1757 In the different flavor channels, a cut is made to reduce the contamination from  $Z \rightarrow \tau\tau$  decays. The  
1758 di- $\tau$  invariant mass,  $m_{\tau\tau}$ , is constructed by assuming that the neutrinos from the  $\tau$  decays were collinear  
1759 with the leptons[? ]. The analysis requires that this mass not be consistent with a  $Z$  by requiring  $m_{\tau\tau} <$   
1760  $m_Z - 25$  GeV.

1761 VBF TOPOLOGICAL CUTS

1762 The characteristic feature of VBF production of the Higgs is the presence of two additional forward jets  
1763 coming from the incoming partons which radiate the vector bosons that make the Higgs. These jets are  
1764 forward because the outgoing partons still carry the longitudinal momentum of the incoming partons.  
1765 Figure 5.2 shows the distribution of the  $\eta$  for the leading jet in a VBF event compared to a background  
1766 top pair production event. As can be seen, the VBF jets tend to be more forward in  $\eta$ , while the  $t\bar{t}$  jets are  
1767 more central.

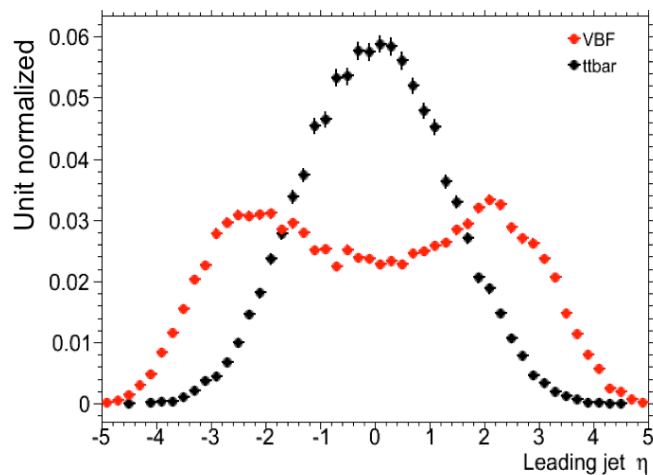


Figure 5.2: Leading jet  $\eta$  in VBF  $H \rightarrow WW^*$  (red) and  $t\bar{t}$  (black)

1768 Because the cross section for VBF production is an order of magnitude smaller than gluon fusion pro-  
1769 duction, these forward jets must be used in order to better reduce background and achieve a good signal  
1770 to background ratio. The dedicated VBF search selection requirements are constructed to maximally  
1771 exploit the features of the unique VBF topology.

1772 Requirements on the VBF jets are collectively referred to as the “VBF topological cuts”. First, a re-  
1773 quirement on the dijet invariant mass of the VBF jets,  $m_{jj}$ , is placed, requiring  $m_{jj} > 600$  GeV. Next,  
1774 the event is required to have a large gap in rapidity between the two VBF jets, or  $\Delta y_{jj} > 3.6$ . Both  
1775 of these cuts put tight requirements on the presence of two forward, high  $p_T$  jets moving in opposite

1776 directions in the longitudinal plane.

1777 Beyond requiring the presence of the two forward VBF jets, the analysis also vetoes on the presence  
1778 of any additional jets that fall between the two VBF jets. This cut is referred to as the central jet veto, or  
1779 CJV. Any events with a third jet with  $p_T > 20$  GeV whose rapidity is between the region defined by the  
1780 two VBF jets are vetoed. This can be expressed in terms of a variable called the jet centrality, defined in  
1781 equation 5.2.

$$C_{j3} = \left| \eta_{j3} - \frac{\eta_{j1} + \eta_{j2}}{2} \right| / \frac{|\eta_{j1} - \eta_{j2}|}{2}, \quad (5.2)$$

1782 Here,  $\eta_{j1}$  and  $\eta_{j2}$  are the pseudorapidities of the leading and subleading jets, respectively, while  $\eta_{j3}$  is  
1783 the pseudorapidity of the extra jet in the event (if one exists). Intuitively,  $C_{j3}$  is zero when  $\eta_{j3}$  is directly  
1784 centered between the two jets and unity when  $\eta_{j3}$  is aligned with either of the VBF jets. Thus, the CJV  
1785 can be expressed as a requirement that  $C_{j3} > 1$ .

1786 The decay products of the Higgs tend to be central as well. Thus, the analysis also requires that both  
1787 leptons in the analysis fall within the rapidity gap defined by the jets. This cut is referred to as the outside  
1788 lepton veto, or OLV. A quantitative way to define the cut is to require that the centrality of each lepton  
1789 (defined analogously to that of the third jet in equation 5.2) correspond to the lepton being within the jet  
1790 rapidity gap, or  $C_\ell < 1$  for both leptons.

1791 Figure 5.3a-c shows the  $m_{jj}$ ,  $\Delta y_{jj}$ , and  $C_{\ell 1}$  variables at the stage where all previous cuts in the se-  
1792 quence have been made. The agreement between data and Monte Carlo is good, and the bottom panels  
1793 show their power in discriminating the VBF signal from the background processes.

1794 The final signal region is also split into two bins of  $m_{jj}$ , with the first bin corresponding to  $600 \text{ GeV} <$   
1795  $m_{jj} < 1 \text{ TeV}$  and the second bin corresponding to  $m_{jj} > 1 \text{ TeV}$ . The first bin has more statistics but  
1796 also a larger contribution from background, while the second bin has lower statistics but a 1:1 signal to  
1797 background ratio.

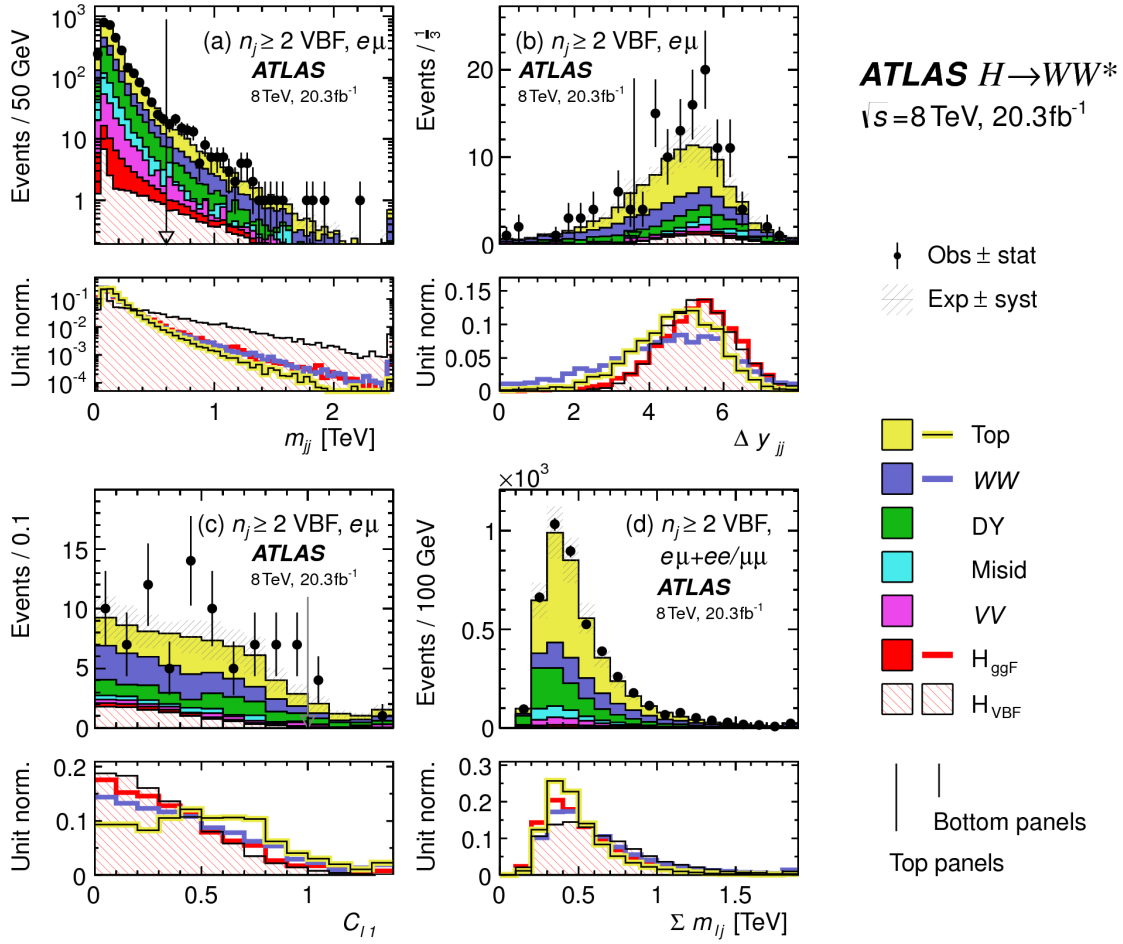


**Figure 5.3:** Distributions of (a)  $m_{jj}$ , (b)  $\Delta y_{jj}$ , (c)  $C_{\ell 1}$ , and (d)  $\sum m_{ij}$ , for the VBF analysis. The top panels compare simulation and data, while the bottom panels show normalized distributions for all background processes and signal[21].

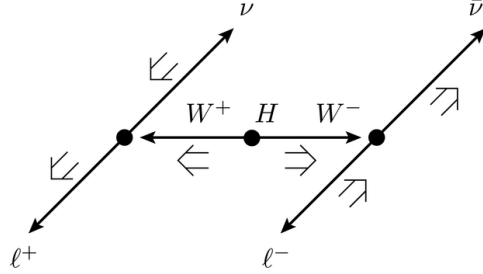


**Figure 5.4:** A cartoon of the WW final state. Momenta are represented with thin arrows, spins with thick arrows. [21]

1798    **HIGGS TOPOLOGICAL CUTS**

1799    The final state leptons will exhibit unique correlations due to the fact that they are arising from the decay  
 1800    of a spin zero resonance. In particular, the spins of the final state leptons and neutrinos must all cancel,  
 1801    as shown in figure 5.4. Because the neutrino has a left handed chirality and the anti-neutrino has a right  
 1802    handed chirality (in the massless neutrino approximation), the spin and momentum of the particles  
 1803    will be anti-aligned and aligned, respectively. In the transverse plane, the momenta of all four final state  
 1804    objects must cancel as well. With the constraint of having both the momenta and the spin alignments  
 1805    cancel, the final state kinematics strongly prefer having a small angle between the leptons in the trans-  
 1806    verse plane (low  $\Delta\phi_{\ell\ell}$ ). This angular correlation will also lead to low values of the di-lepton invariant  
 1807    mass  $m_{\ell\ell}$ . These unique signal final state kinematic correlations will be exploited to define the ultimate  
 1808    signal region.

1809    The analysis places additional requirements on the final state leptons. Two requirements on dilepton  
 1810    kinematics are made that are common with lower multiplicity jet bins as well. The angle between leptons  
 1811    in the transverse plane,  $\Delta\phi_{\ell\ell}$ , is required to be less than 1.8 radians. Additionally, the dilepton mass  $m_{\ell\ell}$   
 1812    is required to be less than 50 GeV.

1813    The cut-based analysis uses  $m_T$  as the final discriminating variable as in the ggF focused analysis. The  
 1814    optimal number of bins in  $m_T$  was found to be three bins, with the bin boundaries at 80 and 130 GeV.

1815    Table 5.7 shows the data and estimated signal and background yields from simulation as each cut de-  
 1816    scribed above is made. The table shows how each cut reduces specific backgrounds and how the overall

1817 signal to background ratio grows through the cutflow.

1818 Figure 5.5 shows an ATLAS event display of a candidate event in the final signal region.

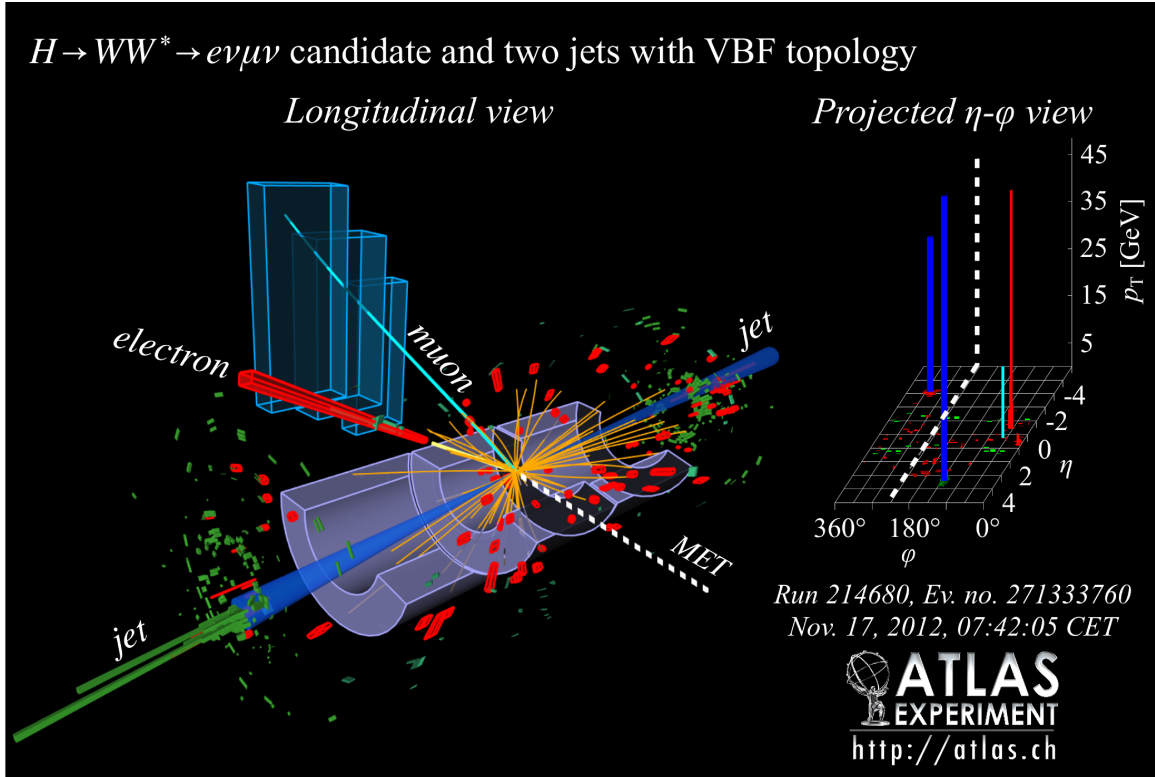


Figure 5.5: Event display of a VBF candidate event[21].

1819 5.4.3 BDT-BASED SELECTION

1820 The boosted decision tree based analysis takes a different philosophy compared to the cut-based. Rather  
1821 than cutting sequentially on many variables, the BDT analysis uses many of these variables as inputs  
1822 to the BDT and the output BDT score ( $O_{\text{BDT}}$ ) as the final discriminant. The BDT is trained with the  
1823 VBF  $H \rightarrow WW^*$  simulation as the signal samples and all other processes as background, including ggF  
1824  $H \rightarrow WW^*$  production. While the BDT based analysis is treated as a separate result, it has significant  
1825 overlap with the cut-based selection.

**Table 5.7:** Event selection for the  $n_j \geq 2$  VBF analysis in the 8 TeV cut-based analysis[21].

Selection	Summary										Composition of $N_{\text{bkg}}$							
	$N_{\text{obs}}/N_{\text{bkg}}$	$N_{\text{obs}}$	$N_{\text{bkg}}$	$N_{\text{signal}}$	$N_{\text{ggF}}$	$N_{\text{VBF}}$	$N_{\text{VH}}$	$N_{WW}^{\text{QCD}}$	$N_{WW}^{\text{EW}}$	$N_{t\bar{t}}$	$N_t$	$N_{\text{top}}$	$N_{Wj}$	$N_{jj}$	$N_{VV}$	$N_{\text{misid}}$	$N_{\text{Drell-Yan}}$	$N_{ee/\mu\mu} N_{\tau\tau}^{\text{QCD}}$
$e\mu$ sample	1.00 ± 0.00	61434	61180	85	32	26	1350	68	51810	2970	847	308	380	51	3260	46		
$n_b = 0$	1.02 ± 0.01	7818	7700	63	26	16	993	43	3000	367	313	193	273	35	2400	29		
$p_T^{\text{sum}} < 15$	1.03 ± 0.01	5787	5630	46	23	13	781	38	1910	270	216	107	201	27	2010	23		
$m_{\tau\tau} < m_Z - 25$	1.05 ± 0.02	3129	2970	40	20	9.9	484	22	1270	177	141	66	132	7.6	627	5.8		
$m_{jj} > 600$	1.31 ± 0.12	131	100	2.3	8.2	—	18	8.9	40	5.3	1.8	2.4	5.1	0.1	15	1.0		
$\Delta y_{jj} > 3.6$	1.33 ± 0.13	107	80	2.1	7.9	—	11.7	6.9	35	5.0	1.6	2.3	3.3	—	11.6	0.8		
$C_{j3} > 1$	1.36 ± 0.18	58	43	1.3	6.6	—	6.9	5.6	14	3.0	1.3	1.3	2.0	—	6.8	0.6		
$C_{\ell 1} < 1, C_{\ell 2} < 1$	1.42 ± 0.20	51	36	1.2	6.4	—	5.9	5.2	10.8	2.5	1.3	1.3	1.6	—	5.7	0.6		
$m_{\ell\ell}, \Delta\phi_{\ell\ell}, m_\tau$	2.53 ± 0.71	14	5.5	0.8	4.7	—	1.0	0.5	1.1	0.3	0.3	0.3	0.6	—	0.5	0.2		
<hr/>																		
$ee/\mu\mu$ sample	0.99 ± 0.01	26949	27190	31	14	10.1	594	37	23440	1320	230	8.6	137	690	679	16		
$n_b, p_T^{\text{sum}}, m_{\tau\tau}$	1.03 ± 0.03	1344	1310	13	8.0	4.0	229	12.0	633	86	26	0.9	45	187	76	1.5		
$m_{jj}, \Delta y_{jj}, C_{j3}, C_\ell$	1.39 ± 0.28	26	19	0.4	2.9	0.0	3.1	3.1	5.5	1.0	0.2	0.0	0.7	3.8	0.7	0.1		
$m_{\ell\ell}, \Delta\phi_{\ell\ell}, m_\tau$	1.63 ± 0.69	6	3.7	0.3	2.2	0.0	0.4	0.2	0.6	0.2	0.2	0.0	0.1	1.5	0.3	0.1		

1826 PRE-TRAINING SELECTION AND BDT INPUTS

1827 Before training, the common preselection cuts described in section 5.4.1 are applied. Additionally, the  
1828 central jet veto and outside lepton veto described in section 5.4.2 are applied. The BDT has eight input  
1829 variables, six of which are also variables that are used in the cut-based analysis. The six shared variables  
1830 are  $p_T^{\text{sum}}$ ,  $m_{jj}$ ,  $\Delta y_{jj}$ ,  $m_{\ell\ell}$ ,  $\Delta\phi_{\ell\ell}$ , and  $m_T$ . The seventh variable input in the BDT is a combination of  
1831 the variables used to do the OLV in the cut-based analysis. The BDT uses as input the sum of lepton  
1832 centralities, or  $\sum C_\ell = C_{\ell 1} + C_{\ell 2}$ . The final BDT input variable,  $\Sigma m_{\ell j}$ , is constructed to account for  
1833 the correlations between the jets and leptons in the event. It is the sum of the invariant masses of all four  
1834 possible lepton-jet combinations.

1835 Figure 5.3d shows the agreement between data and simulation for the  $\Sigma m_{\ell j}$  variable, as well as show-  
1836 ing its discriminating power. Figure 5.6 shows the distributions of the Higgs topological variables that  
1837 are shared between the cut-based and BDT analyses. Figure 5.7 shows the distributions of the VBF topo-  
1838 logical variables shared between the cut-based and BDT analyses. In both cases, the VBF yield has been  
1839 scaled by a factor of 50 to better show the shape difference compared to the backgrounds.

1840 Table ?? summarizes the cuts applied for the cut-based and analyses, as well as which variables are used  
1841 as input to the BDT.

1842 5.5 BACKGROUND ESTIMATION

1843 This section describes the procedures used to estimate backgrounds for the VBF analysis in both the  
1844 cut-based and BDT analyses.

1845 5.5.1 GENERAL STRATEGY

1846 Most of the backgrounds in the VBF analysis have shapes estimated from Monte Carlo simulation but  
1847 normalizations derived from control regions in data. In essence, a normalization factor (denoted with  
1848  $\beta$  or abbreviated as NF) is derived by scaling the MC yield in the control region to the corresponding  
1849 yield in data. Once this factor is derived, it can be used to scale the MC estimate of the background in the

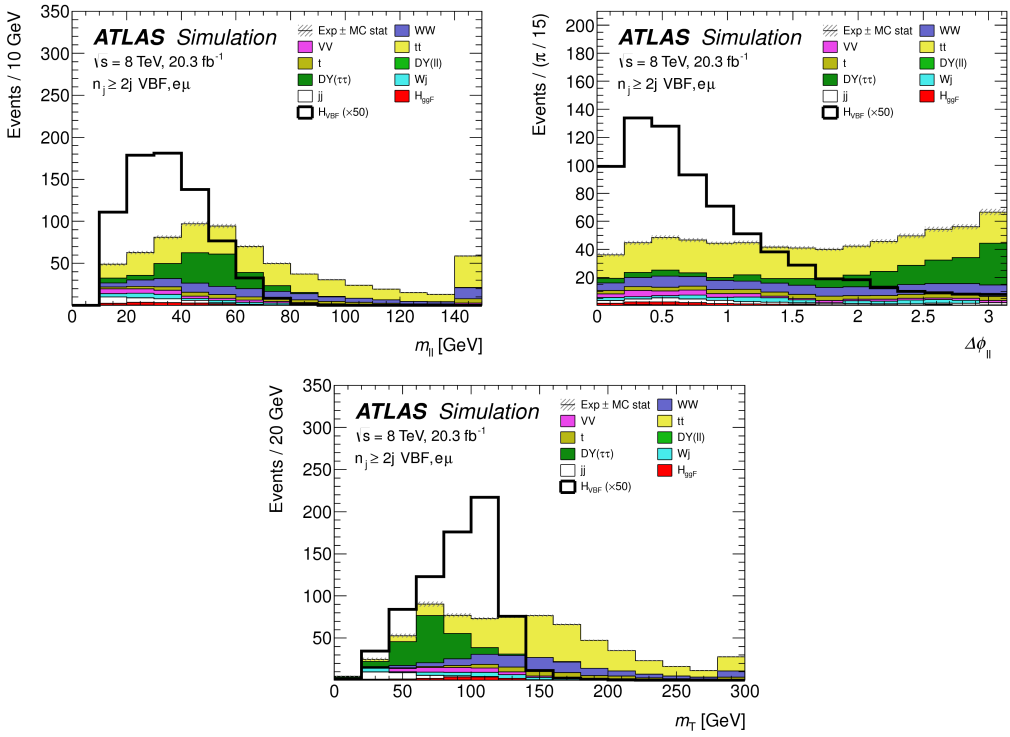


**Figure 5.6:** Distributions of  $m_{\ell\ell}$  (top left),  $\Delta\phi_{\ell\ell}$  (top right), and  $m_T$  (bottom), Higgs topology variables used in the selection requirements of the cut-based signal region and as inputs to the BDT result. These are plotted after all of the BDT pre-training selection cuts[21].

1850 signal region. This is illustrated in equation 5.3.

$$B_{\text{SR}}^{\text{est}} = B_{\text{SR}} \times \frac{N_{\text{CR}}}{B_{\text{CR}}} \equiv B_{\text{SR}} \times \beta \quad (5.3)$$

1851 Here,  $B$  denotes the MC yield prediction in the denoted region, while  $N$  denotes the observed num-  
1852 ber of events in data in the denoted region.

1853 Another way of writing the same equation, in terms of an extrapolation factor  $\alpha$  rather than a nor-  
1854 malization factor  $\beta$ . The overall calculation is exactly the same. However, when phrased in this way, it  
1855 shows how the uncertainty on the background estimation can be reduced. This is shown in equation 5.4.

$$B_{\text{SR}}^{\text{est}} = N_{\text{CR}} \times \frac{B_{\text{SR}}}{B_{\text{CR}}} \equiv N_{\text{CR}} \times \alpha \quad (5.4)$$

1856 Phrased this way, the equation shows that with enough statistics in the control region, a large theoret-

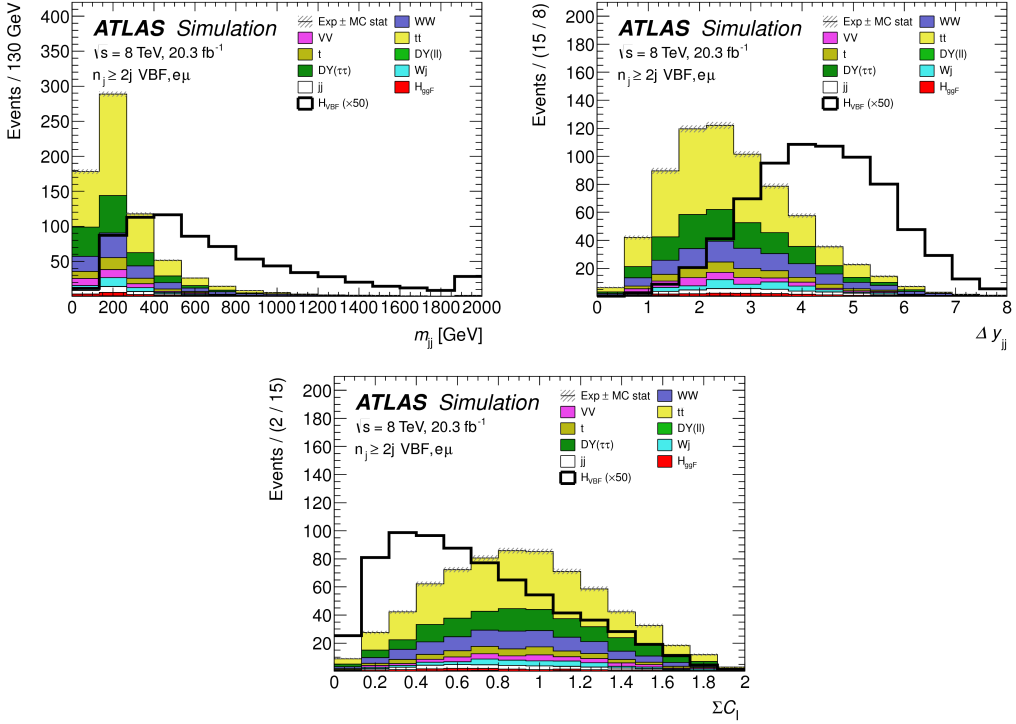


**Figure 5.7:** Distributions of  $m_{jj}$  (top left),  $\Delta y_{jj}$  (top right),  $\sum C_l$  (bottom), VBF topology variables used in the selection requirements of the cut-based signal region and as inputs to the BDT result. These are plotted after all of the BDT pre-training selection cuts[21].

ical uncertainty on the overall background yield in the signal region can be replaced by a small statistical uncertainty coming from the number of data events in the CR and a smaller theoretical uncertainty on the extrapolation from the control region to the signal region.

### 5.5.2 TOP BACKGROUND

The normalization factor  $\beta_t$  for the top background in the VBF analysis is derived in a region required to have one b-tagged jet, or  $n_b = 1$ . In the cut-based analysis, normalization factors are computed at every stage of the cutflow by applying the appropriate cuts in the CR. These NF are then applied to the  $t\bar{t}$  and single top event yields in the SR. In the BDT analysis, a single normalization factor is computed for each bin of  $O_{\text{BDT}}$  after applying the BDT pre-training cuts described previously. The computed normalization factors are derived with all flavor combinations combined in order to decrease statistical uncertainty. Additionally, in the BDT analysis, BDT bins 2 and 3 are merged for the same reason.

1868 Table 5.8 shows the evolution of the  $\beta_t$  through the cut-based selection. Table 5.9 shows the value  
 1869 of the  $\beta_t$  in each bin of  $O_{\text{BDT}}$ . In all cases, the computed factors are relatively consistent with unity,  
 1870 with the largest discrepancy coming in bin 1 of  $O_{\text{BDT}}$ . The normalization factors in the bins of  $O_{\text{BDT}}$   
 1871 are also consistent with those derived in the cut-based signal region, increasing confidence in the BDT  
 1872 estimation.

Cut	$\beta_t$
$p_T^{\text{sum}} < 15 \text{ GeV}$	$1.03 \pm 0.01$
$m_{\tau\tau} < m_Z - 25$	$1.05 \pm 0.01$
$m_{jj} > 600 \text{ GeV}$	$0.96 \pm 0.06$
$\Delta y_{jj} > 3.6$	$1.02 \pm 0.08$
CJV	$1.13 \pm 0.16$
OLV	$1.01 \pm 0.19$
$m_{jj} < 1 \text{ TeV}$	$0.94 \pm 0.19$
$m_{jj} > 1 \text{ TeV}$	$1.48 \pm 0.66$

**Table 5.8:** Top normalization factors computed at each stage of the cut-based selection. Uncertainties are statistical only.

$O_{\text{BDT}}$	$\beta_t$
Bin0	$1.09 \pm 0.02$
Bin1	$1.58 \pm 0.15$
Bin2	$0.95 \pm 0.31$
Bin3	$0.95 \pm 0.31$

**Table 5.9:** Top normalization factors computed for each bin of  $O_{\text{BDT}}$ . Uncertainties are statistical only.

1873 Figure 5.8 shows the  $m_{jj}$  and  $O_{\text{BDT}}$  distributions in the top control region. Overall the modeling  
 1874 looks consistent with the data.

1875 While these normalization factors can be computed and applied to the expected background yields  
 1876 listed in tables like table 5.7, in the end the normalization of the top background is profiled (meaning  
 1877 there is a dedicated Poisson constraint) and allowed to float in the final statistical fit.

### 1878 5.5.3 $Z/\gamma^* \rightarrow \tau\tau$ BACKGROUND

1879 In the different flavor channels, the  $Z/\gamma^* \rightarrow \tau\tau$  background is an important one. Di-tau production  
 1880 can produce an  $e\mu$  final state if each  $\tau$  lepton decays to a different flavor lepton.

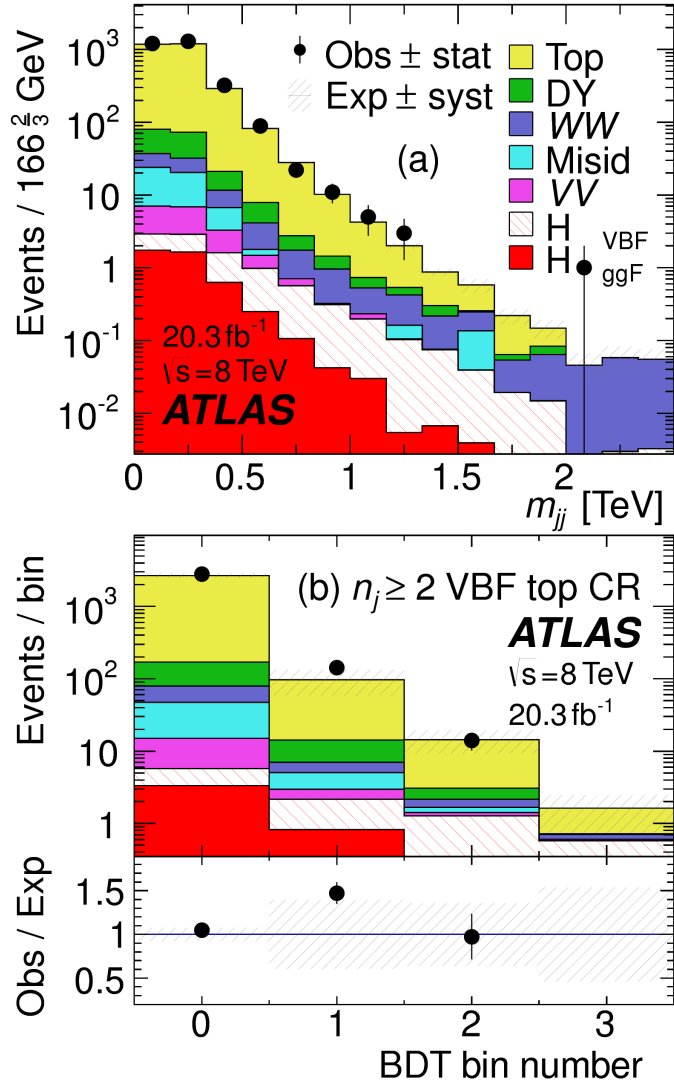


**Figure 5.8:** Distributions of  $m_{jj}$  (a) and  $O_{\text{BDT}}$  (b) in the VBF  $n_b = 1$  top CR [21].

In the BDT analysis, a single normalization factor for the background is derived. A control region is defined using the pre-training selection cuts, except requiring that  $|m_{\tau\tau} - m_Z| < 25 \text{ GeV}$  so that the region is enriched in  $Z/\gamma^* \rightarrow \tau\tau$  background. Additional requirements of  $m_{\ell\ell} < 80(75) \text{ GeV}$  in the different (same) flavor channel, as well as  $O_{\text{BDT}} > -0.48$  are applied to increase the purity of the region. The final  $\beta_{Z/\gamma^* \rightarrow \tau\tau}$  is calculated to be  $0.9 \pm 0.3$  (statistical uncertainty only). Because of the small contribution of this background in the BDT analysis and the large statistical uncertainty, no additional systematics are calculated. The final SR estimate is scaled by this  $\beta$  and not allowed to float in

1888 the fit.

1889 The cut-based corrections are a bit more involved because they need to be applied cut by cut through  
1890 the cutflow, as well as in the final signal region for the fit. The region is defined including all SR cuts  
1891 up to the  $Z/\gamma^* \rightarrow \tau\tau$  veto, which is instead made into a Z mass peak requirement as for the BDT  
1892 region. The  $m_{\ell\ell}$  cut from the BDT region is included as well. The cut-based approach aims to correct  
1893 the normalization of the  $Z/\gamma^* \rightarrow \tau\tau$  background in two ways. First, an overall normalization factor is  
1894 computed from the control region. However, the VBF topological cuts are not included in this region,  
1895 and applying them as is done in the top CR is not feasible due to limited statistics. So, instead, correction  
1896 factors (CF) to the cut efficiencies of the VBF cuts are derived in a same flavor  $Z \rightarrow \ell\ell$  control region,  
1897 which has significantly more statistics. The CF is simply the ratio of the cut efficiencies in data and MC  
1898 derived in this region. In the end, the overall background estimate is given by equation 5.5.

$$N_{Z/\gamma^* \rightarrow \tau\tau}^{\text{est}} = B_{Z/\gamma^* \rightarrow \tau\tau}^{\text{SR}} \times \beta_{\tau\tau} \times \frac{\epsilon_{\text{VBF cuts}}^{\text{data}}}{\epsilon_{\text{VBF cuts}}^{\text{MC}}} \quad (5.5)$$

1899 The hypothesis is that while the normalization correction must be derived in a dedicated region, the  
1900 efficiency of the VBF cuts should not be sensitive to the type of  $Z/\gamma^*$  process and thus the larger control  
1901 region can be exploited to derive the CF. Figure 5.9 shows a shape comparison for the  $m_{jj}$  variable in  
1902  $Z \rightarrow \tau\tau$  events in the signal region and  $Z \rightarrow \ell\ell$  events in the control region. The figure shows that the  
1903 shapes are indeed comparable and thus any CF derived in the same flavor control region can reliably be  
1904 applied in the signal region.

1905 Table 5.10 shows the overall normalization factor  $\beta_{\tau\tau}$  and the efficiency correction factors for the var-  
1906 ious VBF topological cuts. In general, the statistical uncertainties on the cut efficiency corrections are  
1907 quite good, and the MC tends to underestimate the efficiency of the VBF cuts for the  $Z/\gamma^* \rightarrow \tau\tau$  back-  
1908 ground. The overall normalization factor is also consistent with that calculated for the BDT analysis.

#### 1909 5.5.4 $Z/\gamma^* \rightarrow \ell\ell$ BACKGROUND

1910 In the same flavor channels, the  $Z/\gamma^* \rightarrow \ell\ell$  background is dominant and thus must be estimated  
1911 correctly. In both the BDT and cut-based analyses, the background is estimated using the so-called

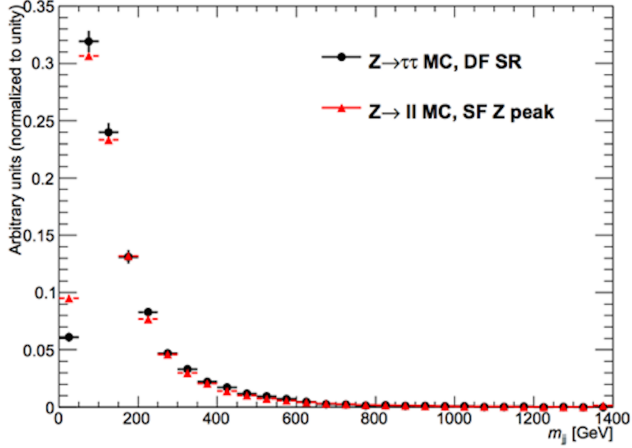


**Figure 5.9:** Comparison of  $m_{jj}$  shape in a same flavor  $Z \rightarrow \ell\ell$  control region and the VBF cut-based signal region.

$\beta_{\tau\tau}$	$0.97 \pm 0.04$
Cut	Correction factors
$m_{jj} > 600 \text{ GeV}$	$1.09 \pm 0.01$
$\Delta y_{jj} > 3.6$	$1.14 \pm 0.02$
CJV	$1.20 \pm 0.02$
OLV	$1.17 \pm 0.03$
$m_{jj} < 1 \text{ TeV}$	$1.17 \pm 0.06$
$m_{jj} > 1 \text{ TeV}$	$1.18 \pm 0.13$

**Table 5.10:**  $Z/\gamma^* \rightarrow \tau\tau$  correction factors for the VBF cut-based analysis. Uncertainties are statistical only.

“ABCD” method. The ABCD method creates four different regions by defining cuts on two variables. One of the regions (A) is the signal region, while the other regions are defined by inverting one of both of the cuts. in this case, the two variables used are  $m_{\ell\ell}$  and  $E_T^{\text{miss}}$ , because inverting either of the SR cuts on these variables will give regions rich in the  $Z/\gamma^* \rightarrow \ell\ell$  background. Figure 5.10 illustrates the general strategy for each region.

In both of the cut-based and BDT analyses, the  $Z$  peak region is defined with  $|m_{\ell\ell} - m_Z| < 15 \text{ GeV}$ . In the cut-based analysis, low  $m_{\ell\ell}$  corresponds to  $m_{\ell\ell} < 50 \text{ GeV}$  (this defines the cut-based SR) while in the BDT it is  $m_{\ell\ell} < 75 \text{ GeV}$ . In the cut-based, high and low  $E_T^{\text{miss}}$  are defined as opposite ends of the 55 GeV cut applied for the signal region definition. The BDT low  $E_T^{\text{miss}}$  region is between 25 and 45 GeV, while the high  $E_T^{\text{miss}}$  region is  $E_T^{\text{miss}} > 45 \text{ GeV}$ .

Once the regions are defined, the final signal region background estimate is done by taking the esti-

<b>Region A (SR)</b>	<b>Region C</b>
High $E_T^{\text{miss}}$	High $E_T^{\text{miss}}$
Low $m_{\ell\ell}$	Z peak
<b>Region B</b>	<b>Region D</b>
Low $E_T^{\text{miss}}$	Low $E_T^{\text{miss}}$
Low $m_{\ell\ell}$	Z peak

**Figure 5.10:** General illustration of the ABCD region definitions for  $Z/\gamma^* \rightarrow \ell\ell$  background estimation.

1923 mate in region B and extrapolating it to the signal region (A) by multiplying it by the ratio of regions  
 1924 C and D. Effectively, the  $Z$  peak region is used to estimate the efficiency of the  $E_T^{\text{miss}}$  cut in data, and  
 1925 then this efficiency is applied in the low  $m_{\ell\ell}$  region. An additional correction is also applied for the non-  
 1926 closure of the method in MC. This is summarized in equations 5.6 and 5.7.

$$N_{Z/\gamma^* \rightarrow \ell\ell}^{\text{SR}} = N_{Z/\gamma^* \rightarrow \ell\ell}^{\text{B}} \times \frac{N_{Z/\gamma^* \rightarrow \ell\ell}^{\text{C}}}{N_{Z/\gamma^* \rightarrow \ell\ell}^{\text{D}}} \times f_{\text{corr}} \quad (5.6)$$

$$f_{\text{corr}} = \frac{B_{\text{MC}}^{\text{A}}/B_{\text{MC}}^{\text{B}}}{B_{\text{MC}}^{\text{C}}/B_{\text{MC}}^{\text{D}}} \quad (5.7)$$

1927 Here, the  $N$  refer to data yields in each region with the non  $Z/\gamma^*$  backgrounds subtracted, while  $B$   
 1928 refer to the  $Z/\gamma^*$  yields in MC in each region.

1929 A normalization factor  $\beta_{\ell\ell}$  is computed for each analysis as the ratio of the predicted data yield to  
 1930 the MC yield in the SR. The shape of the BDT distribution is taken from data region B, while the shape  
 1931 of the  $m_T$  distribution in the cut-based analysis is taken from  $Z/\gamma^*$  MC in the SR. The values of the  
 1932  $\beta_{\ell\ell}$  in the cut-based and BDT analyses from this method are summarized in table 5.11. They are quite  
 1933 consistent with one another within the statistical uncertainties. In the cut-based analysis, the same cut  
 1934 efficiency correction factors shown in table 5.10 are also applied (in product with the  $\beta_{\ell\ell}$ ) in the same  
 1935 flavor channels to this background, as they were derived in the  $Z$  peak region.

	$\beta_t$
BDT Bin 1	$1.01 \pm 0.15$
BDT Bin 2	$0.89 \pm 0.28$
Cut-based	$0.81 \pm 0.21$

**Table 5.11:**  $Z/\gamma^* \rightarrow \ell\ell$  normalization factors for cut-based and BDT analyses. Uncertainties are statistical only.

### 1936 5.5.5 $WW$ AND OTHER DIBOSON BACKGROUNDS

1937 The  $WW$  and other diboson backgrounds have both their shape and normalization taken from MC  
 1938 simulation. They are validated in dedicated control regions and found to agree with data well.  
 1939 As  $WW$  is the largest of these backgrounds and is irreducible, validating the estimate is of particular  
 1940 importance. The validation region is constructed by requiring the pre-selection cuts on leptons and  $m_{\ell\ell}$ ,  
 1941  $n_b = 0$ , and  $m_T > 100$  GeV. The  $m_{T2}$  variable[?] is an additional discriminant that will isolate  
 1942 the  $WW$  background, and a requirement of  $m_{T2} > 160$  GeV is placed to define the  $WW$  validation  
 1943 region. This cut gives a 60% purity for the validation region. The derived normalization factor in the  
 1944 region is  $1.15 \pm 0.19$  and is thus consistent with unity. Figure 5.11 shows the  $m_{T2}$  distribution and how  
 1945 it distinguishes the  $WW$  background.

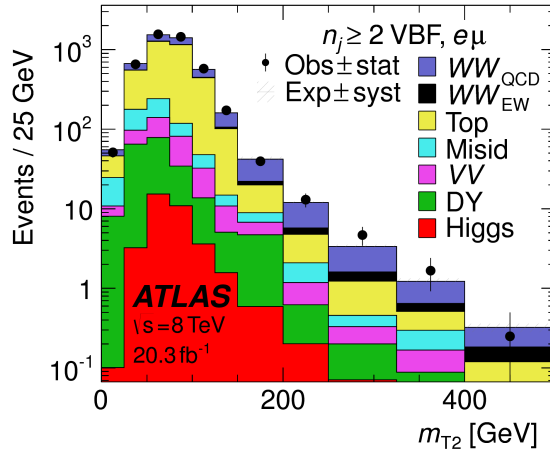


**Figure 5.11:** Distribution of  $m_{T2}$  in the  $WW$  validation region of the VBF analysis[21].

1946 5.5.6 HIGGS PRODUCTION VIA GLUON-GLUON FUSION

1947 Because this analysis is dedicated to measuring the VBF contribution to Higgs production, the com-  
1948 ponent of Higgs production from gluon-gluon fusion is treated as a background. The shape is taken  
1949 directly from simulation, using the generators described in table 5.4. In the final combined fit of all dif-  
1950 ferent signal regions, the normalization is controlled by either a combined signal strength parameter  $\mu$ ,  
1951 which controls the normalization of both ggF and VBF production, or a separate parameter  $\mu_{\text{ggF}}$  de-  
1952 pending on the interpretation being presented in the final results.

1953 5.5.7 BACKGROUNDS WITH MISIDENTIFIED LEPTONS

1954 As discussed previously, the  $W + \text{jets}$  and QCD multijet backgrounds are derived with fully data-driven  
1955 methods. These backgrounds do not make a large contribution to the final VBF signal region but their  
1956 estimation methods are discussed briefly here.

1957  $W + \text{jets}$  BACKGROUND

1958 The  $W + \text{jets}$  background enters the signal region by having one of the jets mis-reconstructed as a lep-  
1959 ton. The background is estimated by constructing a control sample with two leptons, where one lepton  
1960 passes the usual lepton quality cuts but the second lepton fails one of those cuts (also known as the “anti-  
1961 identified” lepton). This control region is rich in the  $W + \text{jets}$  contribution because if a second lepton is  
1962 reconstructed in a  $W + \text{jets}$  event it is likely to be poor quality. The purity of this  $W + \text{jets}$  control sample  
1963 is 85% to 90% depending on the exact configuration of leptons in the final state.

1964 The signal region estimate of  $W + \text{jets}$  is estimated by extrapolation from the control sample to the sig-  
1965 nal region using extrapolation factors derived in a  $Z + \text{jets}$  control sample in data. The extrapolation fac-  
1966 tor is the ratio of the number of lepton candidates satisfying all quality criteria to the number of lepton  
1967 candidates anti-identified. This ratio is measured in bins of  $p_T$  and  $\eta$ . Thus, the final signal region esti-  
1968 mate (binned as the extrapolation factor is binned) is simply the number of events in the anti-identified  
1969 lepton control sample multiplied by the extrapolation factor derived from the  $Z + \text{jets}$  control sample.  
1970 Figure 5.12 shows the extrapolation factors derived for electrons and muons.

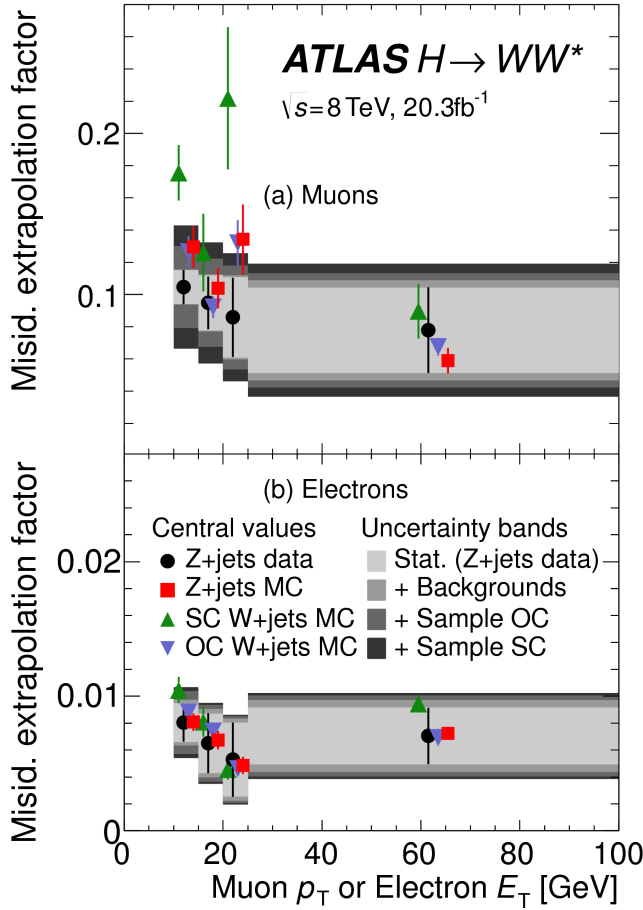


**Figure 5.12:** Extrapolation factors for the  $W+jets$  estimate derived for muons (a) and electrons (b) as a function of lepton  $p_T$ [21].

1971    QCD MULTIJET BACKGROUND

1972    The method for estimating the multijet background is very similar to the  $W+jets$  estimation method.  
 1973    The control sample in this case has two anti-identified leptons but otherwise satisfies all signal region  
 1974    requirements. The extrapolation factor is estimated from a multijet sample and applied twice to the  
 1975    control sample.

1976    5.5.8 BACKGROUND COMPOSITION IN FINAL SIGNAL REGION

1977    After all of these estimation procedures, the final signal region composition can be calculated. The esti-  
 1978    mated yields are all shown in table 5.7. Figure 5.13 shows the relative percentages of the different back-

1979 ground for the different flavor and same flavor final states. In  $e\mu$ , the leading backgrounds are top back-  
 1980 grounds, ggF Higgs, and SM  $WW$  production. In  $ee/\mu\mu$ , the leading background is Drell-Yan, fol-  
 1981 lowed by top and ggF Higgs.

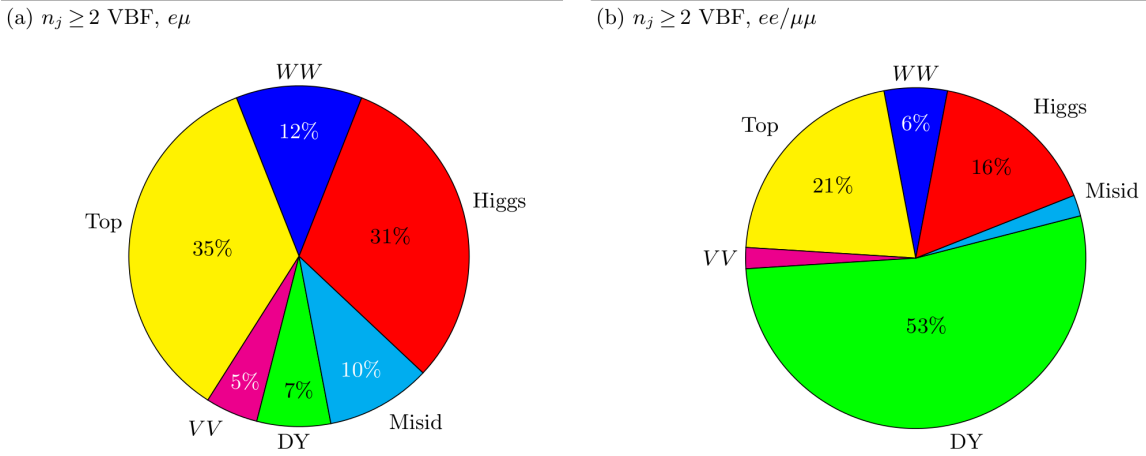


Figure 5.13: Background composition in final VBF signal region[21].

## 1982 5.6 SYSTEMATIC UNCERTAINTIES

1983 There are two main types of systematic uncertainties that are assessed for the analysis. First, theoreti-  
 1984 cal uncertainties associated with the various signal and background yield estimates are discussed. Then,  
 1985 experimental uncertainties due to detector effects are shown. Normalization uncertainties refer to uncer-  
 1986 tainties that affect the cross section of the process in question in the signal region being probed. Shape  
 1987 uncertainties refer to systematic uncertainties that affect the shape of the final discriminating variable  
 1988 (either  $m_T$  or  $O_{BDT}$ ).

### 1989 5.6.1 THEORETICAL UNCERTAINTIES

1990 There are four main components to theoretical uncertainties assigned to signal and background pro-  
 1991 cesses taken from Monte Carlo. Each one is a different source of variation in the overall acceptance for  
 1992 that process. The first involves variation of the QCD renormalization and factorization scales used in  
 1993 the calculation. In this case, the two scales are varied independently and simultaneously by factors of  
 1994 two high or low and quantifying the resulting variation in normalization and shape for the process. This

approximates the correction to the cross section that would come from including the next order of the QCD calculation (referred to as scale uncertainty). Next, there is an uncertainty associated with the PDF set used in generating the events. The uncertainty eigenvectors for the given PDF set are studied, and the envelope of maximal variation is taken as an uncertainty. Finally, there are two uncertainties associated with the choice of MC software (referred to as PDF uncertainty). An uncertainty associated with the generator chosen for the hard scattering process is evaluated by keeping the parton showering software constant but varying the matrix element generator and taking the maximal variation as an uncertainty (referred to as the generator uncertainty). The converse variation can also be done, where the matrix element generator remains constant and the generator used for the underlying event/parton shower modeling is varied (referred to as the UE/PS uncertainty). In cases where the background is normalized in a control region, the systematic uncertainty arises from variations of the extrapolation factor  $\alpha$  between the CR and the SR, which can affect the normalization of the background in the SR.

There are two additional uncertainties that are applied to the Higgs processes as well. First, there are uncertainties assigned to the Higgs total production cross section. Then, there are uncertainties assigned based on the fact that the analysis is done in exclusive jet bins and it is possible for signal events to migrate from one bin to the next depending on the presence or absence of jets. These are assigned using the Jet Veto Efficiency (JVE) procedure[?] for ggF events and the Stewart-Tackmann (ST) method[87] for VBF production.

Table 5.12 shows the total theory uncertainties on the backgrounds in the cut-based analysis. These are the sum in quadrature of the uncertainties from each of the variations described above.

Process	Theory syst. (%)
ggF $H$	48
Top	26
QCD $WW$	37
$Z/\gamma^* \rightarrow \tau\tau$	6.1

**Table 5.12:** Systematic uncertainties for various processes in the cut-based VBF analysis, given in units of % change in yield.  
Values are given for the low  $m_{jj}$  signal region.

Figures 5.14 and 5.15 show the variations in the extrapolation factor from the PDF and QCD uncertainties on the top background estimate, binned in  $m_T$ , for the cut-based analysis. In both cases, there

2017 was no significant shape uncertainty but normalization uncertainties were assigned according to the  
 2018 maximal variation. These uncertainties enter into the 26% total uncertainty on top quoted in table 5.12.  
 2019 While the estimate for the same-flavor  $Z/\gamma^* \rightarrow \ell\ell$  background is data-driven, there is still a sys-  
 2020 tematic uncertainty taken for the non-closure of the method in Monte Carlo. This is taken as the max-  
 2021 imum of the deviation of the non-closure factor  $f_{\text{corr}}$  from unity and its uncertainty, or  $\max(|1 -$   
 2022  $f_{\text{corr}}|, \delta f_{\text{corr}})$ . For the cut-based analysis this non-closure uncertainty 23%, while for the BDT analy-  
 2023 sis it is 17%.

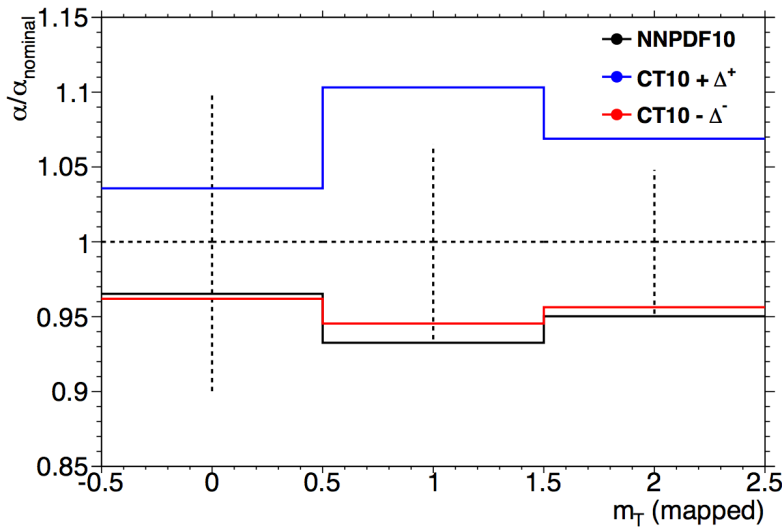
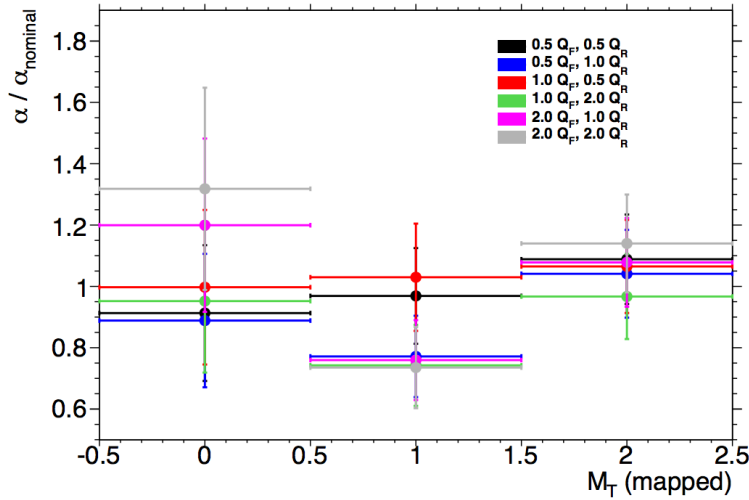


Figure 5.14: Variations in the top background extrapolation factor in the cut-based analysis due to PDF uncertainties, binned in  $m_T$ .

### 2024 5.6.2 EXPERIMENTAL UNCERTAINTIES

2025 In this analysis, the theoretical uncertainties end up being the most dominant, but there are some ex-  
 2026 perimental uncertainties that make a contribution as well. The first is the uncertainty on the measured  
 2027 integrated luminosity, which affects backgrounds whose normalization is taken from MC and is mea-  
 2028 sured to be 2.8% in the 8 TeV dataset [88]. The dominant sources of uncertainty overall are uncertainties  
 2029 on the jet energy scale and resolution and the  $b$ -tagging efficiency. Additional sources include lepton  
 2030 uncertainties on identification, resolution, and trigger efficiency, as well as uncertainties on the missing  
 2031 transverse momentum .



**Figure 5.15:** Variations in the top background extrapolation factor in the cut-based analysis due to QCD scale uncertainties, binned in  $m_T$ .

2032     The jet energy scale uncertainty is split into several independent components, including jet-flavor  
 2033     dependent calorimeter response uncertainties, uncertainties on modeling of pile-up interactions, uncer-  
 2034     tainties on extrapolation from the central to forward detector regions, and MC non-closure [89]. The  
 2035     uncertainty on energy scale for jets used in this analysis ranges from 1% to 7% depending on the jet  $p_T$   
 2036     and  $\eta$ . The jet energy resolution varies from 5% to 20%, with uncertainties ranging from 2% to 40%  
 2037     (the largest uncertainties occurring at the selection threshold).

2038     The b-tagging efficiency is independently measured in data samples enriched in dileptonic decays of  
 2039      $t\bar{t}$  events or in events where a muon is reconstructed in the vicinity of a jet[90, 91]. The efficiencies and  
 2040     their uncertainties are binned in  $p_T$  and decomposed into uncorrelated components using an eigenvec-  
 2041     tor method[? ]. Uncertainties on the efficiency range from 1% to 7.8%. The uncertainty on the rate of  
 2042     misidentification of  $c$ -jets as  $b$ -jets ranges from 6-14%, while the uncertainty on the rate of light jet mis-  
 2043     tagging ranges from 9-19% depending on  $p_T$  and  $\eta$ .

2044     The total experimental uncertainties on different signal and background components are summa-  
 2045     rized in table 5.13. They are compared to the level of other statistical and systematic uncertainties as well.  
 2046     Overall, the experimental uncertainties are sub-dominant compared to the statistical and theoretical  
 2047     uncertainties.

Sample	Total error	Stat. error	Expt. syst. err.	Theo. syst. err.
$n_j \geq 2$ VBF-enriched				
$N_{\text{sig}}$	13	-	6.8	12
$N_{\text{bkg}}$	9.2	4.7	6.4	4.5
$N_{WW}$	32	-	14	28
$N_{\text{top}}$	15	9.6	7.6	8.5
$N_{\text{misid}}$	22	-	12	19
$N_{VV}$	20	-	12	15
$N_{\tau\tau} (\text{DY})$	40	25	31	2.9
$N_{ee/\mu\mu} (\text{DY})$	19	11	15	-

**Table 5.13:** Composition of the post-fit uncertainties (in %) on the total signal ( $N_{\text{sig}}$ ), total background ( $N_{\text{bkg}}$ ), and individual background yields in the VBF analysis[21].

## 2048 5.7 RESULTS

2049 While the combined results of all the  $H \rightarrow WW^*$  sub-analyses will be discussed in the next chapter, this  
 2050 section presents the results of the VBF specific analysis and interpretations.

2051 As table 5.7 shows, the final cut-based signal region contains 20 events in data with  $m_T < 150$  GeV,  
 2052 14 coming from the  $e\mu$  channel and 6 coming from the  $ee + \mu\mu$  channel. The BDT analysis has many  
 2053 more candidates due to its looser selection, and the yields in each bin of  $O_{\text{BDT}}$  are shown in table 5.14.

2054 Figure 5.16(a) shows the final distribution of data candidates compared to the expected  $m_T$  distri-  
 2055 bution for signal and background. The data are very consistent with a VBF Higgs hypothesis. Fig-  
 2056 ure 5.16(b) shows where the data candidates fall in the two-dimensional binning of  $m_T$  and  $m_{jj}$  used  
 2057 in the fit for the cut-based analysis.

2058 Figure 5.17 shows the distributions of  $O_{\text{BDT}}$  and  $m_T$  in the VBF BDT analysis. Again the data are  
 2059 quite consistent with a VBF Higgs hypothesis.

2060 Because the cut-based result is used as a validation for the BDT analysis and the two signal regions are  
 2061 not fully orthogonal, it is interesting to explore which events overlap between the two analyses. Of the  
 2062 twenty events in the cut-based signal region, only seven were not selected by the BDT analysis, while the  
 2063 other thirteen also enter the BDT signal region. Figure ?? shows where the different analysis candidates  
 2064 lie in the  $m_{jj}$ - $m_T$  plane. This shows clearly that the advantage of the BDT analysis is that it can extract

(a) Before the BDT classification

Selection	Summary						Composition of $N_{\text{bkg}}$											
	$N_{\text{obs}}/N_{\text{bkg}}$	$N_{\text{obs}}$	$N_{\text{bkg}}$	$N_{\text{signal}}$	$N_{\text{ggF}}$	$N_{\text{VBF}}$	$N_{\text{VH}}$	$N_{\text{WW}}$	$N_{\text{WW}}^{\text{NEW}}$	$N_{\text{WW}}^{\text{QCD}}$	$N_t$	$N_{\text{missid}}$	$N_{Wj}$	$N_{ij}$	$N_{VV}$	$N_{e\mu/\mu e}$	$N_{\tau\tau}^{\text{QCD}}$	$N_{\tau\tau}^{\text{NEW}}$
$e\mu$ sample	$1.04 \pm 0.04$	718	689	13	15	2.0	90	II	327	42	29	23	31	—	2.2	130	2	—
$ee/\mu\mu$ sample	$1.18 \pm 0.08$	469	397	6.0	7.7	0.9	37	3	132	17	5.2	1.2	10.1	168	23	1	—	—

(b) Bins in  $O_{\text{BDT}}$ 

$e\mu$ sample	Bins in $O_{\text{BDT}}$																	
	Bin 0 (not used)	Bin 1	Bin 2	Bin 3	Bin 4	Bin 5	Bin 6	Bin 7	Bin 8	Bin 9	Bin 10	Bin 11	Bin 12	Bin 13	Bin 14	Bin 15	Bin 16	Bin 17
$ee/\mu\mu$ sample	$1.91 \pm 0.08$	396	345	3.8	1.3	0.8	33	2	123	16	4.1	1.1	8.8	137	20.5	0.5	—	—
Bin 0 (not used)	$0.82 \pm 0.14$	53	45	1.5	2.2	0.1	3.0	0.5	10.4	1.8	0.8	0.2	0.9	26	1.7	0.1	—	—
Bin 1	$1.77 \pm 0.49$	14	7.9	0.6	2.5	—	0.8	0.3	1.1	0.2	0.2	—	0.3	4.4	0.3	0.1	—	—
Bin 2	$6.52 \pm 2.87$	6	0.9	0.2	1.7	—	0.1	0.2	0.2	—	—	—	—	0.7	—	—	—	—
Bin 3	$5.41 \pm 2.32$	6	1.1	0.4	3.1	—	0.3	0.2	0.3	0.1	—	—	0.1	—	0.1	0.1	0.1	0.1

**Table 5.14:** Event selection for the VBF BDT analysis. The event yields in (a) are shown after the preselection and the additional requirements applied before the BDT classification (see text). The event yields in (b) are given in bins in  $O_{\text{BDT}}$  after the classification[21].

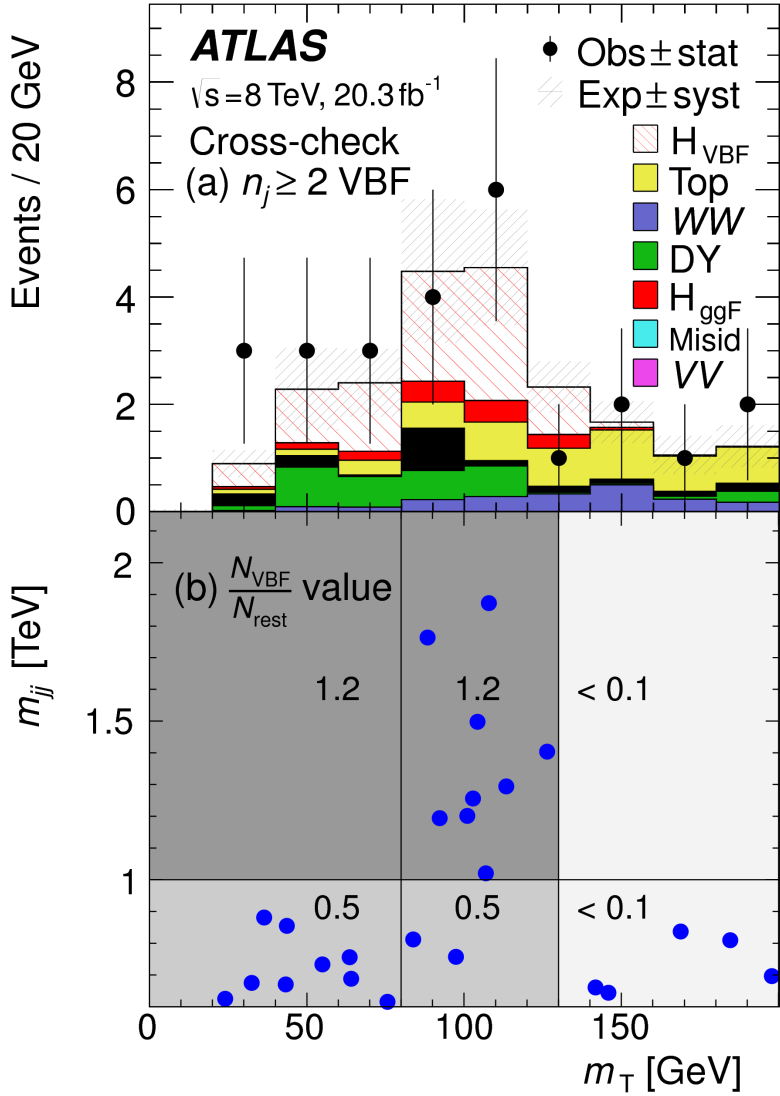


**Figure 5.16:** Postfit distributions in the cut-based VBF analysis. Panel (a) shows the one-dimensional  $m_T$  distribution, while (b) shows the data candidates split into the bins of  $m_T$  and  $m_{jj}$  used in the final fit[21].

signal candidates lower  $m_{jj}$  region due to its ability to recognize correlations with other variables.  
 While the context of these results in the broader  $H \rightarrow WW^*$  statistical analysis will be presented in the next chapter, the significance of the VBF observation can be shown here. In the BDT analysis, the expected signal significance was  $2.7\sigma$ , while the observed significance was  $3.1\sigma$ . In the cut-based analysis, the expected significance was  $2.1\sigma$  and the observed significance was  $3.0\sigma$ . The compatibility between these two results can be evaluated by computing the probability of observing a larger difference

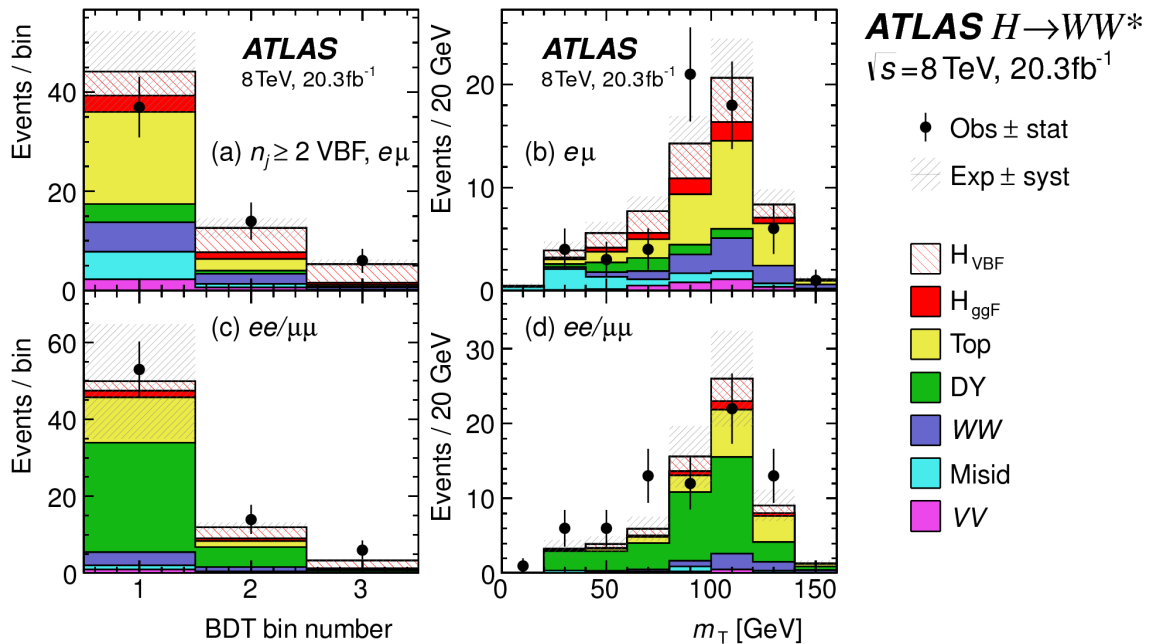


Figure 5.17: Postfit distributions in the BDT VBF analysis[21].

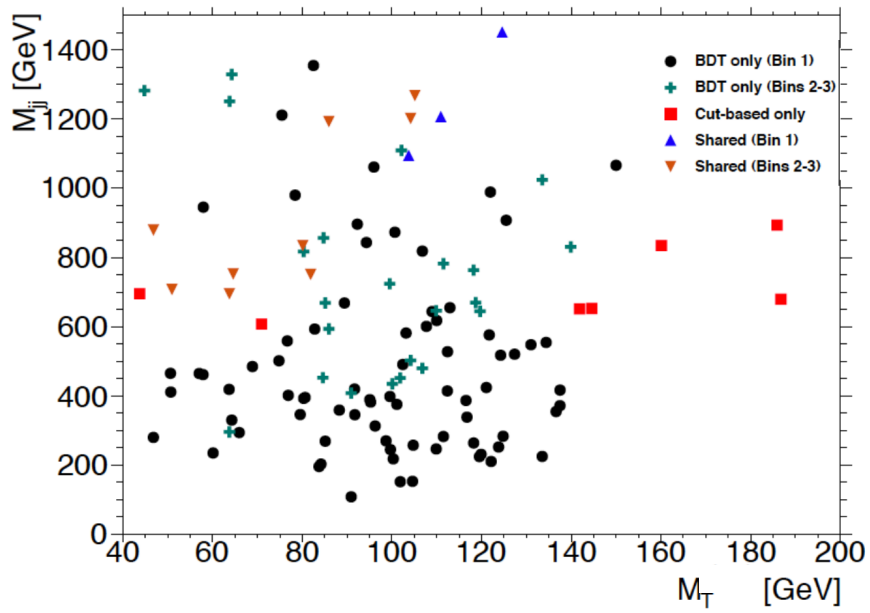


Figure 5.18: Overlap between cut-based and BDT VBF signal region candidates in the  $m_{jj}$ - $m_T$  plane.

2071 in  $Z_0$  values than the one measured. Using toy Monte Carlo with the ggF signal strength fixed to unity  
2072 and considering only statistical uncertainties, this probability is computed to be 79%, indicating good  
2073 agreement between the analyses.

2074 This result represents the first observation of the vector boson fusion production of a Higgs boson.

*The feeling is less like an ending than just another  
starting point.*

Chuck Palahniuk

# 6

2075

2076

## Combined Run I $H \rightarrow WW^* \rightarrow \ell\nu\ell\nu$

2077

## results

2078 6.1 INTRODUCTION

2079 In the final statistical analysis of  $H \rightarrow WW^* \rightarrow \ell\nu\ell\nu$ , the dedicated gluon-gluon fusion and vector  
2080 boson fusion sensitive signal regions are all combined into a single fit to determine the main parameters  
2081 of interest, the Higgs signal strength  $\mu$  and mass  $m_H$ . Therefore, while the specific requirements applied  
2082 for the VBF sensitive analysis are discussed in chapter 5, the final measurement of these parameters can  
2083 only be discussed in combination with the results of the ggF dedicated analysis. For example, because  
2084 ggF Higgs production is considered a background in the VBF analysis, the ggF dedicated signal regions  
2085 can actually constrain the normalization of this background in the VBF dedicated region.

2086 This chapter presents the combined interpretation of results in the  $H \rightarrow WW^* \rightarrow \ell\nu\ell\nu$  analysis

SR category $i$			Fit var.
$n_j$ , flavor	$\otimes m_{\ell\ell}$	$\otimes p_T^{\ell 2}$	
$n_j = 0$			
$e\mu$	$\otimes [10, 30, 55]$	$\otimes [10, 15, 20, \infty]$	$\otimes [e, \mu]$
$ee/\mu\mu$	$\otimes [12, 55]$	$\otimes [10, \infty]$	$m_T$
$n_j = 1$			
$e\mu$	$\otimes [10, 30, 55]$	$\otimes [10, 15, 20, \infty]$	$\otimes [e, \mu]$
$ee/\mu\mu$	$\otimes [12, 55]$	$\otimes [10, \infty]$	$m_T$
$n_j \geq 2$ ggF			
$e\mu$	$\otimes [10, 55]$	$\otimes [10, \infty]$	$m_T$
$n_j \geq 2$ VBF			
$e\mu$	$\otimes [10, 50]$	$\otimes [10, \infty]$	$O_{BDT}$
$ee/\mu\mu$	$\otimes [12, 50]$	$\otimes [10, \infty]$	$O_{BDT}$

**Table 6.1:** All signal regions definitions input into final statistical fit[21].

for gluon fusion and vector boson fusion Higgs production. First, the results of the dedicated gluon fusion search are presented. Then, a comparison of the individual production mode signal strengths ( $\mu_{ggF}$  and  $\mu_{VBF}$  and a measurement of the combined signal strength ( $\mu$ ) are shown. Subsequently, the measured values of the Higgs couplings to fermions and vector bosons is presented. Finally, the cross section measurement for ggF and VBF production are shown.

## 6.2 RESULTS OF DEDICATION GLUON FUSION $H \rightarrow WW^* \rightarrow \ell\nu\ell\nu$ SEARCH

The details of the dedicated gluon fusion  $H \rightarrow WW^* \rightarrow \ell\nu\ell\nu$  search are not discussed in this thesis and instead left to more comprehensive sources[21]. However, a brief summary of the results are essential for describing the results of the full analysis and interpreting the results of the dedicated VBF search in this broader context.

Table 6.1 shows the individual signal regions that were input into the final statistical fit. The ggF dedicated bins use  $m_T$  as their discriminating variable and are separated into bins of  $p_T$  of the subleading lepton as well. The VBF dedicated bin uses the  $O_{BDT}$  distribution as its final discriminant.

Table 6.2 shows the yields in the various signal regions in both data and expected signal and back-

2101 grounds. The yields for signal and background are all scaled according to the final normalizations calcu-  
 2102 lated in the fit.

	$N_{\text{obs}}$	$N_{\text{bkg}}$	$N_{\text{ggF}}$	$N_{\text{VBF}}$
$n_j = 0$	3750	$3430 \pm 90$	$300 \pm 50$	$8 \pm 4$
$n_j = 1$	1596	$1470 \pm 40$	$102 \pm 26$	$17 \pm 5$
$n_j \geq 2, \text{ggF } e\mu$	1017	$960 \pm 40$	$37 \pm 11$	$13 \pm 1.4$
$n_j \geq 2, \text{VBF}$	130	$99 \pm 9$	$7.7 \pm 2.6$	$21 \pm 3$

Table 6.2: Post-fit yields in the different ggF and VBF dedicated signal regions[21].

2103 Figure 6.1 shows the final post-fit  $m_T$  distribution in the  $n_j \leq 1$  regions. The data are very consistent  
 2104 with the hypothesis of ggF Higgs production.

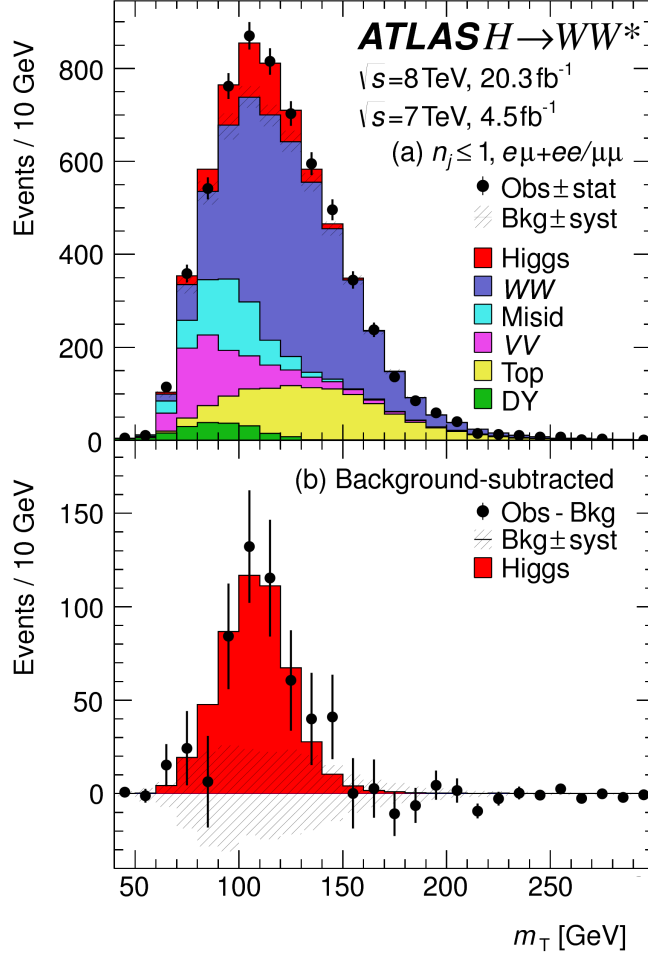


Figure 6.1: Post-fit  $m_T$  distribution in the  $n_j \leq 1$  regions[21].

2105 These yields are used as input, along with the VBF results in chapter 5, for the physical interpretation  
2106 of results presented in subsequent sections.

2107 **6.3 SIGNAL STRENGTH MEASUREMENTS IN ggF AND VBF PRODUCTION**

2108 When all of the signal regions are combined in the fit, there can be a combined measurement of the sig-  
2109 nal strength as well as the individual ggF and VBF signal strengths. The combined signal strength is the  
2110 ratio of the sum of the gluon fusion and VBF cross sections to the theory prediction, or a singal strength  
2111 for the total Higgs production cross section that this analysis is sensitive to. The final measured com-  
2112 bined signal strength  $\mu$  is measured shown in equation 6.1.

$$\begin{aligned} \mu &= 1.09 \quad {}^{+0.16}_{-0.15} \text{ (stat.)} \quad {}^{+0.08}_{-0.07} \left( \begin{array}{l} \text{expt} \\ \text{syst} \end{array} \right) \quad {}^{+0.15}_{-0.12} \left( \begin{array}{l} \text{theo} \\ \text{syst} \end{array} \right) \quad \pm 0.03 \left( \begin{array}{l} \text{lumi} \\ \text{syst} \end{array} \right) \\ &= 1.09 \quad {}^{+0.16}_{-0.15} \text{ (stat)} \quad {}^{+0.17}_{-0.14} \text{ (syst)} \\ &= 1.09 \quad {}^{+0.23}_{-0.21}. \end{aligned} \tag{6.1}$$

2113 Figure 6.2 gives the best fit signal strength  $\hat{\mu}$  as a function of hte hypothesized Higgs mass. The value  
2114 at 125.36 GeVcorresponds to the  $\mu$  quoted in equation 6.1. This value of the Higgs mass is used because  
2115 it is the most precise mass measurement from ATLAS, a result of the combined  $\gamma\gamma$  and  $ZZ$  mass mea-  
2116 surements[? ].

2117 As explained in chapter 3, a probability  $p_0$  can be computed using the test statistic  $q_0$  to quantify the  
2118 probability that the background could fluctuate to produce an excess at least as large as the one observed  
2119 in the data. The local  $p_0$  value is shown in figure 6.3 as a function of  $m_H$ . The minimum  $p_0$  value is  
2120 at  $m_H = 130$  GeV and coresponds to a significance of  $6.1\sigma$ . The curve is relatively flat and the sig-  
2121 nificance is the same at 125.36 GeVwithin the quoted precision. The expected significance for a signal  
2122 with strength  $\mu = 1.0$  is  $5.8\sigma$ . This represents the first discovery level significance measurement in the  
2123  $H \rightarrow WW^* \rightarrow \ell\nu\ell\nu$  analysis.

2124 All the results presented so far in this section have been for the combined gluon fusion and VBF pro-  
2125 duction modes. However, each signal strength can be calculated separately in the likelihood as well.  
2126 There are two ways to do this. First, the likelihood can be parameterized in terms of a single parameter,

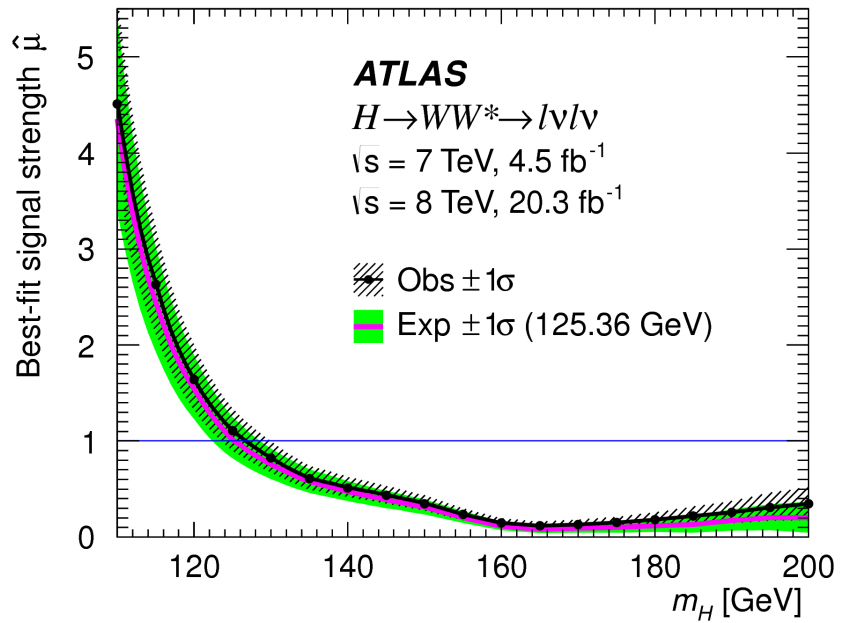


Figure 6.2: Best fit signal strength  $\hat{\mu}$  as a function of hypothesized  $m_H$ [21].

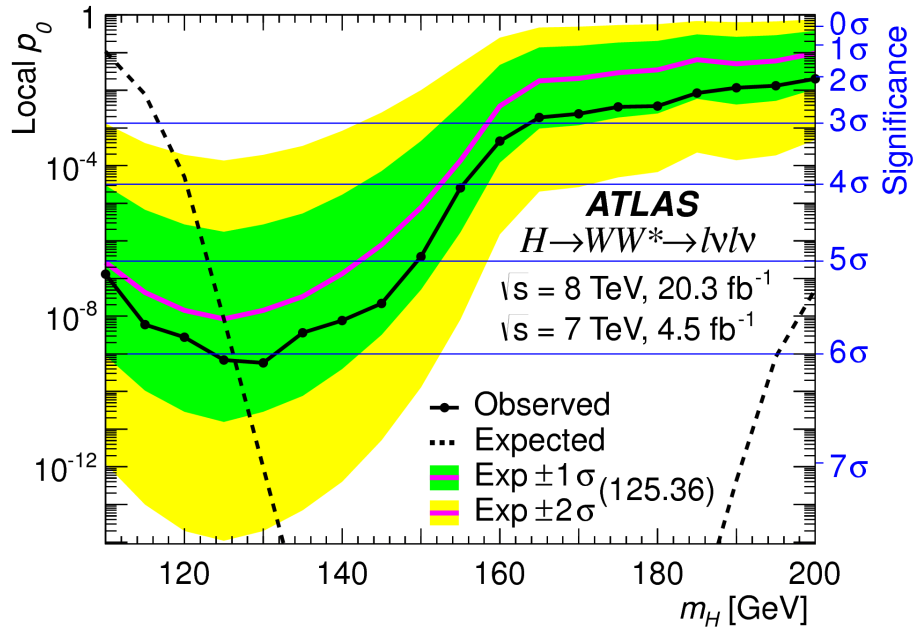
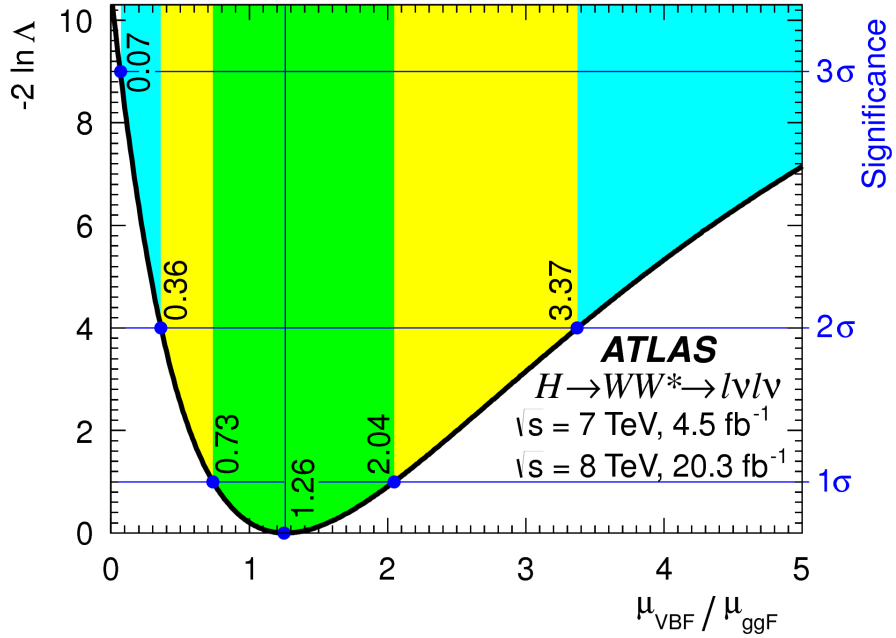


Figure 6.3: Local  $p_0$  as a function of  $m_H$ [21].

<sup>2127</sup> the ratio of the VBF and gluon fusion signal strengths. With this method, the significance of the VBF  
<sup>2128</sup> observation can be evaluated. Figure 6.4 shows the likelihood as a function of the ratio  $\mu_{\text{VBF}}/\mu_{\text{ggF}}$ .



**Figure 6.4:** Likelihood as a function of  $\mu_{\text{VBF}} / \mu_{\text{ggF}}$ [21].

2129     The best fit value of the ratio of signal strengths is shown in equation 6.2. Within the quoted uncer-  
 2130     tainties, it is consistent with a ratio of unity.

$$\frac{\mu_{\text{VBF}}}{\mu_{\text{ggF}}} = 1.26^{+0.61}_{-0.45} \text{ (stat.)}^{+0.50}_{-0.26} \text{ (syst.)} = 1.26^{+0.79}_{-0.53} \quad (6.2)$$

2131     The null hypothesis for VBF production corresponds to a ratio of  $\mu_{\text{VBF}} / \mu_{\text{ggF}} = 0$ . The likelihood  
 2132     in figure 6.4 gives a significance of  $3.2\sigma$  at  $\mu_{\text{VBF}} / \mu_{\text{ggF}} = 0$ , as quoted in chapter 5.

2133     In addition to the ratio of signal strengths, each signal strength can be varied independently in the  
 2134     likelihood as well. Figure 6.5 shows the two dimensional likelihood scan in the  $\mu_{\text{ggF}}-\mu_{\text{VBF}}$  plane. The  
 2135     best fit values of the two signal strengths are shown in equation 6.3. Both are consistent with unity  
 2136     within their uncertainties.

$$\begin{aligned} \mu_{\text{ggF}} &= 1.02 \pm 0.19^{+0.22}_{-0.18} = 1.02^{+0.29}_{-0.26} \\ \mu_{\text{VBF}} &= 1.27 \pm 0.40^{+0.44}_{-0.40} \pm 0.21^{+0.29}_{-0.21} = 1.27^{+0.53}_{-0.45} \cdot \\ &\quad (\text{stat.}) \quad (\text{syst.}) \end{aligned} \quad (6.3)$$

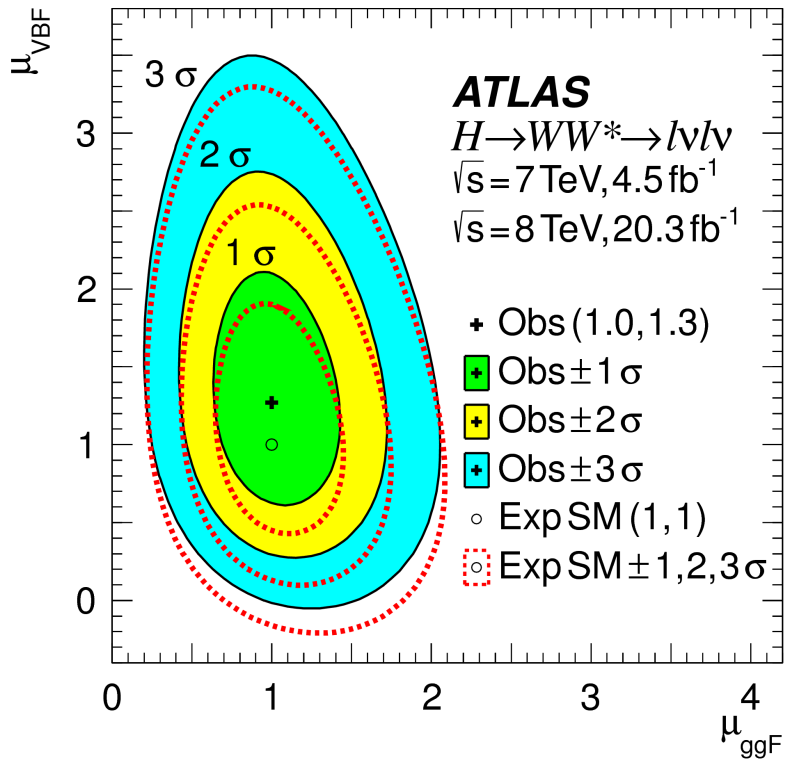


**Figure 6.5:** Likelihood scan as a function of  $\mu_{\text{VBF}}$  and  $\mu_{\text{ggF}}$ [21].

#### 2137 6.4 MEASUREMENT OF HIGGS COUPLINGS TO VECTOR BOSONS AND FERMIONS

2138 Similar to the parameterization of signal strength, the couplings of the Higgs to fermions and bosons can  
 2139 also be parameterized. The parameter of interest in this case is  $\kappa$ , or the ratio of the measured coupling  
 2140 to the standard model expectation. Both the fermion and boson couplings have these so-called scale fac-  
 2141 tors,  $\kappa_F$  for fermions and  $\kappa_V$  for bosons. Gluon fusion production is sensitive to the fermion couplings  
 2142 through the top quark loops in its production, while VBF production is sensitive to the vector boson  
 2143 couplings in its production. Both modes are sensitive to the vector boson couplings in their decays. The  
 2144 signal strengths will have dependence on the coupling scale factors as described in equation 6.4[2].

$$\begin{aligned} \mu_{\text{ggF}} &\propto \frac{\kappa_F^2 \cdot \kappa_V^2}{(\mathcal{B}_{H \rightarrow f\bar{f}} + \mathcal{B}_{H \rightarrow gg}) \kappa_F^2 + (\mathcal{B}_{H \rightarrow VV}) \kappa_V^2} \\ \mu_{\text{VBF}} &\propto \frac{\kappa_V^4}{(\mathcal{B}_{H \rightarrow f\bar{f}} + \mathcal{B}_{H \rightarrow gg}) \kappa_F^2 + (\mathcal{B}_{H \rightarrow VV}) \kappa_V^2}. \end{aligned} \quad (6.4)$$

2145 Figure 6.6 shows the two-dimensional likelihood scan of  $\kappa_F$  and  $\kappa_V$ . The best-fit values are given in  
2146 equation 6.5. The best-fit values are consistent with unity within their uncertainties.

$$\begin{aligned} \kappa_F &= 0.93 & +0.24 & +0.21 & = 0.93 & +0.32 \\ && -0.18 & -0.14 && -0.23 \\ \kappa_V &= 1.04 & +0.07 & +0.07 & = 1.04 & \pm 0.11. \end{aligned} \quad (6.5)$$

(stat.) (syst.)

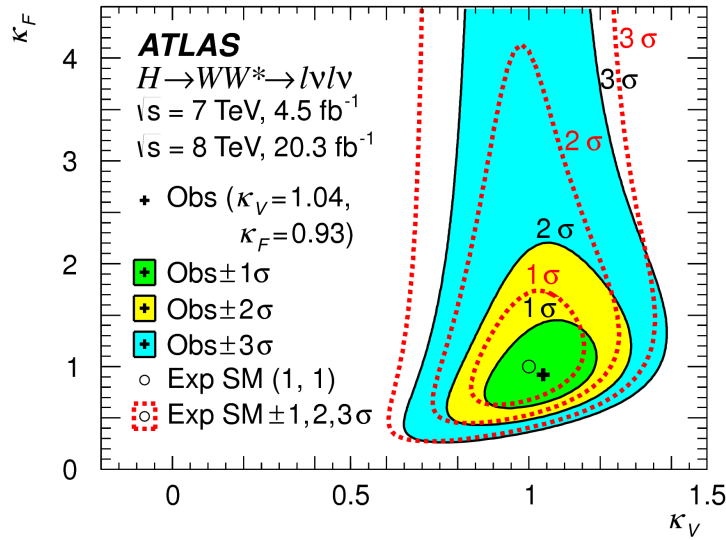


**Figure 6.6:** Likelihood scan as a function of  $\kappa_F$  and  $\kappa_V$ [21].

## 2147 6.5 HIGGS PRODUCTION CROSS SECTION MEASUREMENT

2148 Another measurement that comes naturally from the signal strength numbers quoted earlier is the pro-  
2149 duction cross section and 7 and 8 TeV for both gluon fusion and VBF production. The general equa-  
2150 tion for calculating the cross section is given in equation 6.6.

$$\begin{aligned} (\sigma \cdot \mathcal{B}_{H \rightarrow WW^*})_{\text{obs}} &= \frac{(N_{\text{sig}})_{\text{obs}}}{\mathcal{A} \cdot \mathcal{C} \cdot \mathcal{B}_{WW \rightarrow \ell\nu\ell\nu}} \cdot \frac{1}{\int L dt} \\ &= \hat{\mu} \cdot (\sigma \cdot \mathcal{B}_{H \rightarrow WW^*})_{\text{exp}} \end{aligned} \quad (6.6)$$

2151  $(N_{\text{sig}})_{\text{obs}}$  is the number of events observed in data.  $\mathcal{A}$  is the geometric and kinematic acceptance of  
 2152 the detector, while  $\mathcal{C}$  is the efficiency of the signal region selection for events that are reconstructed in the  
 2153 detector. The branching ratio of a  $WW$  system to leptons must also be divided out. The production  
 2154 cross section depends on the center of mass energy and the production mode desired (gluon fusion or  
 2155 VBF), and so three separate cross section measurements are quoted in equation 6.7.

$$\begin{aligned}
 \sigma_{\text{ggF}}^{\text{7TeV}} \cdot \mathcal{B}_{H \rightarrow WW^*} &= 2.0 \pm 1.7 {}^{+1.2}_{-1.1} = 2.0 {}^{+2.1}_{-2.0} \text{ pb} \\
 \sigma_{\text{ggF}}^{\text{8TeV}} \cdot \mathcal{B}_{H \rightarrow WW^*} &= 4.6 \pm 0.9 {}^{+0.8}_{-0.7} = 4.6 {}^{+1.2}_{-1.1} \text{ pb} \\
 \sigma_{\text{VBF}}^{\text{8TeV}} \cdot \mathcal{B}_{H \rightarrow WW^*} &= 0.51 {}^{+0.17}_{-0.15} {}^{+0.13}_{-0.08} = 0.51 {}^{+0.22}_{-0.17} \text{ pb.}
 \end{aligned} \tag{6.7}$$

(stat.) (syst.)

2156 The predicted cross section values for gluon fusion are  $3.3 \pm 0.4$  pb at 7 TeV and  $4.2 \pm 0.5$  pb  
 2157 at 8 TeV, consistent with the measured values within their uncertainties. For vector boson fusion, the  
 2158 predicted cross section is  $0.35 \pm 0.02$  pb, again consistent with the measured value.

## 2159 6.6 CONCLUSION

2160 The combined analysis of the gluon fusion and vector boson fusion processes in  $H \rightarrow WW^* \rightarrow \ell\nu\ell\nu$   
 2161 in the 7 and 8 TeV datasets has yielded the first discovery level significance for Higgs production in this  
 2162 decay channel. Additionally, precise measurements of the couplings to vector bosons and fermions are  
 2163 given. Finally, signal strengths and cross sections for each production mode are measured. Figure 6.7  
 2164 shows the  $H \rightarrow WW^* \rightarrow \ell\nu\ell\nu$  measurements in comparison with other Higgs decay channels in  
 2165 ATLAS. The measurement of signal strength from this channel remains the most sensitive in both the  
 2166 gluon fusion and VBF production modes for the Run 1 dataset.

**ATLAS**

### Individual analysis

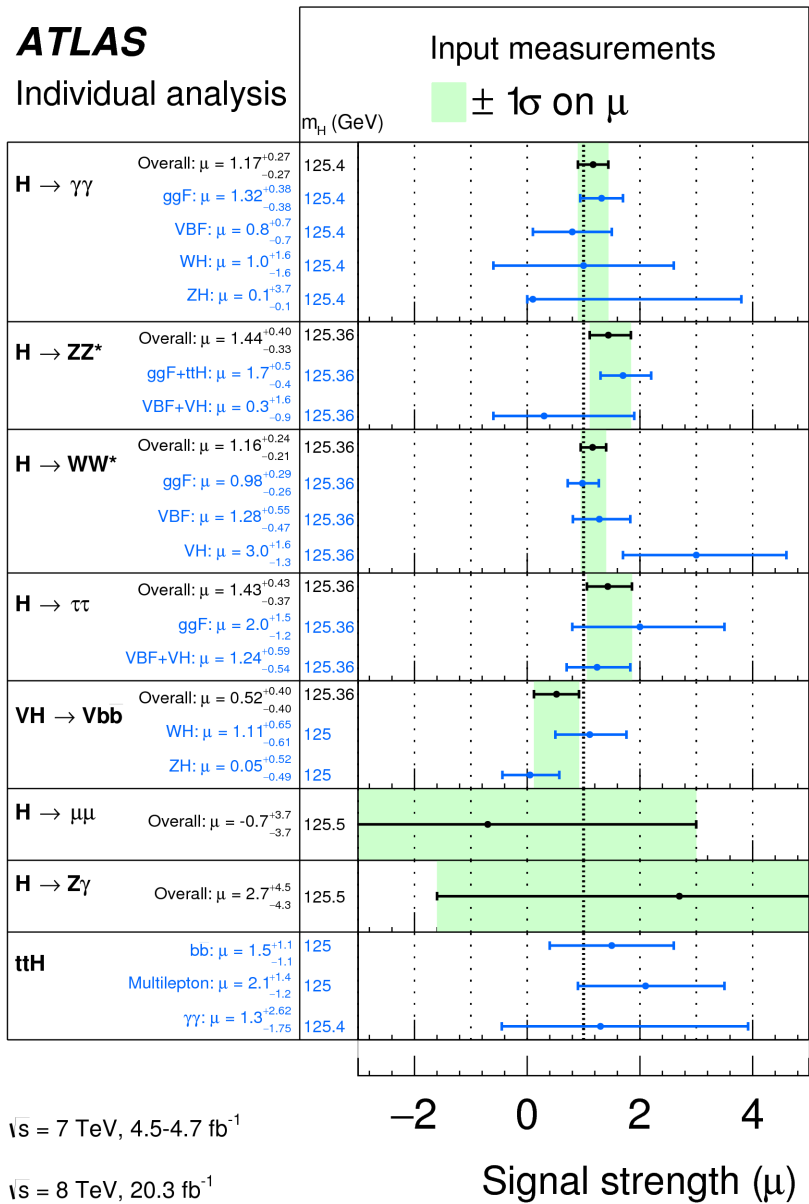


Figure 6.7: Comparison of signal strength measurements in different Higgs decay channels on ATLAS[23].

## Part III

2167

Search for Higgs pair production in the

2168

$HH \rightarrow b\bar{b}b\bar{b}$  channel in LHC Run 2 at  $\sqrt{s} =$

2169

13 TeV

2170

*Passion is in all great searches and is necessary to all  
creative endeavors.*

W. Eugene Smith

# 7

2171

2172

## Search for Higgs pair production in boosted $b\bar{b}b\bar{b}$ final states

2173

2174

### 7.1 INTRODUCTION

2175 After the discovery of the Higgs boson in the ATLAS Run 1 dataset and the subsequent measurements  
2176 of its properties, the Higgs transformed into a potential tool in searches for physics beyond the Stan-  
2177 dard Model. The pair production cross section of the Higgs can be enhanced through BSM physics.  
2178 Studying di-Higgs production also probes the Higgs self-coupling, shedding light on the structure  
2179 of the Higgs potential. This chapter presents a search for resonant production of a Higgs pair in the  
2180  $X \rightarrow HH \rightarrow b\bar{b}b\bar{b}$  final state in  $3.2 \text{ fb}^{-1}$  of data collected at  $\sqrt{s} = 13 \text{ TeV}$ . In particular, this  
2181 chapter focuses on a search for this final state in the regime where  $m_X$  is large ( $\gtrsim 1 \text{ TeV}$ ) and the Higgs  
2182 bosons in the decay are significantly boosted. A tailored selection for this boosted selection, using novel

2183 techniques in jet substructure and  $b$ -tagging, is discussed. Then, the data-driven background estimate is  
 2184 presented. Finally, the results of the search are shown. The signal models used as benchmarks are a spin-  
 2185 2 Randall Sundrum graviton (RSG) and a narrow width spin-0 resonance. These models are described  
 2186 in more detail in Chapter 1. Limits on signal models are reserved for the next chapter where the results of  
 2187 this chapter are combined with the results of a separate selection dedicated to the lower  $m_X$  regime.

## 2188 7.2 MOTIVATION

2189 With the center of mass energy increase from  $\sqrt{s} = 8$  TeV to  $\sqrt{s} = 13$  TeV, the LHC and ATLAS  
 2190 are able to probe new resonances at higher mass scales than previously accessible in Run 1. This is a  
 2191 powerful motivator for searching for a new resonance in the early 13 TeV data. Figure 7.1 shows the  
 2192 ratios of parton luminosities between 8 and 13 TeV for different resonance masses. For a resonance of  
 2193  $M_X = 2$  TeV, the cross section at  $\sqrt{s} = 13$  TeV is roughly a factor of 10 larger than at  $\sqrt{s} = 8$  TeV.

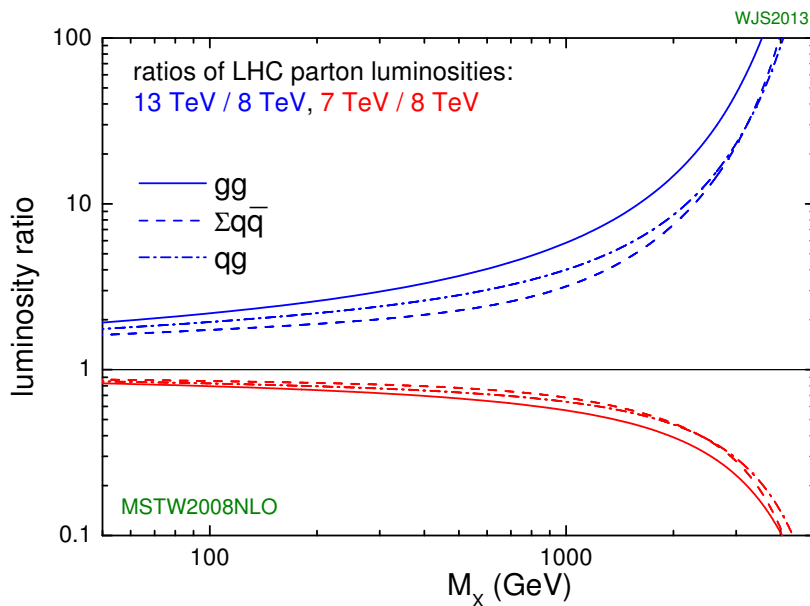


**Figure 7.1:** Parton luminosity ratios as a function of resonance mass  $M_X$  for 13/8 TeV and 7/8 TeV [24].

2194 Higgs pair production offers a vast array of unprobed regions of phase space where searches for BSM  
 2195 physics can be made. Chapter 1 discusses some possibilities for both resonant and non-resonant enhance-

ment of the di-Higgs production cross section. Given the increased mass reach of the LHC in Run 2, it is particularly important to focus on resonant searches at high  $m_X$ . One consideration when conducting a search in the  $HH$  final state is which decay modes of the Higgs to consider. Figure 7.2 shows the branching ratio of the  $HH$  final state for different combinations of decays of each individual Higgs. As the largest branching ratio for the 125 GeV Higgs is  $H \rightarrow b\bar{b}$ , the  $HH \rightarrow b\bar{b}b\bar{b}$  branching ratio is also the largest at 33%.

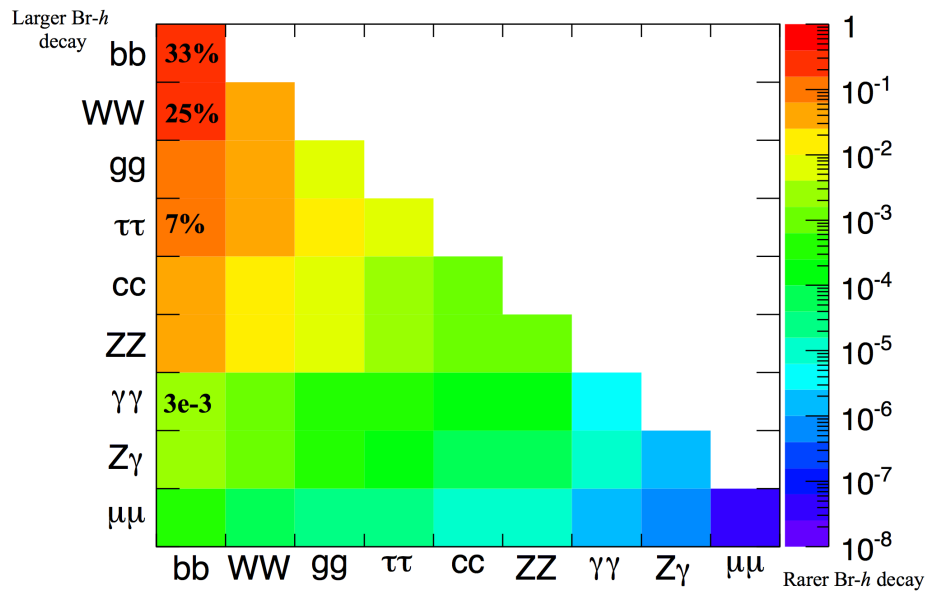


Figure 7.2: Summary of  $HH$  branching ratios [25].

At high  $m_X$ , the Higgs bosons resulting from the decay of a heavy resonance will have large  $p_T$ <sup>\*</sup>. The  $\Delta R$  between the decay products of the Higgs is inversely proportional to the Higgs  $p_T$ , as shown in equation ??.

$$\Delta R \approx \frac{2m}{p_T} \quad (7.1)$$

Figure 7.3 shows the minimum  $\Delta R$  between truth level  $B$  decay vertices in simulation samples for Randall-Sundrum gravitons of different masses. The figure shows that as the mass of the graviton increases, the  $\Delta R$  distribution between the  $b$  quarks in the Higgs decay tends to shift to lower values. Be-

\*In the limit that  $m_H \ell \ell m_X$ , the Higgs  $p_T$  is roughly  $m_X/2$ .

cause of this effect, it is necessary to tailor a selection to target these merged  $b$ -jets.

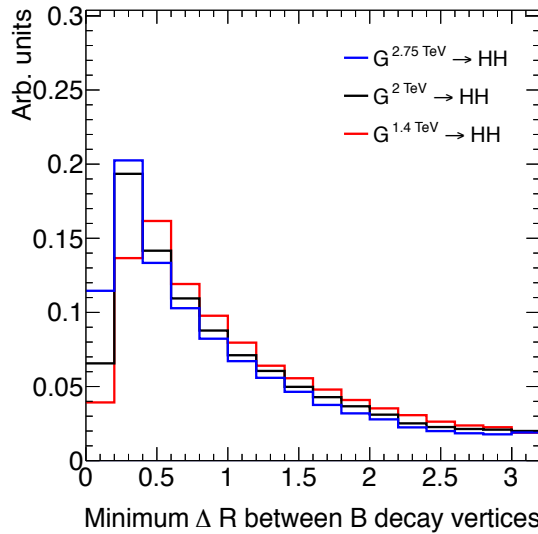


**Figure 7.3:** Minimum  $\Delta R$  between  $B$  decay vertices for different RSG masses in a  $G_{\text{KK}}^* \rightarrow HH \rightarrow 4b$  sample with  $c = 1$

## 7.3 DATA AND SIMULATION SAMPLES

### 7.3.1 SIGNAL MODELS

While the resonance search is by its nature generic (as it is a simple search for a peak in the  $4b$  invariant mass spectrum), there are two signal models that the selection requirements have been optimized for. The first is Randall-Sundrum (RSG) model, where a tower of massive spin-2 Kaluza-Klein gravitons is predicted. The second is a heavy narrow spin-0 resonance, the so-called “heavy Higgs”. This type of resonance arises, for example, in the two Higgs doublet model (2HDM). More details about the physics of these models and their motivation is given in chapter 1.

Signal graviton ( $G_{\text{KK}}^*$ ) events are generated at leading order (LO) with **MADGRAPH5 v2.2.2** [92]. The PDF set used is the **NNPDF2.3 LO** set [93]. For modeling parton shower and hadronization in jets, **PYTHIA 8.186** is used with the A14 tune [80, 94]. The free parameters in the RSG model are the graviton mass and the coupling constant  $c \equiv k/\bar{M}_{\text{Pl}}$ <sup>†</sup>. Both the production cross section and width of the

<sup>†</sup> $k$  is the curvature constant for the warped extra dimension and  $\bar{M}_{\text{Pl}}$  is the Planck mass divided by  $8\pi$

graviton are proportional to  $c^2$ . Samples are generated at both  $c = 1$  and  $c = 2$  for a variety of mass points between 300 GeV and 3 TeV.

The second signal sample is a heavy spin-0 resonance  $H$  with a fixed width of  $\Gamma_H = 1$  GeV. This is generated with **MADGRAPH5** and uses the **CT10** PDF set [83]. The parton shower and hadronization are handled by **HERWIG ++** with the **CTEQ6L1** PDF set and the **UEEE5** event tune [84, 95, 96]. Because the width and branching ratios depend on 2HDM parameters, each mass point generated with this fixed width corresponds to a different point in the 2HDM parameter phase space. Mass points are generated between 300 GeV and 1 TeV as with the RSG signal samples.

### 7.3.2 BACKGROUND SAMPLES

While the dominant **QCD** multijet background is estimated with a fully data-driven method, the sub-dominant backgrounds  $t\bar{t}$  and  $Z + \text{jets}$  are modeled with some input from simulation.

$t\bar{t}$  events are simulated at next-to-leading order (NLO) with the **POWHEG-BOX** version 1 generator using the **CT10** PDF set [97]. The parton shower, hadronization, and underlying event are simulated with **PYTHIA 6.428** with the **CTEQ6L1** PDF set [79]. The Perugia 2012 tune is used [98]. NNLO **QCD** corrections to the cross sections are computed in **Top++ 2.0** [99]. The top quark mass is set to 172.5 GeV. The shapes of distributions in  $t\bar{t}$  are taken from MC while the normalization is taken from data.

Finally, the  $Z + \text{jets}$  background is simulated with **PYTHIA 8.186** and the **NNPDF2.3** LO PDF set. This background is negligible compared to the others and is taken fully from MC.

### 7.3.3 DATA SAMPLE AND TRIGGER

This analysis is done on  $3.2 \text{ fb}^{-1}$  of data taken in 2015 at  $\sqrt{s} = 13$  TeV. The details of the machine conditions during this time can be found in Chapter 2. Only data which was taken during stable beam conditions with all detectors functioning is used. Events must pass a trigger which requires a single 360 GeV large radius ( $R = 1.0$ ) jet to be reconstructed in the HLT. Figure 7.4 shows the trigger efficiency for various trigger options as a function of graviton mass. Above  $m_G > 1$  TeV, the single large radius jet trigger is 99% efficient for events passing the signal selection.

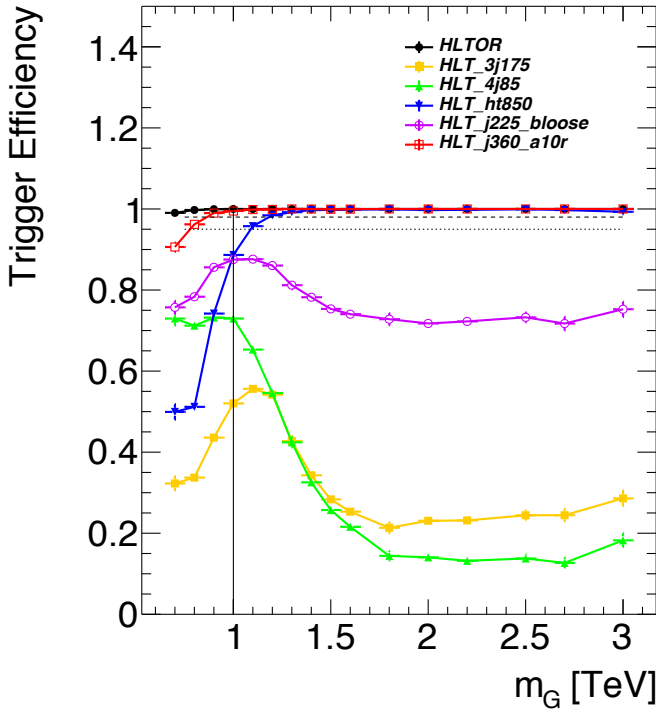


**Figure 7.4:** Trigger efficiency for events passing all signal region selections as a function of mass in  $G_{\text{KK}}^* \rightarrow HH \rightarrow 4b$  samples with  $c = 1$  [26]. In the trigger names, “j” refers to a jet or jets. “ht” refers to  $H_T$ , the scalar sum of transverse momenta in the event. “bloose” refers to a loose  $b$ -tagging requirement applied to the jet. “a10r” refers to anti- $k_T$  jets with  $R = 1.0$ . The numbers at the end are the thresholds on the given quantity in GeV.

2246    7.4    EVENT RECONSTRUCTION AND OBJECT SELECTION

2247    The boosted selection first begins by defining a unique set of objects that can be exploited to increase  
 2248    signal efficiency in the kinematic regime where the final state  $b$ -jets are very merged.

2249    7.4.1    LARGE RADIUS ( $R = 1.0$ ) JETS

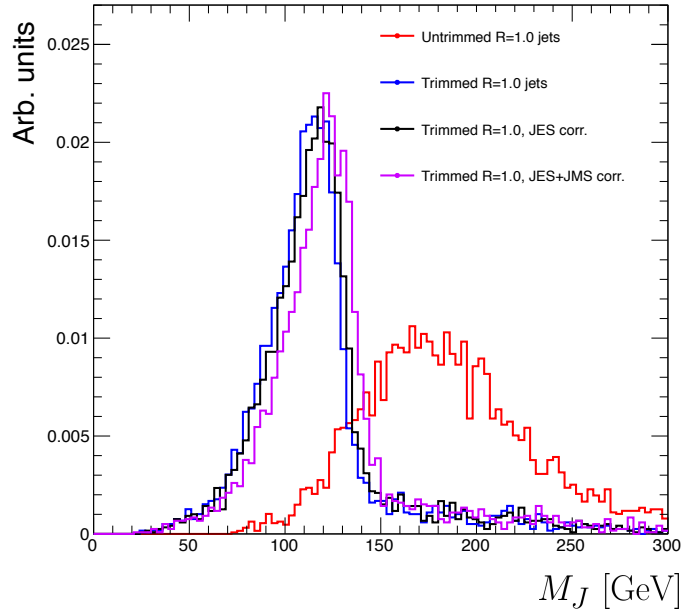
2250    The first step towards reconstructing the final state is to define objects that can be used to measure the  
 2251    kinematics of the Higgs bosons. In the boosted selection anti- $k_T$  jets with a radius parameter of 1.0  
 2252    are used. These jets are much larger in angular size than the typical  $R = 0.4$  jets and are intended to  
 2253    encompass both jets resulting from the Higgs decay<sup>‡</sup>. The jets are built from clusters in the calorimeter

---

<sup>‡</sup>This is in contrast to the resolved selection, which uses two  $R = 0.4$  anti- $k_T$  jets for each Higgs

2254 calibrated with local calibration weighting [17].

2255 Because of the large extent of these jets, great care must be taken to remove potential contributions of  
2256 calorimeter clusters from pile-up. This is done using a technique called jet trimming [100]. With trim-  
2257 ming, the constituents of the large radius jet are re-clustered with a smaller radius with the  $k_T$  algorithm.  
2258 Then, these so-called subjets are removed from the larger jet if  $p_T^{\text{subjet}}/p_T^{\text{jet}} < f_{\text{cut}}$ . In this analysis, the  
2259 subjet radius is  $R = 0.2$  and  $f_{\text{cut}} = 0.05$ . Trimming has been shown to improve the mass resolution  
2260 of large radius jets. Figure 7.5 shows the effect of trimming on the large radius jet mass ( $M_J$ ). Because  
2261 the large radius jet fully contains the higgs decay products, its invariant mass should correspond to the  
2262 125 GeV mass of the Higgs. The trimming algorithm brings the jet mass much closer to the expected  
2263 Higgs mass and improves the mass resolution.



2264 **Figure 7.5:** Comparison of untrimmed and trimmed jet masses for large radius jets in a RSG sample with  $m_{G_{\text{KK}}^*} = 1 \text{ TeV}$ .  
2265 JES (JMS) refers to the standard jet energy (mass) scale calibration for ATLAS [17].

2266 The large radius jets are required to satisfy  $250 < p_T < 1500 \text{ GeV}$ . They must also be within  
2267  $|\eta| < 2.0$  in order to ensure that the full jet is within the inner detector tracking volume. Finally, they  
2268 are required to have  $M_J > 50 \text{ GeV}$ . The upper  $p_T$  cut and lower threshold on mass are applied to  
2269 correspond to the kinematic range where uncertainties are available in ATLAS calibrations [101, 102].

2268 7.4.2 TRACK JETS AND  $b$ -TAGGING

2269 Because the  $b$ -jets from boosted Higgs decays are so close together (as illustrated in figure 7.3), narrow ra-  
2270 dius jets are required to fully resolve both  $b$ -jets. The minimum radius feasible for jets based on calorime-  
2271 ter deposits is determined by the calorimeter granularity. However, because  $b$ -tagging relies on informa-  
2272 tion from the inner detector, it is possible to define another type of jet that can have a smaller radius and  
2273 better  $b$ -tagging resolution. These jets are called “track jets” [27, 102].

2274 Track jets are formed by applying the usual anti- $k_T$  clustering algorithm to tracks that are required  
2275 to be consistent with the primary vertex. After the jet axis has been determined using these tracks, a sec-  
2276 ond step of track association is also performed to add tracks that can be useful for  $b$ -tagging [27]. In this  
2277 analysis, the tracks are clustered with a radius parameter of  $R = 0.2$ . This radius has been shown to  
2278 give good performance in boosted Higgs tagging [27, 102]. Figure 7.6 shows a comparison among dif-  
2279 ferent track jet radii of the efficiency for reconstructing two  $b$ -jets from each Higgs in a RSG sample as a  
2280 function of mass. Track jets with radius of 0.2 give the best performance, especially at high mass.

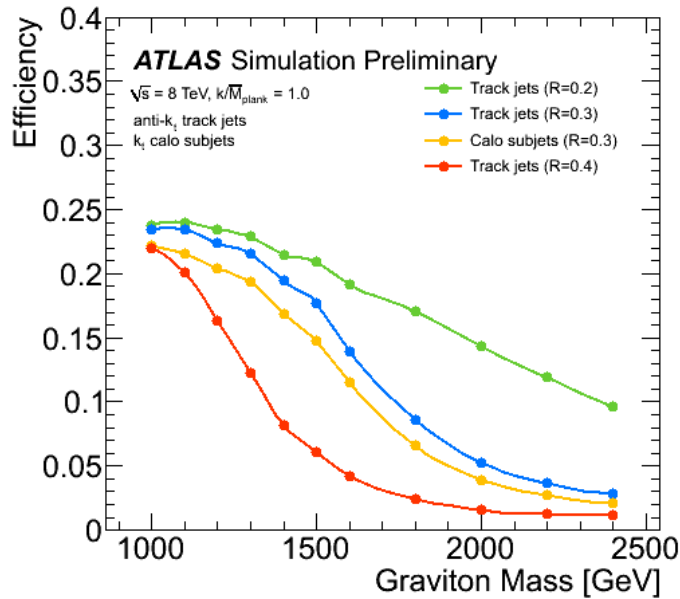


Figure 7.6: Efficiency of finding two  $b$ -jets from each Higgs in an RSG event using calorimeter jets with  $R = 0.3$  or different track jet radii [27]

2281 In this analysis, track jets are required to have  $p_T > 10$  GeV and  $|\eta| < 2.5$ . They must also have at

2282 least two tracks.

2283 **7.4.3 MUONS**

2284 Muons are used in this study to correct the four-momenta of calorimeter jets by accounting for semi-  
2285 leptonic  $b$  decays. The muons used are combined ID and MS muons which must satisfy tight identifica-  
2286 tion requirements [16]. The muons must have  $p_T > 4 \text{ GeV}$  and  $|\eta| < 2.5$ . Table 7.1 summarizes the  
2287 object requirements described in this section.

	$R$	$p_T$	$ \eta $	$M$
Calorimeter jets	1.0	$250 < p_T < 1500 \text{ GeV}$	$< 2.0$	$> 50 \text{ GeV}$
Track jets	0.2	$> 10 \text{ GeV}$	$< 2.5$	-
Muons	-	$4 \text{ GeV}$	$< 2.5$	-

Table 7.1: Summary of requirements on objects used in the  $X \rightarrow HH \rightarrow b\bar{b}b\bar{b}$  search

2288 **7.5 EVENT SELECTION**

2289 The first requirement in the boosted selection is for  $\geq 2$  large radius jets satisfying the selections outlined  
2290 above. The two highest momentum large-R jets in the event are referred to as “Higgs candidates”. The  
2291 leading jet is required to have  $p_T > 350 \text{ GeV}$ .

2292 Track jets satisfying the object selections are matched to Higgs candidate jets via ghost association [103].  
2293 Each Higgs candidate must have at least 2 track jets associated with it. These basic requirements are illus-  
2294 trated in figure 7.7

2295 The QCD multijet background produces less central jets than high mass resonances, so there is an ad-  
2296 ditional requirement that the two Higgs candidates be close together in  $\eta$ . The large-R jets are required  
2297 to satisfy  $|\Delta\eta(JJ)| < 1.7$ .

2298 The final set of requirements ensures that the Higgs candidates are consistent with expected proper-  
2299 ties of the 125.0 GeV Higgs. First, a variable ( $X_{hh}$ ) is defined to measure the consistency of both of the

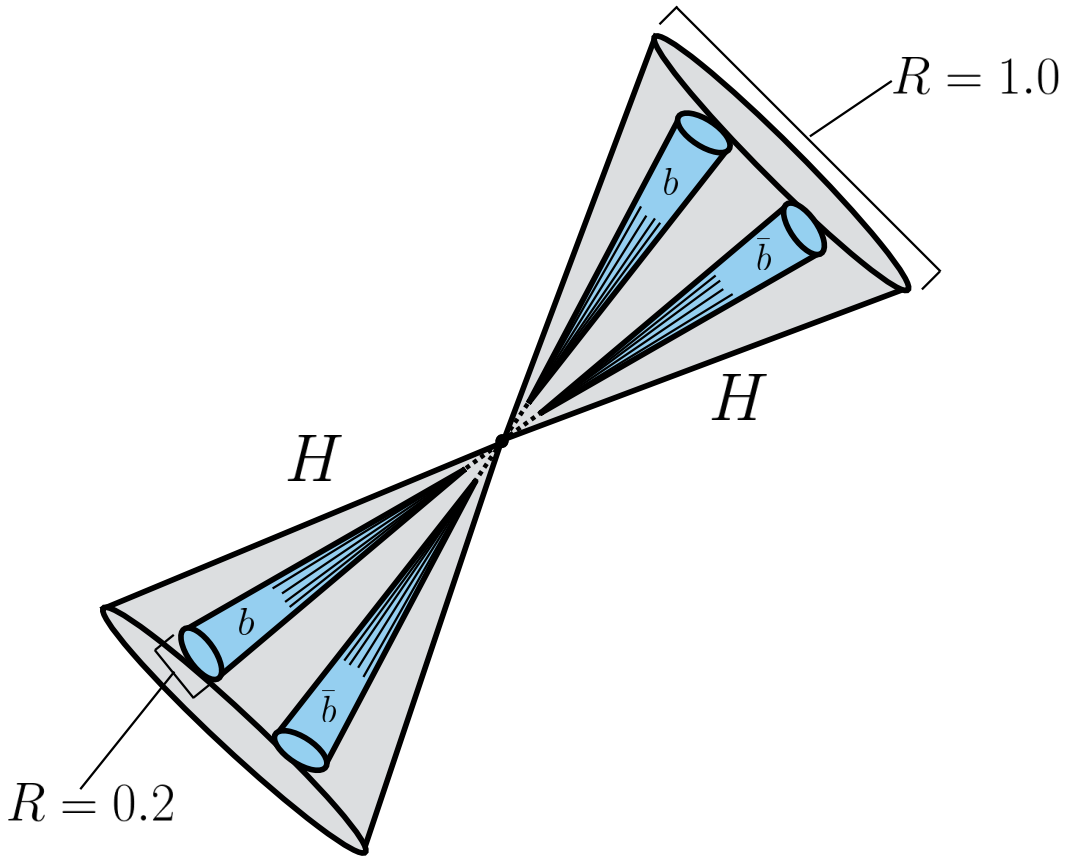


**Figure 7.7:** Illustration of the boosted selection requirements on Higgs candidates. Each large-radius calorimeter jet (Higgs candidate) must contain two track jets

2300    Higgs candidate jets with the SM Higgs mass. This is shown in equation 7.2.

$$X_{hh} = \sqrt{\left(\frac{M_J^{\text{lead}} - 124 \text{ GeV}}{0.1 M_J^{\text{lead}}}\right)^2 + \left(\frac{M_J^{\text{sublead}} - 115 \text{ GeV}}{0.1 M_J^{\text{sublead}}}\right)^2} \quad (7.2)$$

2301    The mass values in the  $X_{hh}$  formula are optimized to maximize signal efficiency. The sub-leading jet  
 2302    typically has a lower mass due to semi-leptonic  $b$  decays and final state radiation.  $X_{hh}$  effectively acts as  
 2303    a  $\chi^2$  measurement of the consistency of the two Higgs candidate masses with the signal hypothesis. The  
 2304    denominators of each term ( $0.1 M$ ) give the uncertainty on the mass measurement for the large radius  
 2305    jets. Events are required to satisfy  $X_{hh} < 1.6$ .

2306    The last requirement applied is on the number of  $b$ -tagged track jets. There are two signal regions de-

2307 fined. The first requires exactly four  $b$ -tagged track jets, two in each Higgs candidate (known as the 4 $b$   
 2308 signal region). At high resonance masses, this requirement is inefficient, so an additional signal region  
 2309 requiring only three  $b$ -tagged track jets is also defined (known as the 3 $b$  signal region). While this has  
 2310 a larger background it is also more efficient for high resonance masses. For both signal regions, thresh-  
 2311 old on MV<sub>2</sub> score is chosen such that the algorithm is 77% efficiency in finding true  $b$ -jets. Different  
 2312 working points were tested and this was found to be optimal. Appendix A has more details on this opti-  
 2313 mization.

2314 Before making the requirement on  $X_{hh}$ , the masses of the Higgs candidates are corrected for semi-  
 2315 leptonic  $b$  decays using muons with the criteria outlined in the previous section. Any muons within a  
 2316  $\Delta R < 0.2$  of a  $b$ -tagged track jet have their four-momenta added to the four-momentum of the Higgs  
 2317 candidate. This correction does not affect the pre-selection requirements but does affect the  $X_{hh}$  re-  
 2318 quirement and the final invariant mass distribution used.

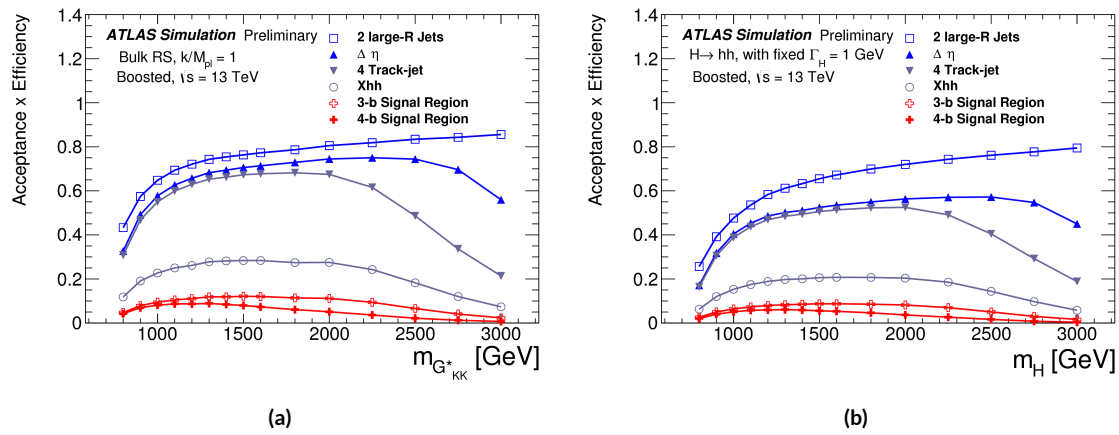


Figure 7.8: Acceptance  $\times$  efficiency as a function of mass for (a) RSG and (b) narrow heavy scalar signal models [28].

2319 Figure 7.8 shows the product of acceptance and efficiency as a function of mass for both the RSG and  
 2320 narrow heavy scalar resonance signal models. After  $m_X > 1$  TeV, the efficiency of the 4 $b$  requirement  
 2321 begins to decline. After  $m_X > 2$  TeV, the efficiency of requiring two track jets in each Higgs candidate  
 2322 begins to decline as well. Both of these behaviors illustrate the difficulty of resolving the merged decay  
 2323 products at high mass. More details on the degradation of the  $b$ -tagging efficiency at high masses are  
 2324 shown in appendix B.

2325     Figure 7.9 shows a more detailed comparison of the signal efficiency in the  $3b$  vs  $4b$  signal regions for  
 2326     the RSG model. The efficiencies shown here are relative to all prior selection requirements.

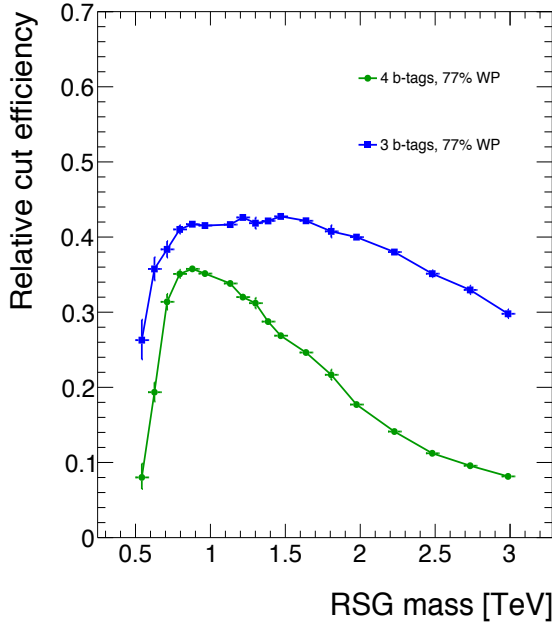


Figure 7.9: Efficiency of requiring 3 or 4  $b$ -tagged track jets vs. RSG mass. The efficiency quoted is relative to the previous selection requirements (rather than an absolute efficiency).

2327     The final discriminating variable used in the boosted analysis is  $M_{2J}$ , the invariant mass of the two  
 2328     Higgs candidates. In order to improve the mass resolution, the four-momenta of each Higgs candidate  
 2329     are scaled by  $m_h/M_J$ . The effect of this correction is small in the boosted analysis but is done for consis-  
 2330     tency with the resolved selection.

2331     Table 7.2 shows the effect of the selection requirements on signal and background simulations as well  
 2332     as data.

## 2333     7.6 DATA-DRIVEN BACKGROUND ESTIMATION

2334     The largest background to this final state is QCD multijet production, constituting 80-90% of the total  
 2335     background. Because of the difficulties in modeling higher order QCD processes, this background is  
 2336     estimated with a fully data-driven method. The only other non-negligible background is  $t\bar{t}$ , constituting

Selection	Data	$m_{G_{KK}^*} = 1\text{TeV}$	$m_{G_{KK}^*} = 2\text{TeV}$	$t\bar{t}$	$Z + \text{jets}$
$N(\text{fiducial large-R jets}) \geq 2$	2202396	23.3	0.48	32345.2	4255.7
leading large-R jet $p_T > 350\text{ GeV}$	1873741	22.9	0.48	26511.7	3649.9
Both large-R jet $m > 50\text{ GeV}$	1854625	21.2	0.47	24369.8	3575.8
Both large-R jet $p_T < 1500\text{ GeV}$	1853601	21.2	0.46	24346.5	3572.9
$ \Delta\eta(JJ)  < 1.7$	1435273	20.8	0.44	20751.0	3265.8
$\geq 2$ track-jets per large-R jet	1224727	19.8	0.40	18234.5	2692.6
$3 b\text{-tags}, X_{hh} < 1.6$	316	3.4	0.067	46.7	2.0
$4 b\text{-tags}, X_{hh} < 1.6$	20	2.9	0.030	1.4	0.0

**Table 7.2:** Effect of boosted selection on data, RSG signal models,  $t\bar{t}$ , and  $Z + \text{jets}$ . The numbers from simulation are normalized with the MC generator cross section and do not take into account the data driven estimates described in section 7.6 [33].

the other 10-20%<sup>§</sup>. Due to the presence of  $t\bar{t}$  in the sideband region where the QCD background will be estimated, the normalization of the QCD and  $t\bar{t}$  backgrounds are simultaneously estimated.

### 7.6.1 MASS REGION DEFINITIONS

The first step in the data-driven background estimate is to define a sideband mass region where the background normalization can be derived. Additionally, a control region is defined where the background estimate can be validated. The control (CR) and sideband (SB) regions are defined using a radial distance in the two-dimensional large-R jet mass plane,  $R_{hh}$ , which is defined in equation 7.3.

$$R_{hh} = \sqrt{(M_J^{\text{lead}} - 124\text{ GeV})^2 + (M_J^{\text{sublead}} - 115\text{ GeV})^2} \quad (7.3)$$

Events in the sideband region are required to fail the signal region  $X_{hh} < 1.6$  requirement and have  $R_{hh} > 35.8\text{ GeV}$ . The control region consists of those events which are not in the signal or sideband regions. Figure 7.10 shows the definition of the signal, control, and sideband mass regions.

Table 7.3 summarizes the mass region selections for the three different regions used in the analysis.

---

<sup>§</sup>The  $Z + \text{jets}$  background is a sub-percent level contribution

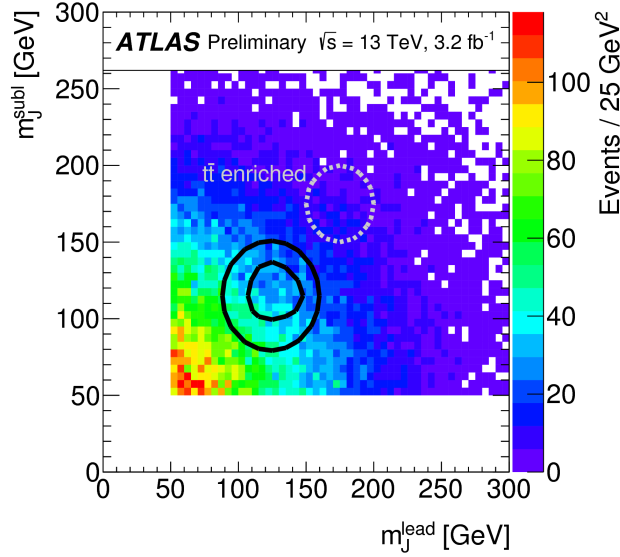


**Figure 7.10:**  $M_J^{\text{sublead}}$  vs.  $M_J^{\text{lead}}$  in a 2  $b$ -tag data sample. The signal region is defined by the inner black contour ( $X_{hh} < 1.6$ ) and the sideband region is defined by the outer contour ( $R_{hh} > 35.8 \text{ GeV}$ ). The region between the black contours is the control region. The mass region which is enriched in  $t\bar{t}$  background is also shown for illustration. [28]

Region	Requirement	Notes
Signal Region (SR)	$X_{hh} < 1.6$	-
Control Region (CR)	$R_{hh} < 35.8 \text{ GeV}$ and $X_{hh} > 1.6$	Used for validation of background estimates
Sideband Region (SB)	$R_{hh} > 35.8 \text{ GeV}$	Used to derive background normalization

**Table 7.3:** Mass region definitions used for background estimation

### 2348 7.6.2 BACKGROUND ESTIMATION

2349 The method for estimating the background in this analysis is similar to the ABCD method presented in  
 2350 Chapter 5. In this case, the two handles used to define different regions for the estimate are the number  
 2351 of  $b$ -tagged track jets and the mass regions. A region requiring exactly two  $b$ -tagged track jets in one large-  
 2352 R jet (referred to as the 2-tag or 2 $b$  region) is defined for use in the background estimate. The number of  
 2353 expected background events in the 3 $b$  and 4 $b$  signal regions is then given by equation 7.4.

$$N_{\text{bkg}}^{3(4)-\text{tag},\text{SR}} = \mu_{\text{Multijet}} N_{\text{Multijet}}^{2-\text{tag},\text{SR}} + \beta_{t\bar{t}} N_{t\bar{t}}^{3(4)-\text{tag},\text{SR}} + N_{Z+\text{jets}}^{3(4)-\text{tag},\text{SR}} \quad (7.4)$$

2354 In this equation,  $N_{\text{bkg}}^{3(4)\text{-tag}}$  is the expected number of background events in the  $3b$  or  $4b$  signal re-  
 2355 gions.  $N_{\text{Multijet}}^{2\text{-tag}}$  is the number of multijet events in the 2-tag region.  $N_{t\bar{t}}^{3(4)\text{-tag}}$  is the number of  $t\bar{t}$   
 2356 events predicted in the MC for the  $3b$  or  $4b$  signal region, and the variable is similarly defined for the  
 2357  $Z+\text{jets}$  background. The  $\beta_{t\bar{t}}$  parameter is a scale factor used to correct the normalization of the  $t\bar{t}$  esti-  
 2358 mate in the signal region.  $\mu_{\text{Multijet}}$  is an extrapolation factor that is derived in the sideband region and  
 2359 used to estimate the ratio of 2-tag events to 3(4)-tag events in the signal region. It is defined in equa-  
 2360 tion 7.5.

$$\mu_{\text{Multijet}} = \frac{N_{\text{Multijet}}^{3(4)\text{-tag,SB}}}{N_{\text{Multijet}}^{2\text{-tag,SB}}} = \frac{N_{\text{data}}^{3(4)\text{-tag,SB}} - \beta_{t\bar{t}} N_{t\bar{t}}^{3(4)\text{-tag,SB}} - N_{Z+\text{jets}}^{3(4)\text{-tag,SB}}}{N_{\text{data}}^{2\text{-tag,SB}} - \beta_{t\bar{t}} N_{t\bar{t}}^{2\text{-tag,SB}} - N_{Z+\text{jets}}^{2\text{-tag,SB}}} \quad (7.5)$$

2361 The  $t\bar{t}$  scale factor ( $\beta_{t\bar{t}}$ ) and the QCD multijet extrapolation factor ( $\mu_{\text{Multijet}}$ ) are estimated together  
 2362 in a simultaneous fit in the sideband region. Then, the number of events in the 2-tag signal region is  
 2363 used, along with the  $t\bar{t}$  estimate in the  $3b$  and  $4b$  signal regions and  $\mu_{\text{Multijet}}$ , to estimate the total num-  
 2364 ber of background events in the two final signal regions. The shape of the final discriminant  $M_{2J}$  is also  
 2365 taken from the 2-tag signal region where there are more statistics. This method is illustrated graphically  
 2366 in figure 7.11.

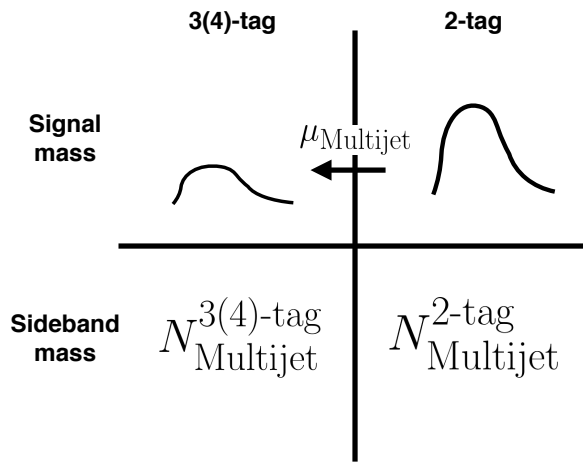
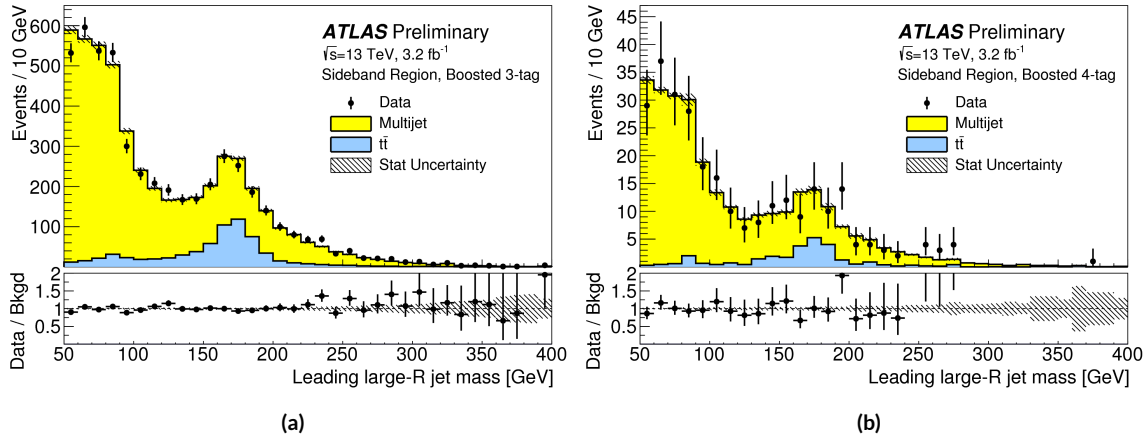


Figure 7.11: An illustration of the data-driven background estimation technique for the boosted analysis

2367 In the  $3b$  region, the fit yields values of  $\mu_{\text{Multijet}} = 0.160 \pm 0.03$  and  $\beta_{t\bar{t}} = 1.02 \pm 0.09$ . In the  $4b$

2368 region, the fit gives  $\mu_{\text{Multijet}} = 0.0091 \pm 0.0007$  and  $\beta_{t\bar{t}} = 0.82 \pm 0.39$ . The uncertainties quoted  
 2369 are statistical only. The larger uncertainties in the  $4b$  values indicate the lower statistics available in that  
 2370 region.

2371 Figure 7.12 shows the distributions of data and background estimates in the  $3b$  and  $4b$  sideband re-  
 2372 gions after the background fit has been done. The normalizations are constrained from the fit to match  
 2373 that of the data, but good modeling of the shape of the mass of the leading large-R jet is seen as well. The  
 2374 shapes of the kinematic distributions in the  $4b$  region are taken from the  $3b$  region due to the better MC  
 2375 statistics in that region.



2376 **Figure 7.12:** Leading large-R jet mass in the  $3b$  (a) and  $4b$  (b) sideband regions. The multijet and  $t\bar{t}$  backgrounds are  
 2377 estimated using the data-driven methods described above. Because their normalizations are derived in the sideband region,  
 2378 the total background normalization is constrained by default to match the normalization of the data [28].

### 2376 7.6.3 BACKGROUND SHAPE FIT

2377 As mentioned in the previous section, the background shape in the 3-tag and 4-tag signal regions is taken  
 2378 from the 2-tag signal mass region. Due to the limited statistics available, the background shapes are ad-  
 2379 ditionally smoothed after being extrapolated to the 3-tag and 4-tag signal regions. Only the data in the  
 2380 range  $900 < M_{2J} < 2000$  GeV is included in the fit due to the limited statistics available above 2 TeV.  
 2381 Both the  $t\bar{t}$  and QCD multijet background are independently fit with an exponential shape,  $y = e^{ax+b}$ .  
 2382 Other shapes are considered and used for the systematic uncertainties. Table 7.4 shows the fit values for

the parameters. Because both the  $3b$  and  $4b$  QCD shapes come from the 2-tag region, the slopes derived are very similar.

	$a$	$b$
QCD ( $4b$ )	$0.00545 \pm 0.00021$	$5.44 \pm 0.24$
$t\bar{t}$ ( $4b$ )	$0.00746 \pm 0.00021$	$4.88 \pm 0.36$
QCD ( $3b$ )	$0.00545 \pm 0.00021$	$8.30 \pm 0.24$
$t\bar{t}$ ( $3b$ )	$0.00746 \pm 0.00021$	$8.58 \pm 0.36$

**Table 7.4:** Parameters derived for exponential fit to background  $M_{2J}$  shape in the  $3b$  and  $4b$  signal regions [33]

#### 7.6.4 VALIDATION OF BACKGROUND ESTIMATE

The background estimate can be validated by using the method to estimate the number of events in the control mass region rather than the signal mass region. Figure 7.13 shows the  $M_{2J}$  distribution in the  $3b$  and  $4b$  control regions, comparing data and background estimates. In both cases, both the background shape and normalization are consistent with the data, indicating good agreement. The ratio of data to the background estimates is also fit to a line in the figure to test for any shape difference. The slope of the line is within  $1\sigma$  (from the fit uncertainties) of flat, further indicating that the data is consistent with the background estimate in the control region.

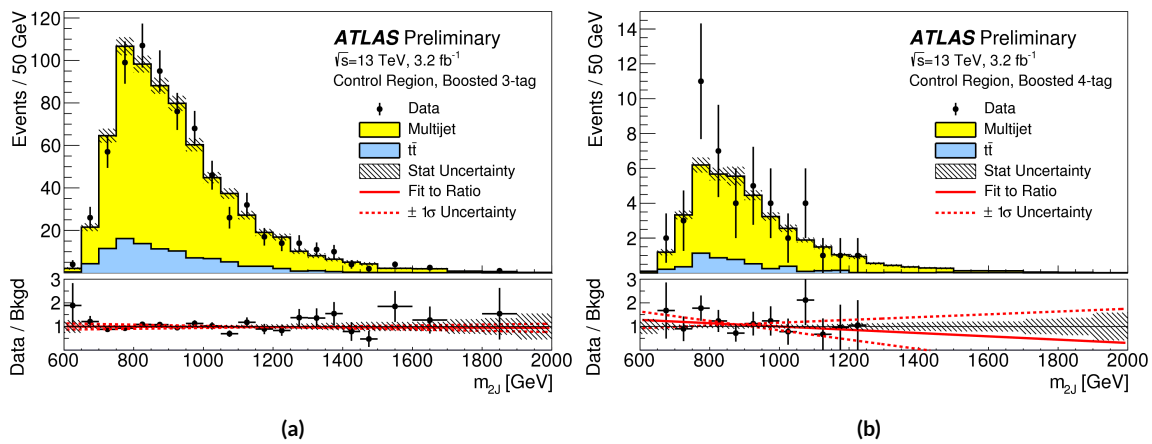


**Figure 7.13:** Di-jet invariant mass ( $M_{2J}$ ) in the  $3b$  (a) and  $4b$  (b) control regions. The multijet and  $t\bar{t}$  backgrounds are estimated using the data-driven methods described above [28].

Table 7.5 shows the yields in data and background estimates in the 3-tag and 4-tag sideband and con-

2394 trol regions. Again, here, it can be seen that the total number of predicted background events from the  
 2395 data driven method is consistent with the number of data events in the region.

Sample (3-tag)	Sideband Region	Control Region
Multijet	$4328 \pm 27$	$607 \pm 10$
$t\bar{t}$	$683.5 \pm 8.1$	$99.6 \pm 3.1$
$Z+jets$	$31.8 \pm 3.7$	$7.7 \pm 1.8$
Total	$5043 \pm 28$	$715 \pm 11$
Data	5043	724
Sample (4-tag)	Sideband Region	Control Region
Multijet	$247.4 \pm 1.5$	$34.7 \pm 0.6$
$t\bar{t}$	$28.4 \pm 1.5$	$5.1 \pm 0.7$
$Z+jets$	$3.4 \pm 1.2$	$0.6 \pm 0.5$
Total	$279.2 \pm 2.5$	$40.3 \pm 1.0$
Data	279	45

Table 7.5: The number of events in data and predicted background events in the boosted 3-tag and 4-tag sideband and control regions. The uncertainties shown are statistical only. [28]

## 2396 7.7 SYSTEMATIC UNCERTAINTIES

2397 The systematic uncertainties in this analysis can be divided into two broad categories. The first type is  
 2398 uncertainties associated with the modeling of the signal processes. The second type of uncertainty is  
 2399 associated with both the shape and normalization of the background prediction.

### 2400 7.7.1 SIGNAL MODELING UNCERTAINTIES

2401 The signal modeling uncertainty has three main components: theoretical uncertainty on the acceptance,  
 2402 experimental uncertainties on the large-R jets, and experimental uncertainties on the track jets related to  
 2403  $b$ -tagging. In this analysis the experimental uncertainties are the most significant.

2404 The first uncertainty on signal modeling is the theoretical uncertainty on the acceptance. As explained  
 2405 in section 5.6.1, there are four components to this uncertainty. The first is related to missing higher order  
 2406 terms from the matrix element calculations which is estimated by varying the QCD renormalization and

2407 factorization scales. The second is uncertainty due to the PDF set used. The third is a generator uncer-  
2408 tainty which is estimated by modifying the generator used to model the underlying event and hadroniza-  
2409 tion. Finally, there is an uncertainty associated with the modeling of the initial state and final state radia-  
2410 tion (ISR/FSR). The total theoretical uncertainty on the signal yield is 3%, and this is dominated by the  
2411 ISR/FSR modeling.

2412 There are uncertainties on the large-R jets in both the jet energy scale (JES) and jet energy resolution  
2413 (JER) as well as the jet mass scale (JMS) and jet mass resolution (JMR). These are evaluated using  $\sqrt{s} =$   
2414 8 TeV data from Run 1 of ATLAS and extrapolated to the Run 2 beam and detector conditions using  
2415 MC<sup>¶</sup>. The details of these uncertainties can be found in reference [[104](#)].

2416 Uncertainties on the track jets are related to the  $b$ -tagging efficiency. The total uncertainty on the sig-  
2417 nal yield due to  $b$ -tagging is evaluated by propagating variations of the  $b$ -tagging efficiency through the  
2418 boosted selection requirements. The uncertainties are calculated jet-by-jet and parameterized as a func-  
2419 tion of  $b$ -jet  $p_T$  and  $\eta$  [[105](#)]. For high  $p_T$   $b$ -jets (with  $p_T > 300$  GeV), the uncertainties are extrapolated  
2420 using MC simulation from the lower  $p_T$   $b$ -jets [[106](#)].

2421 Table 7.6 shows the systematic uncertainties on the signal normalization for models with  $m_{G_{KK}^*} =$   
2422 1.5 TeV and both  $c = 1$  and  $c = 2$  as well as a narrow width heavy scalar. The dominant uncertainty  
2423 comes from  $b$ -tagging and this uncertainty is larger in the 4-tag region than the 3-tag region.

### 2424 7.7.2 BACKGROUND UNCERTAINTIES

2425 Uncertainties on the QCD multijet background normalization and shape are estimated using the control  
2426 mass region. As shown previously, the background predictions in the control region match with the  
2427 data yields within the statistical uncertainty in both the 3-tag and 4-tag control regions. As an additional  
2428 protection, the statistical uncertainty on the background prediction in the control region is assigned as a  
2429 systematic uncertainty on the normalization of the QCD background.

2430 Additional robustness tests are done by varying the definition of the control mass region and the  $b$ -  
2431 tagging requirements used to define the 2-tag sample. In all cases, the effect of the variations is found to

---

<sup>¶</sup>The uncertainties are correspondingly larger due to the uncertainty of this extrapolation.

Source	Background		$G_{KK}^*$	$H$
	$c = 1$	$c = 2$		
Luminosity	-	5.0	5.0	5.0
3-tag				
JER	< 1	< 1	< 1	< 1
JES	2	< 1	< 1	< 1
JMR	1	12	12	11
JMS	5	14	13	17
$b$ -tagging	1	23	22	23
Theoretical	-	3	3	3
Multijet Normalization	3	-	-	-
Statistical	2	1	1	1
Total	7	31	30	33
4-tag				
JER	< 1	< 1	< 1	< 1
JES	< 1	< 1	< 1	< 1
JMR	4	12	13	13
JMS	5	13	13	14
$b$ -tagging	2	36	36	36
Theoretical	-	3	3	3
Multijet Normalization	14	-	-	-
Statistical	3	1	1	1
Total	15	42	42	43

**Table 7.6:** Summary of systematic uncertainties in the total background and signal event yields (expressed in %) in the boosted 3-tag and 4-tag signal regions. Systematic uncertainties on the signal normalization are shown for models with  $m_{G_{KK}^*} = 1.5$  TeV and both  $c = 1$  and  $c = 2$  as well as a narrow width heavy scalar.

2432 be within the statistical uncertainties on the background normalization in the control region.

2433 Shape uncertainties on the background are evaluated using two techniques. First, as shown in figure 7.13, the ratio between the data and background prediction is fit with a linear function. The uncertainties on the slope of this fit are assigned as shape uncertainties. An additional uncertainty is assigned 2434 by using alternate power law fit functions for the smoothing of the background shape. Table 7.7 shows 2435 the alternate shapes used. The largest difference between the nominal fit function and the alternates, 2436 taking into account the  $1\sigma$  uncertainty band on each fit as well, is taken as a shape uncertainty.

2437

Functional Form
$f_1(x) = p_0(1-x)^{p_1}x^{p_2}$
$f_2(x) = p_0(1-x)^{p_1}e^{p_2 x^2}$
$f_3(x) = p_0(1-x)^{p_1}x^{p_2} x$
$f_4(x) = p_0(1-x)^{p_1}x^{p_2} \ln x$
$f_5(x) = p_0(1-x)^{p_1}(1+x)^{p_2} x$
$f_6(x) = p_0(1-x)^{p_1}(1+x)^{p_2} \ln x$
$f_7(x) = \frac{p_0}{x}(1-x)^{p_1-p_2} \ln x$
$f_8(x) = \frac{p_0}{x^2}(1-x)^{p_1-p_2} \ln x$

**Table 7.7:** Alternate fit functions used to model the  $M_{JJ}$  distribution in the QCD multijet background. In the equations,  $x = M_{JJ}/\sqrt{s}$ .

2439     The uncertainties on the  $t\bar{t}$  background are obtained by propagating the various experimental varia-  
 2440     tions (JES, JER, JMS, JMR,  $b$ -tagging) through the analysis selection requirements. Table 7.6 summarizes  
 2441     the background uncertainties in the 3-tag and 4-tag regions.

2442     7.8 RESULTS

2443     Table 7.8 shows the observed yields in the 3-tag and 4-tag signal regions for the boosted analysis com-  
 2444     pared to the predicted number of background events. In the 3-tag region, 316 events are observed with  
 2445     a predicted background of  $285 \pm 19$ . In the 4-tag region, 20 events are observed with a predicted back-  
 2446     ground of  $14.6 \pm 2.4$ . Figure 7.14 shows the  $M_{JJ}$  distribution in the 3-tag and 4-tag regions. There are  
 2447     some small excesses in the data, in particular in the 3-tag region around  $M_{JJ} \approx 900$  GeV and in the  
 2448     region of  $1.6 < M_{JJ} < 2.0$  TeV. The significance of these excesses will be evaluated in the next chapter  
 2449     in the statistical combination with the resolved results.

Sample	Signal Region (3-tag)	Signal Region (4-tag)
Multijet	$235 \pm 14$	$13.5 \pm 2.4$
$t\bar{t}$	$48 \pm 22$	$1.2 \pm 1.0$
$Z+jets$	$2.0 \pm 2.2$	-
Total	$285 \pm 19$	$14.6 \pm 2.4$
Data	316	20
$G_{KK}^*(1000 \text{ GeV}), c = 1$	$3.4 \pm 0.9$	$2.9 \pm 1.1$

**Table 7.8:** Observed yields in the 3-tag and 4-tag signal regions for the boosted analysis compared to the predicted number of background events Errors correspond to the total uncertainties in the predicted event yields. The yields for a graviton with  $m_{G_{KK}^*} = 1 \text{ TeV}$  and  $c = 1$  are also shown. [28]

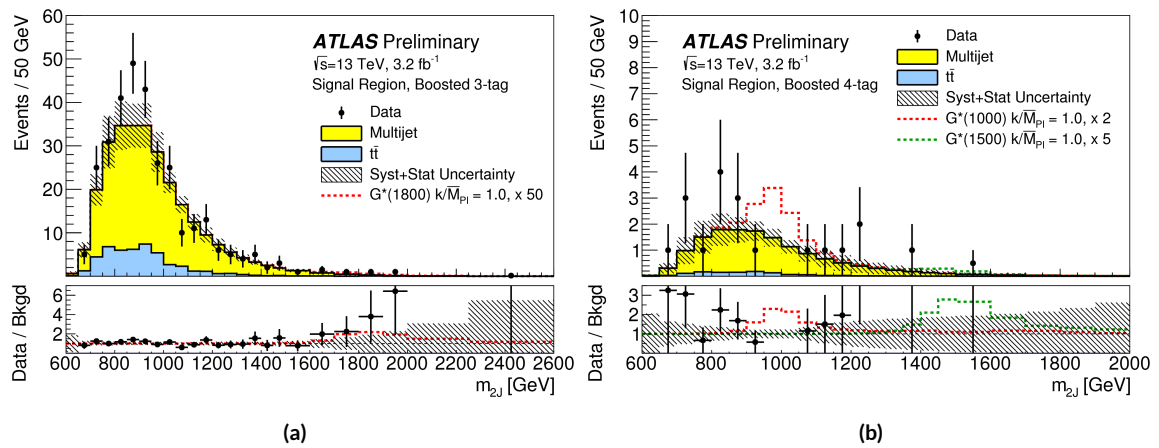


**Figure 7.14:** Di-jet invariant mass ( $M_{2J}$ ) in the  $3b$  (a) and  $4b$  (b) signal regions. The multijet and  $t\bar{t}$  backgrounds are estimated using the data-driven methods described above. In the  $3b$  region, a graviton signal with  $m_{G_{KK}^*} = 1.8 \text{ TeV}$  and  $c = 1$  is overlaid, with the cross section multiplied by a factor of 50 so that the signal is visible. In the  $4b$  region, signals with  $m_{G_{KK}^*} = 1.0 \text{ TeV}$  and  $m_{G_{KK}^*} = 1.5 \text{ TeV}$  are overlaid, both with  $c = 1$  and the yields multiplied by factors of 2 and 5 respectively [28].

*This is a really enlightening quote.*

Tomo Lazovich

# 8

2450

2451

## Combined limits from boosted and resolved searches

2452

2453

### 8.1 INTRODUCTION

2454 In order to cover the full mass range of possible resonances decaying to di-Higgs final states, two distinct  
2455 tailored selections were produced. The resolved selection is more sensitive in the mass range of  $400 < m_X < 1100$  GeV while the boosted selection is more sensitive to masses in the range  $1100 < m_X <$   
2456  $3000$  GeV. Chapter 7 presents the details of the boosted selection and results. In setting limits on spin-2  
2457 Randall-Sundrum graviton (RSG) and narrow width heavy scalar ( $H$ ) models, the results of the boosted  
2458 selection are combined with the results of the resolved selection to cover the full mass range.  
2459

2460 This chapter presents limits on signal models resulting from the  $X \rightarrow HH \rightarrow b\bar{b}b\bar{b}$  search in both  
2461 the resolved and boosted selections. It first presents a brief overview of the resolved results that go into

2462 the limit setting. Then, an overview of the statistical methods used for the search and limit setting is  
2463 given. Finally, limits on the RSG and heavy scalar models are presented.

2464 **8.2 RESOLVED RESULTS**

2465 The details of the resolved selection will not be presented here and can be found in reference [28]. In  
2466 basic terms, the selection searches for four  $R = 0.4$  b-tagged calorimeter jets (where each pair of jets is  
2467 one Higgs candidate). This is distinct from the boosted methodology which searches for merged decay  
2468 products. The backgrounds to the resolved selection are the same as those presented in Chapter 7 for the  
2469 boosted analysis.

2470 Table 8.1 shows the results for data yields and expected background in the resolved signal region. Fig-  
2471 ure 8.1 shows the  $M_{2J}$  distribution in the resolved signal region. The total number of events is consis-  
2472 tent with the prediction and no significant excess is seen. One event in the boosted 4-tag signal is shared  
2473 with the resolved signal region and has a mass of 852 GeV.

Sample	Signal Region Yield
Multijet	$43.3 \pm 2.3$
$t\bar{t}$	$4.3 \pm 3.0$
$Z + \text{jets}$	-
Total	$47.6 \pm 3.8$
Data	46
SM $hh$	$0.25 \pm 0.07$
$G_{\text{KK}}^*(800 \text{ GeV}), c = 1$	$5.7 \pm 1.5$

**Table 8.1:** Observed yields in the resolve selection 4-tag signal region compared to the predicted number of background events Errors correspond to the total uncertainties in the predicted event yields. The yields for a graviton with  $m_{G_{\text{KK}}^*} = 800 \text{ GeV}$  and  $c = 1$  are also shown. [28]

2474 **8.3 SEARCH TECHNIQUE AND RESULTS**

2475 The statistical technique used for the search in this analysis is the same as that used in the  $H \rightarrow WW^*$   
2476 analysis presented in section 3.6.2. The test statistic  $q_0$  is used to define the  $p$ -values which measure the

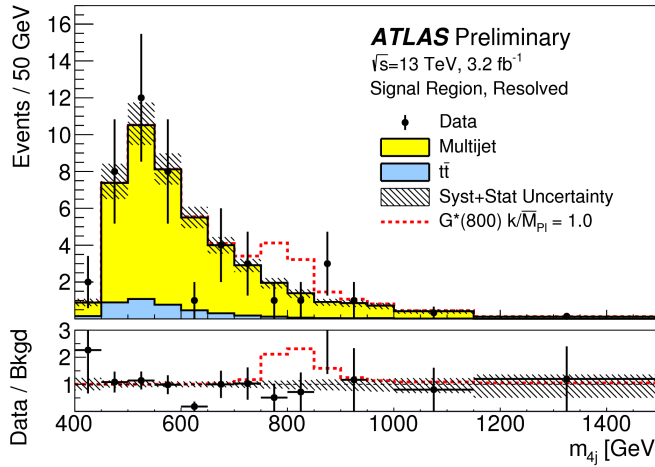


**Figure 8.1:** Di-jet invariant mass ( $M_{2J}$ ) in the resolved signal region. Agraviton signal with  $m_{G^*_{{\rm KK}}} = 800$  GeV and  $c = 1$  is overlaid. [28].

compatibility of the data with the background-only hypothesis corresponding to a signal strength  $\mu = 0$ .

Local  $p_0$  values are computed to quantify the probability that the background could produce a fluctuation greater than or equal to the one observed in the data. In the resolved analysis, no significant excesses are observed. The largest discrepancy with respect to the background only hypothesis occurs near a resonance mass of 900 GeV and is found to be less than  $2\sigma$  in significance.

In the boosted selection, the largest local excess is a broad excess in the  $3b$  signal region that begins near  $M_{2J} \approx 1.7$  GeV. Assuming a  $G^*_{{\rm KK}}$  with this mass and  $c = 1.0$ , the local significance of this excess is  $2.0\sigma$ .

#### 8.4 LIMIT SETTING

In the absence of any significant excess observed in the data, limits on different signal models can be set. This section describes the limit setting procedure and presents combined results of the resolved and boosted analyses.

2490 8.4.1 LIMIT SETTING PROCEDURE

2491 The procedure used for setting exclusion limits in this analysis is the  $\text{CL}_s$  method [107]. The first step in  
 2492 setting the limits is to define a test statistic which will be used. For limit setting, the test statistic is shown  
 2493 in equation 8.1.

$$\tilde{q}_\mu = \begin{cases} -2 \ln \frac{L(\mu, \hat{\theta}(\mu))}{L(0, \hat{\theta}(0))} & \hat{\mu} < 0 \\ -2 \ln \frac{L(\mu, \hat{\theta}(\mu))}{L(\hat{\mu}, \hat{\theta})} & 0 \leq \hat{\mu} < \mu \\ 0 & \hat{\mu} > \mu \end{cases} \quad (8.1)$$

2494 In the above equation,  $\mu$  is the value of the signal strength under test,  $\hat{\mu}$  is the best fit  $\mu$ ,  $\hat{\theta}$  is the  
 2495 best fit value of the nuisance parameters,  $\hat{\theta}$  is the best fit value of the nuisance parameters under the fixed  
 2496  $\mu$  value, and  $L$  is the Poisson likelihood of the data (as described in section 3.6.2).

2497 The test statistic  $\tilde{q}_\mu$  is constructed to protect against two interesting corner cases when setting the  
 2498 upper limit on the cross section. First, it protects against negative signal strengths  $\mu$  which are unphys-  
 2499 ical. Second, it does not count excesses in the data larger than those expected by a signal strength  $\mu$  as  
 2500 evidence against the  $\mu$  hypothesis.

2501 The  $\text{CL}_s$  statistic is constructed by taking a ratio of two probabilities.  $\text{CL}_{s+b}$  is the probability that  
 2502 the signal+background hypothesis would produce a value of the test statistic that is less than or equal  
 2503 to the observed value\*.  $\text{CL}_b$  is the probability that the background only hypothesis will pro-  
 2504 duce a value of the test statistics less than or equal to the observed. The  $\text{CL}_s$  statistic is then the ratio  
 2505  $\text{CL}_{s+b}/\text{CL}_b$ . A 95% upper limit on the cross section is set at the value of  $\mu$  that makes the  $\text{CL}_s$  statistic  
 2506 less than 5%.

2507 In practice, the limits are computed numerically within an asymptotic approximation for the distri-  
 2508 bution of the test statistic  $\tilde{q}_\mu$ . The details of this approximation can be found in reference [70].

2509 The resolved and boosted analyses are combined using a very simple procedure rather than a full sta-  
 2510 tistical combination. For each mass point tested, the limit which gives the most stringent constraint is

---

\*Lower values of  $\tilde{q}_\mu$  mean better compatibility

used. This means that for mass points below 1.1 TeV the resolved signal region is used, while at and above this point the combination of the orthogonal  $3b$  and  $4b$  boosted signal regions is used.

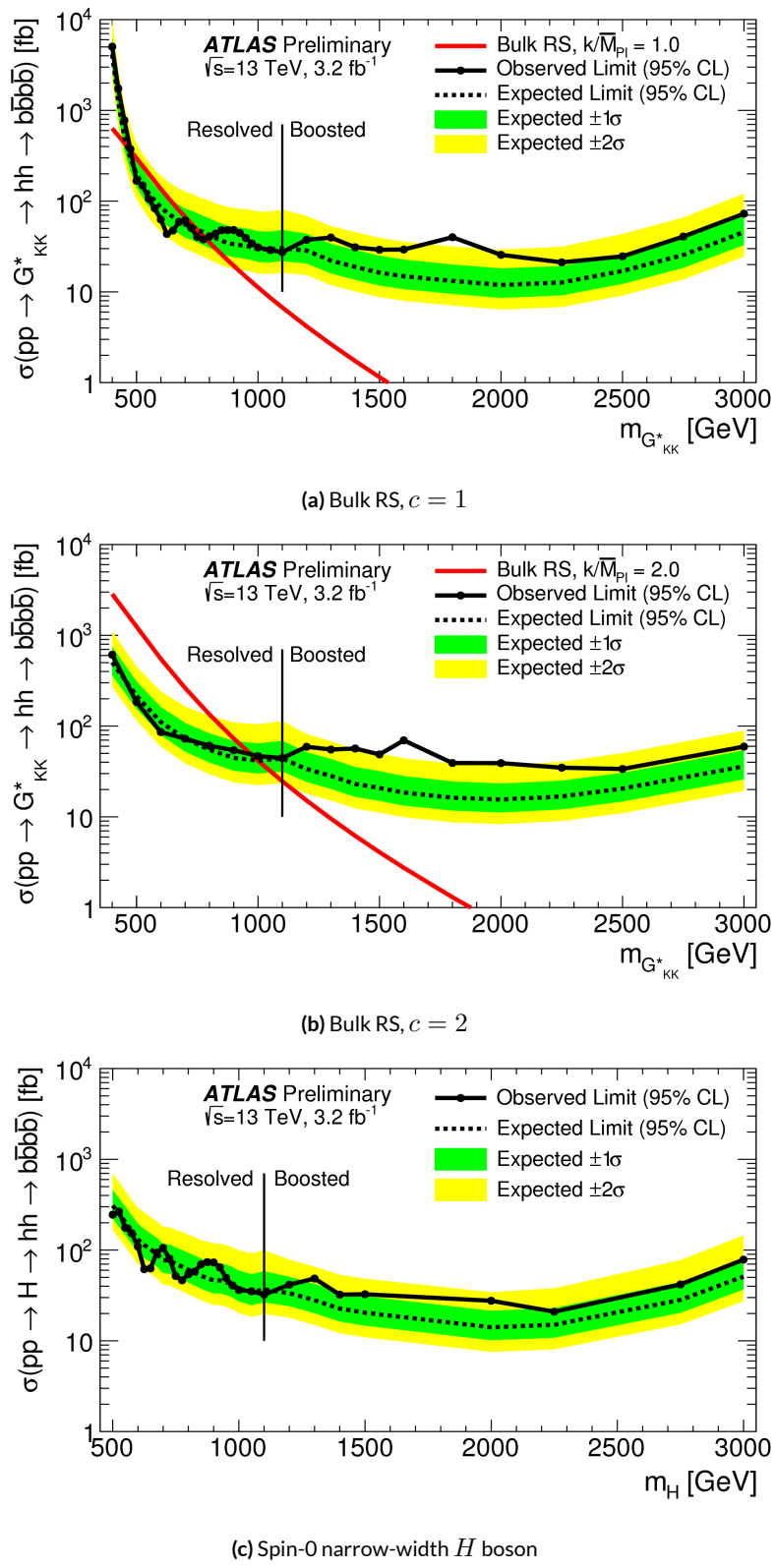
#### 8.4.2 LIMIT SETTING RESULTS

Figure 8.2 shows the combined 95% upper bounds as a function of mass for three different models:  $G_{\text{KK}}^*$  with  $c = 1$ ,  $G_{\text{KK}}^*$  with  $c = 2$ , and a narrow heavy scalar  $H$ .

The cross section of  $\sigma(pp \rightarrow G_{\text{KK}}^* \rightarrow hh \rightarrow b\bar{b}b\bar{b})$  with  $c = 1$  is constrained to be less than 70 fb for masses in the range  $600 < m_{G_{\text{KK}}^*} < 3000$  GeV. For the RSG model with  $c = 2$ , cross sections limits between 40 fb and 200 fb are set for the mass range of  $500 < m_{G_{\text{KK}}^*} < 3000$  GeV. Masses in the range of  $475 < m_{G_{\text{KK}}^*} < 785$  GeV are excluded with  $c = 1$  (with an exclusion of the range 465 to 745 GeV expected). Masses less than 980 GeV are excluded with  $c = 2$  (with an exclusion for masses less than 1 TeV expected).

In the heavy Higgs model, the cross section upper limits for  $\sigma(pp \rightarrow H \rightarrow hh \rightarrow b\bar{b}b\bar{b})$  ranges from 30 to 300 fb in the mass range of  $500 < m_H < 3000$  GeV.

The resolved analysis can also set an upper limit on the Standard Model di-Higgs production cross section discussed in chapter 3. The upper limit on  $\sigma(pp \rightarrow hh \rightarrow b\bar{b}b\bar{b})$  in the Standard Model is constrained to be less than 1.22 pb.



**Figure 8.2:** Expected and observed upper limit as a function of mass for  $G^*_{KK}$  in the RSG model with (a)  $c = 1$  and (b)  $c = 2$ , as well as (c)  $H$  with fixed  $\Gamma_H = 1$  GeV, at the 95% confidence level in the  $CL_s$  method. [28]

2527

## Part IV

2528

## Looking ahead

# 9

2529

2530

## Conclusion

2531 This dissertation presented two distinct studies: the observation and measurement of the Higgs boson  
2532 in the  $H \rightarrow WW^* \rightarrow \ell\nu\ell\nu$  channel at  $\sqrt{s} = 7$  TeV and  $\sqrt{s} = 8$  TeV and a search for Higgs pair  
2533 production in the  $HH \rightarrow b\bar{b}b\bar{b}$  channel at  $\sqrt{s} = 13$  TeV with the ATLAS detector in  $pp$  collisions at  
2534 the Large Hadron Collider.

2535 In the  $H \rightarrow WW^* \rightarrow \ell\nu\ell\nu$ , results from both the discovery of the Higgs boson and the full  
2536 ATLAS Run 1 dataset were presented. With the full  $20.3 \text{ fb}^{-1}$  at  $\sqrt{s} = 8$  TeV and  $4.2 \text{ fb}^{-1}$  at  $\sqrt{s} =$   
2537 7 TeV, ATLAS achieved discovery level significance in the  $H \rightarrow WW^*$  channel alone and obtained  
2538 the first observation of vector boson fusion production in that channel. The combined signal strength  
2539 is measured to be  $\mu = 1.09^{+0.23}_{-0.21}$ . The total observed significance of the  $H \rightarrow WW^*$  process is ob-  
2540 served to be  $6.1\sigma$  (with  $5.8\sigma$  expected). Advanced methods for background reduction and estimation,  
2541 particularly in same-flavor lepton final states, are shown. The VBF signal strength is measured to be  
2542  $\mu_{\text{VBF}} = 1.27^{+0.53}_{-0.45}$  with an observed significance of  $3.2\sigma$  (with  $2.7\sigma$  expected).

2543 These results required many novel innovations. The increase of pileup interactions in the higher in-  
2544 stantaneous luminosity LHC conditions of 2012 led to a degradation of missing transverse momentum  
2545 resolution. As a result, the prominent  $Z/\gamma^*$ +jets background of the same flavor  $H \rightarrow WW^* \rightarrow \ell\nu\ell\nu$   
2546 final states increased greatly. New variables, including a track-based missing transverse momentum and  
2547 a measurement of the balance between the dilepton system and recoiling jets, allowed for significant re-  
2548 duction of this background. In the VBF channel, selections were optimized to exploit the unique VBF  
2549 final state topology. Incorporating these variables into a boosted decision tree technique allowed the  
2550 analysis to exceed the  $3\sigma$  observation threshold.

2551 At  $\sqrt{s} = 13$  TeV, a search for Higgs pair production in the  $b\bar{b}b\bar{b}$  final state with  $3.2 \text{ fb}^{-1}$  was con-  
2552 ducted. A signal region optimized for the boosted final states arising from high mass resonances was  
2553 constructed. This signal region utilized large-radius calorimeter jets and  $b$ -tagging with small radius track  
2554 jets to maximize the signal acceptance. No significant excesses were observed, and upper limits on cross  
2555 sections are placed for spin-2 Randall Sundrum gravitons (RSG) and narrow spin-0 resonances. The  
2556 cross section of  $\sigma(pp \rightarrow G_{\text{KK}}^* \rightarrow hh \rightarrow b\bar{b}b\bar{b})$  with  $k/\bar{M}_{\text{Pl}} = 1$  is constrained to be less than  $70 \text{ fb}$  for  
2557 masses in the range  $600 < m_{G_{\text{KK}}^*} < 3000 \text{ GeV}$ . For the RSG model with  $k/\bar{M}_{\text{Pl}} = 2$ , cross sections  
2558 limits between  $40 \text{ fb}$  and  $200 \text{ fb}$  are set for the mass range of  $500 < m_{G_{\text{KK}}^*} < 3000 \text{ GeV}$ . The cross  
2559 section upper limits for  $\sigma(pp \rightarrow H \rightarrow hh \rightarrow b\bar{b}b\bar{b})$  ranges from  $30$  to  $300 \text{ fb}$  in the mass range of  
2560  $500 < m_H < 3000 \text{ GeV}$ .

# A

2561

2562

Optimization of  $b$ -tagging working point in

2563

$X \rightarrow HH \rightarrow b\bar{b}b\bar{b}$  search

2564

# B

2565

*b*-tagging efficiency at high  $p_{\tau}$

# References

2566

- 2567 [1] K. A. Olive et al. Review of Particle Physics. *Chin. Phys.*, C38:090001, 2014. doi: 10.1088/1674-1137/38/9/090001.
- 2568  
2569 [2] LHC Higgs Cross Section Working Group, S. Heinemeyer, C. Mariotti, G. Passarino, and R. Tanaka (Eds.). Handbook of LHC Higgs Cross Sections: 3, Higgs Properties. 2013.
- 2570  
2571 [3] Kaustubh Agashe, Hooman Davoudiasl, Gilad Perez, and Amarjit Soni. Warped Gravitons at the LHC and Beyond. *Phys. Rev.*, D76:036006, 2007. doi: 10.1103/PhysRevD.76.036006.
- 2572  
2573 [4] Johan Alwall, Michel Herquet, Fabio Maltoni, Olivier Mattelaer, and Tim Stelzer. MadGraph 5:Going Beyond. *JHEP*, 1106:128, 2011. doi: 10.1007/JHEP06(2011)128.
- 2574  
2575 [5] Howard E. Haber and Oscar Stål. New LHC benchmarks for the  $\mathcal{CP}$ -conserving two-Higgs-doublet model. *Eur. Phys. J.*, C75(10):491, 2015. doi: 10.1140/epjc/s10052-015-3697-x.
- 2576  
2577 [6] Lyndon Evans. The Large Hadron Collider. In Holstein, BR and Haxton, WC and Jawahery, A, editor, *ANNUAL REVIEW OF NUCLEAR AND PARTICLE SCIENCE, VOL 61*, volume 61 of *Annual Review of Nuclear and Particle Science*, pages 435–466. 2011. doi: {10.1146/annurev-nucl-102010-130438}.
- 2578  
2579 [7] ATLAS Collaboration. The ATLAS experiment at the CERN Large Hadron Collider. *JINST*, 3: So8003, 2008. doi: 10.1088/1748-0221/3/08/So8003.
- 2580  
2581 [8] Track Reconstruction Performance of the ATLAS Inner Detector at  $\sqrt{s} = 13$  TeV. Technical Report ATL-PHYS-PUB-2015-018, CERN, Geneva, Jul 2015. URL <http://cds.cern.ch/record/2037683>.
- 2582  
2583 [9] ATLAS Collaboration. ATLAS Trigger Operations Public Results. 2015. URL <https://twiki.cern.ch/twiki/bin/view/AtlasPublic/TriggerOperationPublicResults>.
- 2584  
2585 [10] ATLAS Collaboration. ATLAS Luminosity Public Results, Run 1. 2012. URL <https://twiki.cern.ch/twiki/bin/view/AtlasPublic/LuminosityPublicResults>.
- 2586  
2587 [11] ATLAS Collaboration. ATLAS Luminosity Public Results, Run 2. 2015. URL <https://twiki.cern.ch/twiki/bin/view/AtlasPublic/LuminosityPublicResultsRun2>.

- 2592 [12] T Kawamoto, S Vlachos, L Pontecorvo, J Dubbert, G Mikenberg, P Iengo, C Dallapiccola,  
 2593 C Amelung, L Levinson, R Richter, and D Lellouch. New Small Wheel Technical Design Re-  
 2594 port. Technical Report CERN-LHCC-2013-006. ATLAS-TDR-020, CERN, Geneva, Jun 2013.  
 2595 URL <https://cds.cern.ch/record/1552862>. ATLAS New Small Wheel Technical Design  
 2596 Report.
- 2597 [13] Joao Pequenao and Paul Schaffner. An computer generated image representing how ATLAS  
 2598 detects particles. Jan 2013. URL <https://cds.cern.ch/record/1505342>.
- 2599 [14] Electron efficiency measurements with the ATLAS detector using the 2012 LHC proton-proton  
 2600 collision data. Technical Report ATLAS-CONF-2014-032, CERN, Geneva, Jun 2014. URL  
 2601 <https://cds.cern.ch/record/1706245>.
- 2602 [15] Georges Aad et al. Electron and photon energy calibration with the ATLAS detector using LHC  
 2603 Run 1 data. *Eur. Phys. J.*, C74(10):3071, 2014. doi: 10.1140/epjc/s10052-014-3071-4.
- 2604 [16] Georges Aad et al. Measurement of the muon reconstruction performance of the ATLAS detec-  
 2605 tor using 2011 and 2012 LHC proton–proton collision data. *Eur. Phys. J.*, C74(11):3130, 2014. doi:  
 2606 10.1140/epjc/s10052-014-3130-x.
- 2607 [17] Monte Carlo Calibration and Combination of In-situ Measurements of Jet Energy Scale, Jet En-  
 2608 ergy Resolution and Jet Mass in ATLAS. Technical Report ATLAS-CONF-2015-037, CERN,  
 2609 Geneva, Aug 2015. URL <http://cds.cern.ch/record/2044941>.
- 2610 [18] Georges Aad et al. Performance of *b*-Jet Identification in the ATLAS Experiment. 2015.
- 2611 [19] Expected performance of the ATLAS *b*-tagging algorithms in Run-2. Technical Report ATL-  
 2612 PHYS-PUB-2015-022, CERN, Geneva, Jul 2015. URL <http://cds.cern.ch/record/2037697>.
- 2613
- 2614 [20] Performance of Missing Transverse Momentum Reconstruction in ATLAS studied in Proton-  
 2615 Proton Collisions recorded in 2012 at 8 TeV. Technical Report ATLAS-CONF-2013-082, CERN,  
 2616 Geneva, Aug 2013. URL <http://cds.cern.ch/record/1570993>.
- 2617 [21] ATLAS Collaboration. Observation and measurement of Higgs boson decays to WW\* with the  
 2618 ATLAS detector. *Phys. Rev. D*, 92(012006), 2015.
- 2619 [22] Georges Aad et al. Observation of a new particle in the search for the Standard Model Higgs  
 2620 boson with the ATLAS detector at the LHC. *Phys. Lett.*, B716:1–29, 2012. doi: 10.1016/j.physletb.  
 2621 2012.08.020.
- 2622 [23] Georges Aad et al. Measurements of the Higgs boson production and decay rates and coupling  
 2623 strengths using pp collision data at  $\sqrt{s} = 7$  and 8 TeV in the ATLAS experiment. *Eur. Phys. J.*,  
 2624 C76(1):6, 2016. doi: 10.1140/epjc/s10052-015-3769-y.

- 2625 [24] W.J. Stirling. 7/8 and 13/8 TeV LHC luminosity ratios. 2013. URL [http://www.hep.ph.ic.ac.uk/~wstirlin/plots/lhclumi7813\\_2013\\_v0.pdf](http://www.hep.ph.ic.ac.uk/~wstirlin/plots/lhclumi7813_2013_v0.pdf).
- 2626
- 2627 [25] J Alison. Experimental Studies of hh. Oct 2014. URL <http://cds.cern.ch/record/1952581>.
- 2628
- 2629 [26] Baojia (Tony) Tong. Private communication.
- 2630 [27] Flavor Tagging with Track Jets in Boosted Topologies with the ATLAS Detector. Technical Report ATL-PHYS-PUB-2014-013, CERN, Geneva, Aug 2014. URL <https://cds.cern.ch/record/1750681>.
- 2631
- 2632
- 2633 [28] Search for pair production of Higgs bosons in the  $b\bar{b}b\bar{b}$  final state using proton-proton collisions at  $\sqrt{s} = 13$  TeV with the ATLAS detector. Technical Report ATLAS-CONF-2016-017, CERN, Geneva, Mar 2016. URL <https://cds.cern.ch/record/2141006>.
- 2634
- 2635
- 2636 [29] Christopher G. Tully. *Elementary particle physics in a nutshell*. 2011.
- 2637 [30]
- 2638 [31] Mike Lamont for the LHC team. The First Years of LHC Operation for Luminosity Production. International Particle Accelerator Conference, 2013. URL [https://accelconf.web.cern.ch/accelconf/IPAC2013/talks/moyab101\\_talk.pdf](https://accelconf.web.cern.ch/accelconf/IPAC2013/talks/moyab101_talk.pdf).
- 2639
- 2640
- 2641 [32] Paul Collier for the LHC team. LHC Machine Status. CERN Resource Review Board, 2015.
- 2642 URL <https://cds.cern.ch/record/2063924/files/CERN-RRB-2015-119.PDF>.
- 2643
- 2644 [33] Qi Zeng. Private communication.
- 2645
- 2646 [34] Serguei Chatrchyan et al. Observation of a new boson at a mass of 125 GeV with the CMS experiment at the LHC. *Phys. Lett.*, B716:30–61, 2012. doi: 10.1016/j.physletb.2012.08.021.
- 2647
- 2648
- 2649 [35] David Griffiths. *Introduction to elementary particles*. 2008.
- 2650
- 2651 [36] F. Halzen and Alan D. Martin. *QUARKS AND LEPTONS: AN INTRODUCTORY COURSE IN MODERN PARTICLE PHYSICS*. 1984. ISBN 0471887412, 9780471887416.
- 2652
- 2653 [37] Matthew D. Schwartz. *Quantum Field Theory and the Standard Model*. Cambridge University Press, 2014. ISBN 1107034736, 9781107034730. URL <http://www.cambridge.org/us/academic/subjects/physics/theoretical-physics-and-mathematical-physics/quantum-field-theory-and-standard-model>.
- 2654
- 2655 [38] S. Dawson. Introduction to electroweak symmetry breaking. In *High energy physics and cosmology. Proceedings, Summer School, Trieste, Italy, June 29-July 17, 1998*, pages 1–83, 1998. URL <http://alice.cern.ch/format/showfull?sysnb=0301862>.

- 2656 [39] S. L. Glashow. Partial Symmetries of Weak Interactions. *Nucl. Phys.*, 22:579–588, 1961. doi:  
2657 10.1016/0029-5582(61)90469-2.
- 2658 [40] Steven Weinberg. A Model of Leptons. *Phys. Rev. Lett.*, 19:1264–1266, 1967. doi: 10.1103/  
2659 PhysRevLett.19.1264.
- 2660 [41] A. Salam. *Elementary Particle Theory*. Almqvist and Wiksell, Stockholm, 1968.
- 2661 [42] J. Iliopoulos S.L. Glashow and L. Maiani. D2:1285, 1970.
- 2662 [43] R. Keith Ellis, W. James Stirling, and B. R. Webber. QCD and collider physics. *Camb. Monogr.  
2663 Part. Phys. Nucl. Phys. Cosmol.*, 8:1–435, 1996.
- 2664 [44] P. W. Higgs. Broken symmetries and the masses of gauge bosons. 13:508, 1964.
- 2665 [45] P. W. Higgs. Spontaneous symmetry breakdown without massless bosons. 145:1156, 1966.
- 2666 [46] F. Englert and R. Brout. Broken symmetry and the mass of gauge vector mesons. 13:321, 1964.
- 2667 [47] G. S. Guralnik, C. R. Hagen, and T. W. .B. Kibble. Global conservation laws and massless parti-  
2668 cles. *Phys. Rev. Lett.*, 13:585, 1964. doi: 10.1103/PhysRevLett.13.585.
- 2669 [48] Matthew J. Dolan, Christoph Englert, and Michael Spannowsky. New Physics in LHC Higgs  
2670 boson pair production. *Phys. Rev.*, D87(5):055002, 2013. doi: 10.1103/PhysRevD.87.055002.
- 2671 [49] Roberto Contino, Margherita Ghezzi, Mauro Moretti, Giuliano Panico, Fulvio Piccinini, and  
2672 Andrea Wulzer. Anomalous Couplings in Double Higgs Production. *JHEP*, 08:154, 2012. doi:  
2673 10.1007/JHEP08(2012)154.
- 2674 [50] R. Grober and M. Muhlleitner. Composite Higgs Boson Pair Production at the LHC. *JHEP*, 06:  
2675 020, 2011. doi: 10.1007/JHEP06(2011)020.
- 2676 [51] Lisa Randall and Raman Sundrum. A Large mass hierarchy from a small extra dimension. *Phys.  
2677 Rev. Lett.*, 83:3370–3373, 1999. doi: 10.1103/PhysRevLett.83.3370.
- 2678 [52] A. Liam Fitzpatrick, Jared Kaplan, Lisa Randall, and Lian-Tao Wang. Searching for the Kaluza-  
2679 Klein Graviton in Bulk RS Models. *JHEP*, 09:013, 2007. doi: 10.1088/1126-6708/2007/09/013.
- 2680 [53] Julien Baglio, Otto Eberhardt, Ulrich Nierste, and Martin Wiebusch. Benchmarks for Higgs Pair  
2681 Production and Heavy Higgs boson Searches in the Two-Higgs-Doublet Model of Type II. *Phys.  
2682 Rev.*, D90(1):015008, 2014. doi: 10.1103/PhysRevD.90.015008.
- 2683 [54] G. C. Branco, P. M. Ferreira, L. Lavoura, M. N. Rebelo, Marc Sher, and Joao P. Silva. Theory  
2684 and phenomenology of two-Higgs-doublet models. *Phys. Rept.*, 516:1–102, 2012. doi: 10.1016/j.  
2685 physrep.2012.02.002.

- 2686 [55] Jose M. No and Michael Ramsey-Musolf. Probing the Higgs Portal at the LHC Through Reso-  
 2687 nant di-Higgs Production. *Phys. Rev.*, D89(9):095031, 2014. doi: 10.1103/PhysRevD.89.095031.
- 2688 [56] Lyndon R Evans and Philip Bryant. LHC Machine. *J. Instrum.*, 3:S08001, 164 p, 2008. URL  
 2689 <https://cds.cern.ch/record/1129806>. This report is an abridged version of the LHC  
 2690 Design Report (CERN-2004-003).
- 2691 [57] CMS Collaboration. The cms experiment at the cern lhc. *Journal of Instrumentation*, 3(08):  
 2692 S08004, 2008. URL <http://stacks.iop.org/1748-0221/3/i=08/a=S08004>.
- 2693 [58] LHCb Collaoration. The LHCb Detector at the LHC. *JINST*, 3:S08005, 2008. doi: 10.1088/  
 2694 1748-0221/3/08/S08005.
- 2695 [59] ALICE Collaboration. The alice experiment at the cern lhc. *Journal of Instrumentation*, 3(08):  
 2696 S08002, 2008. URL <http://stacks.iop.org/1748-0221/3/i=08/a=S08002>.
- 2697 [60] ATLAS Collaboration. Luminosity Determination in  $pp$  Collisions at  $\sqrt{s} = 7$  TeV Using the  
 2698 ATLAS Detector at the LHC. *Eur. Phys. J.*, C 71:1630, 2011. doi: 10.1140/epjc/s10052-011-1630-5.
- 2699 [61] M Capeans, G Darbo, K Einsweiller, M Elsing, T Flick, M Garcia-Sciveres, C Gemme, H Perneg-  
 2700 ger, O Rohne, and R Vuillermet. ATLAS Insertable B-Layer Technical Design Report. Tech-  
 2701 nical Report CERN-LHCC-2010-013, ATLAS-TDR-19, CERN, Geneva, Sep 2010. URL  
 2702 <https://cds.cern.ch/record/1291633>.
- 2703 [62] Y Giomataris, Ph. Rebourgeard, J.P. Robert, and G. Charpak. Micromegas: a high-granularity  
 2704 position-sensitive gaseous detector for high particle-flux environments. *Nuclear Instruments  
 2705 and Methods in Physics Research Section A: Accelerators, Spectrometers, Detectors and As-  
 2706 sociated Equipment*, 376(1):29 – 35, 1996. ISSN 0168-9002. doi: [http://dx.doi.org/10.1016/0168-9002\(96\)00175-1](http://dx.doi.org/10.1016/0168-9002(96)00175-1). URL <http://www.sciencedirect.com/science/article/pii/0168900296001751>.
- 2708 [63] T Alexopoulos, J. Burnens, R. de Oliveira, G. Glonti, O. Pizzirusso, V. Polychronakos,  
 2709 G. Sekhniaidze, G. Tsipolitis, and J. Wotschack. A spark-resistant bulk-micromegas chamber for  
 2710 high-rate applications. *Nuclear Instruments and Methods in Physics Research Section A: Acceler-  
 2711 ators, Spectrometers, Detectors and Associated Equipment*, 640(1):110 – 118, 2011. ISSN 0168-9002.  
 2712 doi: <http://dx.doi.org/10.1016/j.nima.2011.03.025>. URL <http://www.sciencedirect.com/science/article/pii/S0168900211005869>.
- 2714 [64] Improved electron reconstruction in ATLAS using the Gaussian Sum Filter-based model for  
 2715 bremsstrahlung. Technical Report ATLAS-CONF-2012-047, CERN, Geneva, May 2012. URL  
 2716 <https://cds.cern.ch/record/1449796>.

- 2718 [65] W Lampl, S Laplace, D Lelas, P Loch, H Ma, S Menke, S Rajagopalan, D Rousseau, S Snyder,  
 2719 and G Unal. Calorimeter Clustering Algorithms: Description and Performance. Technical  
 2720 Report ATL-LARG-PUB-2008-002, ATL-COM-LARG-2008-003, CERN, Geneva, Apr 2008.  
 2721 URL <https://cds.cern.ch/record/1099735>.
- 2722 [66] Georges Aad et al. Topological cell clustering in the ATLAS calorimeters and its performance in  
 2723 LHC Run 1. 2016.
- 2724 [67] Matteo Cacciari, Gavin P. Salam, and Gregory Soyez. The Anti-k(t) jet clustering algorithm.  
 2725 *JHEP*, 04:063, 2008. doi: 10.1088/1126-6708/2008/04/063.
- 2726 [68] Georges Aad et al. Performance of Missing Transverse Momentum Reconstruction in Proton-  
 2727 Proton Collisions at 7 TeV with ATLAS. *Eur. Phys. J.*, C72:1844, 2012. doi: 10.1140/epjc/  
 2728 s10052-011-1844-6.
- 2729 [69] Aaron James Armbruster. Discovery of a Higgs Boson with the ATLAS detector. 2013. CERN-  
 2730 THESIS-2013-047.
- 2731 [70] G. Cowan, K. Cranmer, E. Gross, and O. Vitells. Asymptotic formulae for likelihood-based tests  
 2732 of new physics. *Eur. Phys. J.*, C 71:1554, 2011. doi: 10.1140/epjc/s10052-011-1554-0.
- 2733 [71] ATLAS Collaboration. Limits on the production of the Standard Model Higgs Boson in  $pp$   
 2734 collisions at  $\sqrt{s} = 7$  TeV with the ATLAS detector. *Eur. Phys. J.*, C 71:1728, 2011. doi: 10.1140/  
 2735 epjc/s10052-011-1728-9.
- 2736 [72] ATLAS Collaboration. Performance of the ATLAS muon trigger in  $pp$  collisions at  $\sqrt{s} = 8$   
 2737 TeV. *Eur. Phys. J. C*, (arXiv:1408.3179. CERN-PH-EP-2014-154):75. 19 p, Aug 2014. URL <https://cds.cern.ch/record/1749694>.
- 2739 [73] ATLAS collaboration. Electron trigger performance in 2012 ATLAS data, 2015. ATLAS-COM-  
 2740 DAQ-2015-091.
- 2741 [74] Paolo Nason. A new method for combining NLO QCD with shower Monte Carlo algorithms.  
 2742 *JHEP*, 11:040, 2004.
- 2743 [75] B. P. Kersevan and E. Richter-Was. The Monte Carlo event generator AcerMC version 2.0 with  
 2744 interfaces to PYTHIA 6.2 and HERWIG 6.5. 2004.
- 2745 [76] Nikolas Kauer and Giampiero Passarino. Inadequacy of zero-width approximation for a light  
 2746 Higgs boson signal. 2012.
- 2747 [77] T. Gleisberg, Stefan Hoeche, F. Krauss, M. Schonherr, S. Schumann, et al. Event generation with  
 2748 SHERPA 1.1. *JHEP*, 0902:007, 2009. doi: 10.1088/1126-6708/2009/02/007.

- 2749 [78] Michelangelo L. Mangano et al. ALPGEN, a generator for hard multiparton processes in  
 2750 hadronic collisions. *JHEP*, 0307:001, 2003. doi: 10.1088/1126-6708/2003/07/001.
- 2751 [79] Torbjorn Sjostrand, Stephen Mrenna, and Peter Z. Skands. PYTHIA 6.4 Physics and Manual.  
 2752 *JHEP*, 0605:026, 2006. doi: 10.1088/1126-6708/2006/05/026.
- 2753 [80] Torbjorn Sjostrand, Stephen Mrenna, and Peter Z. Skands. A Brief Introduction to PYTHIA 8.1.  
 2754 *Comput.Phys.Commun.*, 178:852–867, 2008. doi: 10.1016/j.cpc.2008.01.036.
- 2755 [81] G. Corcella et al. HERWIG 6: An event generator for hadron emission reactions with interfering  
 2756 gluons (including super-symmetric processes) . *JHEP*, 01:010, 2001. doi: 10.1088/1126-6708/2001/  
 2757 01/010.
- 2758 [82] J. M. Butterworth, Jeffrey R. Forshaw, and M. H. Seymour. Multiparton interactions in photo-  
 2759 production at HERA. *Z. Phys.*, C 72:637, 1996. doi: 10.1007/s002880050286.
- 2760 [83] Jun Gao, Marco Guzzi, Joey Huston, Hung-Liang Lai, Zhao Li, et al. The CT10 NNLO Global  
 2761 Analysis of QCD. *Phys.Rev.*, D89:033009, 2014. doi: 10.1103/PhysRevD.89.033009.
- 2762 [84] P. M. Nadolsky. Implications of CTEQ global analysis for collider observables. *Phys. Rev.*, D 78:  
 2763 013004, 2008. doi: 10.1103/PhysRevD.78.013004.
- 2764 [85] A. Sherstnev and R. S. Thorne. Parton distributions for the LHC. *Eur. Phys. J.*, C 55:553, 2009.  
 2765 doi: 10.1140/epjc/s10052-008-0610-x.
- 2766 [86] S. Agostinelli et al. GEANT4, a simulation toolkit. *Nucl. Instrum. Meth.*, A 506:250, 2003. doi:  
 2767 10.1016/S0168-9002(03)01368-8.
- 2768 [87] I. Stewart and F. Tackmann. Theory uncertainties for Higgs mass and other searches using jet  
 2769 bins. *Phys. Rev.*, D 85:034011, 2012. doi: 10.1103/PhysRevD.85.034011.
- 2770 [88] ATLAS Collaboration. Luminosity Determination in  $pp$  Collisions at  $\sqrt{s} = 7$  TeV Using the  
 2771 ATLAS Detector at the LHC. *Eur. Phys. J.*, C 71:1630, 2011. doi: 10.1140/epjc/s10052-011-1630-5.
- 2772 [89] Jet energy scale and its systematic uncertainty in proton-proton collisions at  $\sqrt{s} = 7$  tev with  
 2773 atlas 2011 data. *ATLAS-CONF-2013-004*, 2013.
- 2774 [90] Calibrating the  $b$ -tag efficiency and mistag rate in  $35 \text{ pb}^{-1}$  of data with the atlas detector.  
 2775 *ATLAS-CONF-2011-089*, 2011.
- 2776 [91] ATLAS Collaboration. Measurement of the  $b$ -tag Efficiency in a Sample of Jets Containing  
 2777 Muons with  $5 \text{ fb}^{-1}$  of Data from the ATLAS Detector. *ATLAS-CONF-2012-043*, 2012. URL  
 2778 <http://cdsweb.cern.ch/record/1435197>.

- 2779 [92] J. Alwall et al. The automated computation of tree-level and next-to-leading order differential  
2780 cross sections, and their matching to parton shower simulations. *JHEP*, 07:079, 2014.
- 2781 [93] Richard D. Ball et al. Parton distributions with LHC data. *Nucl. Phys. B*, 867:244, 2013.
- 2782 [94] ATLAS Collaboration. ATLAS Run 1 Pythia8 tunes. (ATL-PHYS-PUB-2014-021), Nov 2014.  
2783 URL <https://cds.cern.ch/record/1966419>.
- 2784 [95] M. Bahr et al. Herwig++ Physics and Manual. *Eur. Phys. J. C*, 58:639–707, 2008. doi: 10.1140/  
2785 epjc/s10052-008-0798-9.
- 2786 [96] Stefan Gieseke, Christian Rohr, and Andrzej Siódak. Colour reconnections in Herwig++. *Eur.*  
2787 *Phys. J. C*, 72:2225, 2012. doi: 10.1140/epjc/s10052-012-2225-5.
- 2788 [97] Simone Alioli, Paolo Nason, Carlo Oleari, and Emanuele Re. A general framework for imple-  
2789 menting NLO calculations in shower Monte Carlo programs: the POWHEG BOX. *JHEP*, 06:  
2790 043, 2010.
- 2791 [98] Peter Zeiler Skands. Tuning Monte Carlo Generators: The Perugia Tunes. *Phys. Rev. D*, 82:  
2792 074018, 2010. doi: 10.1103/PhysRevD.82.074018.
- 2793 [99] Michal Czakon and Alexander Mitov. Top++: A Program for the Calculation of the Top-Pair  
2794 Cross-Section at Hadron Colliders. 2011.
- 2795 [100] D. Krohn, J. Thaler, and L.-T. Wang. Jet Trimming. *JHEP*, 02:084, 2010. doi: 10.1007/  
2796 JHEP02(2010)084.
- 2797 [101] ATLAS Collaboration. Identification of Boosted, Hadronically Decaying W Bosons and Com-  
2798 parisons with ATLAS Data Taken at  $\sqrt{s} = 8$  TeV. 2015.
- 2799 [102] Expected Performance of Boosted Higgs ( $\rightarrow b\bar{b}$ ) Boson Identification with the ATLAS Detector  
2800 at  $\sqrt{s} = 13$  TeV. Technical Report ATL-PHYS-PUB-2015-035, CERN, Geneva, Aug 2015. URL  
2801 <https://cds.cern.ch/record/2042155>.
- 2802 [103] Matteo Cacciari and Gavin P. Salam. Pileup subtraction using jet areas. *Phys. Lett. B*, 659:119,  
2803 2008. doi: 10.1016/j.physletb.2007.09.077.
- 2804 [104] ATLAS Collaboration. Identification of boosted, hadronically-decaying  $W$  and  $Z$  bosons in  
2805  $\sqrt{s} = 13$  TeV Monte Carlo Simulations for ATLAS. (ATL-PHYS-PUB-2015-033), Aug 2015.  
2806 URL <https://cds.cern.ch/record/2041461>.
- 2807 [105] ATLAS Collaboration. Calibration of  $b$ -tagging using dileptonic top pair events in a combina-  
2808 torial likelihood approach with the ATLAS experiment. (ATLAS-CONF-2014-004), 2014. URL  
2809 <http://cds.cern.ch/record/1664335>.

<sup>2810</sup> [106] ATLAS Collaboration. Performance of  $b$ -Jet Identification in the ATLAS Experiment. 2015.

<sup>2811</sup> [107] Alexander L. Read. Presentation of search results: The CL(s) technique. *J. Phys. G*, 28:2693,  
<sup>2812</sup> 2002. doi: 10.1088/0954-3899/28/10/313.



**T**HIS THESIS WAS TYPESET using L<sup>A</sup>T<sub>E</sub>X, originally developed by Leslie Lamport and based on Donald Knuth's T<sub>E</sub>X.

The body text is set in 11 point Egenolff-Berner Garamond, a revival of Claude Garamont's humanist typeface. The above illustration, *Science Experiment 02*, was created by Ben Schlitter and released under CC BY-NC-ND 3.0. A template that can be used to format a PhD dissertation with this look & feel has been released under the permissive AGPL license, and can be found online at [github.com/asm-products/Dissertate](https://github.com/asm-products/Dissertate) or from its lead author, Jordan Suchow, at [suchow@post.harvard.edu](mailto:suchow@post.harvard.edu).